Layered Calcium Cobaltite Based Ceramics for Thermoelectric Applications

A thesis submitted to The University of Manchester for the degree of Doctor of Philosophy

in the Faculty of Science and Engineering

Year of Submission

2021

Jincheng Yu

Department of Materials

List of Contents

List of Contents 1

List of Figures 6

List of Tables 17

Abstract 19

Declaration 20

Copyright Statement 21

Acknowledgements 22

Glossary of Terms 24

1. Introduction 25

1.1 Overview 25

1.2 Objectives 27

1.3 Introduction to Chapters 28

References 29

2. Literature Review 32

2.1 Definition and History of Thermoelectric Effects 32

2.2 Basic Principles 33

2.2.1 Seebeck Coefficient 33

2.2.2 Peltier Coefficient 36

2.2.3 Thomson Coefficient 37

2.2.4 Electrical Conductivity 38

2.2.5 Thermal Conductivity 40

2.2.6 Thermoelectric Figure of Merit 43

2.3 Optimisation of Thermoelectric Properties 44

2.3.1 Element Doping 45

2.3.2 Nano-sized Materials 46

2.3.3 Phonon-Glass Electron-Crystal (PGEC) 48

2.4 Thermoelectric Applications 48

2.5 Layered Thermoelectric Oxides 50

2.5.1 Bi-Cu-Ch-O System (Ch = S, Se, Te) 50

2.5.2 Na-Co-O System 52

2.5.3 Bi-AE-Co-O System (AE = Ca, Sr, Ba) 54

2.6 Ca-Co-O System – Model Thermoelectric Material 55

2.6.1 Crystal Structure 55

2.6.2 Electrical Transport 57

2.6.3 Thermal Transport 58

2.6.4 Anisotropy of Textured Polycrystalline Samples 60

2.6.5 Effects of Fabrication Routes 61

2.6.6 Effects of Inclusions 63

2.6.7 Effects of Calcium-site Doping 64

2.6.8 Effects of Cobalt-site Doping 66

2.6.9 Effects of Dual Doping 67

References 68

3. Experimental Methods 80

3.1 Raw Materials 80

3.2 Powder Preparation 80

3.3 Ceramic and Film Preparation 81

3.4 Density and Porosity Measurement 82

3.5 X-ray Diffraction (XRD) 83

3.6 XRD Refinement 85

3.7 Scanning Electron Microscopy (SEM) 87

3.8 Transmission Electron Microscopy (TEM) 90

3.9 X-Ray Photoelectron Spectroscopy (XPS) 92

3.10 Electrical Transport Properties Measurement 93

3.10.1 Electrical Conductivity Measurement 93

3.10.2 Seebeck Coefficient Measurement 94

3.11 Thermal Conductivity Measurement 95

3.11.1 Specific Heat Capacity Measurement 95

3.11.2 Thermal Diffusivity Measurement 96

References 97

4. Modulation of Electrical Transport in Calcium Cobaltite Ceramics and Thick Films 100

4.1 Introduction 100

4.2 Characterisation of Raw Materials 101

4.2.1 XRD Analysis 101

4.2.2 SEM Analysis 102

4.3 Characterisation of Calcined Powders 103

4.3.1 XRD Analysis 103

4.3.2 SEM-EDS Analysis 104

4.4 Calcium Cobaltite Ceramics Prepared by Solid State Reaction 105

4.4.1 Density and Porosity 105

4.4.2 XRD Analysis 106

4.4.3 SEM-EDS Analysis 109

4.4.4 TEM Analysis 112

4.4.5 Electrical Transport 113

4.5 Calcium Cobaltite Thick Films Prepared by Screen Printing 118

4.5.1 XRD Analysis 118

4.5.2 SEM-EDS Analysis 122

4.5.3 XPS Analysis 126

4.5.4 Electrical Transport 128

4.6 Summary 131

References 132

5. Enhancing Thermoelectric Performance of Calcium Cobaltite Ceramics by Optimising Chemical Composition and the Annealing Process 138

5.1 Introduction 138

5.2 $Ca_{3-x}Bi_xCo_yO_{9+\delta}$ Ceramics Prepared by the SPS Route 139

5.2.1 Density 139

5.2.2 XRD Analysis 139

5.2.3 SEM-EDS Analysis 140

5.2.4 XPS Analysis 144

5.2.5 Electrical Transport 145

5.3 SPS-processed $Ca_{3-x}Bi_xCo_yO_{9+\delta}$ Ceramics Annealed at Different Temperatures 149

5.3.1 Density 149
5.3.2 XRD Analysis 149
5.3.3 SEM-EDS Analysis 153
5.3.4 TEM Analysis 157
5.3.5 XPS Analysis 160
5.3.6 Electrical Transport 163
5.3.7 Thermal Transport 169
5.3.8 Thermoelectric Figure of Merit (ZT) 173
5.4 Summary 173
References 174
6. Tuning the Power Factor of Cold Sintered Calcium Cobaltite Ceramics by Optimising Heat-treatment 181
6.1 Introduction 181
6.2 Density and Porosity 182
6.3 XRD Analysis 183
6.4 SEM-EDS Analysis 187
6.5 XPS Analysis 196
6.6 Electrical Transport 197
6.7 Summary 201
References 201
7. Modulation of Thermoelectric Response in Calcium Cobaltite Ceramics Through Co-doping via Different Fabrication Routes 204
7.1 Introduction 204
7.2 Density and Porosity 205
7.3 XRD Analysis 206
7.4 SEM-EDS Analysis 209
7.5 TEM Analysis 215
7.6 XPS Analysis 218
7.7 Electrical Transport 219
7.8 Thermal Transport 223

7.9 Thermoelectric Figure of Merit (ZT) 226

7.10 Summary 227

References 228

8. Conclusions and Recommendations for Future Work 232

8.1 Conclusions 232

8.1.1 Modulation of electrical transport in calcium cobaltite ceramics and thick films 233

8.1.2 Enhancing thermoelectric performance of calcium cobaltite ceramics by optimising chemical composition and annealing process 234

8.1.3 Tuning the power factor of cold sintered calcium cobaltite ceramics by optimising heat-treatment 235

8.1.4 Modulation of thermoelectric response in calcium cobaltite ceramics through co-doping via different fabrication routes 236

8.2 Recommended experiments for Future Work 237

8.2.1 Rietveld refinement fitting for XRD data 237

8.2.2 Optimising the loading content and selection of the substrate for film fabrication 237

8.2.3 Elemental doping at Co sites in calcium cobaltite 238

8.2.4 Direct measurement of carrier concentration and mobility via the Hall effect 238

8.2.5 Preparing thicker cold sintered calcium cobaltite ceramics 238

8.2.6 Advanced characterisation of synthesized samples 238

8.3 Scientific direction for Future Work 239

9. Appendix: List of Papers and Presentations 239

Final word count (excluding the bibliography and appendices)**: 52386**

List of Figures

Fig. 1.1 Efficiency of 'best practice mechanical' heat engines compared with an optimistic thermoelectric estimate (the average ZT values are presented), taken from Vining [13]....26

Fig. 2.1 Seebeck Effect for power generation, taken from Zhang and Zhao [2] 32

Fig. 2.2 Peltier Effect for active refrigeration, taken from Zhang and Zhao [2].....33

Fig. 2.3 Density of states for metals and semiconductors, taken from Biswas et al. [11] ...34

Fig. 2.4 The effects of temperature (a) and carrier concentration (b) on band asymmetry in density of states for $SrTiO_3$, taken from Abutaha et al. [14].....35

Fig. 2.5 Schematic diagram for Ohm's Law.....38

Fig. 2.6 The ratio of conversion efficiency to the Carnot efficiency as a function of the average ZT, taken from Tritt [9] 44

Fig. 2.7 The thermoelectric properties dependence of the carrier concentration (Trends shown were modelled from Bi_2Te_3), taken from Snyder and Toberer [38].....45

Fig. 2.8 Ionic processes for donor level (a) and accepter level (b) in the energy band (the solid sphere is the electron and the hollow sphere is the hole) 46

Fig. 2.9 DoS for a bulk 3D crystalline semiconductor, a 2D quantum well, a 1D nanowire or nanotube, and a 0D quantum dot, taken from Dresselhaus et al. [37] 47

Fig. 2.10 Thermoelectric module showing the direction of heat flow on both cooling and power generation, taken from Snyder and Toberer [38].....49

Fig. 2.11 (a) Crystal structure of BiCuChO, taken from Zhou et al. [60]; (b) ZT vs. temperature of typical current thermoelectric materials, taken from Zhao et al. [39] 51

Fig. 2.12 (a) The schematic figure for band gap tuning (CB: conduction band; VB: valence band), (b) Dependence of electrical conductivity on temperature for Te doped BiCuSeO, taken from Liu et al. [68] 52

Fig. 2.13 Crystal structure of four different phases of sodium cobaltites (Symbols A, B, and C in the schematic figures represent layers of oxygen with different stacking sequences), taken from Lei et al. [73].....53

Fig. 2.14 (a) Crystal structure of $Bi_2Sr_2Co_2O_y$, taken from Ohtaki [85]; (b) ZT vs T for $Bi_2Sr_2Co_2O_y$ whisker (1), p-b-Zn_4Sb_3 (2), p-TeAgGeSb (3), p-$CeFe_4Sb_{12}$ (4), and p-Si-Ge alloy (5), taken from Funahashi and Shikano [87].....55

Fig. 2.15 (a) The structure of pristine CCO with an approximate 5/3 unit cell along the [100] and (b) [010] (X_3 represents the rock salt layer), taken from Hu et al. [98]; (c) Simplified CCO structure for one unit cell plus an extra CoO_2 layer, taken from Ohtaki [85].....56

Fig. 2.16 The projection of the misfit average structure $[Ca_2CoO_3][CoO_2]_{1.62}$ along the *b* axis and the central layer is characterized by split disordered sites for Co and O, taken from Grebille et al. [102] 56

Fig. 2.17 (a) HRTEM images of $Ca_3Co_4O_9$ in [100] zone-axis, taken from Masset et al. [96]; (b) Theoretical calculated image for $Ca_3Co_4O_9$ in [100] zone-axis, taken from Masset et al. [96]; (c) SAED patterns of $Ca_3Co_4O_9$ in [001] zone-axis, taken from Seo et al. [103] 57

Fig. 2.18 Single crystal $Ca_3Co_4O_9$: (a) SEM image; (b) Electrical resistivity vs. T; (c) Seebeck coefficient vs. T, taken from Shikano and Funahashi [104].....57

Fig. 2.19 Electrical resistivity (a) and Seebeck coefficient (b) of polycrystalline $Ca_3Co_4O_9$ samples as a function of temperature (sample groups: (1) 900 ºC/1 h + manual grinding; (2) 900 ºC/10 h + manual grinding; (3) 900 ºC/20 h + manual grinding; (4) 900 ºC/20 h + ball milling), adapted from Obata et al. [105].....58

Fig. 2.20 (a) Temperature dependences of thermal conductivity for single crystal $Ca_3Co_4O_9$; (b) Phonon thermal conductivity vs. T^{-1} plot for single crystal $Ca_3Co_4O_9$, taken from Shikano and Funahashi [104].....59

Fig. 2.21 Behaviour of polycrystalline $Ca_3Co_4O_9$ samples: (a) Temperature dependence of thermal conductivity, (b) phonon thermal conductivity, (c) carrier thermal conductivity, (d) lattice thermal conductivity vs. 1000/T plot, taken from Gunes et al. [108] 60

Fig. 2.21 Temperature dependence of the power factor (a) and ZT values (b) for textured calcium cobaltite in different directions (the label for the direction is with respect to the pressure direction), taken from Wu et al. [111] 61

Fig. 2.22 Temperature dependence of the electrical resistivity (a), Seebeck coefficient (b) and power factor (c) of $Ca_3Co_4O_9$ prepared by solid-state reaction (blue), attrition milling (black), coprecipitation with ammonium carbonate (green) and oxalic acid (red), taken from Sotelo et al. [114].....62

Fig. 2.23 Temperature dependence of the electrical resistivity (a) and power factor (b) of $Ca_3Co_4O_9$ prepared by conventional solid-state reaction, hot pressing and SPS route, taken from Kenfaui et al. [115].....63

Fig. 2.24 Temperature dependence of the electrical resistivity (a), Seebeck coefficient (b) and power factor (c) of $Ca_3Co_4O_9$ with different levels of Ag addition, taken from Mikami et al. [124] 64

Fig. 2.25 Temperature dependence of the electrical resistivity (a), Seebeck coefficient (b), thermal conductivity (c) and ZT values (d) of Ba doped $Ca_3Co_4O_9$, taken from Carvillo et al. [129] 65

Fig. 2.26 Temperature dependence of the electrical resistivity (a), Seebeck coefficient (b), thermal conductivity (c) and ZT values (d) of $Ca_3Co_{4-x}M_xO_9$ (M = Fe, Mn and Cu), taken from Wang et al. [12] 66

Fig. 2.27 Temperature dependence of the electrical resistivity (a), Seebeck coefficient (b), thermal conductivity (c) and ZT values (d) of $Ca_{3-x-y}Ag_xLu_yCo_4O_{9+\delta}$ ceramics, taken from Nong et al. [133] 67

Fig. 3.1 Diagram showing how the pellets were used for property measurements (A. for SEM; B. for XRD and XPS; C. for ZEM; D: for TEM; E: for DSC; F: for LFA).....82

Fig. 3.2 Diagram illustrating Bragg's law, adapted from Cullity et al. [2].....84

Fig. 3.3 Bragg-Brentano Geometry for XRD Setup, adapted from Bocher [3].....84

Fig. 3.4 Schematic diagram for the profile intensity partitioning, taken from Le Bail et al. [7] 86

Fig. 3.5 Schematic diagram of interaction effects of the incident beam with the sample, adapted from Zhou et al. [8].....87

Fig. 3.6 Diagram of a typical SEM with different detectors along with the signal outputs, taken from Inkson et al. [9].....89

Fig. 3.7 Diagram of the internal structure of a transmission electron microscopy, taken from Carter and Williams [14].....91

Fig. 3.8 Photoelectron emission process, taken from Sardela [16].....92

Fig. 3.9 Setup for the Ulvac ZEM-III instrument, taken from the operation manual [17] ..93

Fig. 3.10 Schematic representation of the four probe mode, taken from Hasegawa et al. [18] 94

Fig. 3.11 The specific heat capacity ($\mathbf{C_p}$) calculation using the ratio method, taken from O'Neill [19] 96

Fig. 3.12 Schematic diagram of laser flash technique, taken from Borup et al. [23].....97

Fig. 4.1 XRD patterns of the raw materials (a. $CaCO_3$; b. Co_3O_4; c. Bi_2O_3) 102

Fig. 4.2 SE (a, c, e) and BSE (b, d, f) SEM images of the raw materials (a,b: $CaCO_3$; c.d: Co_3O_4; e,f: Bi_2O_3) 103

Fig. 4.3 XRD patterns of $Ca_{2.7}Bi_{0.3}Co_yO_{9+\delta}$ powders calcined at 1203 K for 12 h (a. overall view, b. enlarged region).....104

Fig. 4.4 SE (a-c) and BSE (d-f) SEM images of $Ca_{2.7}Bi_{0.3}Co_yO_{9+\delta}$ powders calcined at 1203 K for 12 h 105

Fig. 4.5 Bulk density (a) and porosity (b) of $Ca_{2.7}Bi_{0.3}Co_yO_{9+\delta}$ (y = 3.92, 3.96 and 4.0) ceramics prepared by solid state reaction as a function of cobalt content 106

Fig. 4.6 XRD patterns of $Ca_{2.7}Bi_{0.3}Co_yO_{9+\delta}$ (y = 3.92, 3.96 and 4.0) ceramics prepared by solid state reaction (a. overall view, b. enlarged region) 107

Fig. 4.7 Le Bail refinement data for $Ca_{2.7}Bi_{0.3}Co_yO_{9+\delta}$ ceramics (a. y = 4.0, b. y = 3.96, c. y = 3.92) 108

Fig. 4.8 Refined lattice parameters for $Ca_{2.7}Bi_{0.3}Co_yO_{9+\delta}$ ceramics prepared by solid state reaction.....109

Fig. 4.9 BSE SEM images of sintered surfaces for $Ca_{2.7}Bi_{0.3}Co_yO_{9+\delta}$ ceramics prepared by solid state reaction (a. y = 4.0; b. y = 3.96; c. y = 3.92).....110

Fig. 4.10 (a) SEM image of the fracture surface of $Ca_{2.7}Bi_{0.3}Co_{3.96}O_{9+\delta}$ bulk ceramic and (b) the corresponding EDS line analysis 111

Fig. 4.11 (a) SEM image of the fracture surface of $Ca_{2.7}Bi_{0.3}Co_{3.96}O_{9+\delta}$ bulk ceramic and (b-d) the corresponding EDS point analyses at sites 1-3.....112

Fig. 4.12 TEM data for $Ca_{2.7}Bi_{0.3}Co_{3.92}O_{9+\delta}$ ceramic sintered at 1203 K for 12 h (a. bright field TEM image; b. dark field TEM image; c. HRTEM image; d. high magnification of the circular region in Fig. 4.4.3(c); e. [001] SAED patterns) 113

Fig. 4.13 Electrical transport properties of $Ca_{2.7}Bi_{0.3}Co_yO_{9+\delta}$ ceramics as a function of temperature (a. electrical conductivity; b. Seebeck coefficient; c. power factor).....115

Fig. 4.14 $\ln(\sigma T)$ as a function of reciprocal temperature (a) and calculated activation energy (b) for $Ca_{2.7}Bi_{0.3}Co_yO_{9+\delta}$ ceramics prepared by solid state reaction (the lines are linearly fitted by a least-square method).....115

Fig. 4.15 The electrical conductivity of $Ca_{2.7}Bi_{0.3}Co_yO_{9+\delta}$ (y = 3.92, 3.96 and 4.0) ceramics as a function of porosity (a), average grain size (b) and lattice parameter *c* (c) 117

Fig. 4.16 Calculated carrier concentration and carrier mobility for $Ca_{2.7}Bi_{0.3}Co_yO_{9+\delta}$ ceramics prepared by solid state reaction 117

Fig. 4.17 XRD patterns of as-received $Ca_{2.7}Bi_{0.3}Co_{3.92}O_{9+\delta}$ thick films and films sintered at different sintering conditions (a. 1153 K for 4, 8 and 12 h; b. 1203 K for 4, 8 and 12 h) . 119

Fig. 4.18 Lotgering factors for $Ca_{2.7}Bi_{0.3}Co_{3.92}O_{9+\delta}$ thick films sintered at 1153 K and 1203 K for 4, 8 and 12 h 119

Fig. 4.19 Le Bail refinement data for sintered $Ca_{2.7}Bi_{0.3}Co_{3.92}O_{9+\delta}$ thick films (a. 1153 K_4 h, b. 1153 K_8 h, c. 1153 K_12 h, d. 1203 K_4 h, e. 1203 K_8 h, f. 1203 K_12 h) 121

Fig. 4.20 Refined lattice parameters for $Ca_{2.7}Bi_{0.3}Co_yO_{9+\delta}$ thick films sintered at 1153 K and 1203 K for 4, 8 and 12 h 122

Fig. 4.21 BSE SEM images of $Ca_{2.7}Bi_{0.3}Co_yO_{9+\delta}$ thick films sintered under the following conditions: a-c: 1153 K for 4, 8 and 12 h; e-f: 1203 K for 4, 8 and 12 h 124

Fig. 4.22 SE SEM images for the fracture surface of $Ca_{2.7}Bi_{0.3}Co_yO_{9+\delta}$ thick films sintered at 1203 K for 8 h (a. thickness of Al_2O_3 substrate, b. thickness of CCO film, c. morphology near the top surface, d. morphology near the interface, e. schematic diagram for grain distributions in the order-disorder regions) 126

Fig. 4.23 High-resolution XPS spectra of Co 2p 3/2 for $Ca_{2.7}Bi_{0.3}Co_{3.92}O_{9+\delta}$ thick films sintered at different temperatures (a. 1153 K; b. 1203 K) for 4, 8 and 12 h 127

Fig. 4.24 Electrical conductivity (a), Seebeck coefficient (b) and power factor (c) of $Ca_{2.7}Bi_{0.3}Co_yO_{9+\delta}$ thick films sintered at 1153 and 1203 K for 4-12 h as a function of temperature 130

Fig. 4.25 Electrical conductivity (a) and Seebeck coefficient (b) at 323 K for $Ca_{2.7}Bi_{0.3}Co_yO_{9+\delta}$ thick films sintered at different temperature as a function of dwelling time 131

Fig. 5.1 Density of $Ca_{3-x}Bi_xCo_yO_{9+\delta}$ ceramics prepared by the SPS route as a function of (a) bismuth and (b) cobalt content 139

Fig. 5.2 XRD patterns of $Ca_{3-x}Bi_xCo_yO_{9+\delta}$ ceramics prepared by the SPS route (a. overall view, b. enlarged region) 140

Fig. 5.3 Backscattered electron SEM images of polished surfaces for $Ca_{2.7}Bi_{0.3}Co_yO_{9+\delta}$ ceramics (a-c: y = 4.0, 3.96 and 3.92, respectively) and $Ca_{3-x}Bi_xCo_{3.92}O_{9+\delta}$ ceramics (c-e: x = 0.3, 0.2 and 0.1, respectively) prepared by the SPS route 141

Fig. 5.4 EDS mapping data for the polished surfaces of $Ca_{2.7}Bi_{0.3}Co_{3.92}O_{9+\delta}$ ceramics prepared by the SPS route 143

Fig. 5.5 EDS point analyses for the main phase in $Ca_{2.7}Bi_{0.3}Co_{3.92}O_{9+\delta}$ ceramics prepared by the SPS route 143

Fig. 5.6 XPS survey spectra for $Ca_{3-x}Bi_xCo_yO_{9+\delta}$ ceramics prepared by the SPS route 144

Fig. 5.7 High resolution core-level spectra of Co 2p 3/2 for $Ca_{3-x}Bi_xCo_yO_{9+\delta}$ ceramics prepared by the SPS route 145

Fig. 5.8 Electrical transport properties of SPS-processed $Ca_{3-x}Bi_xCo_yO_{9+\delta}$ ceramics as a function of temperature (a. electrical conductivity; b. Seebeck coefficient; c. power factor) 147

Fig. 5.9 Electrical conductivity (a) and Seebeck coefficient (b) at 823 K for SPS-processed $Ca_{2.7}Bi_{0.3}Co_yO_{9+\delta}$ ceramics as a function of cobalt content 148

Fig. 5.10 ln(σT) as a function of reciprocal temperature (a) and calculated activation energies (b) for $Ca_{3-x}Bi_xCo_yO_{9+\delta}$ ceramics prepared by the SPS route (The lines are linearly fitted by a least-square method) 148

Fig. 5.11 Density of SPS-processed $Ca_{3-x}Bi_xCo_yO_{9+\delta}$ ceramics annealed at different temperatures for 12 h (a. as a function of bismuth content, b. as a function of cobalt content) 149

Fig. 5.12 XRD patterns of SPS-processed $Ca_{3-x}Bi_xCo_yO_{9+\delta}$ ceramics annealed for 12 h at temperatures of (a) 1023 K and (b) 1203 K 150

Fig. 5.13 Lotgering factors for SPS-processed $Ca_{3-x}Bi_xCo_yO_{9+\delta}$ ceramics annealed at 1203 K for 12 h as a function of bismuth and cobalt content 151

Fig. 5.14 Le Bail refinement data for SPS-processed $Ca_{3-x}Bi_xCo_yO_{9+\delta}$ ceramics annealed at 1203 K for 12 h (a. x = 0.3, y = 4.0; b. x = 0.3, y = 3.96; c. x = 0.3, y = 3.92; d. x = 0.2, y = 3.92; e. x = 0.1, y = 3.92) 152

Fig. 5.15 Refined lattice parameters for SPS-processed $Ca_{3-x}Bi_xCo_yO_{9+\delta}$ ceramics annealed at 1203 K for 12 h as a function of bismuth and cobalt content 153

Fig. 5.16 Backscattered electron SEM images of polished surfaces for SPS-processed $Ca_{3-x}Bi_xCo_yO_{9+\delta}$ ceramics annealed at 1023 K (a-e) and 1203 K (f-j) 154

Fig. 5.17 EDS mapping data for polished surfaces of SPS-processed $Ca_{2.7}Bi_{0.3}Co_{3.92}O_{9+\delta}$ ceramics annealed at 1023 K (a) and 1203 K (b) 155

Fig. 5.18 Secondary electron SEM images of fracture surfaces for SPS-processed $Ca_{3-x}Bi_xCo_yO_{9+\delta}$ ceramics annealed at 1203 K 157

Fig. 5.19 TEM data for SPS-processed $Ca_{2.7}Bi_{0.3}Co_{3.92}O_{9+\delta}$ ceramics annealed at 1203 K; sample prepared by FIB method (a. low magnification; b. high-resolution; c. SAED patterns) 158

Fig. 5.20 TEM data for SPS-processed $Ca_{2.7}Bi_{0.3}Co_{3.92}O_{9+\delta}$ ceramics annealed at 1203 K prepared by the standard crushing method (a. SAED pattern in [001] zone axis; b. corresponding HRTEM image) 159

Fig. 5.21 TEM data for SPS-processed $Ca_{2.7}Bi_{0.3}Co_{3.92}O_{9+\delta}$ ceramics annealed at 1203 K prepared by the standard crushing method (a: low magnification ; b: [100] HRTEM image; c: the corresponding FFT image in [100] zone axis; d: the inverse FFT image of the rectangular region) 159

Fig. 5.22 High-resolution XPS spectra of Ca 2p for SPS-processed $Ca_{3-x}Bi_xCo_yO_{9+\delta}$ ceramics annealed at 1203 K 161

Fig. 5.23 High-resolution XPS spectra of Co 2p 3/2 for SPS-processed $Ca_{3-x}Bi_xCo_yO_{9+\delta}$ ceramics annealed at 1203 K 162

Fig. 5.24 High-resolution XPS spectra of O 1s for SPS-processed $Ca_{3-x}Bi_xCo_yO_{9+\delta}$ ceramics annealed at 1203 K 163

Fig. 5.25 Electrical transport properties of SPS-processed $Ca_{3-x}Bi_xCo_yO_{9+\delta}$ ceramics annealed at 1023 K (a-c) and 1203 K (d-f) 165

Fig. 5.26 Electrical conductivity and Seebeck coefficient at 323 K for annealed SPS-processed $Ca_{3-x}Bi_xCo_yO_{9+\delta}$ ceramics as a function of bismuth content (a, b) and cobalt content (c, d) 167

Fig. 5.27 $\ln(\sigma T)$ versus as a function of reciprocal temperature (a) and calculated activation energy (b) for SPS-processed $Ca_{3-x}Bi_xCo_yO_{9+\delta}$ ceramics annealed at 1203 K (The lines are linearly fitted by a least-square method) 168

Fig. 5.28 Calculated carrier concentration and mobility for SPS-processed $Ca_{3-x}Bi_xCo_yO_{9+\delta}$ ceramics annealed at 1203 K as a function of bismuth content (a) and cobalt content (b) 168

Fig. 5.29 (a) Total κ ($\perp ab$) and (b) lattice and electronic κ ($\perp ab$) for SPS-processed $Ca_{3-x}Bi_xCo_yO_{9+\delta}$ ceramics annealed at 1203 K 169

Fig. 5.30 (a) $\kappa_{lattice}$ as a function of the reciprocal temperature and (b) the phonon mean free path as a function of bismuth and cobalt content 171

Fig. 5.31 (a) (κ//ab) /(κ ⊥ ab) ratios for $Ca_3Co_4O_9$ based ceramics prepared by the SPS route; (b) κ(//ab) for textured $Ca_{2.7}Bi_{0.3}Co_4O_{9+\delta}$ ceramics in our work and previous studies 172

Fig. 5.32 Temperature dependence of total κ parallel (κ//ab) and perpendicular (κ ⊥ ab) to the *ab* plane for SPS-processed $Ca_{3-x}Bi_xCo_yO_{9+\delta}$ ceramics annealed at 1203 K (estimated using the optimised (κ//ab) /(κ ⊥ ab) ratio) 172

Fig. 5.33 Temperature dependence of ZT//ab values (calculated using the estimated thermal conductivity) of SPS-processed samples annealed at 1203 K 173

Fig. 6.1 Bulk density and porosity of cold sintered $Ca_{2.7}Bi_{0.3}Co_{3.92}O_{9+\delta}$ ceramics prepared from (a) the single-fired powders and (b) double-fired powders.....183

Fig. 6.2 XRD patterns of $Ca_{2.7}Bi_{0.3}Co_{3.92}O_{9+\delta}$ powders calcined at different conditions...184

Fig. 6.3 XRD patterns of cold sintered $Ca_{2.7}Bi_{0.3}Co_{3.92}O_{9+\delta}$ ceramics annealed at 1203 K for different times: (a) S1A0: 0h, S1A12: 12 h, S1A24: 24 h, and (b) S2A0: 0 h, S2A12: 12 h, S2A24: 24 h 184

Fig. 6.4 Le Bail refinement data for annealed $Ca_{2.7}Bi_{0.3}Co_{3.92}O_{9+\delta}$ ceramics prepared by cold sintering (a. S1A12, b. S1A24, c. S2A12, d. S2A24) 186

Fig. 6.5 Backscattered electron SEM images for $Ca_{2.7}Bi_{0.3}Co_{3.92}O_{9+\delta}$ powders calcined at 1203 K for 12 h (a, b) and powders calcined twice at 1203 K for 12 h (c, d).....188

Fig. 6.6 Backscattered electron SEM images for polished surfaces of cold sintered $Ca_{2.7}Bi_{0.3}Co_{3.92}O_{9+\delta}$ ceramics prepared from the single-fired powders (a, b: S1A0; c, d: S1A12; e, f: S1A24; a, c, e: low magnification; b, d, f: high magnification) 189

Fig. 6.7 EDS mapping data for polished surfaces of cold sintered $Ca_{2.7}Bi_{0.3}Co_{3.92}O_{9+\delta}$ ceramics prepared from single-fired powders (a. S1A0; b. S1A12; c. S1A24; the scale bar inset is 10 μm).....190

Fig. 6.8 Backscattered electron SEM images for polished surfaces of cold sintered $Ca_{2.7}Bi_{0.3}Co_{3.92}O_{9+\delta}$ ceramics prepared from the double-fired powders (a, b: S2A0; c, d: S2A12; e, f: S2A24; a, c, e: low magnification; b, d, f: high magnification) 192

Fig. 6.9 EDS mapping data for polished surfaces of cold sintered $Ca_{2.7}Bi_{0.3}Co_{3.92}O_{9+\delta}$ ceramics prepared from the double-fired powders (a. S2A0; b. S2A12; c. S2A24; the scale bar inset is 10 μm).....193

Fig. 6.10 Volume fractions of phases for cold sintered $Ca_{2.7}Bi_{0.3}Co_{3.92}O_{9+\delta}$ ceramics annealed under different conditions (main: calcium cobaltite; bright: Bi-rich phase; dark: Ca-Co-O compound; grey: cobalt oxide).....195

Fig. 6.11 Secondary electron SEM images of fracture surfaces for cold sintered $Ca_{2.7}Bi_{0.3}Co_{3.92}O_{9+\delta}$ ceramics (a. S1A12; b. S1A24; c. S2A12; d. S2A24) 195

Fig. 6.12 High-resolution XPS spectra of Co 2p 3/2 for annealed cold sintered $Ca_{2.7}Bi_{0.3}Co_{3.92}O_{9+\delta}$ ceramics (a. S1A12 and S1A24; b. S2A12 and S2A24).....196

Fig. 6.14 Electrical conductivity (a), Seebeck coefficient (b) and power factor (c) of cold sintered $Ca_{2.7}Bi_{0.3}Co_{3.92}O_{9+\delta}$ ceramics as a function of temperature, and power factors compared with previous work (d) [8,9].....198

Fig. 6.15 Electrical conductivity and Seebeck coefficient at 800 K for cold sintered $Ca_{2.7}Bi_{0.3}Co_{3.92}O_{9+\delta}$ ceramics as a function of annealing time (a, b), Lotgering factor (c, d) and porosity (e, f) 199

Fig. 6.16 (a) $\ln(\sigma T)$ as a function of reciprocal temperature and (b) calculated activation energies for $Ca_{2.7}Bi_{0.3}Co_{3.92}O_{9+\delta}$ ceramics prepared by cold sintering (the lines are fitted by a linear least-square method) 200

Fig. 7.1 Density and porosity of $Ca_{2.63}Bi_{0.3}M_{0.07}Co_{3.92}O_{9+\delta}$ (M = Sr and Ba) ceramics prepared by different fabrication routes 206

Fig. 7.2 XRD patterns of $Ca_{2.63}Bi_{0.3}M_{0.07}Co_{3.92}O_{9+\delta}$ (M = Sr and Ba) ceramics prepared by different fabrication routes.....207

Fig. 7.3 Lotgering factors for $Ca_{2.63}Bi_{0.3}M_{0.07}Co_{3.92}O_{9+\delta}$ (M = Sr and Ba) ceramics prepared by different fabrication routes.....207

Fig. 7.4 Le Bail refinement data for $Ca_{2.63}Bi_{0.3}M_{0.07}Co_{3.92}O_{9+\delta}$ (M = Sr and Ba) ceramics prepared by different fabrication routes (a. Sr_SSR, b. Ba_SSR, c. Sr_SPSAn, d. Ba_SPSAn) 208

Fig. 7.5 Backscattered electron SEM images of sintered (a, b) and polished (c-f) surfaces for $Ca_{2.63}Bi_{0.3}M_{0.07}Co_{3.92}O_{9+\delta}$ (M = Sr and Ba) ceramics prepared by different fabrication routes 211

Fig. 7.6 Backscattered electron SEM images of polished surfaces and corresponding EDS data for SPS-processed $Ca_{2.63}Bi_{0.3}Sr_{0.07}Co_{3.92}O_{9+\delta}$ ceramics annealed at 1203 K for 24 h (a. low magnification: ×1k; b. high magnification: ×10k) 212

Fig. 7.7 EDS point spectra of the main phase for $Ca_{2.63}Bi_{0.3}M_{0.07}Co_{3.92}O_{9+\delta}$ (M = Sr and Ba) ceramics prepared by different fabrication routes (a-f: sites 1-6 in Fig. 7.5).....213

Fig. 7.8 EDS mapping data for sintered and polished surfaces for $Ca_{2.63}Bi_{0.3}M_{0.07}Co_{3.92}O_{9+\delta}$ (M = Sr and Ba) ceramics prepared by different fabrication routes (a, b: sintered surfaces; c, d: polished surfaces; the inserted scale bars represent 10 μm) 214

Fig. 7.9 Secondary electron SEM images of fracture surfaces for $Ca_{2.63}Bi_{0.3}M_{0.07}Co_{3.92}O_{9+\delta}$ (M = Sr and Ba) ceramics prepared by different fabrication routes 215

Fig. 7.10 TEM images (a, c) and corresponding SAED patterns (b, d) of $Ca_{2.63}Bi_{0.3}Ba_{0.07}Co_{3.92}O_{9+\delta}$ ceramic prepared by solid state reaction 216

Fig. 7.11 HRTEM data for $Ca_{2.63}Bi_{0.3}Ba_{0.07}Co_{3.92}O_{9+\delta}$ ceramic prepared by solid state reaction (a. HRTEM image; b. FFT image of Area 1; c. FFT image of Area 2; d. IFFT image of Area 1; e. IFFT image of Area 2) 217

Fig. 7.12 TEM image (a) and corresponding SAED patterns (b) of secondary phases in SPS-processed $Ca_{2.63}Bi_{0.3}Sr_{0.07}Co_{3.92}O_{9+\delta}$ ceramics annealed at 1203 K for 24 h 217

Fig. 7.13 High-resolution XPS spectra of Co 2p 3/2 for $Ca_{2.63}Bi_{0.3}M_{0.07}Co_{3.92}O_{9+\delta}$ (M = Sr and Ba) ceramics prepared by different fabrication routes 218

Fig. 7.14 Electrical conductivity (a), Seebeck coefficient (b) and power factor (c) of $Ca_{2.63}Bi_{0.3}M_{0.07}Co_{3.92}O_{9+\delta}$ (M = Sr and Ba) ceramics prepared by different fabrication routes 221

Fig. 7.15 Electrical conductivity as a function of reciprocal temperature (a), calculated activation energies (b), calculated carrier concentration (c) and calculated carrier mobility (d) for $Ca_{2.63}Bi_{0.3}M_{0.07}Co_{3.92}O_{9+\delta}$ (M = Sr and Ba) ceramics prepared by different fabrication routes.....222

Fig. 7.16 Electrical conductivity and Seebeck coefficient at 323 K for $Ca_{2.63}Bi_{0.3}M_{0.07}Co_{3.92}O_{9+\delta}$ (M = Sr and Ba) ceramics prepared by SSR and SPSAn routes as a function of porosity (a, b), Lotgering factor (c, d) and average grain size (e, f).....223

Fig. 7.17 Total thermal conductivity (a) and lattice and electronic thermal conductivity (b) of $Ca_{2.63}Bi_{0.3}M_{0.07}Co_{3.92}O_{9+\delta}$ (M = Sr and Ba) ceramics prepared by different fabrication routes.....224

Fig. 7.18 (a) Lattice thermal conductivity as a function of reciprocal temperature and (b) phonon mean free path length of $Ca_{2.63}Bi_{0.3}M_{0.07}Co_{3.92}O_{9+\delta}$ (M = Sr and Ba) ceramics prepared by different fabrication routes.....226

Fig. 7.19 ZT values for $Ca_{2.63}Bi_{0.3}M_{0.07}Co_{3.92}O_{9+\delta}$ (M = Sr and Ba) ceramics prepared by different fabrication routes.....227

List of Tables

Table 3.1 Details of chemicals used for powder synthesis 80

Table 3.2 The parameters for X-ray powder diffraction instrumental setup.....85

Table 4.1 EDS point analyses for sites 1-3 in Fig. 4.4.....105

Table 4.2 EDS point analyses of different sites (sites 1-4) on SEM images in Fig. 4.9 111

Table 4.3 EDS point analyses at different sites (sites 1-6) shown in SEM images of thick films (Fig. 4.21) 123

Table 4.4 Fractions of cobalt ions in $Ca_{2.7}Bi_{0.3}Co_{3.92}O_{9+\delta}$ thick films sintered at 1153 K and 1203 K for 4, 8 and 12 h 127

Table 5.1 Volume fractions of phases in SPS-processed $Ca_{3-x}Bi_xCo_yO_{9+\delta}$ ceramics 142

Table 5.2 EDS point analysis for sites 1-3 in the surface of $Ca_{2.7}Bi_{0.3}Co_{3.92}O_{9+\delta}$ in the SEM image (Fig. 5.4).....143

Table 5.3 Concentrations of cobalt ions in $Ca_{3-x}Bi_xCo_yO_{9+\delta}$ ceramics prepared by the SPS route.....145

Table 5.4 Volume fractions of phases in SPS-processed $Ca_{3-x}Bi_xCo_yO_{9+\delta}$ ceramics annealed at different temperatures 155

Table 5.5 EDS point analyses of different sites 1-5 on the SEM image in Fig. 5.16 156

Table 5.6 Concentrations of cobalt ions in SPS-processed $Ca_{3-x}Bi_xCo_yO_{9+\delta}$ ceramics annealed at 1203 K.....162

Table 5.7 Oxygen concentrations in SPS-processed $Ca_{3-x}Bi_xCo_yO_{9+\delta}$ samples annealed at 1203 K.....163

Table 6.1 List of compositions, heat-treatment conditions and sample codes for cold sintered samples.....182

Table 6.2 Calculated Lotgering factors of annealed cold sintered $Ca_{2.7}Bi_{0.3}Co_{3.92}O_{9+\delta}$ ceramics.....185

Table 6.3 Refined lattice parameters for annealed $Ca_{2.7}Bi_{0.3}Co_yO_{9+\delta}$ ceramics prepared by cold sintering.....186

Table 6.4 EDS point analyses at sites 1-5 on the SEM images in Fig. 6.5 187

Table 6.5 EDS point analyses at sites 1-10 on the SEM images in Fig. 6.7 191

Table 6.6 EDS point analyses at sites 1-10 on the SEM images in Fig. 6.9 194

Table 6.7 Concentrations of cobalt ions in annealed cold sintered $Ca_{2.7}Bi_{0.3}Co_{3.92}O_{9+\delta}$ ceramics.....197

Table 7.1 List of compositions, fabrication routes, heat-treatment conditions and sample codes for synthesized samples 205

Table 7.2 Refined lattice parameters for $Ca_{2.63}Bi_{0.3}M_{0.07}Co_{3.92}O_{9+\delta}$ (M = Sr and Ba) ceramics prepared by different fabrication routes.....209

Table 7.3 EDS point analyses at sites 1-17 on the SEM images in Fig. 7.5.....212

Table 7.4 Volume fractions of different phases in $Ca_{2.63}Bi_{0.3}M_{0.07}Co_{3.92}O_{9+\delta}$ (M = Sr and Ba) ceramics prepared by different fabrication routes.....213

Table 7.5 Concentrations of cobalt ions in $Ca_{2.63}Bi_{0.3}M_{0.07}Co_{3.92}O_{9+\delta}$ (M = Sr and Ba) ceramics prepared by different fabrication routes.....219

Table 8.1 The power factor and ZT value of the optimal composition in different chapters 232

Abstract

Layer-structured calcium cobaltite is considered a promising p-type thermoelectric material due to its intrinsically low thermal conductivity and good high-temperature stability. In this study, the effects of composition, heat-treatment and fabrication route on the thermoelectric performance of calcium cobaltite-based materials were investigated in detail.

$Ca_{2.7}Bi_{0.3}Co_yO_{9+\delta}$ (y = 3.92-4.0) ceramics were prepared by solid state reaction. By introducing 2.0 at.% cobalt deficiency and 10.0 at.% Bi^{3+} substitution for Ca^{2+} in calcium cobaltite, the largest lattice expansion was achieved and poorly conducting secondary phases were efficiently reduced. However, the electrical conductivity showed strong dependence on porosity; the lowest porosity in $Ca_{2.7}Bi_{0.3}Co_{3.92}O_{9+\delta}$ ceramic resulted in much reduced carrier scattering, thereby leading to the highest power factor of 98.0 $\mu Wm^{-1}K^{-2}$ at 823 K. The optimal composition ($Ca_{2.7}Bi_{0.3}Co_{3.92}O_{9+\delta}$) was selected for fabrication of thick films by screen printing. When thick films were sintered at 1203 K for 8 h, the single-phase products exhibited the maximum power factor of 55.5 $\mu Wm^{-1}K^{-2}$ at 673 K. The enhanced electrical conductivity resulted mainly from the increased carrier concentration and increased mobility through control of the microstructure. An order-disorder transition in the structural arrangements of grains near the interface between the film and substrate is believed to result from constrained sintering caused by tensile stresses.

Highly dense $Ca_{3-x}Bi_xCo_yO_{9+\delta}$ (x = 0.1-0.3; y = 3.92-4.0) ceramics were successfully prepared by liquid-phase-assisted spark plasma sintering. The electrical conductivity of the original SPS-processed samples was severely limited by poorly conducting secondary phases. By annealing at 1023 K in air, the reaction forming calcium cobaltite was promoted, the texture was improved and more oxygen diffused into the crystal lattice, thereby leading to increased carrier concentration and mobility. Doping with 'heavy' Bi ions helped to increase lattice parameters and phonon scattering, while cobalt deficiency provided opportunities to generate crystalline defects. As a result, the maximum ZT value (//ab) of 0.16 at 823 K was achieved in $Ca_{2.7}Bi_{0.3}Co_{3.92}O_{9+\delta}$ ceramic annealed at 1203 K for 12 h.

Both single-fired and double-fired $Ca_{2.7}Bi_{0.3}Co_{3.92}O_{9+\delta}$ powders were densified by cold sintering. A double calcination process helped to reduce secondary phases in the resulting powders, thereby modifying phase composition and texture development in the cold sintered ceramics. The electrical conductivity was significantly enhanced by extending the annealing time, due to reduction of secondary phases and decreased grain boundary density. The maximum power factor of 0.28 $mWm^{-1}K^{-1}$ at 823 K was obtained for cold sintered samples prepared from the double-calcined powders annealed at 1203 K for 24 h.

$Ca_{2.63}Bi_{0.3}M_{0.07}Co_{3.92}O_{9+\delta}$ (M = Sr and Ba) ceramics were prepared by solid state reaction and spark plasma sintering. Bi and Sr dopants were confirmed to enter the crystal lattice, whilst the Ba dopant participated in forming Ba-rich phases. The electrical conductivity of the solid state synthesized samples was limited by the high porosity, although thermal conductivity was significantly reduced. The annealed Bi/Sr co-doped, SPS-processed samples showed enhanced electrical conductivity mainly due to the combined effects of severe lattice expansion, higher densification and improved texture. Furthermore, phonon transport was inhibited because of the higher porosity, atomic mass variations and strain field effects. The maximum ZT value of 0.14 at 800 K was achieved in both the solid state synthesized Bi/Ba co-doped and the annealed SPS-processed Bi/Sr co-doped samples.

Jincheng Yu for Doctor of Philosophy at The University of Manchester

'Layered Calcium Cobaltite Based Ceramics for Thermoelectric Applications'

Declaration

No portion of the work referred to in the thesis has been submitted in support of an application for another degree or qualification of this or any other university or other institute of learning.

Copyright Statement

i. The author of this thesis (including any appendices and/or schedules to this thesis) owns certain copyright or related rights in it (the "Copyright") and s/he has given The University of Manchester certain rights to use such Copyright, including for administrative purposes.

ii. Copies of this thesis, either in full or in extracts and whether in hard or electronic copy, may be made only in accordance with the Copyright, Designs and Patents Act 1988 (as amended) and regulations issued under it or, where appropriate, in accordance with licensing agreements which the University has from time to time. This page must form part of any such copies made.

iii. The ownership of certain Copyright, patents, designs, trade marks and other intellectual property (the "Intellectual Property") and any reproductions of copyright works in the thesis, for example graphs and tables ("Reproductions"), which may be described in this thesis, may not be owned by the author and may be owned by third parties. Such Intellectual Property and Reproductions cannot and must not be made available for use without the prior written permission of the owner(s) of the relevant Intellectual Property and/or Reproductions.

iv. Further information on the conditions under which disclosure, publication and commercialisation of this thesis, the Copyright and any Intellectual Property University IP Policy (see http://documents.manchester.ac.uk/display.aspx?DocID=24420), in any relevant Thesis restriction declarations deposited in the University Library, The University Library's regulations (see http://www.library.manchester.ac.uk/about/regulations/) and in The University's policy on Presentation of Theses.

Acknowledgements

In my eyes, the past four years I spent at The University of Manchester were a wonderful time for me. It was really an important experience, which coached me to master these four things: the confidence glowing on my face, the kindness hidden within my heart, the bones melting in my blood and the toughness engraving in my life. I will benefit from these priceless treasures.

I would like to show my deepest respect and gratitude toward my main supervisor, Prof. Robert Freer, who has kindly guided me all the time. Thank you very much for your patience and insightful comments which enable me an independent researcher during my PhD program. I am also grateful for the immediate support provided to get me through the difficulties I came across in both my experiments and my life.

I would like to thank Dr David Lewis, who took over the position of my co-supervisor in my third year. Thank you for your constructive suggestions and warm encouragement during the Christmas lunch, which is indeed an inspiration to me and helps me to develop optimistic personalities.

I also thank my colleague, Dr Feridoon Azough, for his initial guidance and part of TEM characterisation work during my first year. Working with Feridoon must be an invaluable and unforgettable experience for me, which enables me a strong-willed man who is not afraid of facing upcoming challenges in the future. I am also grateful for Prof. Robert Cernik who generously shares his expertise and kindly helps me with XRD refinement work.

I appreciate the tuition fee waiver from University of Manchester and the living expense provided by China Scholarship Council. Without their financial support, I cannot pursue my PhD degree as expected.

I would like to thank Department of Materials at University of Manchester for the facilities required for the completion of my PhD program. I would like to thank the following technicians: Dr John Warren and Mr. Gary Harrison for their help with XRD training and measurements; Mr. Michael Faulkner and Dr Patrick Hill for their assist with SEM training; Mr. Matthew Smith and Dr Duc The-Ngo for their help with TEM training; Dr Ben Spencer for his help with XPS measurement and data analysis; Mr. Andrew Wallwork for LFA training and measurements; Dr Chloe Loveless for her help with DSC measurements.

I also would like to thank my colleagues and friends for their support during this journey: Dr Diana Talia Alvarez Ruiz for her kind help and being a good mentor; Dr Dursun Ekren

for his useful advice on my experimental work; Dr George Miller for his constructive suggestions and being a good office mate; Dr Yizhe Li for the fruitful discussion on data analysis; Mr. Xiaodong Liu for his assist with SEM and TEM characterisation; Mr. Ziqi Yang and Mr. Bing Wang for their help with the powder preparation; Mr. Dongchen Hu, Ms. Yu Liu, Mr. Yibing Zhu and Ms. Bingying Xie for being supportive friends.

I am really grateful for receiving immediate assist from my good friends: Mr. Yabin Chang, Mr. Qiance Zhang and Mr. Wei Li at the University of Manchester. I also would like to thank my bosom friend, Mr. Jiawei Li, for his moral support and helping through hard times during the past few years.

Finally, I would like to express my gratitude towards my family members. I am very grateful for my mother who has always supported and encouraged me to pursue my interest. This thesis is also dedicated to my deceased father, who will live in my heart forever.

Glossary of Terms

S	Seebeck coefficient
σ	Electrical conductivity
C_p	Specific heat capacity
q	Carrier charge
k_b	Boltzmann constant
E_f	Fermi level
T	Absolute temperature
π	Pi
e	Electronic charge
E_g	Band gap
μ(ε)	Energy correlated carrier mobility
C_e	Electronic specific heat
η_F	Reduced Fermi level
m*	Effective mass
γ	Scattering factor
Π	Peltier coefficient
I	Electrical current intensity
V	Voltage
R	Electrical resistance
j	Electrical current density
E	Electric filed density
μ	Carrier mobility
τ	Relaxation time
E_h	Activation energy
κ	Thermal conductivity
L_0	Lorenz constant
L_p	Mean free path of phonon
v_s	Velocity of sound
Γ	Disorder scattering parameter
ω	Phonon frequency
ZT	Thermoelectric figure of merit
E_c	Minimum conduction band
E_v	Maximum valence band

1. Introduction

1.1 Overview

Energy supply and its usage, involving industries such as clothing, food, housing and transportation are closely related to the development of human society. Up to now, fuel and coal are still the main energy resources due to the abundant storage and advanced mining technologies. However, these non-renewable resources are mainly responsible for excessive emissions of carbon dioxide, accelerating the process of global warming [1]. In addition, waste gases generated from their combustion, including sulphur dioxide and nitrogen dioxide, enable the formation of acid rain, thereby causing the corrosion of the soil and architecture. Unfortunately, these natural resources are gradually diminishing owing to the overexploitation which poses serious threats to habitats of both human beings and animals. Therefore, to cope with the energy and ecological crisis, the development of clean and renewable energies is critical and in high demand.

The use of nuclear energy since the 1950s efficiently reduces the environmental pollution caused by fossil fuels [2]. In general, nuclear energy is a highly efficient resource with rich mineral deposits. The storage of uranium and thorium to produce nuclear fission on earth can be guaranteed for thousands of years. However, the disposal of the spent fuel rods is a big challenge as they are likely to remain highly radioactive for a long time. The nuclear fusion reactors are able to provide huge energy supply but require a sophisticated control system. Additional efforts are still needed to optimise the monitoring equipment and reaction efficiency, leading to stringent requirements for relative risk assessment and safety management, thereby restricting commercial applications. Another promising substitute is solar energy. This emerging energy source is of much interest because of its rich abundance, non-toxicity and sustainability. Although considerable amounts of solar radiation can be received on earth, the energy density is still at a low level. As a result, investigations regarding increasing the energy yield by improving the solar conversion rate are still ongoing.

Energy harvesting from the waste energy also turns out to be a popular strategy. It was reported that more than sixty percent of energy generated is lost, most of which is in the form of waste heat [3]. Thermoelectric (TE) materials are able to achieve conversion between heat and electricity, providing a promising approach to take full advantages of energy utilization. Existing thermoelectric systems with no pollutants usually have a small size, good stability and limited working temperature range [4,5]. Due to their wide applications from radioisotope thermoelectric generators for space missions, to waste heat

recovery modules for automotive, aerospace and industrial environment [6,7], TE materials have drawn increasing attention from governments and research institutes.

In reality, the energy conversion is realised through the thermoelectric generator (TEG) based on the principle of the Seebeck Effect [8], which offers the opportunity to convert heat into electricity by coupling a p-type with a n-type semiconductor in a temperature gradient. Since the 1950s, radioisotope thermoelectric generators (RTGs) have played important roles in satellites and space probes, like Voyager 2 and Apollo 12, as the main power source [9-11]. Nowadays, automobiles equipped with thermoelectric modules are developed in order to ease the energy crisis and environmental pollution. According to the Carnot Law, the theoretical maximum efficiency of an energy harvesting device is in the range of 70-80 % [12,13]. In marked contrast, the average efficiency of major power generation machines is 30-50 % [13], whilst current thermoelectric harvesters (Fig. 1.1) have very modest performance. This indicates further improvements are required to modify the thermoelectric performance.

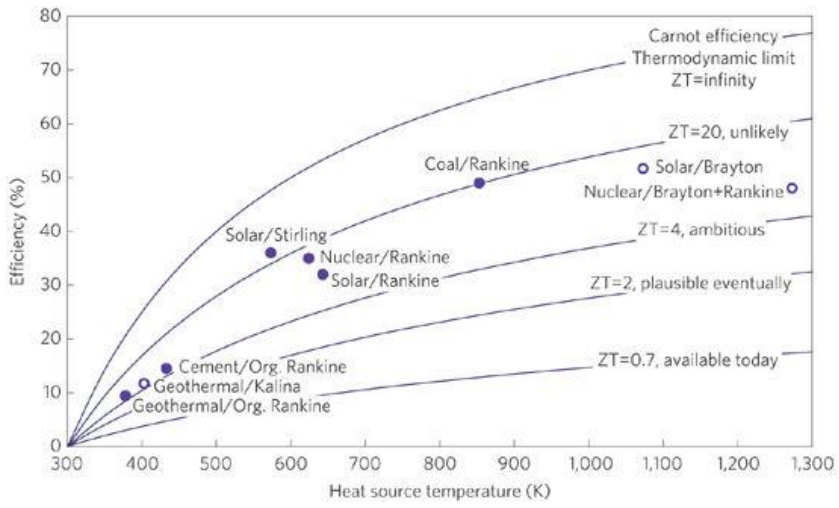

Fig. 1.1 Efficiency of 'best practice mechanical' heat engines compared with an optimistic thermoelectric estimate (the average ZT values are presented), taken from Vining [13]

The Peltier Effect [14], is the opposite effect to the Seebeck Effect; it is used extensively for active cooling by applying a voltage difference between the open junction ends of two different types of thermoelectric materials. For example, it can be employed to produce cooling components in a refrigerator as well as a laptop [15], with the aim of creating a cool environment for either food storage or CPU running.

Apart from the potential in energy harvesting and active cooling, thermoelectric devices stand out because of their mechanical structure. As thermoelectric materials can achieve the static transformation of energy, the conversion between heat and electricity is nearly realised without any moving components, which means unnecessary vibrations can be prevented in practical applications. As a consequence, the service life is extended by limiting the damage to both devices and attached parts. In addition, less noise and radiation pollution will be generated, which is beneficial to our health and environment. At present, the major concern lies in proposing an approach to improve the thermoelectric performance so as to increase the working efficiency of the thermoelectric generator and the refrigerator, which is critical to the competition between the thermoelectric module and the traditional power supply.

Selecting high-performance candidate materials for thermoelectric devices is also a key point. Qualified materials are identified according to the dimensionless figure of merit ZT (defined as $S^2T/\rho\kappa$, where S is the Seebeck coefficient, ρ is the electrical resistivity, κ is the thermal conductivity and T is the absolute temperature) [6, 7, 16, 17]. A higher ZT value reflecting a higher conversion efficiency, is usually expected on the basis of a large thermo-electromotive force, high electrical conductivity and low thermal conductivity.

Traditional TE materials are based on antimony, lead, and bismuth tellurides, which are restricted by nature of their toxic and expensive components and the low resistance to oxidation with atmospheric oxygen at high temperatures. However, these disadvantages are not encountered in metal oxide based compounds. In the past two decades, there has been increasing interest in oxide thermoelectric materials because of their high chemical and thermal stability and the relative abundance of their constituent species [6]. Whilst, most oxides are limited by their high thermal conductivity and modest electrical conductivity [18,19], several show very promising properties.

1.2 Objectives

Among various oxide-based thermoelectric materials, the layer-structured cobaltites are considered as promising p-type thermoelectric materials due to their intrinsically low thermal conductivity and good high temperature stability. With a structure able to accommodate substituting elements and the opportunity to generate defects by controlling processing conditions, they provide an excellent framework to enhance thermoelectric properties.

In this work, layer-structured calcium cobaltite ($Ca_3Co_4O_9$) based ceramics and thick films are investigated for thermoelectric applications within the middle temperature range (298-823 K). The main objective is to understand the factors controlling the processing-microstructure-property relationships of these materials and thereby improve the thermoelectric properties of synthesized materials by maximising the electrical conductivity or minimising the thermal conductivity. The approaches to realising enhanced thermoelectric performance in this study are: introducing bismuth substitution and cobalt deficiency; use of different preparation techniques (solid state reaction, spark plasma sintering and cold sintering); optimising heat-treatment process (calcination, sintering and annealing conditions); utilising dual doping strategies (Bi/Ba co-doping and Bi/Sr co-doping).

1.3 Introduction to Chapters

The main body of this thesis (Chapters 4-7) presents details about the preparation and characterisation of high-quality calcium cobaltite based materials.

Chapter 4 demonstrates electrical transport modulation of calcium cobaltite ceramics and thick films by controlling cobalt deficiency and sintering conditions. The optimal composition was firstly determined by traditional solid state reaction and was then subject to screen printing to fabricate thick films. With fixed bismuth substitution, the formation of Co-containing secondary phases was regulated by increasing cobalt deficiency. The impurity-free calcium cobaltite thick was obtained by simply controlling the sintering temperatures and dwell time. The grain growth mechanism near the interface between the film and substrate was also analysed. As a result, the maximum power factor of 55.5 $\mu Wm^{-1}K^{-2}$ was achieved for $Ca_{2.7}Bi_{0.3}Co_{3.92}O_{9+\delta}$ thick films at 673 K due to the modified microstructure.

Chapter 5 concentrates on enhanced thermoelectric performance of SPS-processed $Ca_{3-x}Bi_xCo_yO_{9+\delta}$ ($x = 0.1$-0.3; $y = 3.92$-4.0) ceramics by controlling chemical compositions and annealing conditions. With appropriate Bi_2O_3 addition, the densification and texture were enhanced by inducing liquid phase sintering. The 'heavy' Bi doping also helped to enhance phonon scattering by inducing the atomic mass fluctuation. By increasing cobalt deficiency, Co-containing secondary phases were reduced and crystalline defects were generated. Optimised air-annealing processing enabled the complete reaction, forming calcium cobaltite and assisting oxygen diffusion into the crystal lattice. As a result, the electrical conductivity of calcium cobaltite was enhanced without degrading the Seebeck coefficients

and the out-of-plane thermal conductivity was reduced by about 20 %. A high ZT value of 0.16 was finally achieved for $Ca_{2.7}Bi_{0.3}Co_{3.92}O_{9+\delta}$ ceramic at 823 K.

Chapter 6 presents an efficient approach to enhance the thermoelectric performance of cold sintered calcium cobaltite by optimising calcination and post annealing process. The optimal composition ($Ca_{2.7}Bi_{0.3}Co_{3.92}O_{9+\delta}$) was selected for cold sintering. The double calcination and annealing process helped to reduce the secondary phases in both calcined powders and cold sintered ceramics. By extending the annealing time, the volume fractions of the main phase were significantly increased and oxygen diffusion into the lattice was promoted. Meanwhile, the double calcination and annealing also led to an increased grain size and enhanced texture. As a consequence, the maximum power factor (0.28 $mWm^{-1}K^{-1}$ at 823 K) was obtained for cold sintered $Ca_{2.7}Bi_{0.3}Co_{3.92}O_{9+\delta}$ due to the optimised heat-treatment.

Chapter 7 focuses on the effects of co-doping and different fabrication routes on thermoelectric performance of $Ca_{2.63}Bi_{0.3}M_{0.07}Co_{3.92}O_{9+\delta}$ (M = Ba; Sr) ceramics. Different preparation techniques, including the solid-state reaction and spark plasma sintering, were employed to fabricate calcium cobaltite based ceramics. The roles of different dopants in determining the crystal structure and microstructure were identified. Both the power factor and thermal conductivity of annealed SPS-processed Bi/Sr co-doped sample were enhanced due to the combined effects of high density, strong texture and lattice distortion. By contrast, the solid state synthesized Bi/Ba co-doped sample showed inferior transport properties, but lower thermal conductivity, mainly due to the high porosity. As a result, the maximum ZT value of 0.14 was achieved in both the solid state synthesized $Ca_{2.63}Bi_{0.3}Ba_{0.07}Co_{3.92}O_{9+\delta}$ and annealed SPS-processed $Ca_{2.63}Bi_{0.3}Sr_{0.07}Co_{3.92}O_{9+\delta}$ ceramics at 800 K.

References

[1] Z.M. Jiang, Reflections on energy issues in China, J. Shanghai Jiaotong Univ. 13 E (2008) 257–274.

[2] W.A. Gamson, A. Modigliani, Media Discourse and Public Opinion on Nuclear Power: A Constructionist Approach, Am. J. Sociol. 95 (1989) 1–37.

[3] W.H.J. Graus, M. Voogt, E. Worrell, International comparison of energy efficiency of fossil power generation, Energy Policy. 35 (2007) 3936–3951.

[4] G.S. Nolas, J. Sharp, J. Goldsmid, Thermoelectrics: basic principles and new materials developments, Sci. Technol. 45 (2013) 228.

[5] J. He, T.M. Tritt, Advances in thermoelectric materials research: Looking back and moving forward, Science 357 (2017) eaak9997.

[6] S. Walia, S. Balendhran, H. Nili, S. Zhuiykov, G. Rosengarten, Q.H. Wang, M. Bhaskaran, S. Sriram, M.S. Strano, K. Kalantar-zadeh, Transition metal oxides - Thermoelectric properties, Prog. Mater. Sci. 58 (2013) 1443–1489.

[7] C. Wan, Y. Wang, N. Wang, W. Norimatsu, M. Kusunoki, K. Koumoto, Development of novel thermoelectric materials by reduction of lattice thermal conductivity, Sci. Technol. Adv. Mater. 11 (2010) 44306.

[8] T.J. Seebeck, Ueber die magnetische Polarisation der Metalle und Erze durch Temperaturdifferenz, Ann. Phys. 82 (1826) 253–286.

[9] G.H. Rinehart, Design characteristics and fabrication of radioisotope heat sources for space missions, Prog. Nucl. Energy. 39 (2001) 305–319.

[10] P.J. Bateman, Thermoelectric power generation, in: Contemp. Phys., IET (1961) 302–311.

[11] J. Yang, T. Caillat, Thermoelectric materials for space and automotive power generation, MRS Bull. 31 (2006) 224–229.

[12] S. Carnot, Réflexions sur la puissance motrice du feu, Vrin, 1824.

[13] C.B. Vining, An inconvenient truth about thermoelectrics, Nat. Mater. 8 (2009) 83–85.

[14] D.C. Spanner, The peltier effect and its use in the measurement of suction pressure, J. Exp. Bot. 2 (1951) 145–168.

[15] X.F. Zheng, C.X. Liu, Y.Y. Yan, Q. Wang, A review of thermoelectrics research - Recent developments and potentials for sustainable and renewable energy applications, Renew. Sustain. Energy Rev. 32 (2014) 486–503.

[16] K. Koumoto, R. Funahashi, E. Guilmeau, Y. Miyazaki, A. Weidenkaff, Y. Wang, C. Wan, Thermoelectric ceramics for energy harvesting, J. Am. Ceram. Soc. 96 (2013) 1–23.

[17] B. Poudel, Q. Hao, Y. Ma, Y. Lan, A. Minnich, B. Yu, X. Yan, D. Wang, A. Muto, D. Vashaee, X. Chen, J. Liu, M.S. Dresselhaus, G. Chen, Z. Ren, High-thermoelectric performance of nanostructured bismuth antimony telluride bulk alloys, Science 320

(2008) 634–638

[18] J. Lan, Y. Lin, A. Mei, C. Nan, Y. Liu, B. Zhang, J. Li, High-temperature electric properties of polycrystalline La-doped $CaMnO_3$ ceramics, J. Mater. Sci. Technol. 25 (2009) 535–538.

[19] P.H. Tsai, T. Norby, T.T. Tan, R. Donelson, Z.D. Chen, S. Li, Correlation of oxygen vacancy concentration and thermoelectric properties in $Na_{0.73}CoO_{2-\delta}$, Appl. Phys. Lett. 96 (2010) 141905.

2. Literature Review

2.1 Definition and History of Thermoelectric Effects

The conversion between heat and electricity can be realised by thermoelectric effects, including Seebeck effect, Peltier effect and Thomson effect, which are generally associated with the current effects caused by temperature gradient or thermal effects produced by a voltage difference.

The Seebeck effect was named after German physicist Thomas Johann Seebeck who discovered the deflection of a compass needle near a closed loop made from two different metals with temperature differences between their joints in 1821 [1]. This behaviour can be described by Fig. 2.1 [2], where a closed circuit is built upon a light bulb and two materials referred as P (p-type) and N (n-type). If a temperature difference ΔT exists between the ends of materials, charge carriers (holes or electrons) are driven by diffusion from the hot end to the cold end, giving rise to the electrical current that lights the bulb [3]. Essentially, the heat re-equilibration between both sides in a thermal gradient is realised by migration of charge carriers as a natural response.

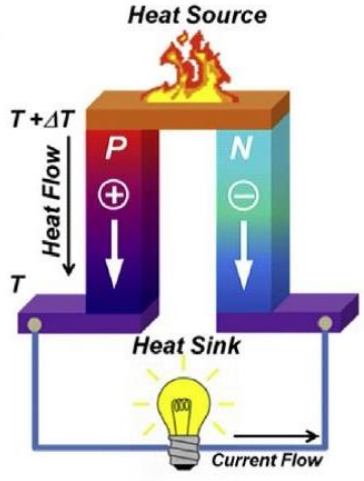

Fig. 2.1 Seebeck Effect for power generation, taken from Zhang and Zhao [2]

The Peltier effect can be considered as the opposite of the Seebeck effect. In 1834, French physicist Jean Charles Athanase Peltier noticed the presence of cooling or heating effects when an electrical current flowed through the joints between two different conductors [4]. As Fig. 2.2 shows, a battery is linked with both n-type and p-type conductors in a closed circuit. The active cooling at the electrified junctions is attributed to the potential differences of carriers in a voltage gradient [3,5]. When the carriers flow between two sides through the

junction, the carriers release/absorb heat in order to reach a new balance, and a macroscopic exotherm/endotherm arises as a result.

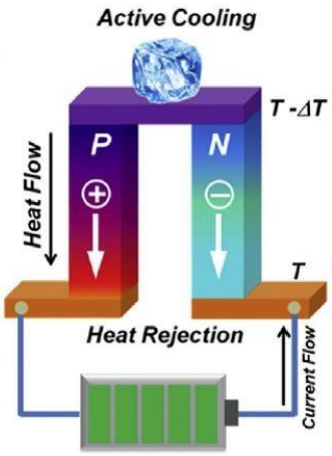

Fig. 2.2 Peltier Effect for active refrigeration, taken from Zhang and Zhao [2]

In 1851, Lord Kelvin (William Thomson) predicted a new thermal effect when an electrical current passes through a non-uniform single conductor, referred as the Thomson Effect [6,7]. In theory, the Thomson Effect can be regarded as a continuous version of Peltier effect and the Thomson coefficient is defined as $T\Delta S/\Delta T$ (S is the Seebeck coefficient and T is the absolute temperature).

2.2 Basic Principles

2.2.1 Seebeck Coefficient

As introduced in Section 2.1, it is known that an electric field can be developed from the temperature differences at joints of two different conductors in a closed circuit. Therefore, the Seebeck coefficient is defined as the ratio between the voltage gradient and the thermal gradient, shown in Equation (2.1) [8]:

$$\mathbf{S} = \Delta\mathbf{V} / \Delta\mathbf{T} \qquad \textbf{(2.1)}$$

where **S** is the Seebeck coefficient, Δ**V** is the voltage difference, and Δ**T** is the temperature difference.

The Seebeck coefficient can also be approximately regarded as the heat per carrier over temperature, shown in Equation (2.2) [9]:

$$S = C_p / q \quad (2.2)$$

where C_p is the specific heat capacity and **q** is the carrier charge.

Generally, mobile valence electrons existing in the thermal gradient play a vital role in determining the Seebeck coefficient. It is acknowledged that the Seebeck coefficient of a classical electron gas approaches $k_b / e \approx 86.2$ μV/K (k_b is the Boltzmann constant and **e** is the electron charge) [10]. For metals and degenerate semiconductors, carrier transport is more likely to occur near the Fermi level (E_f) and the number of carriers equals to k_bT / E_f. As the Fermi energy is close to the conduction band, the energy needed to ionise electrons from the valence band approximately equals to the energy needed for achieving conduction, shown in Fig. 2.3 [11]. According to Equation (2.2), the Seebeck coefficient can be expressed as Equation (2.3) by substitution of C_e / q and **N**:

$$S \sim (k_b / e) [(k_bT) / E_f] \quad (2.3)$$

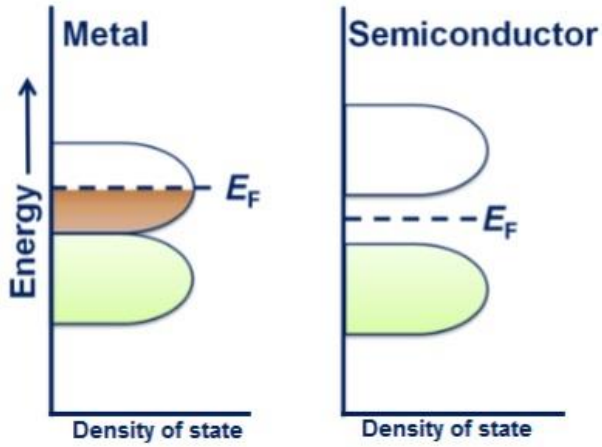

Fig. 2.3 Density of states for metals and semiconductors, taken from Biswas et al. [11]

The Seebeck coefficient can be evaluated by Mott's equation (Equation (2.4)) [12]:

$$S = C_e/n + \pi^2 k_b^2 T/3e[\partial \ln \mu(\varepsilon)/\partial \varepsilon]_{\varepsilon=Ef} \quad (2.4)$$

where **S** is the Seebeck coefficient, C_e **i**s the electronic specific heat, **n** is the carrier concentration, k_b is the Boltzmann constant, **T** is the temperature, **e** is the electronic charge, $\mu(\varepsilon)$ is the energy correlated carrier mobility. It is acknowledged that the simple Drude model (C_e/n), the first term in Equation (2.4), dominates the changes to Seebeck coefficients.

Assuming a single parabolic band (SPB) model, S can be also described by Equation (2.5) [13]:

$$S = \frac{k_b}{e}\left[\eta_F - \frac{(\gamma+2.5)F_{(\gamma+1.5)}(\eta_F)}{(\gamma+1.5)F_{(\gamma+0.5)}(\eta_F)}\right] \quad (2.5)$$

where k_b is the Boltzmann constant, **e** is the electronic charge, η_F is the reduced Fermi level and γ is the scattering factor (this parameter can reflect energy filtering effects, which is able to be enhanced through increasing interface and grain boundary densities [13]).

The Seebeck coefficient can be alternatively described by Equation (2.6), using the degenerate Fermi gas model [14]:

$$S = C_n n^{-2/3} m^*(\gamma + 1)T \quad (2.6)$$

where C_n is the basic physical constant ($C_n = 8\pi^{8/3}k_b^2(3^{5/3}eh^2)$), **n** is the carrier concentration, **m*** is the effective mass, γ is the scattering factor and **T** is the absolute temperature. In order to provide insight into the relationship between **S**, γ and **n**, Equation (2.6) can be simplified as Equation (2.7) [15]:

$$S \sim \gamma - \ln(n) \quad (2.7)$$

Abutaha et al. [14] investigated the effects of **T** and **n** on asymmetry in density of states for $SrTiO_3$. Fig. 2.4(a) demonstrates that DoS can be broadened by increasing temperature, indicating that the band asymmetry is increased. Fig. 2.4(b) shows a shift of Fermi level towards the conduction band with enhanced carrier concentration, suggesting a decrease in the band asymmetry. It can be concluded that a higher temperature or lower carrier concentration is able to enlarge the Seebeck coefficient.

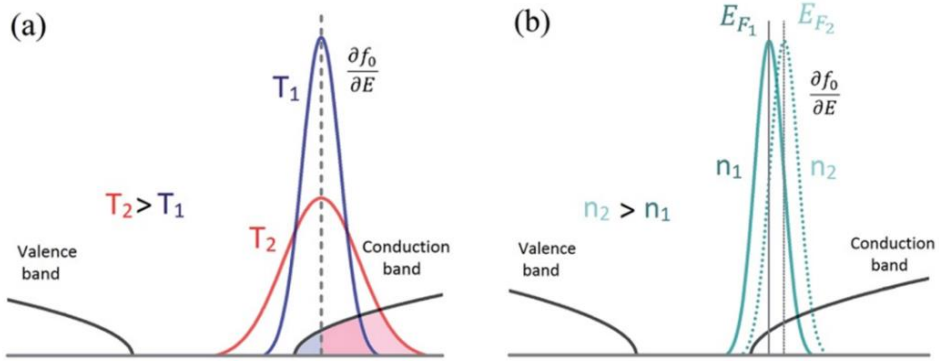

Fig. 2.4 The effects of temperature (a) and carrier concentration (b) on band asymmetry in density of states for $SrTiO_3$, taken from Abutaha et al. [14]

However, the case is different for a non-degenerate semiconductor, where the conduction band is significantly higher than the Fermi level, shown in Fig. 2.3. In order to be electrically conductive, electrons need to absorb enough energy to overcome the band gap and then

occupy the partially filled conduction band. As the carrier concentration and transport are heavily limited by the band gap, a higher voltage gradient is generated, resulting in a higher thermoelectric power. The Seebeck coefficient is therefore described by Equation (2.8) [9]:

$$\mathbf{S \sim (k_b / e) [E_g / (k_b T)]} \qquad \mathbf{(2.8)}$$

where $\mathbf{E_g}$ is the band gap energy.

The Seebeck coefficient in both Equations (2.3) and (2.7) are based on the theory of electronic conduction. In addition, the Seebeck coefficient for semiconductors can be expressed by the Heikes formula. Assuming there is no pining for cations and negligible effects of the vibration entropy, the modified Heikes formula can be written as a function of the carrier concentration [16,17], shown in Equations (2.9):

$$\mathbf{S_{(T\rightarrow\infty)} = -\frac{K_b}{e} \ln\left(\frac{1-n}{n}\right)} \qquad \mathbf{(2.9)}$$

where **n** is the carrier concentration. It can be found that thermopower depends highly on the carrier concentration. Lower carrier concentration leads to a higher Seebeck coefficient, consistent with Equation (2.4).

For the layered p-type calcium cobaltite in this study, the carrier concentration and Seebeck coefficient can be specifically expressed using Equations (2.10) and (2.11) through transformation of the modified Heikes formula [18]:

$$\mathbf{n = (A_s/V)\{1/[\exp(Se/k_b)/\beta + 1]\}} \qquad \mathbf{(2.10)}$$

$$\mathbf{S = (-k_b/e)\ln\{[g_3/g_4][x/(1-x)]\}} \qquad \mathbf{(2.11)}$$

where **n** is the carrier concentration, **S** is the Seebeck coefficient, $\mathbf{A_s}$ is the number of available sites per unit ($\mathbf{A_s}$ = 4 for $Ca_3Co_4O_9$ unit cell), **V** is the volume of unit cell, **e** is the electronic charge, $\mathbf{k_b}$ is the Boltzmann constant, **β** is a parameter related to the spin values for multi-valent Co^{3+}/Co^{4+} cations (**β** is 1/6 for stable low-spin states of Co^{3+} and Co^{4+}), $\mathbf{g_3}$ and $\mathbf{g_4}$ are the numbers of configurations of the Co^{3+} and Co^{4+} ions, and **x** is the concentration ratio of $Co^{4+}/(Co^{3+}+Co^{4+})$. Here, Equations (2.10) and (2.11) are only employed to evaluate approximate levels of **n** and **S**, assuming there are stable low-spin states for cobalt ions.

2.2.2 Peltier Coefficient

The Peltier effect can be regarded as the reverse behaviour of the Seebeck effect, through which heat release or absorption is realised by placing a closed circuit into a voltage gradient.

The Peltier coefficient is introduced to describe the amount of heat carried per unit charge; the heat generation at the junction of two conductors per unit time is therefore defined as Equation (2.12):

$$\mathbf{Q = \Pi_{AB} I} \qquad \textbf{(2.12)}$$

where **Q** is the generated heat, $\mathbf{\Pi_{AB}}$ is the difference of Peltier coefficients between two different conductors (A and B), and **I** is the electrical current.

According to the Kelvin relationship [6], the Peltier coefficient can also be evaluated by the Seebeck coefficient directly, shown in Equation (2.13):

$$\mathbf{\Pi = ST} \qquad \textbf{(2.13)}$$

where **Π** is the Peltier coefficient**, S** is the Seebeck coefficient and **T** is the temperature.

In fact, inevitable Joule heat will be generated when the electrical current flows through the circuit due to the electrical resistivity, which has negative effects on active cooling. Therefore, materials with low electrical resistance are commonly selected as candidates for refrigeration applications.

2.2.3 Thomson Coefficient

As mentioned in Section 2.1, the Thomson effect is essentially a continuous version of the Peltier effect and used to describe the cooling or heating response of a current-carrying conductor in a thermal gradient. The link between the Seebeck coefficient, the Peltier coefficient and Thomson coefficient can be established based on the Kelvin relationship [6], shown in Equation (2.14):

$$\mathbf{\tau = d\Pi / dT - S} \qquad \textbf{(2.14)}$$

where **τ** is the Thomson coefficient, **Π** is the Peltier coefficient, **S** is the Seebeck coefficient and **T** is the absolute temperature.

By using Equation (2.13) to substitute the corresponding component in Equation (2.14), the Thomson coefficient can also be expressed by Equation (2.15):

$$\mathbf{\tau = TdS / dT} \qquad \textbf{(2.15)}$$

Notably, the Thomson coefficient is different from both the Seebeck coefficient and the Peltier coefficient because it is the only one determined from individual materials rather than pairs of materials among these thermoelectric effects.

2.2.4 Electrical Conductivity

When a voltage **V** is applied across a uniform conductor with the length of **L** and the cross-sectional dimension of **S**, displayed in Fig. 2.5, the electrical current density can be calculated from Ohm's law [19], shown in Equation (2.16):

$$\mathbf{I = V / R} \tag{2.16}$$

where **I** is the electrical current intensity, **V** is the voltage and **R** is the electrical resistance.

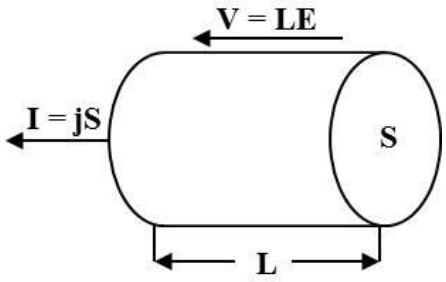

Fig. 2.5 Schematic diagram for Ohm's Law

Given that the magnitude of both the electrical current and electric field are also uniform, the current density (**j**) and electric filed density (**E**) can be described using Equations (2.17) and (2.18):

$$\mathbf{j = I / S} \tag{2.17}$$

$$\mathbf{E = V / L} \tag{2.18}$$

Where **S** is the cross-sectional dimension and **L** is the length of the conductor.

By comparing Equations (2.17) and (2.18) with Equation (2.16), then Equation (2.19) can be obtained after transformation:

$$\mathbf{j = (L / SR)\, E = (1 / \rho)\, E} \tag{2.19}$$

where **ρ** is the electrical resistivity ($\rho = SR / L$).

The reciprocal of the electrical resistivity is defined as the electrical conductivity **σ** (Equation (2.20)) and thus Equation (2.19) is simplified as Equation (2.21):

$$\sigma = 1 / \rho \tag{2.20}$$

$$j = \sigma E \tag{2.21}$$

Basically, the conductive behaviour in conductors results from the directional migration of carriers driven by the electric field. If each carrier with the charge of **q** drifts at a speed of **v** in the electric field, then **j** can be defined as the total charge of carriers that pass through per unit cross-section dimension per unit time, shown in Equation (2.22):

$$j = nqv \tag{2.22}$$

where **n** is the charge carrier concentration and **v** is the average velocity of charge carriers.

Therefore, the electrical conductivity can be further described as Equation (2.23):

$$\sigma = nq(v/E) = nq\mu \tag{2.23}$$

where **μ** is the carrier mobility (transport velocity of carriers in the unit electric field; **μ = v / E**).

On the other hand, **v** is essentially reflected by the carrier mobility from a microscopic point of view, which is closely related to electrical conduction mechanisms in different materials. Band gap theory indicates that materials can be conductive if the electrons inside reach the Fermi energy. The electron can be more easily excited to achieve conduction for metals due to their natural electronic state configuration. However, for semiconductors, there is a smaller number of carriers contributing to conduction due to a certain distance between the Fermi level and the conduction band edge. Drude put forward a free electron model to define the electrical conductivity [20], shown in Equation (2.24):

$$\sigma = nq^2\tau / m^* \tag{2.24}$$

where **τ** is the collision time (the average time between scattering events) and **m*** is the effective mass. Equation (2.24) provides the idea that electrical conductivity can be maximised by increasing **n** and **τ** or reducing **m***, which can be realised through control of microstructure or band engineering.

Notably, the temperature also plays a vital part in determining electrical conductivity. For semiconductors, thermal activation and variable range hopping are the main conduction mechanisms used for explaining the temperature dependence of electrical conductivity.

Thermal activation model: The band gap can be overcome by thermally excited charge carriers that are transformed into degenerate (non-localised) states. The relationship between the electrical conductivity and the temperature (Equation (2.25)) is derived according to the Arrhenius Law [9], using the small polaron hopping model (SPH) [21,22]:

$$\boldsymbol{\sigma = \sigma_0 / T \exp\left(-\frac{E_h}{k_b T}\right)} \qquad \textbf{(2.25)}$$

where $\boldsymbol{\sigma_0}$ is a pre-exponential factor associated with carrier mobility and temperature, $\boldsymbol{E_h}$ is the activation energy, $\boldsymbol{k_b}$ is the Boltzmann constant and **T** is the temperature. It is obvious that $\boldsymbol{\sigma}$ can be significantly enhanced if $\boldsymbol{k_b T \gg E_h}$. For a polycrystalline material, $\boldsymbol{E_h}$ is not only determined by the band gap but also the grain boundary density. A large grain boundary density can filter low-energy carriers, thereby increasing the activation energy.

Variable range hopping model (VRH): If the energy between the neighbouring energy states reaches a high level, the potential difference of excitation is more likely to be reduced due to hopping of carriers into other localised states. Commonly, charge carriers in amorphous materials and disordered semiconductors are non-degenerate within wide energy ranges, which can be explained by Equation (2.26) in terms of by Mott's law [23]:

$$\boldsymbol{\sigma = \sigma_0 \exp\left[-\left(\frac{T_0}{T}\right)^{\frac{1}{4}}\right]} \qquad \textbf{(2.26)}$$

where $\boldsymbol{T_0}$ is the characteristic temperature in inverse proportion to the electronic density of states (DoS) near the Fermi level.

2.2.5 Thermal Conductivity

In accordance with Fourier's law of heat conduction [24], the rate of heat passing through a cross-sectional area of a material in a thermal gradient is determined by the thermal conductivity, displayed in Equation (2.27):

$$\boldsymbol{Q = -\kappa A \Delta T} \qquad \textbf{(2.27)}$$

where **Q** is the rate of heat transfer, $\boldsymbol{\kappa}$ is the thermal conductivity, **A** is the dimension of cross section and $\boldsymbol{\Delta T}$ is the temperature difference.

The ability to conduct heat in a solid material is usually reflected by the total thermal conductivity composed of the thermal conductivity from both lattice vibrations and electronic components, shown in Equation (2.28):

$$\kappa = \kappa_e + \kappa_l \quad (2.28)$$

where κ is the total thermal conductivity, κ_e is the thermal conductivity caused by lattice vibrations and κ_l is the thermal conductivity governed by charge movement. In metals, the main charge carriers turn out to be the electrons and thus the total thermal conductivity largely depends on the thermal conductivity resulting from electron movements. As for semiconductors, the phonon propagation also plays an important role in heat conduction in addition to the effects of electronic contribution, where the total thermal conductivity is expressed as the sum of these two factors.

The Wiedemann-Franz relationship (Equation (2.29)) shows that κ_e is directly proportional to the electrical conductivity [25], which can be enhanced via doping of charge carriers, such that:

$$\kappa_e = \sigma L_0 T \quad (2.29)$$

where σ is the electrical conductivity, L_0 is the Lorenz constant (2.45×10^{-8} $W\Omega/K^2$ for free electrons) and T is the temperature.

Thermal conduction is a complicated process in semiconductors and insulators where the heat flow can propagate in a three-dimensional space [26]. For polycrystalline samples, lattice vibrations are mainly determined by phonon-phonon scattering, point defect scattering and grain boundary scattering, shown in Equation (2.30) [27]:

$$1 / \kappa_l = 1 / \kappa_{phonon} + 1 / \kappa_{defect} + 1 / \kappa_{boundary} \quad (2.30)$$

where κ_{phonon}, κ_{defect} and $\kappa_{boundary}$ represent the thermal conductivity contribution from phonons, point defects and grain boundaries, respectively.

In addition to the scattering mechanisms mentioned above, phonon transport is also influenced by the crystal structure and ionic size. In order to describe the phonon interactions more precisely, the mean free path of a random walk model is utilised to describe lattice thermal conductivity based on the classic kinetic theory of gas, shown in Equation (2.31) [28]:

$$\kappa_l = \frac{1}{3} C_v L_p v_s \quad (2.31)$$

where C_v is the specific heat capacity of the lattice, L_p is the mean free path of phonon before collisions occur, v_s is the velocity of sound or the average particle velocity. Compared to C_v and v_s, the mean free path L_p is the only parameter that can be easily altered in Equation

(2.31); the control of mean free path is an efficient way to modify the lattice thermal conductivity.

For elemental doping strategy, it is easy to induce point defect scattering to enhance the phonon scattering, the effects of which can be described by the Debye–Callaway model [29,30], using Equations (2.32-2.35):

$$\tau_D^{-1} = A\omega^4 = [V/(4\pi v^3)]\Gamma\omega^4 \quad (2.32)$$

$$\Gamma = \Gamma_{MF} + \Gamma_{SF} \quad (2.33)$$

$$\Gamma_{MF} = \frac{\sum_{i=1}^{n} C_i \left(\frac{\bar{M}_i}{\bar{M}}\right)^2 f_i^1 f_i^2 \left(\frac{M_i^1 - M_i^2}{\bar{M}_i}\right)^2}{\sum_{i=1}^{n} C_i} \quad (2.34)$$

$$\Gamma_{SF} = \frac{\sum_{i=1}^{n} C_i \left(\frac{\bar{M}_i}{\bar{M}}\right)^2 f_i^1 f_i^2 \varepsilon_i \left(\frac{r_i^1 - r_i^2}{\bar{r}_i}\right)^2}{\sum_{i=1}^{n} C_i} \quad (2.35)$$

where τ_D is the relaxation time for point defect scattering, **A** is a constant independent of temperature and frequency, ω is the phonon frequency, **V** is the volume per atom, **v** is the velocity of sound, Γ is the disorder scattering parameter, Γ_{MF} and Γ_{SF} are the scattering parameters related to mass fluctuation and strain filed, C_i is the relative degeneracy of the site, $\bar{M}_i$ and $\bar{r}_i$ are the average mass and radius of dopant, f_i is the fractional occupation and ε_i is the amplitude of thermal vibration of the atoms.

If the mass variation is the dominating mechanism, the mean free path can also be described by Equation (2.36) [31]:

$$1/L_p = (a^3/4\pi v^4)\omega^4 c(\delta M/M)^2 \quad (2.36)$$

where L_p is the mean free path of phonons, a^3 is the volume per atom, **v** is the transverse wave speed, ω is the phonon frequency, **c** is the concentration per atom, **M** is the average mass of the host atom and $\delta M+M$ is the average mass of the solute atom.

For the porous materials, the effects of the porosity on the total thermal conductivity can be evaluated using Equation (2.37) [32]:

$$\kappa = \kappa_0(1 - \nu)/(1 + \beta\nu) \quad (2.37)$$

where κ is the measured total thermal conductivity, κ_0 is the idea bulk thermal conductivity with zero pore, ν is the volume fractions of pores and β is the pore shape factor (β =1.0~3.0 for spherical pores).

2.2.6 Thermoelectric Figure of Merit

In order to rank the thermoelectric materials, a dimensionless term called thermoelectric figure of merit (ZT value) is proposed to evaluate the thermoelectric properties. In general, thermoelectric figure of merit is determined by the Seebeck coefficient, electrical conductivity, and thermal conductivity, which can be calculated from Equation (2.38) [33,34]:

$$\mathbf{ZT = S^2\sigma T/\kappa} \quad \textbf{(2.38)}$$

where **S** is the Seebeck coefficient, **σ** is the electrical conductivity, **κ** is the thermal conductivity and **T** is the temperature. As Equation (2.38) shows, a high Seebeck coefficient and electrical conductivity along with a low thermal conductivity will lead to a high ZT value. In addition, another acknowledged parameter employed to characterise the thermoelectric performance is the power factor [35,36], which is extensively used if the thermal conductivity is unavailable. The definition of the power factor is displayed in Equation (2.39):

$$\mathbf{PF = S^2\,\sigma} \quad \textbf{(2.39)}$$

As the contribution from thermal conductivity to thermoelectric figure of merit cannot be ignored, the result evaluated only by the power factor is limited to some extent. For example, low ZT values can be obtained via a combination of both high power factor and thermal conductivity.

A pair of semiconductors (one n-type and one p-type materials) are usually coupled together to assemble a thermoelectric generator (TEG), which helps to convert waste heat into electrical power. The working principle of the TEG is similar with traditional heat engine, where heat is transferred from a hot junction to a cold sink; the conversion efficiency is governed by Carnot efficiency, shown in Equation (2.40) [37]:

$$\mathbf{\eta_{carnot} = (T_h - T_c) / T_h} \quad \textbf{(2.40)}$$

where $\mathbf{\eta_{carnot}}$ is the Carnot efficiency, $\mathbf{T_h}$ is the temperature of the hot end and $\mathbf{T_c}$ is the temperature of the cold end.

The conversion efficiency of a TEG can be defined by the Carnot efficiency and thermoelectric figure of merit using Equation (2.41) [2]:

$$\mathbf{\eta = W / Q_h = \frac{T_h - T_c}{T_h} \times \frac{\sqrt{1+ZT_{ave}}-1}{\sqrt{1+ZT_{ave}}+(T_c/T_h)}} \quad \textbf{(2.41)}$$

where **η** is the working efficiency of the thermoelectric module, **W** is the delivered power, $\mathbf{Q_h}$ is the total heat flow, and $\mathbf{ZT_{ave}}$ is the average ZT value of both p-type and n-type legs (the ZT value per leg is averaged between $\mathbf{T_h}$ and $\mathbf{T_c}$ using the temperature-dependent ZT curve). The ratio of conversion efficiency to the Carnot efficiency as a function of the average ZT in a fixed thermal gradient is shown in Fig. 2.6 [9]. It shows the conversion efficiency increases with increasing average ZT values, but the rate of increase gradually slows down when the average ZT value exceeds 2.0, suggesting that the conversion efficiency should be tailored for a particular temperature range.

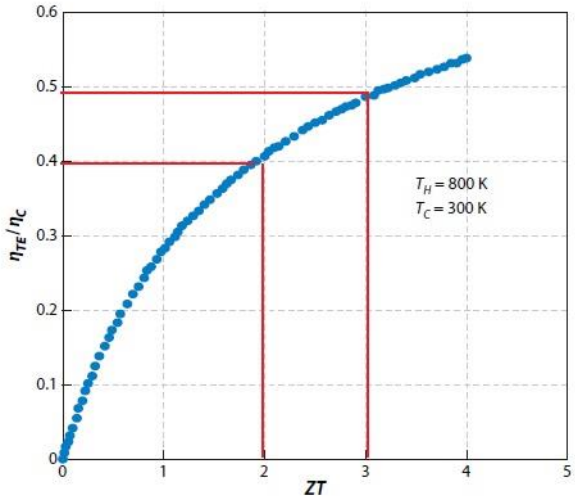

Fig. 2.6 The ratio of conversion efficiency to the Carnot efficiency as a function of the average ZT, taken from Tritt [9]

2.3 Optimisation of Thermoelectric Properties

In general, the strategies for improving ZT values should be established on the optimisation of different thermoelectric parameters, including **σ**, **S** and **κ**. Ideally, we aim to synthesize a sample with low thermal conductivity and high electrical conductivity as well as high Seebeck coefficients. However, some conflicting relationships among these thermoelectric parameters need to be considered while designing the candidate material.

Snyder et al. [38] summarised the carrier concentration dependence of ZT values modelled from Bi_2Te_3. As Fig. 2.7 shows, **σ** and **κ** share a similar upward trend when the carrier concentration rises from 10^{18} cm^{-3} to 10^{21} cm^{-3}, but this trade-off has negative effects on maximising the ZT value according to Equation (2.38). The ZT value peaks at a maximum when the carrier concentration is over ~10^{19} cm^{-3}, mainly due to the restriction of **S** despite the continuous increase of **σ**. A larger carrier concentration is directly responsible for

increasing **σ** but corresponds to a lower **S**, consistent with Equations (2.23) and (2.9), respectively. Although the maximum power factor is achieved with the carrier concentration of about 10^{20} cm^{-3}, its overall variation is in line with that of ZT value. This work suggests that the control of carrier concentration is the key to enhancing the thermoelectric properties.

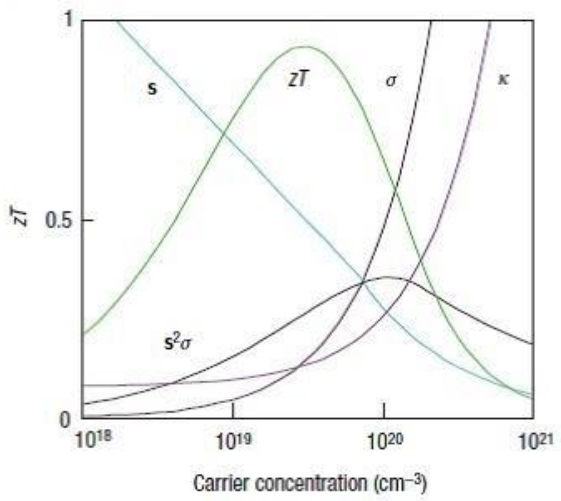

Fig. 2.7 The thermoelectric properties dependence of the carrier concentration (Trends shown were modelled from Bi_2Te_3), taken from Snyder and Toberer [38]

Another challenge is to keep the balance between **σ** and **S** based on control of the effective mass **m***. As mentioned in Section 2.2, **m*** plays an important part in determining **σ** and **S**. According to Equations (2.24) and (2.6), a small **m*** leads to an increase in **σ** but a reduction in **S**. It is acknowledged that element doping can be a useful approach to enhancing the carrier mobility but is also likely to modify the band structure, hence the electronic density of states (DoS). It is possible that **σ** is enhanced via increasing the carrier mobility at expense of lowering **S**, resulting in slight changes to the power factor. All in all, a compromise should be eventually reached among different thermoelectric parameters in order to enlarge the ZT value.

2.3.1 Element Doping

By doping suitable elements into available sites in the crystal lattice of candidate materials, the carrier concentration or mobility can be controlled and thus ideal thermoelectric properties can be obtained. A donor level or accepter level can be introduced into the band gap of the semiconductor by donor or accepter doping, shown in Fig. 2.8. For donor doping, the donor level is neutral when fully occupied by electrons. By increasing the temperature,

the electrons are excited into the conduction band and thus the donor level becomes positively charged, shown in Fig. 2.8(a). By contrast, as Fig. 2.8(b) shows, the accepter doping can help introduce holes into the valence band. Apart from enhancing the carrier concentration, impurity dopants are able to strengthen phonon scattering, thereby reducing the thermal conductivity.

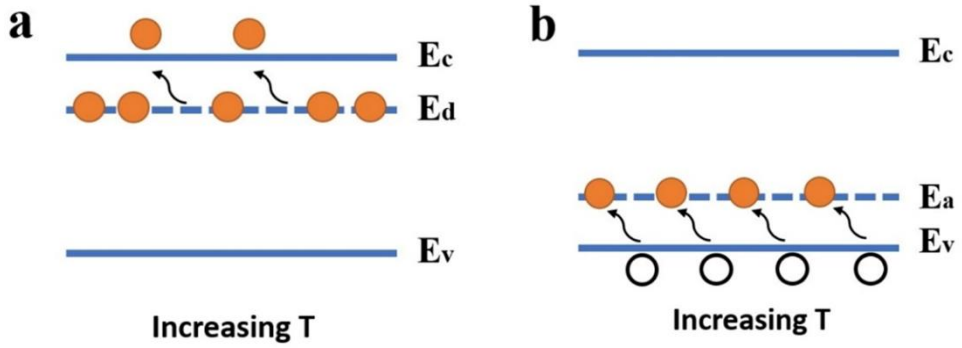

Fig. 2.8 Ionic processes for donor level (a) and accepter level (b) in the energy band (the solid sphere is the electron and the hollow sphere is the hole)

For example, BiCuSeO oxyselenide is a typical thermoelectric material, where holes can be generated via partial substitution of Bi^{3+} by Ba^{2+} in the $(Bi_2O_2)^{2+}$ layers that perform as charge reservoirs and then move into the conductive $(Cu_2Se_2)^{2-}$ layers, thereby enhancing the carrier concentration [39]. Li et al. [40] reported that the ZT value of BiCuSeO could be improved from 0.81 to 1.1 at 923 K when 12.5 at.% Bi^{3+} were substituted by Ba^{2+}, where the carrier concentration reached 1.1×10^{21} cm^{-3}. The effect of Pr doping on the transport properties of polycrystalline $SrTiO_3$ was studied by Dehkordi et al. [41]. Their theoretical calculations indicated that its power factor peaked at 2.0 $Wm^{-1}K^{-1}$ when the carrier concentration was 4.5×10^{21} cm^{-3}, basically matching the experimental results (the highest power factor was 1.8 $Wm^{-1}K^{-1}$ with the carrier concentration of 2.3×10^{21} cm^{-3}). Moreover, Li et al. [42] adjusted the ratio of Fe/Cu in $Cu_{1-x}Fe_{1+x}S_2$ to control the carrier concentration within 3.4×10^{19}-7×10^{20} cm^{-3}. At the same time, the lattice thermal conductivity was reduced by enhancing phonon scattering through the substitution of Cu by Fe, leading to over 50 % enhancement in the ZT value as a result.

2.3.2 Nano-sized Materials

Phonons can be scattered by grain boundaries between randomly oriented grains or defects generated between different interfaces, based on which nanomaterials are constructed to

increase the grain boundary density, thereby enhancing phonon scattering and reducing lattice thermal conductivity. On the other hand, low dimensional materials can also optimise the electrical transport properties. As Fig. 2.9 shows, due to the quantum confinement effects, the energy band structure is modified in the form of several sharp and dispersionless sub-bands when the grain size approaches nanometre length scales [43]. By controlling the dimension of the material, the energy band is likely to be near the Fermi level and the density of states at Fermi level is therefore enhanced, giving rise to an increase in Seebeck coefficient.

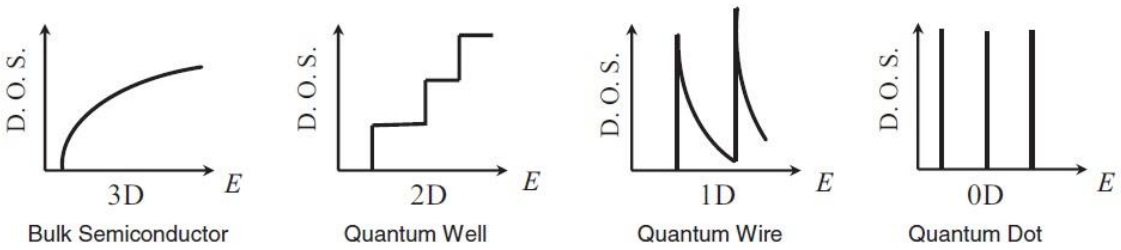

Fig. 2.9 DoS for a bulk 3D crystalline semiconductor, a 2D quantum well, a 1D nanowire or nanotube, and a 0D quantum dot, taken from Dresselhaus et al. [37]

At present, the fabrication processing of proposed bulk nanomaterials is generally divided into two steps. Firstly, various chemical or physical methods like mechanical alloying process [44] and melt spinning technique [45] are applied to grow fine grains or amorphous particles. Secondly, rapid sintering methods such as spark plasma sintering are used to avoid abnormal growth of grains during the densification process.

It was reported in 1981 that the ZT value of polycrystalline SiGe alloys was firstly improved by reducing the grain size to enhance grain boundary scattering; polycrystalline SiGe with grain size of 1.0 μm showed superior thermoelectric properties compared to single crystal SiGe [46]. After that, 50 nm-sized Si nanowires for thermoelectric applications were fabricated by an aqueous electroless etching method; 100 times smaller thermal conductivity was achieved and the ZT value reached 0.6 at 300 K [47]. Moreover, p-type $(Bi,Sb)_2Te_3$ was prepared by a mechanical alloying process in Ar atmosphere and its grain size was controlled within 50 nm. Results showed that the lattice thermal conductivity of sintered nanomaterials from as-prepared powders had fallen by half, enabling the ZT value to increase to 1.4 at 373 K [48].

The shortcomings of traditional methods for thermoelectric nanomaterials design lie in the reduction of electrical conductivity with enhanced carrier scattering. One of the solutions is to precipitate in-situ coherent nanocrystals in the precursor phase, where the electrical

conductivity can remain unchanged due to the weak scattering of carriers. For example, rod-like Sb with a thickness of 4.0 μm was prepared on InSb substrates by forming crystals in InSb-Sb eutectic alloys [49]. A significant decline in the thermal conductivity was observed when the size of rod-like Sb reduced to the nanoscale, while there was no obvious change in the Seebeck coefficient and electrical conductivity because of the coherent grain boundary between the parent phase and the precipitated phase.

2.3.3 Phonon-Glass Electron-Crystal (PGEC)

Slack [50] put forward the concept of phonon-glass electron-crystal, where the thermoelectric material is expected to have both the low thermal conductivity of a glass and the ideal electric transport performance of crystals. Meanwhile, it is pointed out that such materials are usually semiconductors with a narrow bandgap and high carrier mobility. The unique properties of a PGEC make it possible that the electrical conductivity is maximised while the thermal conductivity is minimised, thereby overcoming the trade-off relationship between these two factors to achieve a higher ZT value. Mahan et al. [51] also proposed that a qualified thermoelectric material should have specific characteristics with the band gap E_g of 0.25 eV at 300 K with the carrier mobility remaining at 2000 cm^2V/s, in addition to the low lattice thermal conductivity. Recently, many new materials such as half-Heusler alloys, clathrates, and skutterudites, with potential to be modified for PGEC have become heated topics in the thermoelectric field [28].

2.4 Thermoelectric Applications

Most thermoelectric applications are realised by a typical thermoelectric module as shown in Fig. 2.10 [38]. Heat can be converted into electricity, when a temperature difference exists across the module elements. On the other hand, a thermal gradient can be presented via the thermoelectric module in temperature cooling devices if an electric field is applied into the circuit. Therefore, the function of the thermoelectric module varies under different working conditions.

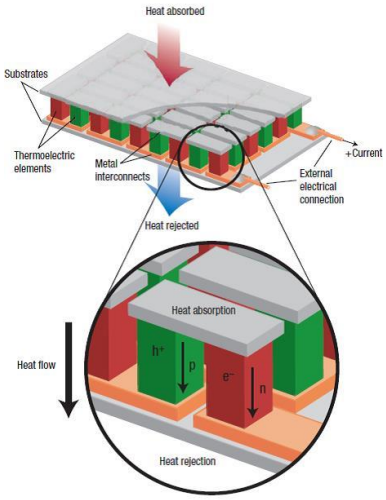

Fig. 2.10 Thermoelectric module showing the direction of heat flow on both cooling and power generation, taken from Snyder and Toberer [38]

N-type and p-type materials are the basic components, which are coupled together to achieve power generation or temperature cooling. However, the low voltage output or poor refrigerating efficiency in a single couple cannot meet the requirement for practical applications due to the low ZT value. Therefore, a series of couples are frequently connected in an array to form a module. It is not hard to understand that the combination of high-efficiency n-type and p-type materials contributes to obtaining good thermoelectric performance, but how to minimise the negative effects on the thermal gradient and electrical conductivity should be taken into consideration in this design as well. In view of this, Koumoto et al. [52] used silver paste electrodes containing oxide powders instead of copper electrodes. In addition, the thermal expansion between electrical connectors and legs should be well controlled because cracks will be generated at specific operating temperatures if a serious misfit between thermal expansion coefficients exists, which degrades the mechanical, electrical and thermal properties.

Thermoelectric generators have reliably provided power in vehicles activated by internal combustion engines, chemical industry systems, deep space probes etc. [53–56]. For instance, NASA has used a radioisotope thermoelectric power plant made of thermoelectric materials to power aviation detectors successfully [53]. The Hesse Company installed 72 thermoelectric conversion modules in the exhaust pipe of truck, the driving process of which could provide 2-3 kW of electrical power in total [54]. Similarly, the fuel efficiency of a BMW 530i was also significantly improved by using waste gas for power generation [55]. In addition, the power generation efficiency of a power station system could be increased by

5-7 % via installing thermoelectric converters in the boiler furnace of the heat power station [56].

Thermal management for computers or engines is realised by solid-state Peltier coolers [57]. For example, a vast range of hotspots inside the machine can decrease the service life and mechanical properties of components and this problem could be efficiently solved by promotion of thermoelectric cooling devices [58]. Furthermore, this effect can be applied for cooling infrared sensors, water coolers, cream dispensers and hotel room refrigerators [59]. As a result, the use of thermoelectric cooling devices helps to improve our quality of life.

2.5 Layered Thermoelectric Oxides

2.5.1 Bi-Cu-Ch-O System (Ch = S, Se, Te)

BiCuChO (Ch = S, Se, Te) oxyselenide (Fig. 2.11(a)) shows a ZrCuSiAs-type structure belonging to P4/nmm space group, where the $(Bi_2O_2)^{2+}$ oxide layers and $(Cu_2Ch_2)^{2-}$ chalcogenide layers stack perpendicularly along the c axis of the tetragonal unit cell [60]. It was first reported by Kholodkovskaya et al. as a superconducting material in 1993 [61]. Subsequently, BiCuChO was considered as a promising thermoelectric candidate due to its intrinsically low thermal conductivity and the moderate power factor produced from its low electrical conductivity and large Seebeck coefficient [2]. For example, BiCuSeO is a p-type semiconductor with a wide band gap of 0.8 eV, where intrinsic Cu vacancies generated holes as majority carriers [39]. With a very low electrical conductivity of 1.12 S/cm at room temperature, it still exhibited a ZT value of 0.5 at 923 K, due to a high Seebeck coefficient of 425 μVK^{-1} and a low thermal conductivity of 0.4 $Wm^{-1}K^{-1}$ at 923 K [39]. However, its ZT values within the temperature range of 273-1000 K still stand out compared to many other thermoelectric materials (Fig. 2.11(b)) [39]. Therefore, recent studies have mainly focused on the enhancement in power factor by element doping, such as substitutions by Sr, Ca, Mg, Zn, Na, Ag, etc., in order to achieve a desirable ZT value [62–66].

It was reported that the ZT value of undoped BiCuSeO (0.4 at 873 K) could be boosted to 0.76 at 873 K by Sr substitution for Bi, due to the increased Seebeck coefficient caused by two-dimensional confinement of the charge carriers [62]. Strategies including creating Cu vacancies or substituting Bi by Mg/Ca/Ba in BiCuSeO were also adopted to enhance carrier concentration. Liu et al. [67] optimised the ZT value of BiCuSeO to 0.81 at 923 K by increasing Cu deficiency to generate more Cu vacancies. Li et al. [63] reported that ZT value

of Mg doped BiCuSeO reached 0.67 at 923 K with over 30 times enhancement in room temperature electrical conductivity resulting from increased hole concentration. Similarly, Ba doping in BiCuSeO can give rise to an enhanced carrier concentration and decreased thermal conductivity, leading to a high ZT value of ~1.1 at 923 K [40].

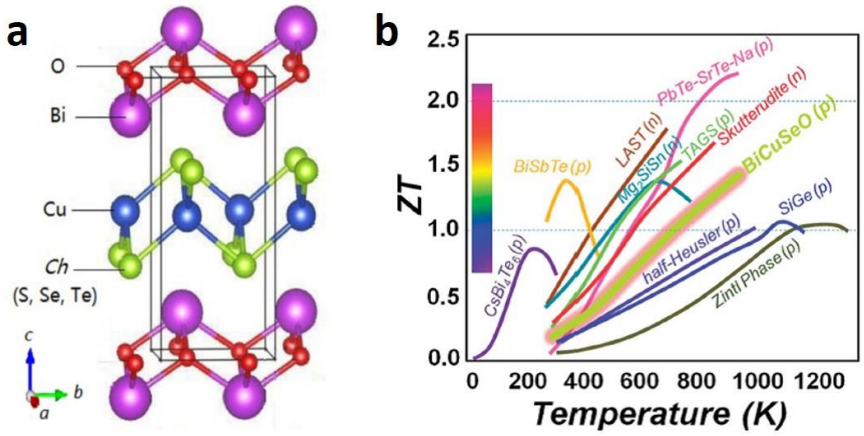

Fig. 2.11 (a) Crystal structure of BiCuChO, taken from Zhou et al. [60]; (b) ZT vs. temperature of typical current thermoelectric materials, taken from Zhao et al. [39]

In addition, the band structure of BiCuSeO can be modified by substituting Te for Se or Ag for Cu, which plays a vital part in improving the ZT value. As Fig. 2.12 shows, when 6 mol% Te was doped into Se sites, the band gap was reduced from 0.8 eV to 0.65 eV, which made it easier for electrons to be excited into the conduction band, leaving the same amount of holes in the valence band, thereby increasing the electrical conductivity with a resulting ZT value of 0.71 at 923 K [68]. However, there sometimes needs to be an adjustment of the balance between carrier concentration and Seebeck coefficients. For instance, the carrier concentration of BiCuSeO could be significantly enhanced by Sr doping, which can be easily explained by the change in electron content, whereas there was no obvious increase in the ZT value due to the severe reduction in Seebeck coefficient [69]. Although BiCuChO (Ch = S, Se, Te) shows excellent thermoelectric performance, the toxicity of the raw materials, consisting of Ch elements, limits its mass production/exploitation.

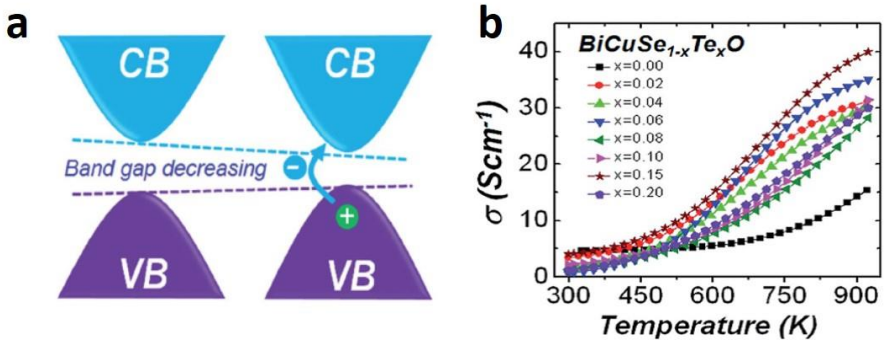

Fig. 2.12 (a) The schematic figure for band gap tuning (CB: conduction band; VB: valence band), (b) Dependence of electrical conductivity on temperature for Te doped BiCuSeO, taken from Liu et al. [68]

2.5.2 Na-Co-O System

Sodium cobalt oxide (Na_xCoO_2, denoted as NCO) is a typical misfit-layered transition metal oxide built upon the alternative stacking of a single Na ion layer and subsystems of two-dimensional CoO_2 layers along the *c*-axis [70]. The CoO_2 layers are usually made up of the edge-sharing CoO_6 octahedra and are able to provide holes as the charge carriers due to a mixed valence of Co^{3+} and Co^{4+}, which takes a key role in the electrical transport. Different symmetry sites near the two adjacent CoO_2 layers are randomly occupied by Na ions, forming a disordered structure responsible for scattering phonon. Basically, a wide range of non-stoichiometry (0-1) in Na_xCoO_2 enables the formation of four types of crystal structures with changes in sodium concentrations: β for $0.55 \leq x \leq 0.6$, γ for $0.5 \leq x \leq 0.7$, α′ for $x = 0.75$ and α for $0.9 \leq x \leq 1$ [71,72], shown in Fig. 2.13. In contrast to previous studies, Lei et. al [73] reported that the γ phase could form at slightly larger compositions (x ranges from 0.68 to 0.76), and other types of sodium cobaltites in single phase forms could only exist when x was fixed at 0.67, 0.83 and 1. Their study also indicated that for $Na_{0.75}CoO_2$ the α′ phase could transform into the γ phase when the sintering temperature increased from 773 to 1173 K [73]. At low temperatures, with Na concentration of 0.26-0.42, sodium cobaltite containing intercalated water undergoes a superconducting transition [74]. However, by increasing Na concentration to over 0.5, it exhibits a high thermoelectric power [75,76], showing a potential for it to be used for thermoelectric devices. Fujita et al. [77] also predicted that the calculated ZT value for single crystal $NaCo_2O_4$ could exceed 1.0 at 800 K.

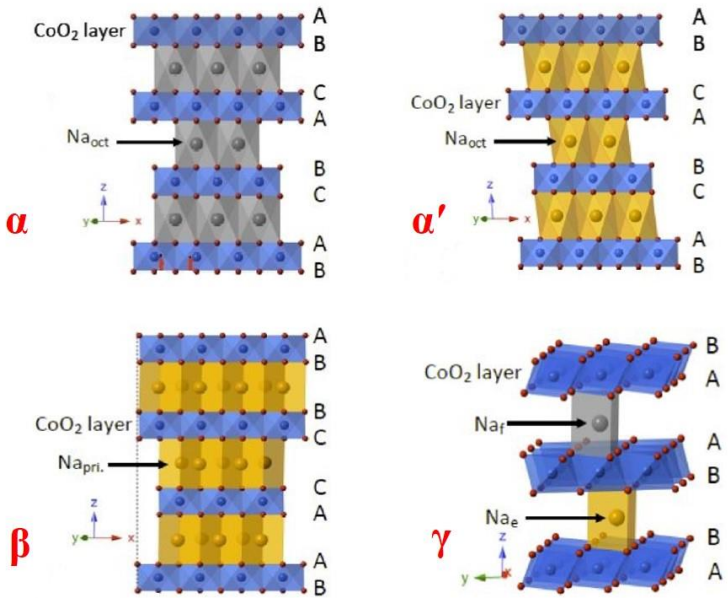

Fig. 2.13 Crystal structure of four different phases of sodium cobaltites (Symbols A, B, and C in the schematic figures represent layers of oxygen with different stacking sequences), taken from Lei et al. [73]

Various preparation techniques have been employed to fabricate sodium cobaltites, including solid state reaction [76], sol-gel method [78], hydrothermal reaction [79], mechanical alloying [71] and spark plasma sintering [80], among which the solid-state reaction (the mixed oxide route) is extensively used due to its simple processing and low cost. However, there are still three main problems regarding phase separation and low stability of Na-Co-O system awaiting solutions [81]: (i) the vaporization of sodium oxide (Na_2O) during the synthesis process at high temperatures; (ii) the formation of the impurity secondary phases such as Co_3O_4 and CoO; (iii) the formation of sodium hydroxide (NaOH) due to the chemical instability by reactions in a humid environment.

In order to improve thermoelectric performance of sodium cobaltites, the effects of Na concentration, Na-site doping, and Co-site doping have been investigated. Krasutskaya et al. [82] reported that the ZT values of sodium cobaltite prepared by the mixed oxide route depended highly on the Na concentration: the value was boosted from 0.1 to 1.1 at 800 K by increasing Na content from 0.55 to 0.89. Nagira et al. [83] also prepared polycrystalline samples of $(Na_{1-y}M_y)_xCo_2O_4$ (M = K, Sr, Y, Nd, Sm and Yb; y = 0.01-0.35) by the solid state reaction method and found that Sr substituted sample showed superior ZT values compared to other elements; the highest ZT of 0.42 at 765 K was achieved with Sr content fixed at 0.1. Ito et al. [84] investigated the effects of Co-site substitution by Mn and Ni for polycrystalline ceramic samples of $Na_xCo_{1-y}M_yO_2$ (M = Mn and Ni; y = 0, 0.03, 0.05 and 0.10). The results

indicated that Ni substitution made larger contributions to reducing the electrical resistivity, thereby achieving the highest ZT value of 0.88 at 960 K with the Ni content of 0.05.

2.5.3 Bi-AE-Co-O System (AE = Ca, Sr, Ba)

Similar to Na_xCoO_2, $Bi_2AE_2Co_2O_y$ has a structure which is alternately stacked with a conductive CoO_2 layer and an insulating $Bi_2AE_2O_4$ layer along the *c* axis but shows a highly anisotropic crystal structure due to the misfit nature of the lattice structures along the *b* axis [85]. In fact, the path of electrical conduction here is independent of that of the thermal transport, indicating that the lattice thermal conductivity can be altered by choosing a suitable insulating layer via inhibiting phonon activities. In general, the misfit layered oxides can be described as $[Bi_2AE_2O_4](CoO_2)_{b1/b2}$ (AE = Ca, Sr, Ba), where b_1/b_2 is the misfit parameter reflecting the ratio between the lattice parameter of CoO_2 layers and rock salt layers along the *b* axis and usually ranges from 1.69 to 1.98.

As Fig. 2.14(a) shows, the crystal structure of $Bi_2Sr_2Co_2O_y$ belongs to the C2/c space group and the lattice parameters are: a = 4.90 Å, b_1 = 5.11 Å, b_2 = 2.81 Å, c = 29.86 Å and β = 93.45° [86]. The single-crystalline $Bi_2Sr_2Co_2O_y$ whisker first synthesized by Funahashi et al. [87] in 2002, achieved the ZT value of 1.1 at 973 K (Fig. 2.14(b)), sparking interest in thermoelectric response modulation for this misfit cobaltite. Although the ZT value of $Bi_2Sr_2Co_2O_y$ whisker is comparable to some traditional thermoelectric alloys, the polycrystalline ceramics are considered to be better candidates for practical applications and large-scale production. However, the complex grain boundaries and defects inside the polycrystalline samples can be regarded as recombination centres for charge carriers, giving rise to a reduction in electrical conductivity and hence the ZT value. Although traditional mixed oxide routes can be implemented easily, porosity and impurity phases introduced by the incomplete reaction cannot be avoided. In order to enhance the densification and grain growth of $Bi_2Sr_2Co_2O_y$, various approaches including solid state reaction sintering, hot press sintering, spark plasma sintering, solution based synthesis and annealing process are also employed to prepare $Bi_2Sr_2Co_2O_y$ bulk materials [87,88]. For example, Sotelo et al. [89] reported that by use of the solution based synthesis route the fractions of cobaltite main phase were increased along with enhanced density and uniformity when 15 mol% cobalt deficiency was introduced in the nominal composition. In addition, the thermoelectric properties of $Bi_2Sr_2Co_2O_y$ could also be enhanced by substituting Bi by Pb/Ba [90,91] or inserting La/Ca [92,93] in AE sites, due to the increase in carrier concentration or reduction in lattice thermal

conductivity. Another useful strategy is to fabricate $Bi_2Sr_2Co_2O_y$ based composites with additives. For instance, Ag proved to be an efficient additive, which helped to improve the ZT values of $Bi_2Sr_2Co_2O_y$ based ceramics to over 0.25 at 1000 K [94,95].

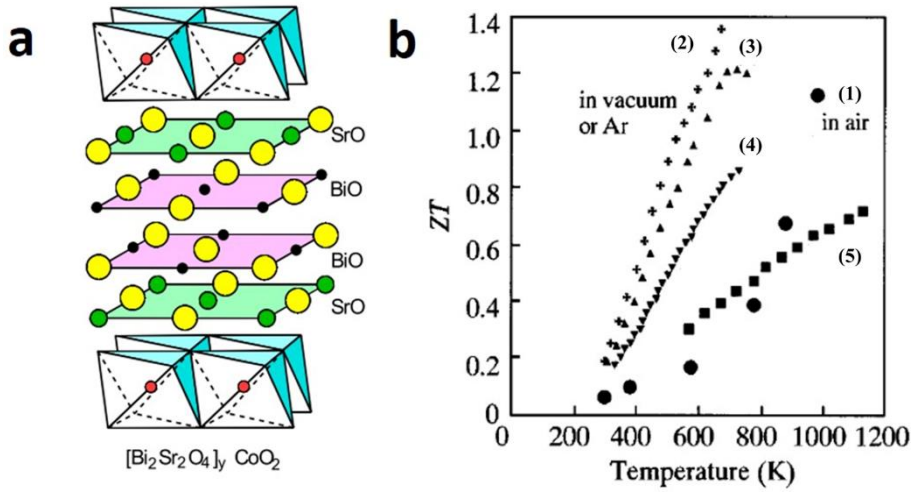

Fig. 2.14 (a) Crystal structure of $Bi_2Sr_2Co_2O_y$, taken from Ohtaki [85]; (b) ZT vs T for $Bi_2Sr_2Co_2O_y$ whisker (1), p-b-Zn_4Sb_3 (2), p-TeAgGeSb (3), p-$CeFe_4Sb_{12}$ (4), and p-Si-Ge alloy (5), taken from Funahashi and Shikano [87]

2.6 Ca-Co-O System – Model Thermoelectric Material

2.6.1 Crystal Structure

Calcium cobaltite ($Ca_3Co_4O_9$) is also a promising p-type thermoelectric oxide with a modulated misfit structure. The crystal structure of single crystal $Ca_3Co_4O_9$ prepared by flux method was first reported by Masset et al. [96] in 2000, and then precisely determined as $[Ca_2CoO_3]_{0.62}CoO_2$ by Miyazaki et al. [97]. As Fig. 2.15 shows, this monoclinic structure presents incommensurate periodicities between the CoO_2 layers and rock salt layers along the *b* axis, thereby demonstrating two different lattice constants *b* (b_1 = 4.56 Å; b_2 = 2.82 Å) along with the same parameter values of *a* and *c* (*a* = 4.83 Å; *c* = 10.84 Å) [98,99]. In fact, the misfit ratio between the $[CoO_2]$ layer and the $[Ca_2CoO_3]$ layer is not exactly a rational number but approaches the golden ratio $\tau \approx (1: 0.618)$ [99]. Similar to Na_xCoO_2, there is mixed valences of Co^{3+} and Co^{4+} in the CoO_2 layer, where Co^{4+} among Co^{3+} is able to regulate the hole concentration, and the low spin Co^{3+} is mainly responsible for its large Seebeck coefficient [100]. The rock salt layer enables low lattice thermal conductivity through inhibiting phonon transport [101].

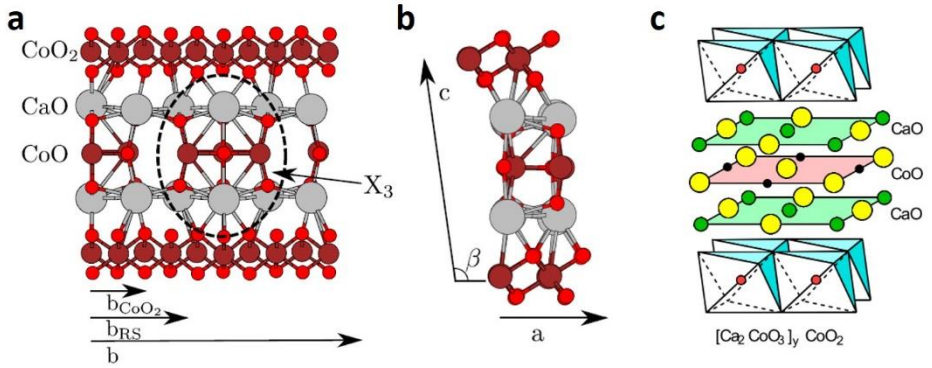

Fig. 2.15 (a) The structure of pristine CCO with an approximate 5/3 unit cell along the [100] and (b) [010] (X_3 represents the rock salt layer), taken from Hu et al. [98]; (c) Simplified CCO structure for one unit cell plus an extra CoO_2 layer, taken from Ohtaki [85]

As the modulated crystal structure of $Ca_3Co_4O_9$ cannot be easily refined using common XRD analysis software such as Topas or Jade, the average structure of $Ca_3Co_4O_9$ was also adopted for approximate estimation of the lattice parameters [102], shown in Fig. 2.16.

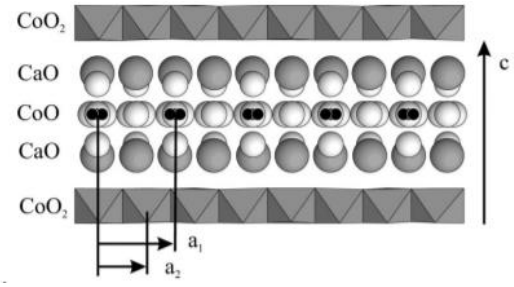

Fig. 2.16 The projection of the misfit average structure $[Ca_2CoO_3][CoO_2]_{1.62}$ along the *b* axis and the central layer is characterized by split disordered sites for Co and O, taken from Grebille et al. [102]

Masset et al. [96] also examined the crystal structure of $Ca_3Co_4O_9$ by High-Resolution Transmission Electron Microscopy (Fig. 2.17(a)); the interplanar distance between the AO layers (highlighted dark arrows) is estimated to be 10.7 Å, in good agreement with (001) crystal plane of $Ca_3Co_4O_9$. The theoretical, calculated, image for $Ca_3Co_4O_9$ in [100] zone-axis confirmed this structure was built upon on alternating stacking of CoO_2 layers and rock salt layers, which can be described by the formula $[Co_{0.5}CaO_{1.5-x}]_2[CoO_2]_{1.62}$ (Fig. 2.17(b)). Based on analysis of the SAED patterns in [001] zone-axis in Fig. 2.28(c), Seo et al. [103] observed two set of diffraction spots separately in the crystal lattice of $Ca_3Co_4O_9$; the calculated lattice parameter *b* for the rock salt layer and CoO_2 layer was 4.56 Å and 2.82 Å,

respectively, matching well with the results reported by Masset et al. [96] and Miyazaki et al. [97].

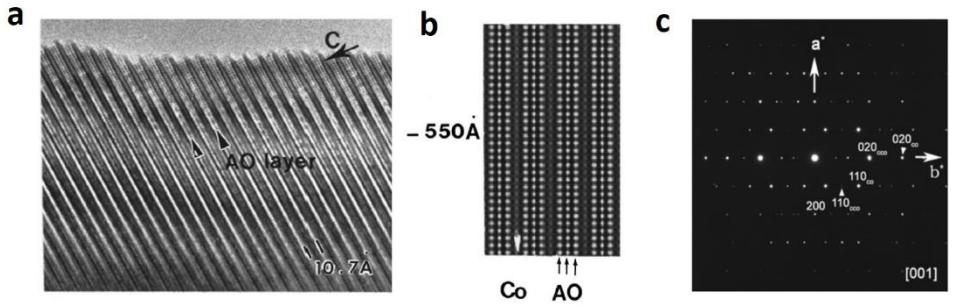

Fig. 2.17 (a) HRTEM images of $Ca_3Co_4O_9$ in [100] zone-axis, taken from Masset et al. [96]; (b) Theoretical calculated image for $Ca_3Co_4O_9$ in [100] zone-axis, taken from Masset et al. [96]; (c) SAED patterns of $Ca_3Co_4O_9$ in [001] zone-axis, taken from Seo et al. [103]

2.6.2 Electrical Transport

Shikano et al. [104] prepared the single crystal $Ca_3Co_4O_9$ from $CaCO_3$, Co_3O_4, $CaCl_2•2H_2O$ and $SrCl_2$ powders by the flux method (Fig. 2.18(a)); the highest ZT value reached 0.87 at 973 K. The electrical transport properties of the as-prepared sample are shown in Fig. 2.18(b) and (c). It is apparent that the electrical conductivity fluctuates around 410.0-500.0 S/cm with the corresponding Seebeck coefficient varying from 110.0 to 250.0 μV/K within the temperature range of 200-1000 K. The low electrical resistivity of the as-prepared sample is attributed to high carrier mobility in the single crystal.

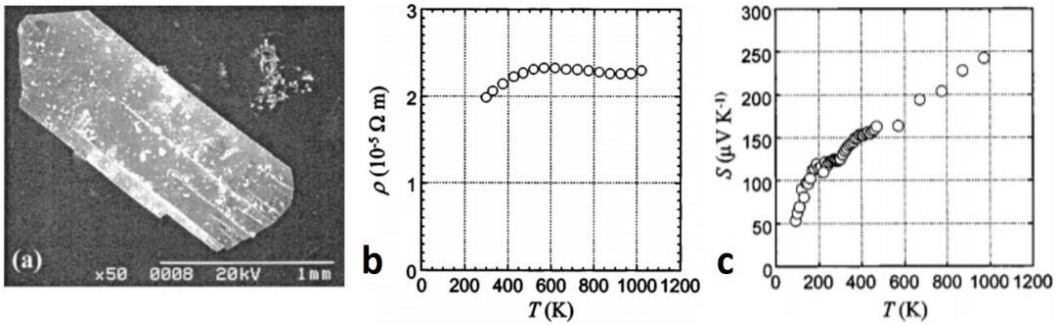

Fig. 2.18 Single crystal $Ca_3Co_4O_9$: (a) SEM image; (b) Electrical resistivity vs. T; (c) Seebeck coefficient vs. T, taken from Shikano and Funahashi [104]

Obata et al. [105] investigated the effects of calcination conditions and grinding processes on electrical transport properties of polycrystalline $Ca_3Co_4O_9$ samples prepared by solid state reaction; results are shown in Fig. 2.19. The Seebeck coefficients are almost constant (120.0-

160.0 μV/K), whereas the electrical conductivity varies from 22.0 to 40.0 S/cm within the temperature range of 373-1073 K. Basically, the electrical conductivity in polycrystalline samples is heavily restricted by the resultant densification and grain boundary density, thereby significantly lower compared to the single crystal. As Fig. 2.19(a) displays, the samples of group c shows the lowest electrical resistivity due to the lowest grain boundary density among all sample groups. By extending the calcination time and manual grinding, the processing leads to a lager grain size and reduced grain boundaries, thereby weakening carrier scattering and improving carrier mobility. The inferior transport properties of the polycrystalline sample compared to the single crystal is also probably related to its anisotropy. Lim et al. [106] developed texture in $Ca_3Co_4O_9$ ceramics by spark plasma sintering and found that the overall electrical conductivity can be enhanced by grain alignment, where the in-plane electrical conductivity nearly quadrupled compared to the out-of-plane value for samples sintered at 1233 K.

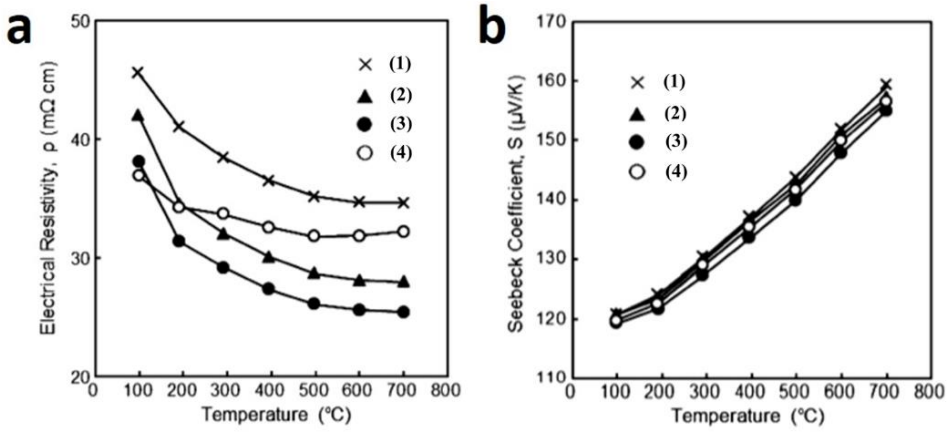

Fig. 2.19 Electrical resistivity (a) and Seebeck coefficient (b) of polycrystalline $Ca_3Co_4O_9$ samples as a function of temperature (sample groups: (1) 900 ºC/1 h + manual grinding; (2) 900 ºC/10 h + manual grinding; (3) 900 ºC/20 h + manual grinding; (4) 900 ºC/20 h + ball milling), adapted from Obata et al. [105]

2.6.3 Thermal Transport

Shikano et al. [104] measured the thermal conductivity of single crystal $Ca_3Co_4O_9$ (Fig. 2.20(a)). The overall thermal conductivity shows a decrease from 3.2 $Wm^{-1}K^{-1}$ to 2.8 $Wm^{-1}K^{-1}$ when the temperature increases from 273 K to 1000 K, basically matching the computational results of Rébola et al. [99]. The electronic thermal conductivity only reaches 0.45 $Wm^{-1}K^{-1}$ at 273 K, which is significantly lower than the contribution from phonons, suggesting that the phonon thermal conductivity takes a dominate role at low temperatures. By contrast, the electronic thermal conductivity can be enhanced to 1.0 $Wm^{-1}K^{-1}$ with the

lattice thermal conductivity of 1.8 $Wm^{-1}K^{-1}$ at 1000 K. Fig. 2.20(b) indicates that the heat conduction does not follow the typical phonon mode, which is probably related to the phonon-phonon interaction induced by a misfit structure between the CoO_2 layers and rock salt layers [107].

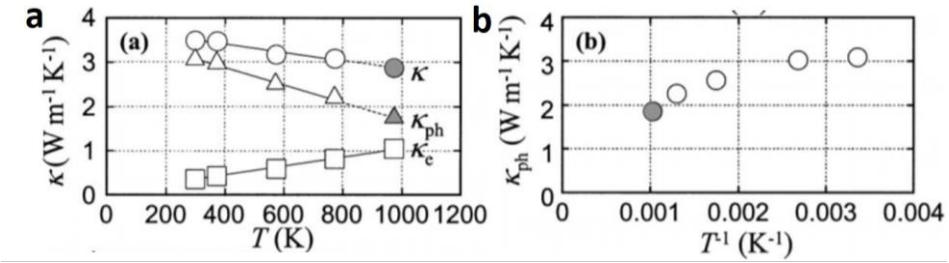

Fig. 2.20 (a) Temperature dependences of thermal conductivity for single crystal $Ca_3Co_4O_9$; (b) Phonon thermal conductivity vs. T^{-1} plot for single crystal $Ca_3Co_4O_9$, taken from Shikano and Funahashi [104]

Gunes et al. [108] investigated the effects of grain size on thermal conductivity of polycrystalline $Ca_3Co_4O_9$ ceramics prepared by the sol-gel method (Fig. 2.21(a)). As expected, the thermal conductivity of polycrystalline $Ca_3Co_4O_9$ ceramics varies from 0.3 to 1.0 $Wm^{-1}K^{-1}$, significantly lower than that of the single crystal. As grain boundary density can be enhanced by reducing the grain size to the nanoscale, the grain boundary scattering become more pronounced. The evidence is that the overall thermal conductivity can be dramatically reduced by reducing the grain size from 2.0 μm to 18.0 nm. As indicated by Fig. 2.21(b) and (c), the phonon thermal conductivity takes a dominating role during the heat transfer, similar to the single crystal $Ca_3Co_4O_9$. Fig. 2.21(d) shows the lattice thermal conductivity vs. 1000/T plot for polycrystalline $Ca_3Co_4O_9$, where two different scattering mechanisms are revealed. The plot can be divided into two parts: a linear region and a nonlinear region. The linear range can be described by an Umklapp process, representing characteristic phonon-phonon scattering [109]. The other can be ascribed to grain boundary scattering owing to higher porosity or smaller grain size [110]. The transformation temperature decreases with grain size, which indicates that phonon propagation can be effectively hindered by a high grain boundary density at low temperatures.

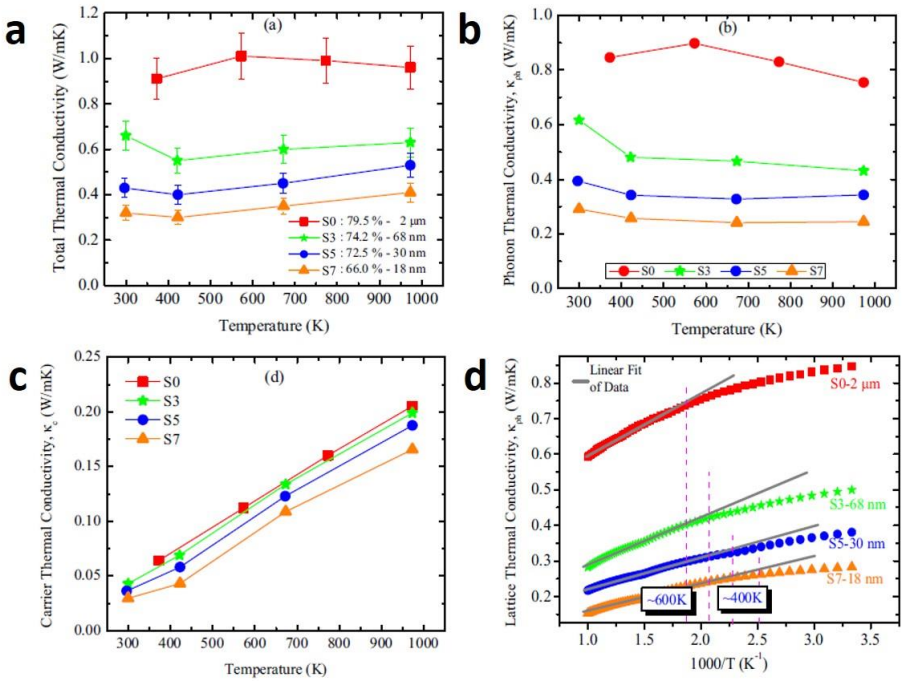

Fig. 2.21 Behaviour of polycrystalline $Ca_3Co_4O_9$ samples: (a) Temperature dependence of thermal conductivity, (b) phonon thermal conductivity, (c) carrier thermal conductivity, (d) lattice thermal conductivity vs. 1000/T plot, taken from Gunes et al. [108]

2.6.4 Anisotropy of Textured Polycrystalline Samples

With naturally high aspect ratio (*a-b/c*) planes, calcium cobaltite grains are able to develop texture parallel to the *ab* plane, stacking along the *c* axis, if an external pressure or magnetic field is applied. These highly textured samples can demonstrate strong anisotropy of thermoelectric properties in different directions. Basically, along the *ab* plane, the electrical conductivity and thermal conductivity will be maximised while the Seebeck coefficient will be minimised [111,112], due to the reduced grain boundary barriers; the case for crossing the *ab* plane is opposite. For example, Lim et al. [106] reported that the power factor and thermal conductivity parallel to the *ab* plane for textured calcium cobaltite could reach 500.0 $\mu Wm^{-1}K^{-2}$ and 3.1 $Wm^{-1}K^{-1}$ at 1200 K, showing about 400 % and 200 % increase compared to the data perpendicular to the *ab* plane, respectively. Wu et al. [111] also reported 50 % higher ZT value at 823 K parallel to the *ab* plane compared to the opposite direction for calcium cobaltite prepared by auto-combustion synthesis and spark plasma sintering, shown in Fig. 2.21. Interestingly, Srivastava et al. [112] found the ZT values for textured $SrTiO_3$/graphene composites in both directions were quite similar owing to the contrasting effects among different thermoelectric parameters. The anisotropy differences for reported textured samples are probably related to the degree of grain orientation. The texture of

calcium cobaltite is developed due to its plate-like features, while that for $SrTiO_3$ mainly results from the assistance of plate-like graphene. As a very large Lotgering factor (over 0.90) for calcium cobaltite was obtained by Wu et al., the effect of the anisotropy becomes more pronounced (Fig. 2.21).

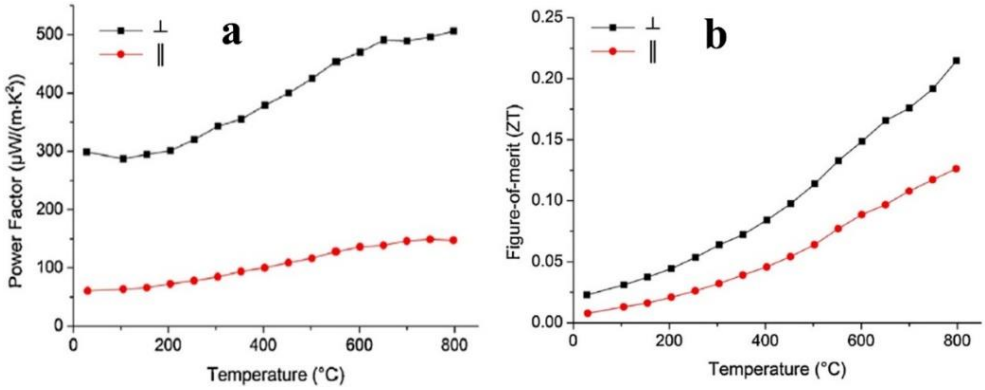

Fig. 2.21 Temperature dependence of the power factor (a) and ZT values (b) for textured calcium cobaltite in different directions (the label for the direction is with respect to the pressure direction), taken from Wu et al. [111]

2.6.5 Effects of Fabrication Routes

Fabrication routes play an important part in determining the thermoelectric properties of calcium cobaltite because the grain size and microstructure of synthesized samples can be significantly influenced with respect to preparation techniques. Many fabrication methods including solid-state reaction [113–115], sol-gel method [113,116], coprecipitation method [114], hot pressing [115], spark plasma sintering [117], and high-magnetic-field sintering [118] have been employed to modify the thermoelectric performance of $Ca_3Co_4O_9$; their advantages or disadvantages are easily distinguished. Overall, the mixed oxide route is widely used due to its simple process and low cost, but the purity of the product still needs to be improved. Although wet chemical routes such as sol-gel method and coprecipitation method are able to synthesize ultrafine powders, they are usually time-consuming and have low yield. Hot pressing, SPS route and high-magnetic-field sintering enable optimised thermoelectric performance of synthesized materials by inducing texture. However, well-controlled experimental conditions and sophisticated instruments are required, and large-scale production cannot be easily realised.

Sotelo et al. [114] investigated the effects of solid state reaction, attrition milling and coprecipitation method on the electrical transport properties of $Ca_3Co_4O_9$ ceramics, shown in Fig. 2.22. It is apparent that the Seebeck coefficient is insensitive to fabrication routes,

varying from 122.0 to 240.0 µV/K for all samples. By marked contrast, samples prepared by wet chemical routes show much lower electrical resistivity compared to samples prepared by the mixed oxide route, due to the smaller grain size, stronger and cleaner grain boundaries, and higher fractions of primary phase ($Ca_3Co_4O_9$). As a result, the highest power factor reaches 0.44 $mWm^{-1}K^{-2}$ for samples prepared by coprecipitation with oxalic acid at 1073 K. Kenfaui et al. [115] compared the electrical transport properties of $Ca_3Co_4O_9$ ceramics prepared by conventional solid state reaction, hot pressing and SPS route, shown in Fig. 2.23. With a similar Seebeck coefficient variation (170 µV/K at 800 K), the sample prepared by hot pressing shows the lowest electrical resistivity (8.0 mΩcm at 850 K) and highest power factor (550 $\mu Wm^{-1}K^{-2}$ at 850 K) because of the improved carrier mobility caused by the strongest texture and highest density.

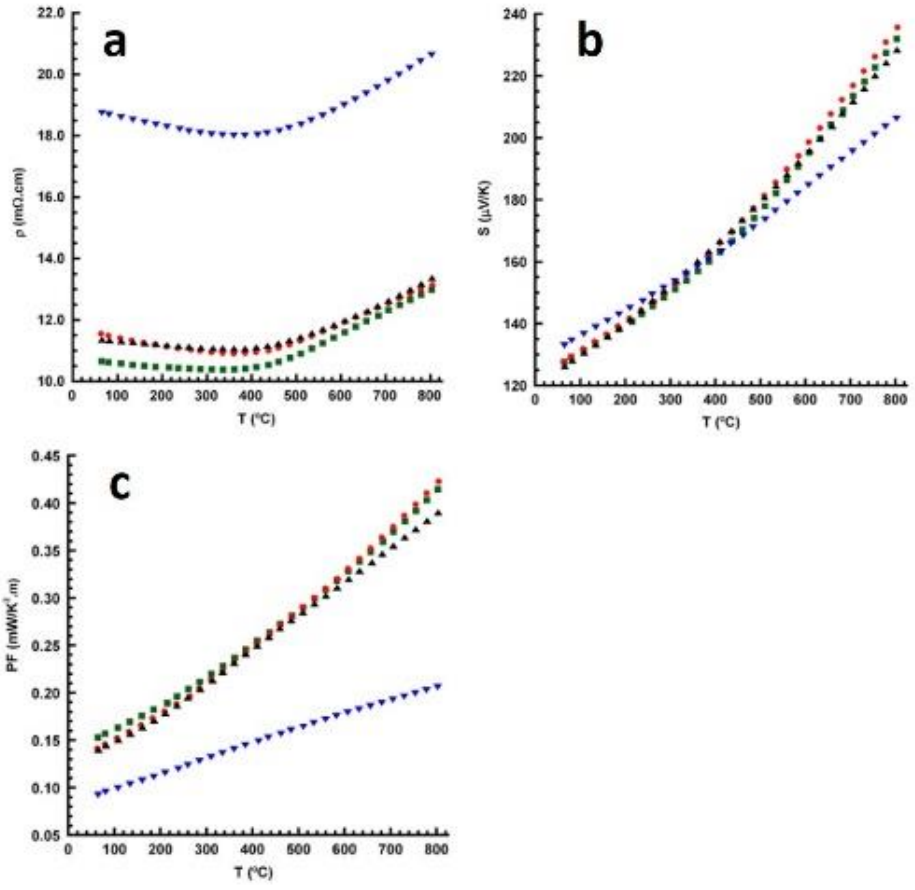

Fig. 2.22 Temperature dependence of the electrical resistivity (a), Seebeck coefficient (b) and power factor (c) of $Ca_3Co_4O_9$ prepared by solid-state reaction (blue), attrition milling (black), coprecipitation with ammonium carbonate (green) and oxalic acid (red), taken from Sotelo et al. [114]

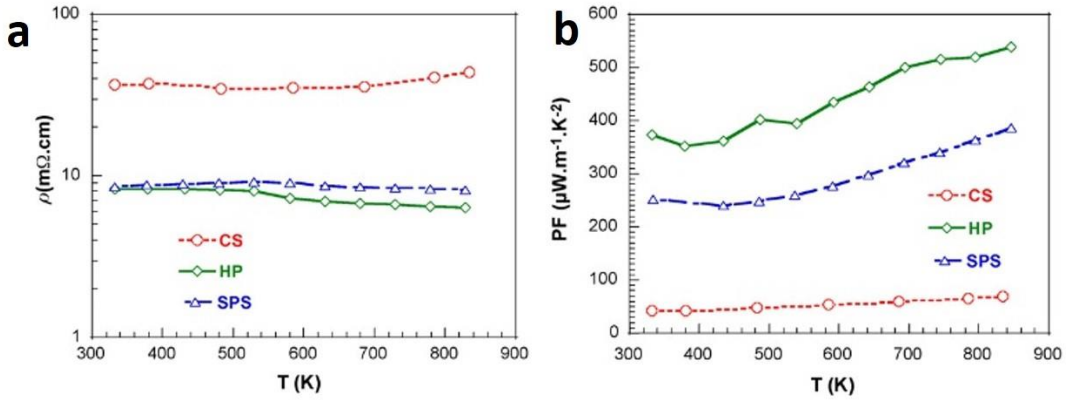

Fig. 2.23 Temperature dependence of the electrical resistivity (a) and power factor (b) of $Ca_3Co_4O_9$ prepared by conventional solid-state reaction, hot pressing and SPS route, taken from Kenfaui et al. [115]

2.6.6 Effects of Inclusions

Many additives have been employed to fabricate $Ca_3Co_4O_9$ based composites to improve the thermoelectric properties by either enlarging the power factor or reducing the thermal conductivity. These inclusions can play key roles in controlling the grain growth, texture development, lattice strain filed, vacancies, carrier conductive path and porosity. Amaveda et al. [119] and Wang et al. [120] selected carbides as the additives to enhance the power factor of $Ca_3Co_4O_9$. The former prepared calcium cobaltite with addition of 0.25 wt.% TiC nanoparticles, where the Seebeck coefficient is increased due to the strengthened grain boundary scattering caused by smaller grain size; the thermal conductivity was also lowered due to the high porosity, thereby leading to a ZT of 0.16 at 1073 K , which is ~40 % higher than the pure control group. Interestingly, the latter found addition of SiC could enlarge the grain size, opposite to the effects brought by TiC, but improved the texture of $Ca_3Co_4O_9$. As a consequence, 3 wt.% SiC-added $Ca_3Co_4O_9$ with the Lotgering factor of 0.685 showed the highest power factor of 125 $\mu Wm^{-1}K^{-2}$ at 973 K owing to the enhanced carrier mobility.

Chen et al. [121] achieved an obvious enhancement in Seebeck coefficient of $Ca_3Co_4O_9$ (160.0 to 200.0 μV/K at 923 K) without degrading electrical conductivity by 3.0 wt.% $Na_{0.77}CoO_2$ addition, which could be explained by the compressive strain on $Ca_3Co_4O_9$ induced via the mismatch of thermal expansion coefficients between calcium cobaltite and sodium cobaltite. Rasekh et al. [122] also prepared $Ca_3Co_4O_9$ based composites with another layered cobaltite $Bi_2Ca_2Co_{1.7}O_x$ as additives by the electrically assisted laser floating zone technique (EALFZ) for single crystals. The large thermopower of obtained samples (300 μV/K at 923 K) is attributed to more oxygen vacancies in the thermoelectric

$Bi_2Ca_2Co_{1.7}O_x$ phase introduced by the EALFZ, resulting in a high power factor of 0.31 $mWm^{-1}K^{-2}$ at 923 K.

Highly conductive metallic Ag is also a frequently used inclusion for tuning the thermoelectric performance of $Ca_3Co_4O_9$, but the final ZT value is still restricted by the large thermal conductivity of Ag, which is almost two orders higher than that of the $Ca_3Co_4O_9$ matrix. Wang et al. [123] and Mikami et al. [124] investigated the effect of Ag additions on thermoelectric performance of $Ca_3Co_4O_9$ by high-pressure synthesis and the mixed oxide route, respectively. As Fig. 2.24 shows, with the Ag content rising to 10 wt.% the electrical resistivity of composites is significantly lowered, mainly due to the intrinsically high electrical conductivity of Ag. Meanwhile, over 10.0 wt.% Ag addition is more likely to generate agglomerations, thereby providing a new carrier transport route in the system, and thus increasing carrier mobility.

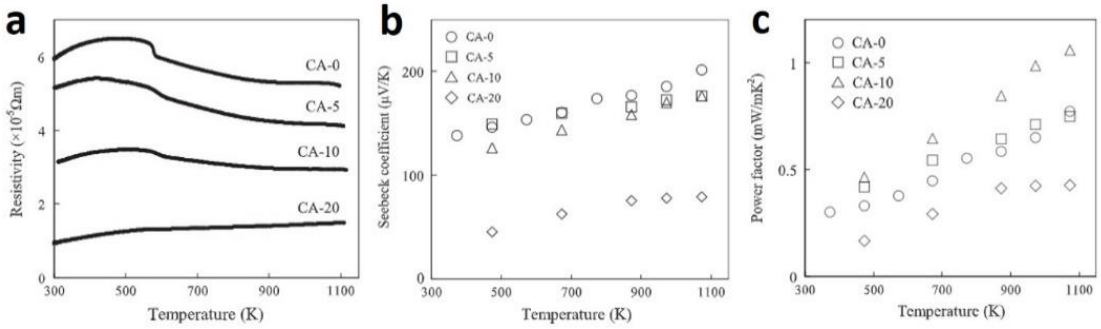

Fig. 2.24 Temperature dependence of the electrical resistivity (a), Seebeck coefficient (b) and power factor (c) of $Ca_3Co_4O_9$ with different levels of Ag addition, taken from Mikami et al. [124]

Kahraman et al. [125] further studied the mechanism of enhanced transport properties with the addition below 10 wt.% and found that the increased electrical conductivity could be ascribed to improved carrier mobility due to the reduction of porosity and improved sinterability originating from the Ag-generated liquid phase. Song et al. [126] reduced the Ag inclusions to nanoscale by a two-step SPS route, achieving a ZT value of 0.14 at 923 K by improved texture and enhanced grain boundary scattering.

2.6.7 Effects of Calcium-site Doping

Tuning thermoelectric properties of $Ca_3Co_4O_9$ by Ca-site doping is a popular strategy. By substituting suitable cations for Ca^{2+} in the rock salt layer, the carrier concentration and

mobility as well as the thermal conductivity can be modified accordingly. Zhang et al. [127] improved the ZT value of $Ca_3Co_4O_9$ to 0.21 at 1223 K via enhanced carrier concentration induced by optimised substitution of Ca^{2+} by Ag^{+}. Constantinescu et al. [128] reported that the power factor of $Ca_3Co_4O_9$ could be enhanced to 0.33 $mWm^{-1}K^{-2}$ at 1073 K by 2.3 at.% Na^{+} substitution for Ca^{2+}. The carrier concentration was enhanced by Na^{+} substitution for Ca^{2+}, due to the increase of Co^{4+} concentration for elevating the average cobalt valence, and the carrier mobility was improved by the weakened grain boundary scattering resulting from the grain growth facilitated by the Na-rich liquid phase.

Carvillo et al. [129] and Boyle et al. [130] prepared highly dense calcium cobaltite through the high-pressure synthesis, showing improved densification. It was also found that dopant (Ba and Bi) segregation at grain boundaries contributed to improving the texture and hence the carrier mobility of calcium cobaltite. The segregation also enabled more pronounced carrier filtering effects at grain boundaries, thereby increasing the thermopower (Fig. 2.25). Meanwhile, phonon scattering could be enhanced due to the heavier atomic mass of Ba and Bi than Ca. As a result, very high ZT values of $Ca_{2.95}Ba_{0.05}Co_4O_9$ and $Ca_{2.8}Bi_{0.2}Co_4O_9$ ceramics of 0.52 (Fig. 2.25(d)) and 0.43 were obtained at 1023 K, respectively.

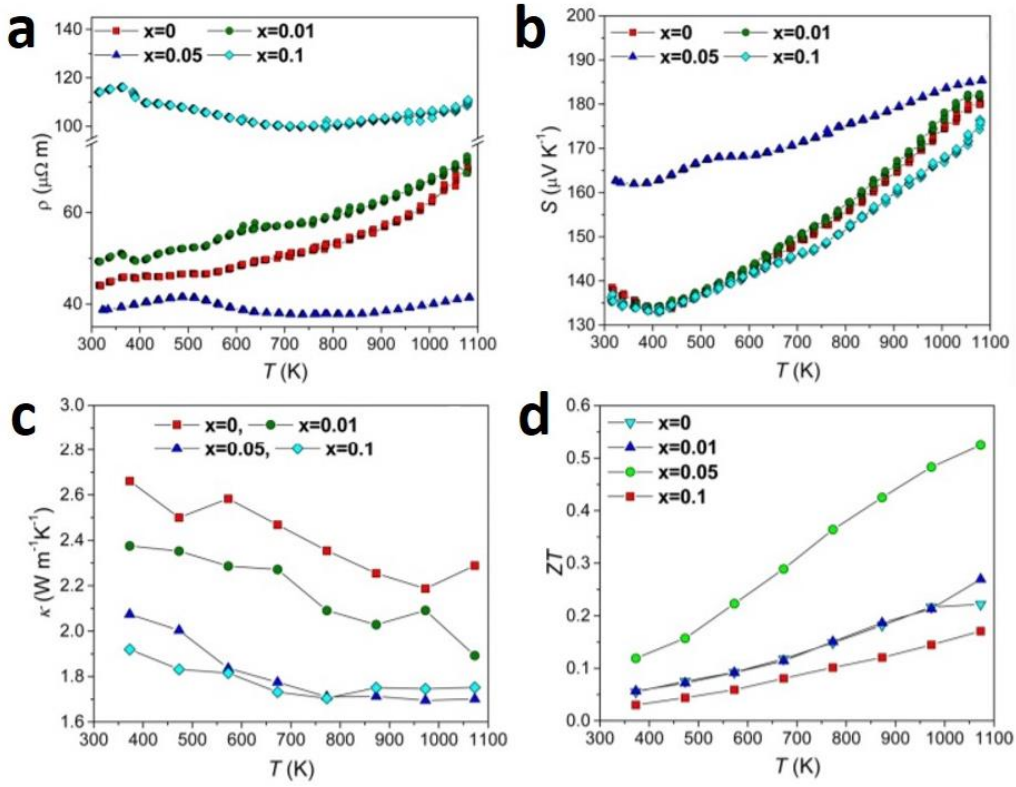

Fig. 2.25 Temperature dependence of the electrical resistivity (a), Seebeck coefficient (b), thermal conductivity (c) and ZT values (d) of Ba doped $Ca_3Co_4O_9$, taken from Carvillo et al. [129]

2.6.8 Effects of Cobalt-site Doping

The electronic density of states and the effective mass can be modified by changes in the electronic structure due to different Co ions states in $Ca_3Co_4O_9$. Therefore, doping suitable elements into Co-sites becomes a popular strategy to control the electrical transport properties.

Huang et al. [131] investigated thermoelectric response of $Ca_3Co_{4-x}Ir_xO_9$ at low temperatures, where the Ir doping extended the electronic band in the vicinity of the Fermi level, which decreased E_v and thus enlarged the band gap, leading to the enhancement in the activation energy and carrier localization. As a consequence, the Seebeck coefficient significantly increased although the carrier concentration was partially neutralised by the electrons induced by Ir^{4+}. Wang et al. [12] investigated the effects of different dopants (Fe, Mn and Cu) in Co-sites on the thermoelectric performance of $Ca_3Co_4O_9$. As Fig. 2.26 shows, there are three different forms of transport properties: ρ decreases while S increase (Fe doing); both ρ and S increase (Mn doping); both ρ and S decrease (Cu doping). The changes brought by Mn or Cu doping can be explained by changes of carrier concentrations due to valence differences between dopant ions, while the unexpected enhancement in Seebeck coefficient in Fe doped samples is caused by the increase in effective mass. Wu et al. [132] further investigated the mechanism of enhanced electrical conductivity in $Ca_3Co_{4-x}Fe_xO_9$ ceramics, where the substitution of Co site by Fe in the rock salt layer enabled a more ordered structure in the CoO_2 layer, which reduced the carrier scattering and increased the carrier mobility.

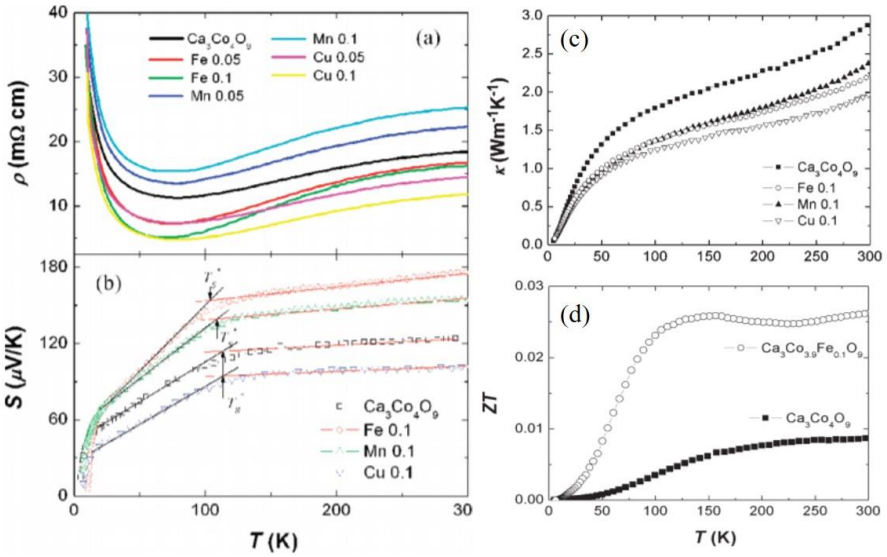

Fig. 2.26 Temperature dependence of the electrical resistivity (a), Seebeck coefficient (b), thermal conductivity (c) and ZT values (d) of $Ca_3Co_{4-x}M_xO_9$ (M = Fe, Mn and Cu), taken from Wang et al. [12]

2.6.9 Effects of Dual Doping

There are limited studies reporting effects of dual doping on thermoelectric performance of $Ca_3Co_4O_9$, but several results are still of possible interest. Although most of enhancement mechanisms in dual doped calcium cobaltite are awaiting further exploration, this strategy provides novel ideas to design high-performance thermoelectrics by grains boundary engineering and interfaces modification.

Liu et al. [15] prepared $Ca_{2.8}Ba_{0.1}Pr_{0.1}Co_4O_{9+\delta}$ ceramics by sol-gel method; the power factor reached 462.0 $\mu Wm^{-1}K^{-2}$ at 973 K, about 13.7 % higher than that of the undoped calcium cobaltite. It was found that Ba/Pr co-doping supressed grain growth, thereby increasing the thermopower by increased carrier scattering. The induced lattice distortion and stress concentration acted as scattering centres and the changes of effective mass were also suspected to contribute. Nong et al. [133] reported a boost in ZT value of $Ca_{2.8}Ag_{0.05}Lu_{0.15}Co_4O_{9+\delta}$ (0.61 at 1118 K) by Ag/Lu dual doping, which was the highest value among calcium cobaltite prepared by the SPS route (Fig. 2.27). Although the mechanisms for the rise in Seebeck coefficient and decrease in thermal conductivity are unclear, the compositional clustering followed by the formation of a fine-scale distribution of nano Ag precipitates was suspected to play an important role here. Song et al. [134] fabricated Lu/Ga co-doped $Ca_3Co_4O_9$ with Ag inclusions and ascribed the increased ZT value to the significant reduction of thermal conductivity because the formation of nanostructures and point defects among the interfaces increased phonon scattering.

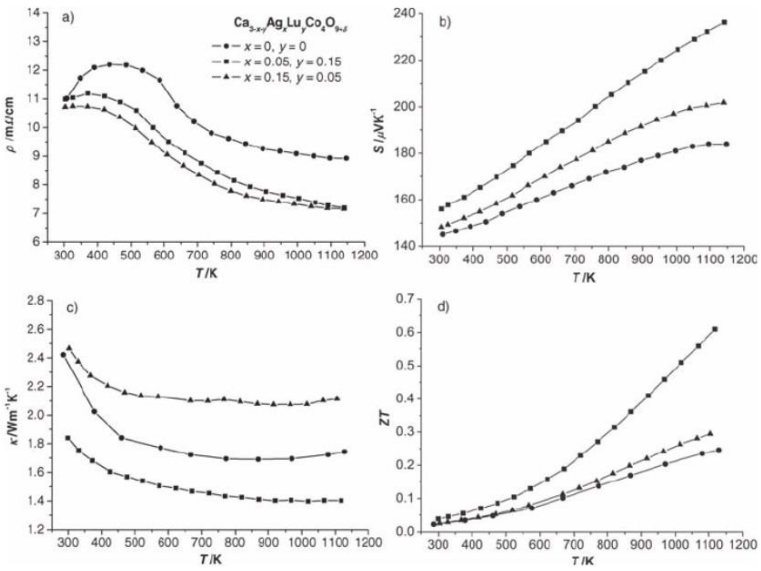

Fig. 2.27 Temperature dependence of the electrical resistivity (a), Seebeck coefficient (b), thermal conductivity (c) and ZT values (d) of $Ca_{3-x-y}Ag_xLu_yCo_4O_{9+\delta}$ ceramics, taken from Nong et al. [133]

References

[1] T.J. Seebeck, Ueber die magnetische Polarisation der Metalle und Erze durch Temperaturdifferenz, Ann. Phys. 82 (1826) 253–286.

[2] X. Zhang, L.D. Zhao, Thermoelectric materials: Energy conversion between heat and electricity, J. Mater. 1 (2015) 92–105.

[3] J.F. Li, W.S. Liu, L.D. Zhao, M. Zhou, High-performance nanostructured thermoelectric materials, NPG Asia Mater. 2 (2010) 152–158.

[4] J. C. Peltier, Nouvelles experiences sur la caloricite des courants electriques, in: Ann. Chim. Phys. (1834) 371–386.

[5] E. Lenz, Einige Versuche im Gebiete des Galvanismus, Ann. Phys. 120 (1838) 342–349.

[6] W. Thomson, XV. On the Dynamical Theory of Heat, with numerical results deduced from Mr Joule's Equivalent of a Thermal Unit, and M. Regnault's Observations on Steam, Trans. R. Soc. Edinburgh. 20 (1853) 261–288.

[7] W. Thomson, 4. On a Mechanical Theory of Thermo-Electric Currents., Proc. R. Soc. Edinburgh. 3 (1857) 91–98.

[8] M. Hamid Elsheikh, D.A. Shnawah, M.F.M. Sabri, S.B.M. Said, M. Haji Hassan, M.B. Ali Bashir, M. Mohamad, A review on thermoelectric renewable energy: Principle parameters that affect their performance, Renew. Sustain. Energy Rev. 30 (2014) 337–355.

[9] T.M. Tritt, Thermoelectric phenomena, materials, and applications, Annu. Rev. Mater. Res. 41 (2011) 433–448.

[10] J. Yang, T. Caillat, Thermoelectric materials for space and automotive power generation, MRS Bull. 31 (2006) 224–229.

[11] A. Biswas, K.S. Kim, Y.H. Jeong, Metal–Insulator Transitions and Non-Fermi Liquid Behaviors in 5d Perovskite Iridates, in: Perovskite Mater. Synth. Characterisation, Prop. Appl., IntechOpen, (2016).

[12] Y. Wang, Y. Sui, P. Ren, L. Wang, X. Wang, W. Su, H. Fan, Strongly Correlated Properties and Enhanced Thermoelectric Response in $Ca_3Co_{4-x}M_xO_9$ (M = Fe, Mn, and Cu), Chem. Mater. 22 (2010) 1155–1163.

[13] B. Madavali, H.S. Kim, K.H. Lee, S.J. Hong, Enhanced Seebeck coefficient by energy filtering in Bi-Sb-Te based composites with dispersed Y_2O_3 nanoparticles, Intermetallics 82 (2017) 68-75.

[14] A.I. Abutaha, S.R. Sarath Kumar, A. Mehdizadeh Dehkordi, T.M. Tritt, H.N. Alshareef, Doping site dependent thermoelectric properties of epitaxial strontium titanate thin films, J. Mater. Chem. C. 2 (2014) 9712–9719.

[15] Z.Y. Liu, F.P. Zhang, J.X. Zhang, X. Zhang, Q.M. Lu, X.Y. Yang, Enhanced electrical transport by texture modulation and co-doping for $Ca_3Co_4O_{9+\delta}$ materials, Results Phys. 6 (2016) 203–208.

[16] R.R. Heikes, Thermoelectricity, Interscience Publ. (1961).

[17] C. Wood, Materials for thermoelectric energy conversion, Reports Prog. Phys. 51 (1988) 459–539.

[18] H. Taguchi, M. Sonoda, M. Nagao, Relationship between Angles for Mn–O–Mn and Electrical Properties of Orthorhombic Perovskite-Type $(Ca_{1-x}Sr_x)MnO_3$, J. Solid State Chem. 137 (1998) 82–86.

[19] R.A. Millikan, Elements of Electricity: A Practical Discussion of the Fundamental Laws and Phenomena of Electricity and Their Practical Applications in the Business and Industrial World, American Technical Society, 1917.

[20] P. Drude, Zur Elektronentheorie der Metalle; II. Teil. Galvanomagnetische und thermomagnetische Effecte, Ann. Phys. 308 (1900) 369–402.

[21] W. Khan, A.H. Naqvi, M. Gupta, S. Husain, R. Kumar, Small polaron hopping conduction mechanism in Fe doped $LaMnO_3$, J. Chem. Phys. 135 (2011) 54501.

[22] A. Banerjee, S. Pal, B.K. Chaudhuri, Nature of small-polaron hopping conduction and the effect of Cr doping on the transport properties of rare-earth manganite $La_{0.5}Pb_{0.5}Mn_{1-x}Cr_xO_3$, J. Chem. Phys. 115 (2001) 1550–1558.

[23] M. Viret, L. Ranno, J.M.D. Coey, Colossal magnetoresistance of the variable range hopping regime in the manganites, J. Appl. Phys. 81 (1997) 4964–4966.

[24] F. Bonetto, J.L. Lebowitz, L. Rey-Bellet, Fourier'S Law: a Challenge To Theorists, in: Math. Phys. 2000, Imperial College Press and World Scientific Publishing (2000) 128–150.

[25] R. Franz, G. Wiedemann, Ueber die Wärme-Leitungsfähigkeit der Metalle, Ann. Phys. 165 (1853) 497–531.

[26] S.J. Blundell, K.M. Blundell, Concepts in Thermal Physics, OUP Oxford (2010).

[27] E.S. Toberer, A. Zevalkink, G.J. Snyder, Phonon engineering through crystal chemistry, J. Mater. Chem. 21 (2011) 15843–15852.

[28] J.R. Sootsman, D.Y. Chung, M.G. Kanatzidis, New and old concepts in thermoelectric materials, Angew. Chemie - Int. Ed. 48 (2009) 8616–8639.

[29] G.K. Ren, J.L. Lan, K.J. Ventura, X. Tan, Y.H. Lin, C.W. Nan, Contribution of point defects and nano-grains to thermal transport behaviours of oxide-based thermoelectrics, Npj Comput. Mater. 2 (2016) 16023.

[30] Y. Zheng, M. Zou, W. Zhang, D. Yi, J. Lan, C.W. Nan, Y.H. Lin, Electrical and thermal transport behaviours of high-entropy perovskite thermoelectric oxides, J. Adv. Ceram. 10 (2021) 377–384.

[31] H. Zhou, D. Yi, Z. Yu, L. Xiao, Preparation and thermophysical properties of CeO_2 doped $La_2Zr_2O_7$ ceramic for thermal barrier coatings, J. Alloys Compd. 438 (2007) 217–221.

[32] J.L. Mi, T.J. Zhu, X.B. Zhao, J. Ma, Nanostructuring and thermoelectric properties of bulk skutterudite compound $CoSb_3$, J. Appl. Phys. 101 (2007) 54314.

[33] E. Altenkirch, Elektrochemische Kälteerzeugung und reversible elektrische Heizung, Phys. Zeitschrift. 12 (1911) 920–924.

[34] A.F. Ioffe, L.S. Stil'Bans, E.K. Iordanishvili, T.S. Stavitskaya, A. Gelbtuch, G. Vineyard, Semiconductor thermoelements and thermo-electric cooling, Sol. Energy. 4 (1960) 27.

[35] N.T. Hung, A.R.T. Nugraha, R. Saito, Size effect in thermoelectric power factor of nondegenerate and degenerate low-dimensional semiconductors, Mater. Today Proc. 4 (2017) 12368–12373.

[36] V. Vargiamidis, S. Foster, N. Neophytou, Thermoelectric Power Factor in Nanostructured Materials With Randomized Nanoinclusions, Phys. Status Solidi Appl. Mater. Sci. 215 (2018) 1700997.

[37] M.J. Moran, H.N. Shapiro, Fundamentals of Engineering Thermodynamics, Second

Edition, John Wiley & Sons (1993).

[38] G.J. Snyder, E.S. Toberer, Complex thermoelectric materials, Nat. Mater. 7 (2008) 105–114.

[39] L.D. Zhao, J. He, D. Berardan, Y. Lin, J.F. Li, C.W. Nan, N. Dragoe, BiCuSeO oxyselenides: new promising thermoelectric materials, Energy Environ. Sci. 7 (2014) 2900–2924.

[40] J. Li, J. Sui, Y. Pei, C. Barreteau, D. Berardan, N. Dragoe, W. Cai, J. He, L.D. Zhao, A high thermoelectric figure of merit ZT > 1 in Ba heavily doped BiCuSeO oxyselenides, Energy Environ. Sci. 5 (2012) 8543–8547.

[41] A.M. Dehkordi, S. Bhattacharya, T. Darroudi, H.N. Alshareef, T.M. Tritt, New insights on the synthesis and electronic transport in bulk polycrystalline Pr-doped $SrTiO_{3-\delta}$, J. Appl. Phys. 117 (2015) 55102.

[42] Y. Li, T. Zhang, Y. Qin, T. Day, G. Jeffrey Snyder, X. Shi, L. Chen, Thermoelectric transport properties of diamond-like $Cu_{1-x}Fe_{1+x}S_2$ tetrahedral compounds, J. Appl. Phys. 116 (2014) 203705.

[43] M.S. Dresselhaus, G. Chen, M.Y. Tang, R. Yang, H. Lee, D. Wang, Z. Ren, J.P. Fleurial, P. Gogna, New directions for low-dimensional thermoelectric materials, Adv. Mater. 19 (2007) 1043–1053.

[44] B. Poudel, Q. Hao, Y. Ma, Y. Lan, A. Minnich, B. Yu, X. Yan, D. Wang, A. Muto, D. Vashaee, X. Chen, J. Liu, M.S. Dresselhaus, G. Chen, Z. Ren, High-thermoelectric performance of nanostructured bismuth antimony telluride bulk alloys, Science. 320 (2008) 634–638.

[45] W. Xie, X. Tang, Y. Yan, Q. Zhang, T.M. Tritt, Unique nanostructures and enhanced thermoelectric performance of melt-spun BiSbTe alloys, Appl. Phys. Lett. 94 (2009) 102111.

[46] D.M. Rowe, V.S. Shukla, N. Savvides, Phonon scattering at grain boundaries in heavily doped fine-grained silicon–germanium alloys, Nature. 290 (1981) 765–766.

[47] A.I. Hochbaum, R. Chen, R.D. Delgado, W. Liang, E.C. Garnett, M. Najarian, A. Majumdar, P. Yang, Enhanced thermoelectric performance of rough silicon nanowires, Nature. 451 (2008) 163–167.

[48] O. Rabin, Y.M. Lin, M.S. Dresselhaus, Anomalously high thermoelectric figure of merit in $Bi_{1-x}Sb_x$ nanowires by carrier pocket alignment, Appl. Phys. Lett. 79 (2001) 81–83.

[49] W.K. Liebmann, E.A. Miller, Preparation, phase-boundary energies, and thermoelectric properties of InSb-Sb eutectic alloys with ordered microstructures, J. Appl. Phys. 34 (1963) 2653–2659.

[50] G. Slack, New Materials and Performance Limits for Thermoelectric Cooling, CRC Handb. Thermoelectr. (1995) 407–440.

[51] G. Mahan, B. Sales, Thermoelectric materials: New approaches to an old problem, Phys. Today. 50 (1997) 42–47.

[52] K. Koumoto, I. Terasaki, R. Funahashi, Complex oxide materials for potential thermoelectric applications, MRS Bull. 31 (2006) 206–210.

[53] S. Cai, S. He, Retrospection of development for radioisotope power systems in space and its prospect of application in new century, Chinese J. Nucl. Sci. Eng. 24 (2004) 97–104.

[54] R. Venkatasubramanian, E. Siivola, T. Colpitts, B. O'Quinn, Thin-film thermoelectric devices with high room-temperature figures of merit, Nature. 413 (2001) 597–602.

[55] J.K. Panya Yodovard Jongjit Hirunlabh, The potential of waste heat thermoelectric power generation from diesel cycle and gas turbine cogeneration plants, Energy Sources. 23 (2001) 213–224.

[56] H. Li, Z. Zhu, Y. Wu, X. Wu, H. Zhou, Y. Hua, M. Sun, T. Su, C. Ji, Progress of application and research of thermoelectric materials, Mater. Rev. 2012 (2012) 15.

[57] X.F. Zheng, C.X. Liu, Y.Y. Yan, Q. Wang, A review of thermoelectrics research - Recent developments and potentials for sustainable and renewable energy applications, Renew. Sustain. Energy Rev. 32 (2014) 486–503.

[58] D.R. Brown, T.B. Stout, J.A. Dirks, N. Fernandez, The prospects of alternatives to vapor compression technology for space cooling and food refrigeration applications, Energy Eng. 109 (2012) 7–20.

[59] S.B. Riffat, X. Ma, Thermoelectrics: a review of present and potential applications, Appl. Therm. Eng. 23 (2003) 913–935.

[60] D. Zou, S. Xie, Y. Liu, J. Lin, J. Li, Electronic structures and thermoelectric properties of layered BiCuOCh oxychalcogenides (Ch = S, Se and Te): first-principles calculations, J. Mater. Chem. A. 1 (2013) 8888–8896.

[61] L.N. Kholodkovskaya, L.G. Akselrud, A.M. Kusainova, V.A. Dolgikh, B.A. Popovkin, BiCuSeO: Synthesis and Crystal Structure, in: Mater. Sci. Forum, Trans Tech Publ. (1993) 693–696.

[62] L.D. Zhao, D. Berardan, Y.L. Pei, C. Byl, L. Pinsard-Gaudart, N. Dragoe, $Bi_{1-x}Sr_xCuSeO$ oxyselenides as promising thermoelectric materials, Appl. Phys. Lett. 97 (2010) 92118.

[63] J. Li, J. Sui, C. Barreteau, D. Berardan, N. Dragoe, W. Cai, Y. Pei, L.D. Zhao, Thermoelectric properties of Mg doped p-type BiCuSeO oxyselenides, J. Alloys Compd. 551 (2013) 649–653.

[64] Y.L. Pei, J. He, J.F. Li, F. Li, Q. Liu, W. Pan, C. Barreteau, D. Berardan, N. Dragoe, L.D. Zhao, High thermoelectric performance of oxyselenides: intrinsically low thermal conductivity of Ca-doped BiCuSeO, NPG Asia Mater. 5 (2013) e47–e47.

[65] Y. Liu, Y. Zheng, B. Zhan, K. Chen, S. Butt, B. Zhang, Y. Lin, Influence of Ag doping on thermoelectric properties of BiCuSeO, J. Eur. Ceram. Soc. 35 (2015) 845–849.

[66] G. Ren, S. Butt, C. Zeng, Y. Liu, B. Zhan, J. Lan, Y. Lin, C. Nan, Electrical and Thermal Transport Behavior in Zn-Doped BiCuSeO Oxyselenides, J. Electron. Mater. 44 (2015) 1627–1631.

[67] Y. Liu, L.D. Zhao, Y. Liu, J. Lan, W. Xu, F. Li, B.P. Zhang, D. Berardan, N. Dragoe, Y.H. Lin, C.W. Nan, J.F. Li, H. Zhu, Remarkable Enhancement in Thermoelectric Performance of BiCuSeO by Cu Deficiencies, J. Am. Chem. Soc. 133 (2011) 20112–20115.

[68] Y. Liu, J. Lan, W. Xu, Y. Liu, Y.L. Pei, B. Cheng, D.B. Liu, Y.H. Lin, L.D. Zhao, Enhanced thermoelectric performance of a BiCuSeO system via band gap tuning, Chem. Commun. 49 (2013) 8075–8077.

[69] C. Barreteau, D. Bérardan, E. Amzallag, L. Zhao, N. Dragoe, Structural and Electronic Transport Properties in Sr-Doped BiCuSeO, Chem. Mater. 24 (2012) 3168–3178.

[70] M. Roger, D.J.P. Morris, D.A. Tennant, M.J. Gutmann, J.P. Goff, J.-U. Hoffmann, R.

Feyerherm, E. Dudzik, D. Prabhakaran, A.T. Boothroyd, N. Shannon, B. Lake, P.P. Deen, Patterning of sodium ions and the control of electrons in sodium cobaltate, Nature. 445 (2007) 631–634.

[71] S. Pršić, S.M. Savić, Z. Branković, S. Vrtnik, A. Dapčević, G. Branković, Mechanochemically assisted solid-state and citric acid complex syntheses of Cu-doped sodium cobaltite ceramics, J. Alloys Compd. 640 (2015) 480–487.

[72] W. Zhang, K. Zhu, J. Liu, J. Wang, K. Yan, P. Liu, Y. Wang, Influence of the phase transformation in Na_xCoO_2 ceramics on thermoelectric properties, Ceram. Int. 44 (2018) 17251–17257.

[73] Y. Lei, X. Li, L. Liu, G. Ceder, Synthesis and Stoichiometry of Different Layered Sodium Cobalt Oxides, Chem. Mater. 26 (2014) 5288–5296.

[74] C.T. Lin, D.P. Chen, A. Maljuk, P. Lemmens, Sodium cobaltates: Crystal growth, structure, thermoelectricity, and superconductivity, J. Cryst. Growth. 292 (2006) 422–428.

[75] I. Terasaki, Y. Sasago, K. Uchinokura, Large thermoelectric power in $NaCo_2O_4$ single crystals, Phys. Rev. B. 56 (1997) R12685–R12687.

[76] P. Liu, G. Chen, Y. Cui, H. Zhang, F. Xiao, L. Wang, H. Nakano, High temperature electrical conductivity and thermoelectric power of Na_xCoO_2, Solid State Ionics. 179 (2008) 2308–2312.

[77] K. Fujita, T. Mochida, K. Nakamura, High-temperature thermoelectric properties of $Na_xCoO_{2-\delta}$ single crystals, Jpn. J. Appl. Phys. 40 (2001) 4644–4647.

[78] C.J. Liu, J.Y. Liao, T.W. Wu, B.Y. Jen, Preparation and transport properties of aqueous sol-gel synthesized $NaCo_2O_{4-\delta}$, J. Mater. Sci. 39 (2004) 4569–4573.

[79] M. Miclau, K. Bokinala, N. Miclau, Low-temperature hydrothermal synthesis of the three-layered sodium cobaltite P3-Na_xCoO_2 ($x\sim0.60$), Mater. Res. Bull. 54 (2014) 1–5.

[80] W. Zhang, P. Liu, Y. Wang, K. Zhu, G. Tai, J. Liu, J. Wang, K. Yan, J. Zhang, Textured Na_xCoO_2 ceramics sintered from hydrothermal platelet nanocrystals: growth mechanism and transport properties, J. Electron. Mater. 47 (2018) 4070–4077.

[81] J.Y. Tak, K.H. Lee, J.Y. Kim, C.H. Lim, W.S. Seo, Y.S. Lim, H.K. Cho, S.M. Choi,

Optimization of synthesis conditions of $Na_{0.75}CoO_2$ for high thermoelectric performance, J. Electron. Mater. 44 (2015) 1408–1412.

[82] D. Vengust, B. Jančar, T. Sever, A. Šestan, V. Bobnar, Z. Kutnjak, N. Daneu, D. Suvorov, M. Spreitzer, Improved environmental stability of thermoelectric ceramics based on intergrowths of $Ca_3Co_4O_9$–$Na_{0.75}CoO_2$, Ceram. Int. 47 (2021) 11687–11693.

[83] T. Nagira, M. Ito, S. Katsuyama, K. Majima, H. Nagai, Thermoelectric properties of $(Na_{1-y}M_y)_xCo_2O_4$ (M = K, Sr, Y, Nd, Sm and Yb; y = 0.01∼0.35), J. Alloys Compd. 348 (2003) 263–269.

[84] M. Ito, T. Nagira, Effect of the Polymerized Complex Process on Doping Limit of Thermoelectric $Na_xCo_{1-y}M_yO_2$ (M = Mn, Ni), Mater. Trans. 46 (2005) 1456–1461.

[85] M. Ohtaki, Oxide thermoelectric materials for heat-to-electricity direct energy conversion, Nov. Carbon Resour. Sci. Newsl. 3 (2010) 1–6.

[86] H. Leligny, D. Grebille, O. Pérez, A.C. Masset, M. Herveieu, C. Michel, B. Raveau, A bismuth cobaltite with an intrinsically modulated misfit layer structure: $Bi_{0.87}SrO_{22}$ $CoO_{21.8}$, Comptes Rendus l'Académie Des Sci. Ser. IIC Chem. 2 (1999) 409–414.

[87] R. Funahashi, M. Shikano, $Bi_2Sr_2Co_2O_y$ whiskers with high thermoelectric figure of merit, Appl. Phys. Lett. 81 (2002) 1459–1461.

[88] J.C. Diez, S.H. Rasekh, M.A. Madre, E. Guilmeau, S. Marinel, A. Sotelo, Improved thermoelectric properties of Bi-M-Co-O (M = Sr, Ca) misfit compounds by laser directional solidification, J. Electron. Mater. 39 (2010) 1601–1605.

[89] A. Sotelo, S. Rasekh, M.A. Madre, E. Guilmeau, S. Marinel, J.C. Diez, Solution-based synthesis routes to thermoelectric $Bi_2Ca_2Co_{1.7}O_x$, J. Eur. Ceram. Soc. 31 (2011) 1763–1769.

[90] A. Sotelo, E. Guilmeau, S. Rasekh, M.A. Madre, S. Marinel, J.C. Diez, Enhancement of the thermoelectric properties of directionally grown Bi–Ca–Co–O through Pb for Bi substitution, J. Eur. Ceram. Soc. 30 (2010) 1815–1820.

[91] H.C. Hsu, W.L. Lee, K.K. Wu, Y.K. Kuo, B.H. Chen, F.C. Chou, Enhanced thermoelectric figure-of-merit ZT for hole-doped $Bi_2Sr_2Co_2O_y$ through Pb substitution, J. Appl. Phys. 111 (2012) 103709.

[92] J.J. Shen, X.X. Liu, T.J. Zhu, X.B. Zhao, Improved thermoelectric properties of La-

doped $Bi_2Sr_2Co_2O_9$-layered misfit oxides, J. Mater. Sci. 44 (2009) 1889–1893.

[93] L.H. Yin, R. Ang, Z.H. Huang, Y. Liu, S.G. Tan, Y.N. Huang, B.C. Zhao, W.H. Song, Y.P. Sun, Exotic reinforcement of thermoelectric power driven by Ca doping in layered $Bi_2Sr_{2-x}Ca_xCo_2O_y$, Appl. Phys. Lett. 102 (2013) 141907.

[94] A. Sotelo, M.A. Torres, G. Constantinescu, S. Rasekh, J.C. Diez, M.A. Madre, Effect of Ag addition on the mechanical and thermoelectric performances of annealed $Bi_2Sr_2Co_{1.8}O_x$ textured ceramics, J. Eur. Ceram. Soc. 32 (2012) 3745–3751.

[95] S. Wang, Z. Bai, H. Wang, Q. Lü, J. Wang, G. Fu, High temperature thermoelectric properties of $Bi_2Sr_2Co_2O_y$/Ag composites, J. Alloys Compd. 554 (2013) 254–257.

[96] A.C. Masset, C. Michel, A. Maignan, M. Hervieu, O. Toulemonde, F. Studer, B. Raveau, J. Hejtmanek, Misfit-layered cobaltite with an anisotropic giant magnetoresistance: $Ca_3Co_4O_9$, Phys. Rev. B. 62 (2000) 166–175.

[97] Y. Miyazaki, M. Onoda, T. Oku, M. Kikuchi, Y. Ishii, Y. Ono, Y. Morii, T. Kajitani, Modulated Structure of the Thermoelectric Compound $[Ca_2CoO_3]_{0.62}CoO_2$, J. Phys. Soc. Japan. 71 (2002) 491–497.

[98] X. Hu, P.J. Phillips, D. Mazumdar, J.C. Idrobo, S. Kolesnik, A. Gupta, S. Ogut, R.F. Klie, Atomic and electronic structure of Ti substitution in $Ca_3Co_4O_9$, J. Appl. Phys. 120 (2016) 205105.

[99] A. Rébola, R.F. Klie, P. Zapol, S. Öğüt, Phonon and thermal transport properties of the misfit-layered oxide thermoelectric $Ca_3Co_4O_9$ from first principles, Appl. Phys. Lett. 104 (2014) 251910.

[100] W. Koshibae, K. Tsutsui, S. Maekawa, Thermopower in cobalt oxides, Phys. Rev. B. 62 (2000) 6869–6872.

[101] Y. Zhang, J. Zhang, Rapid reactive synthesis and sintering of textured $Ca_3Co_4O_9$ ceramics by spark plasma sintering, J. Mater. Process. Technol. 208 (2008) 70–74.

[102] D. Grebille, S. Lambert, F. Bouree, V. Petricek, Contribution of powder diffraction for structure refinements of aperiodic misfit cobalt oxides, J. Appl. Crystallogr. 37 (2004)

[103] W. Seo, S. Lee, Y. Lee, M. Lee, Y. Masuda, K. Koumoto, High-resolution transmission electron microscopy study of $Ca_3Co_4O_9$, Microscopy. 53 (2004) 397–

401.

[104] M. Shikano, R. Funahashi, Electrical and thermal properties of single-crystalline $(Ca_2CoO_3)_{0.7}CoO_2$ with a $Ca_3Co_4O_9$ structure, Appl. Phys. Lett. 82 (2003) 1851–1853.

[105] K. Obata, Y. Chonan, T. Komiyama, T. Aoyama, H. Yamaguchi, S. Sugiyama, Grain-oriented $Ca_3Co_4O_9$ thermoelectric oxide ceramics prepared by solid-state reaction, J. Electron. Mater. 42 (2013) 2221–2226.

[106] C.H. Lim, W.S. Seo, S. Lee, Y.S. Lim, J.Y. Kim, H.H. Park, S.M. Choi, K.H. Lee, K. Park, Anisotropy of the thermoelectric figure of merit (ZT) in textured $Ca_3Co_4O_9$ ceramics prepared by using a spark plasma sintering process, J. Korean Phys. Soc. 66 (2015) 794–799.

[107] H. Leligny, D. Grebille, O. Perez, A.C. Masset, M. Hervieu, C. Michel, B. Raveau, CR Sci. Paris IIc, Chim 2, 409 (1999), Acta Crystallogr., Sect. B Struct. Sci. 56 (2000) 173.

[108] M. Gunes, M. Ozenbas, Effect of grain size and porosity on phonon scattering enhancement of $Ca_3Co_4O_9$, J. Alloys Compd. 626 (2015) 360–367.

[109] S. Raghavan, M.J. Mayo, H. Wang, R.B. Dinwiddie, W.D. Porter, The effect of grain size, porosity and yttria content on the thermal conductivity of nanocrystalline zirconia, Scr. Mater. 39 (1998) 1119–1125.

[110] H. Lee, D. Vashaee, D.Z. Wang, M.S. Dresselhaus, Z.F. Ren, G. Chen, Effects of nanoscale porosity on thermoelectric properties of SiGe, J. Appl. Phys. 107 (2010) 94308.

[111] N. Wu, T.C. Holgate, N. Van Nong, N. Pryds, S. Linderoth, High temperature thermoelectric properties of $Ca_3Co_4O_{9+\delta}$ by auto-combustion synthesis and spark plasma sintering, J. Eur. Ceram. Soc. 34 (2014) 925–931.

[112] D. Srivastava, C. Norman, F. Azough, D. Ekren, K. Chen, M.J. Reece, I.A. Kinloch, R. Freer, Anisotropy and enhancement of thermoelectric performance of $Sr_{0.8}La_{0.067}Ti_{0.8}Nb_{0.2}O_{3-\delta}$ ceramics by graphene additions, J. Mater. Chem. A. 7 (2019) 24602–24613.

[113] A. Sotelo, G. Constantinescu, S. Rasekh, M.A. Torres, J.C. Diez, M.A. Madre, Improvement of thermoelectric properties of $Ca_3Co_4O_9$ using soft chemistry synthetic methods, J. Eur. Ceram. Soc. 32 (2012) 2415–2422.

[114] A. Sotelo, S. Rasekh, M.A. Torres, P. Bosque, M.A. Madre, J.C. Diez, Effect of synthesis methods on the $Ca_3Co_4O_9$ thermoelectric ceramic performances, J. Solid State Chem. 221 (2015) 247–254.

[115] D. Kenfaui, D. Chateigner, M. Gomina, J.G. Noudem, Texture, mechanical and thermoelectric properties of $Ca_3Co_4O_9$ ceramics, J. Alloys Compd. 490 (2010) 472–479.

[116] Y.F. Zhang, J.X. Zhang, Q.M. Lu, Q.Y. Zhang, Synthesis and characterization of $Ca_3Co_4O_9$ nanoparticles by citrate sol-gel method, Mater. Lett. 60 (2006) 2443–2446.

[117] D. Kenfaui, G. Bonnefont, D. Chateigner, G. Fantozzi, M. Gomina, J.G. Noudem, $Ca_3Co_4O_9$ ceramics consolidated by SPS process: Optimisation of mechanical and thermoelectric properties, Mater. Res. Bull. 45 (2010) 1240–1249.

[118] Y. Huang, B. Zhao, J. Fang, R. Ang, Y. Sun, Tunning of microstructure and thermoelectric properties of $Ca_3Co_4O_9$ ceramics by high-magnetic-field sintering, J. Appl. Phys. 110 (2011) 123713.

[119] H. Amaveda, O.J. Dura, M. Mora, M.A. Torres, G. Guelou, M.A. Madre, S. Marinel, A. Sotelo, Tuning $Ca_3Co_4O_9$ thermal and transport properties by TiC nanoparticles addition, Boletín La Soc. Española Cerámica y Vidr. (2020).

[120] X. Wang, X. Liu, W. Yan, S. Hou, X. Liu, Significant enhancement in Seebeck coefficient and power factor of $Ca_3Co_4O_9$ thermoelectric ceramics by SiC addition, J. Alloys Compd. 785 (2019) 698–705.

[121] C. Chen, T. Zhang, R. Donelson, D. Chu, R. Tian, T.T. Tan, S. Li, Thermopower and chemical stability of $Na_{0.77}CoO_2/Ca_3Co_4O_9$ composites, Acta Mater. 63 (2014) 99–106.

[122] S. Rasekh, N.M. Ferreira, F.M. Costa, G. Constantinescu, M.A. Madre, M.A. Torres, J.C. Diez, A. Sotelo, Development of a new thermoelectric $Bi_2Ca_2Co_{1.7}O_x+Ca_3Co_4O_9$ composite, Scr. Mater. 80 (2014) 1–4.

[123] Y. Wang, Y. Sui, J. Cheng, X. Wang, W. Su, Comparison of the high temperature thermoelectric properties for Ag-doped and Ag-added $Ca_3Co_4O_9$, J. Alloys Compd. 477 (2009) 817–821.

[124] M. Mikami, N. Ando, R. Funahashi, The effect of Ag addition on electrical properties of the thermoelectric compound $Ca_3Co_4O_9$, J. Solid State Chem. 178 (2005) 2186–

2190.

[125] F. Kahraman, M.A. Madre, S. Rasekh, C. Salvador, P. Bosque, M.A. Torres, J.C. Diez, A. Sotelo, Enhancement of mechanical and thermoelectric properties of $Ca_3Co_4O_9$ by Ag addition, J. Eur. Ceram. Soc. 35 (2015) 3835–3841.

[126] M.E. Song, H. Lee, M.G. Kang, W. Li, D. Maurya, B. Poudel, S. Priya, Anisotropic Thermoelectric Performance and Sustainable Thermal Stability in Textured $Ca_3Co_4O_9$/Ag Nanocomposites, ACS Appl. Energy Mater. 2 (2019) 4292–4301.

[127] F. Zhang, Q. Lu, T. Li, X. Zhang, J. Zhang, X. Song, Preparation and thermoelectric transport properties of Ba-, La- and Ag-doped $Ca_3Co_4O_9$ oxide materials, J. Rare Earths. 31 (2013) 778–783.

[128] G. Constantinescu, S. Rasekh, M.A. Torres, P. Bosque, J.C. Diez, M.A. Madre, A. Sotelo, Effect of Na doping on the $Ca_3Co_4O_9$ thermoelectric performance, Ceram. Int. 41 (2015) 10897–10903.

[129] P. Carvillo, Y. Chen, C. Boyle, P.N. Barnes, X. Song, Thermoelectric Performance Enhancement of Calcium Cobaltite through Barium Grain Boundary Segregation, Inorg. Chem. 54 (2015) 9027–9032.

[130] C. Boyle, P. Carvillo, Y. Chen, E.J. Barbero, D. Mcintyre, X. Song, Grain boundary segregation and thermoelectric performance enhancement of bismuth doped calcium cobaltite, J. Eur. Ceram. Soc. 36 (2016) 601–607.

[131] Y. Huang, B. Zhao, S. Lin, W. Song, Y. Sun, Renormalized bands and low-temperature colossal thermopower induced by Ir doping in $Ca_3Co_4O_9$ system, J. Appl. Phys. 114 (2013) 93709.

[132] T. Wu, T.A. Tyson, J. Bai, K. Pandya, C. Jaye, D. Fischer, On the origin of enhanced thermoelectricity in Fe doped $Ca_3Co_4O_9$, J. Mater. Chem. C. 1 (2013) 4114–4121.

[133] N. Van Nong, N. Pryds, S. Linderoth, M. Ohtaki, Enhancement of the thermoelectric performance of p-type layered oxide $Ca_3Co_4O_{9+\delta}$ through heavy doping and metallic nanoinclusions, Adv. Mater. 23 (2011) 2484–2490.

[134] M.E. Song, H. Lee, M.G. Kang, W. Li, D. Maurya, B. Poudel, J. Wang, M.A. Meeker, G.A. Khodaparast, S.T. Huxtable, S. Priya, Nanoscale texturing and interfaces in compositionally modified $Ca_3Co_4O_9$ with enhanced thermoelectric performance, ACS Omega. 3 (2018) 10798–10810.

3. Experimental Methods

3.1 Raw Materials

The powders used for fabricating calcium cobaltite ceramics and thick films were prepared from commercial oxides using the mixed oxide route. The details of chemicals for powder synthesis are all specified in Table 3.1.

Table 3.1 Details of chemicals used for powder synthesis

Compound Name	Chemical Formula	Molecular weight	Purity	Particle size	Supplier	CAS Number
Calcium carbonate	$CaCO_3$	100.09	99.8 %	-	Sigma Aldrich	471-34-1
Cobalt (II, III) oxides	Co_3O_4	165.86	99.7 %	2.0-6.0 μm	Alfa Aesar	1308-06-1
Bismuth (III) oxides	Bi_2O_3	465.96	99.8 %	10.0 μm	Sigma Aldrich	1304-76-3
Strontium carbonate	$SrCO_3$	147.63	99.9 %	-	Sigma Aldrich	1633-05-2
Barium carbonate	$BaCO_3$	197.34	99.8 %	1.0 μm	Alfa Aesar	513-77-9
Propan-2-ol	C_3H_8O	60.11	99.97 %	-	Fisher Scientific	67-63-0
YSZ balls	-	-	-	7.22 mm	PI-KEM	-

3.2 Powder Preparation

Stoichiometric mixtures of $CaCO_3$, Bi_2O_3, Co_3O_4, $SrCO_3$ and $BaCO_3$ were weighed according to nominal compositions: $Ca_{3-x}Bi_xCo_yO_{9+\delta}$ (x = 0.1-0.3; y = 3.92-4.0) and $Ca_{2.63}Bi_{0.3}M_{0.07}Co_{3.92}O_{9+\delta}$ (M = Sr and Ba), respectively. Batches of 100.0 g weighed powders for each composition were transferred into polyethylene bottles. Then zirconia balls and Propan-2-ol were added into the mixture; the mass ratio was fixed at 2:1:2. Subsequently, the sealed bottles were placed in a vibrating ball mill for 24 h to obtain uniform milky slurries. After drying at 363 K for 24 h, the mixed powders were transferred into an alumina crucible, and calcined at 1203 K for 12 h in air using a muffle furnace. The heating and cooling rates were both set as 453 K/h during the heat-treatment. Notably, the same calcination process was repeated for batches of $Ca_{2.7}Bi_{0.3}Co_{3.92}O_{9+\delta}$ powders; both the single fired and double-fired $Ca_{2.7}Bi_{0.3}Co_{3.92}O_{9+\delta}$ powders would be subject to cold sintering.

3.3 Ceramic and Film Preparation

The calcined powders were wet milled for a further 24 h and dried using the same procedures as described in Section 3.2. After that, the dried powders were reground and sieved using 60 mesh manually. The calcium cobaltite ceramics were prepared by the solid-state reaction route, spark plasma sintering (SPS) and cold sintering. The calcium cobaltite thick films were prepared by screen printing.

For solid state synthesis of calcium cobaltite bulks at the University of Manchester, batches of calcined $Ca_{2.7}Bi_{0.3}Co_yO_{9+\delta}$ (y = 3.92-4.0) powders for each composition were uniaxially pressed with a steel die in 20 mm diameter, using a More® hydraulic press under 40 MPa. The green bulks were eventually pressure-less sintered for 12 h in air at 1203 K using a muffle furnace.

For the calcium cobaltite bulks prepared by the SPS route, batches of calcined $Ca_{3-x}Bi_xCo_yO_{9+\delta}$ (x = 0.1-0.3; y = 3.92-4.0) and $Ca_{2.63}Bi_{0.3}M_{0.07}Co_{3.92}O_{9+\delta}$ (M = Sr and Ba) powders were transferred into a graphite die with a diameter of 20 mm and sintered at 1023 K for 5 min under a pressure of 50 MPa in a vacuum of ~5 Pascal, using an HPD 25/1, FCT systems (Germany) SPS furnace at Queen Mary, University of London, by Prof. Michael J. Reece. The following heat-treatment was conducted at the University of Manchester. The original SPS-processed $Ca_{3-x}Bi_xCo_yO_{9+\delta}$ (x = 0.1-0.3; y = 3.92-4.0) ceramics were annealed for 12 h in air at 1023 K or 1203 K, respectively. The original SPS-processed $Ca_{2.63}Bi_{0.3}M_{0.07}Co_{3.92}O_{9+\delta}$ (M = Sr and Ba) ceramics were annealed for 24 h in air at 1203 K.

For the calcium cobaltite bulks prepared by cold sintering at the University of Oulu by Dr Mikko Nelo, 3.6 g of single-fired and double-fired $Ca_{2.7}Bi_{0.3}Co_{3.92}O_{9+\delta}$ powders were firstly mixed individually with 1M acetic acid. For compaction, the mixtures were transferred into a 20 mm diameter steel die, where thin steel plates were used on pistons to protect the samples. Subsequently, the die was pressed under 390 MPa for 60 min at room temperature, after which the pressure was gradually lowered to 85 MPa. When the pressure was stable at 85 MPa, the press plates were heated to 673 K for 60 min, followed by cooling to 373 K before releasing the pressure. All samples were removed from the die at room temperature. The cold sintered ceramics prepared from both the single-fired and double fired powders were finally annealed at 1023 K for each of 12 and 24 h in air at the University of Manchester.

Calcium cobaltite thick films were prepared at the University of Surrey by Prof. Robert Dorey. Calcined $Ca_{2.7}Bi_{0.3}Co_{3.92}O_{9+\delta}$ powders (55.7 wt.%), terpinol (40.8 wt.%), PVB (1.6 wt.%) and ethylcellulose (2.0 wt.%) were mixed to prepare inks for screen printing.

Subsequently, five layers of paste were screen printed onto clean high-purity alumina substrates (5 mm × 25 mm × 2 mm) using a DEK 245 screen-printer with a mesh screen of 25 cm^2 and a squeegee speed of 4 cm/s. The as-deposited films were dried at 403 K for 1 h and then sintered at 1153 K and 1203 K for each of 4, 8 and 12 h in air at the University of Manchester.

Both the sintered thick films and ceramics were characterised at the University of Manchester. However, the sintered ceramics were first cut into pieces for characterisation, as shown in Fig. 3.1. Bars A, B and C were cut followed by grinding and polishing on the cross-sections for scanning electron microscopy (SEM), X-ray diffraction (XRD) and electrical transport properties measurement (ZEM). Bar B was recycled for X-ray photoelectron spectroscopy (XPS). Section D was used for transmission electron microscopy (TEM) by standard crushing method or focused ion beam (FIB). Sections E and F were ground into discs for specific heat capacity measurements (DSC) and thermal diffusivity measurements (LFA), respectively.

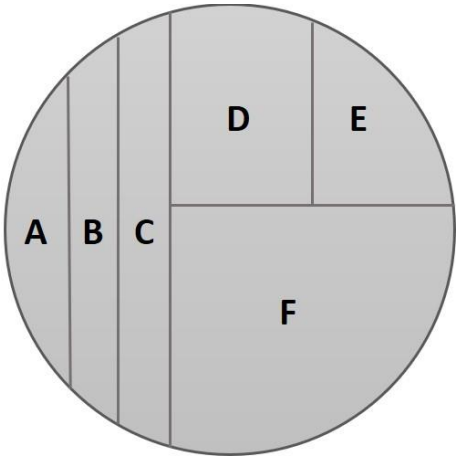

Fig. 3.1 Diagram showing how the pellets were used for property measurements (A. for SEM; B. for XRD and XPS; C. for ZEM; D: for TEM; E: for DSC; F: for LFA)

3.4 Density and Porosity Measurement

In this study, the density of sintered samples was determined by the Archimedes' method [1]. The samples were firstly weighed by an Ohaus® AS120® balance with a precision of ± 0.0001 g according to the operation manual, denoted as $\mathbf{m_{dry}}$. Then they were soaked in distilled water ($\boldsymbol{\rho_{liquid}}$ = 1.0 g/cm^3) to measure the suspended weight ($\mathbf{m}_{sus}$). After drying with a clean paper towel, the saturated samples were reweighed ($\mathbf{m}_{sat}$) in air. The bulk density ($\boldsymbol{\rho}$) was finally calculated from Equation (3.1):

$$\rho = \frac{m_{dry}\rho_{liquid}}{m_{sat}-m_{sus}} \quad (3.1)$$

The apparent porosity (**P**) of sintered samples was then calculated from Equation (3.2):

$$P = \frac{m_{sat}-m_{dry}}{m_{sat}-m_{sus}} \times 100\% \quad (3.2)$$

The theoretical density (ρ_{the}) was calculated by summing mass of all atoms per unit cell, shown in Equation (3.3):

$$\rho_{the} = \frac{ZM}{a^3 N_A} \quad (3.3)$$

where **Z** is the number of atoms in a unit cell, **M** is the molecular mass, a^3 is the volume of the unit cell and N_A is the Avogadro number (6.023×10^{23} molecules/mole).

The relative density (ρ_{rel}) was determined by the ratio of the bulk density and theoretical density (Equation (3.4)), through which the degree of densification of sintered samples can be estimated.

$$\rho_{rel} = \frac{\rho}{\rho_{the}} \times 100\% \quad (3.4)$$

3.5 X-ray Diffraction (XRD)

X-ray diffraction was utilised to characterise the phase composition and crystal structure of obtained samples. In general, X-rays are generated by ionising the Cu source or decelerating the incident electrons to produce Bremsstrahlung radiation. When the X-ray beam with a short wavelength is directed onto the sample surface, interactions between the beam and atomic layers will occur, thereby resulting in X-ray diffraction under specific conditions. According to Bragg's law, by adjusting the angle between the incident X-ray and atomic layer, high-intensity diffraction peaks will be revealed once the path difference between two waves is equal to $n\lambda$. The Bragg conditions can be well explained by Equation (3.5) and described by Fig. 3.2 .

$$n\lambda = 2d\sin\theta \quad (3.5)$$

where **n** is the integer, λ is the wavelength of the X-ray beam, **d** is the interplanar distance between two crystal planes and θ is the Bragg angle representing the scattering angle between the incident X-ray and the crystal plane.

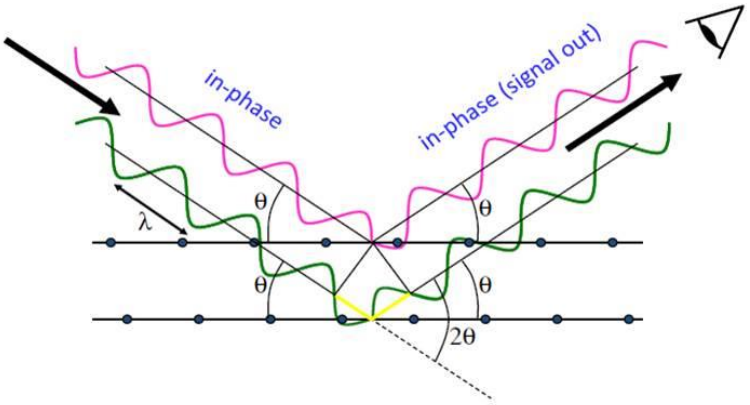

Fig. 3.2 Diagram illustrating Bragg's law, adapted from Cullity et al. [2]

The internal structure and operation mechanism for the Bragg spectrometer are displayed in Fig. 3.3. In fact, the X-ray beam is able to scatter in many directions due to randomly orientated grains in the polycrystalline samples. In order to collect all possible diffraction peaks, rotation of the sample can be controlled by tilting the incident beam angle. Finally, a Fourier transform is employed to convert the initial data into the form of one-dimensional diffraction patterns.

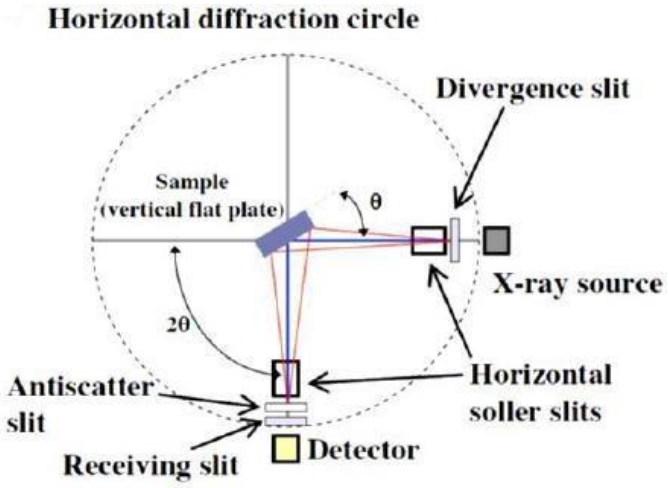

Fig. 3.3 Bragg-Brentano Geometry for XRD Setup, adapted from Bocher [3]

Before XRD testing, the surface of each sample was ground with a 1200 SiC paper in order to provide a smooth area for X-ray penetration without deflection. To be precise, the PANalytical X'Pert Pro® diffractometer was used for examination; relevant experimental parameters are presented in Table 3.2.

Table 3.2 The parameters for X-ray powder diffraction instrumental setup

Diffractometer	PANalytical X'Pert
Radiation Source, Wavelength	Copper k_α and k_β ($\lambda_{k\alpha}$= 1.5406 Å, $\lambda_{k\beta}$ =1.5444 Å)
Divergence slit	Fixed
Generator Voltage	40 kV
Tube Current	40 mA
Scan angle (2θ)	5-75°
Step size	0.033°
Step time	400 s

The grain orientation is characterised by Lotgering factors calculated from Equation (3.6) [4], using the collected XRD patterns [5]:

$$\mathbf{F = (p-p_0)/(1-p_0)} \qquad \mathbf{(3.6)}$$

where p = ΣI (00l) / ΣI (hkl) (Σ I is the total counts of peaks for synthesized samples) and p_0 = ΣI_0 (00l) / ΣI_0 (hkl) (ΣI_0 is the total counts of peaks for randomly oriented samples calculated from the standard PDF card of calcium cobaltite (JCPDS: # 05-001-0461). As a larger Lotgering factor reflects an enhanced preferred grain orientation, the changes in the value can be used for describing the texture development.

3.6 XRD Refinement

The collected XRD patterns were indexed using PDF cards stored in X'Pert Highscore Plus Software. The crystal structure was refined by Jana2006 software using a least squares method to obtain the lattice parameters.

Jana2006 software functions on the basis of the Le Bail method by profile intensity partitioning [6], where the peak intensities are set to an arbitrary value **y(cal)** (treated as "calculated" values) and the partitioning observed profile points **y(obs)** result in a series of "observed" intensity values. As Fig. 3.4 shows, the red line with white dots represents the observed profile and the black line with red dots represents the calculated values. Taking the black filled dots as an example, the observed peak intensity for peak 1 (**I_{obs}(1)**) is calculated from Equation (3.7):

$$\mathbf{I_{obs}(1)} = \sum_{i=1}^{n} \boldsymbol{y_i(obs)}[\boldsymbol{y_i(1)/y_i(cal)}] \qquad \mathbf{(3.7)}$$

Similarly, the observed peak intensity for peak 2 ($\mathbf{I_{obs}(2)}$) can be calculated from Equation (3.8):

$$\mathbf{I_{obs}(2)} = \sum_{i=1}^{n} \boldsymbol{y_i(obs)}[\boldsymbol{y_i(2)/y_i(cal)}] \qquad \mathbf{(3.8)}$$

where $\mathbf{y_i(cal)=y_i(1)+y_i(2)}$; this summation is taken over all profile points **i** contributing to the peak intensity and is not limited to just two peaks as illustrated in Fig. 3.4. Although the observed intensity values are biased by the starting calculated values, they are on average closer to the true value for peak intensities than any arbitrary values and thus are thereafter utilised instead of a structural model for the least-squares fitting.

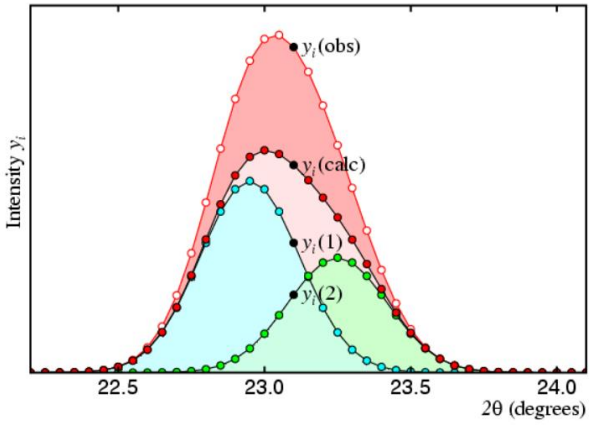

Fig. 3.4 Schematic diagram for the profile intensity partitioning, taken from Le Bail et al. [7]

Generally, Le Bail refinement aims to minimise the parameter **R**, which is the sum of weighted squared differences of intensities between observed data and calculated data, given by Equation (3.9):

$$\mathbf{R} = \sum_{i=1}^{n} \boldsymbol{w_i}[\boldsymbol{y_i(obs)} - \boldsymbol{y_i(cal)}]^2 \qquad \mathbf{(3.9)}$$

where **n** is the total number of the data point, $\mathbf{w_i}$ is the weighting of the data points, $\mathbf{y_i(obs)}$ and $\mathbf{y_i(cal)}$ (**i** = 1, 2, 3 ……) are the intensity of specific data point for the observed data and calculated data, respectively.

The quality of the refinement is generally judged by three important parameters: the expected **R** ($\mathbf{R_{exp}}$), the weighted profile **R** ($\mathbf{R_{wp}}$) and the goodness of fit (**GoF**).

The quality of the experimental data can be assessed by the expected **R** using Equation (3.10):

$$\mathbf{R_{exp}} = \left[\frac{n-p}{\sum_{i=1}^{n} w_i(y_i(obs))^2}\right]^{1/2} \qquad \mathbf{(3.10)}$$

where **p** is the total number of refined parameters and $\mathbf{R_{exp}}$ is a statistical evaluation of the noise of the data. A smaller $\mathbf{R_{exp}}$ indicates a better quality.

The weighted profile **R** is defined as the square root of ratio between **R** and the sum of weighted observed intensities, as described by Equation (3.11):

$$\mathbf{R_{wp}} = \left[\frac{R}{\sum_{i=1}^{n} w_i(y_i(obs))^2}\right]^{1/2} \quad \textbf{(3.11)}$$

The goodness of fit is a factor in combination of both $\mathbf{R_{exp}}$ and $\mathbf{R_{wp}}$, shown in Equation (3.12):

$$\mathbf{GoF^2} = [\mathbf{R_{wp}}/\mathbf{R_{exp}}]^2 \quad \textbf{(3.12)}$$

Basically, smaller $\mathbf{R_{wp}}$ and **GoF** values mean a higher quality of the refinement.

3.7 Scanning Electron Microscopy (SEM)

The thermoelectric performance of a material can be influenced by the formation of secondary phases, interfaces, grain size and porosity. Therefore, scanning electron microscopy (SEM) was employed to investigate the microstructure of synthesized samples and energy dispersive X-ray spectroscopy (EDX) was used to determine the chemical compositions of detected phases.

Basically, SEM works on the basis of rastering a focused electron beam, generated by the thermionic emission, which is able to interact with the surface of the sample, thereby producing a range of signals such as secondary electrons (SE), backscattered electrons (BSE) characteristic X-rays, cathodoluminescence and Auger electrons, shown in Fig. 3.5. By collecting these signals via different detectors, the images of selected areas can be generated.

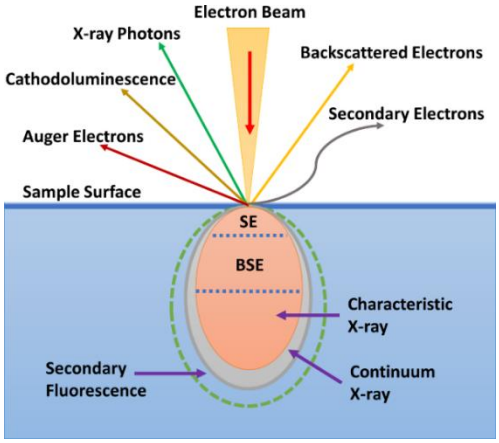

Fig. 3.5 Schematic diagram of interaction effects of the incident beam with the sample, adapted from Zhou et al. [8]

Secondary electrons resulting from the inelastic interaction between the incident electron beam and the outer shell electrons of the atoms at a small angle are usually of low energy (~ 2-5 eV). These electrons are released from the sample surface, giving detailed information about the topographical contrast.

By marked contrast, the elastic scattering events are responsible for the generation of backscattered electrons, where the electron beam is scattered by the atomic nucleus of the elements at a relatively high angle (> 90°) with the energy higher than 50 eV. The BSE images can provide additional information regarding the phase composition because contrast difference can be seen if the electron beam collides with nucleus with different atomic numbers. There are several factors affecting the yield of backscattered electrons, including the surface topography, atomic number and the sensitivity to the beam. It is generally believed that a parabolic growth in the BSE yield will be revealed with an increase in the atomic number.

Energy dispersive X-ray spectroscopy works by directing a strongly focused electron beam onto the sample surface, where the electrons in the ground state are ejected from the initial shell, thereby providing holes for electrons from an outer shell and generating the characteristic X-rays owing to the release of differential energy between the initial shell and the present shell. Different elements have their unique characteristic X-rays, so the chemical composition of detected phases can be determined accordingly.

As Fig. 3.6 shows, in a SEM instrument, the tungsten filament, LaB_6 crystals or FEG sources are usually selected to be electrically heated in a high vacuum, in order to generate a high energy electron beam before the thermal or field emission. After passing through the condenser and objective lenses, a focused and convergent beam is produced and is then used for scanning sample surfaces with the help of the scanning coils. The signals generated during the interaction between the beam and material are collected by different detectors and the output of relative information presents as images after computer processing. As for the field emission gun, the differences in working voltage (thousands of volts) originate from the single crystal filament. The beam usually has a smaller spot size and lower energy distribution, which contributes to higher resolution.

The surfaces of obtained samples were characterised by SEM in this study. Each surface was firstly ground with 1200 SiC paper and then washed by the ethanol. After drying, the sample was attached to a round sample holder with a conductive tape. In this investigation, TESCAN MIRA3 SC and FEI Sirion FEG-SEM were employed to examine the samples, both of which

are fitted with SEM and BSE detectors. In addition, an EDX detector is installed in the TESCAN MIRA3 SC to further analyse the chemical composition.

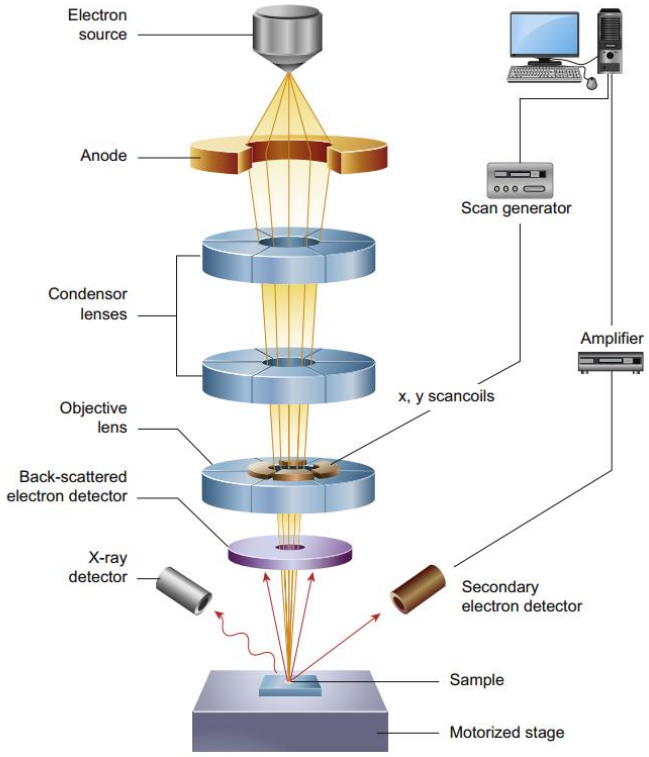

Fig. 3.6 Diagram of a typical SEM with different detectors along with the signal outputs, taken from Inkson et al. [9]

Based on collected backscattered electron SEM images, the volume fraction of each secondary phase was estimated by Image J software according to the different phase contrast for each composition [10]. The average grain size of polycrystalline samples was evaluated by the linear intercept method [11]. A few test lines with a fixed length were used to intercept several grains in the SEM images. Considering the magnification and correction factor, the average grain size was calculated by counting the number of intercepted grain boundaries according to Equation (3.13) [12]:

$$\mathbf{D_{ave} = 1.273L/N} \qquad \mathbf{(3.13)}$$

where $\mathbf{D_{ave}}$ is the average grain size, the correction factor is 1.273 for oriented grains with irregular shapes on the transverse planar section [13], **L** is the length of test lines and **N** is the total number of intercepts.

3.8 Transmission Electron Microscopy (TEM)

Transmission electron microscopy (TEM) can help collect valuable information of the as-prepared samples, including the particle morphology, crystal structure, defect distribution (stacking faults, point defects, etc.) and chemical composition, through which the relationship between thermoelectric properties and microstructure can be well understood.

In a TEM instrument, a thin sample will be illuminated with a uniform electron beam excited by a high voltage in a high vacuum. Electrons can be stopped and deflected by some parts of the sample, thereby forming different brightness contrast in the phosphorescent screen or viewed by the CCD (Charged Coupled Device) camera.

The internal structure of a TEM instrument mainly consists of three systems, shown in Fig. 3.7. The top part is the illumination system composed of the electronic gun and gun deflectors, responsible for generating an electron beam along the optical axis. The condenser lens and objective lens system in the middle are used to control the beam path and beam parameters. The last part (projection system) including the intermediate and projector lens as well as the imaging devices enables the conversion between image view and diffraction view. In general, the electron beam is emitted from the electronic gun along the optical axis in the chamber by controlling the lens and coils. Different scattering events are produced by the interaction between the electrons and samples once the beam is directed onto the sample surface, thereby forming an image at the image plane which can be detected using the phosphorescent screen or CCD camera (Fig. 3.7(b)). The electron diffraction patterns can also be collected by projecting the back focal plane into the image detector (Fig. 3.7(a)). The High-Resolution Transmission Electron microscopy mode (HRTEM) has a resolution of 0.1 nm and is able to provide useful information regarding atomic positions in the crystal lattice. Different defects including dislocations and stacking faults can be distinguished in the generated phase contrast image resulting from the interference between the diffracted and transmitted electrons. By orienting the sample along a specific zone axis, the atomic columns of the observed sample can be presented.

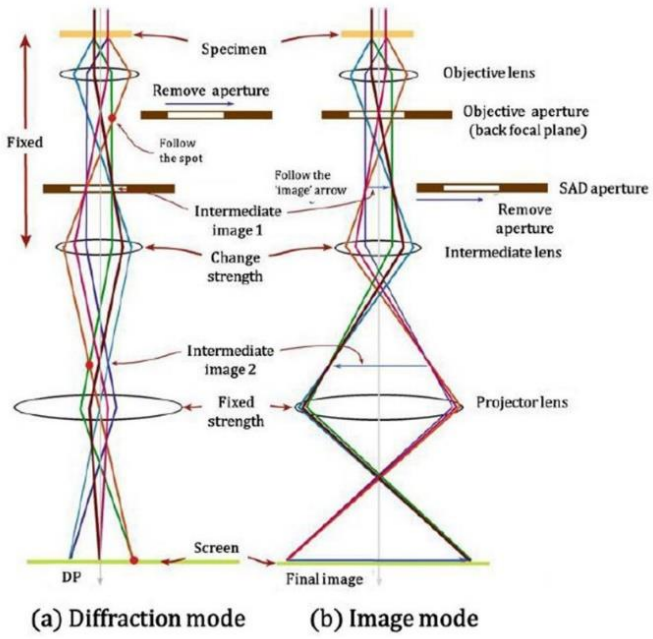

Fig. 3.7 Diagram of the internal structure of a transmission electron microscopy, taken from Carter and Williams [14]

There are many methods for TEM sample preparation. In this study, the TEM samples were prepared by a standard crushing method and use of a focused ion beam (FIB). Actually, a thin sample can be easily formed by crushing the material into fine particles, but the sample thickness is usually non-uniform and strain may be introduced to change the interface behaviour. FIB sample preparation with a uniform thickness is good for observing the interfaces between different phases. However, part of the sample may be contaminated by platinum if the thinning process is inadequate.

For the standard crushing method, the polycrystalline sample was crushed in an agate mortar manually and then the resulting particles were dispersed into an organic solvent such as alcohol, acetone or chloroform. The obtained suspension was finally dropped onto a copper TEM grid covered with holey carbon film and dried in a fume cupboard.

For the focused ion beam method, a layer of platinum with the thickness of around 1.0 μm was coated onto the surface of the ceramic sample. An ion beam was then employed to dig two trenches above and below the platinum in the area of interest. A J-shaped trench was cut when the thickness of sample reached about 1.0 μm. A micromanipulator was subsequently operated to attach the sample onto the FIB grid through platinum deposition. Finally, the sample was properly positioned and subject to a thinning process to remove unnecessary materials using a smaller beam current.

3.9 X-Ray Photoelectron Spectroscopy (XPS)

X-Ray Photoelectron Spectroscopy (XPS) is widely used to determine the surface chemical composition and ionic states of materials. The operating principle of XPS is shown in Fig. 3.8. High-energy X-rays (**hν**) reach the sample surface and then interact with electrons in inner layers which will be ejected from the shell as photoelectrons when adequate energy is provided. The kinetic energy ($\mathbf{E_k}$) of the released electron can be calculated from the absorbed energy and the atomic core level binding energy ($\mathbf{E_b}$) relative to the fermi level ($\mathbf{E_f}$) according to Equation (3.14):

$$\mathbf{E_k = h\nu - E_b - \phi_{sp}} \qquad \mathbf{(3.14)}$$

where ϕ_{sp} is work function of the spectrometer (about 4-5 eV) [15].

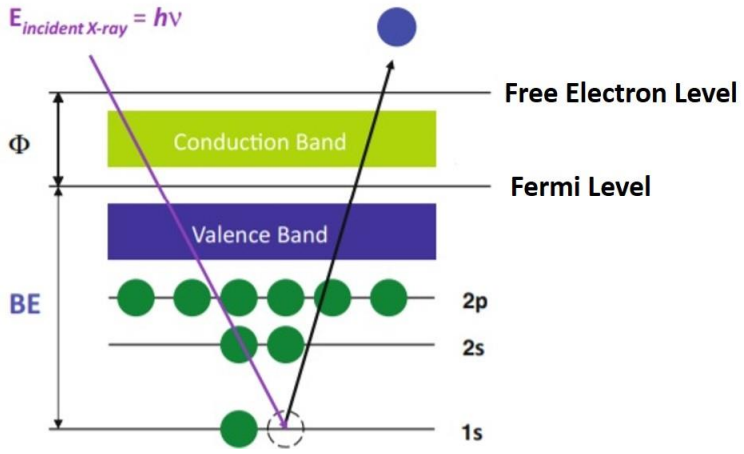

Fig. 3.8 Photoelectron emission process, taken from Sardela [16]

The depth for XPS analysis is limited to ~10.0 nm in the normal instrument, beyond which the scattering effect among the excited electrons becomes more pronounced and the energy loss cannot be avoided. At first, a quick survey scan is usually performed to identify the element constituents of synthesized materials. Subsequently, a high-resolution scan with a longer dwell time is conducted to characterise the ionic states.

In this study, the sample for X-ray diffraction test was also used for XPS analysis. The XPS data were collected by a monochromatic Al Kα source (E = 1486.69 eV) using a Kratos Axis Ultra spectrometer. The photoelectron analysis was conducted by a 180° hemispherical analyser with a mean radius of 165 mm. C 1s peak (285 eV) was used to calibrate the binding energy. CASA XPS software was employed to fit the XPS data by constraining peak

dimensions, peak location and FWHM via a mix of Lorentzian and Gaussian characters, based on the background subtracted from the Linear approximation.

3.10 Electrical Transport Properties Measurement

Electrical transport properties (electrical conductivity and Seebeck coefficients) measurements were carried out using an Ulvac ZEM-III. The setup of the ZEM-III is presented in Fig. 3.9; the sample is tightly fixed between the upper and lower current electrodes in the heating furnace and two probes equipped with a thermocouple are directed onto the sample surface. In this system, the power supply provides a constant current for the closed circuit, offering a low current to weaken the Joule heating effect through reversing the polarity every 300 ms. The temperature difference setting heater is responsible for generating a small thermal gradient. The thermal electromotive force and the temperature difference can be measured instantly by the built-in nano-voltmeter and thermocouples, respectively. The heating furnace enables a changeable temperature environment for the sample. In addition, a Ni cap is used to cover both the sample and electrodes, which is beneficial to balancing the temperature distribution.

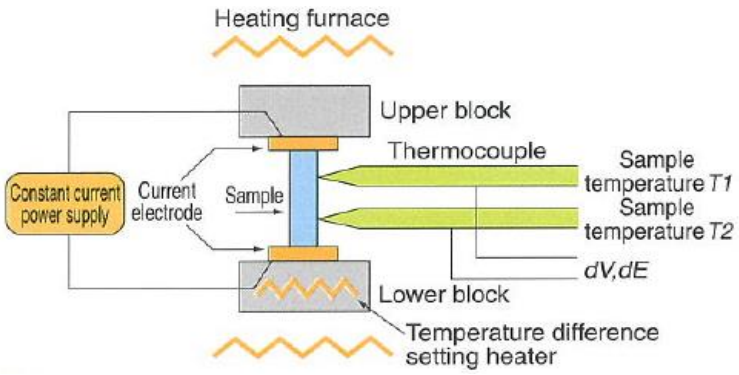

Fig. 3.9 Setup for the Ulvac ZEM-III instrument, taken from the operation manual [17]

3.10.1 Electrical Conductivity Measurement

The temperature dependence of electrical conductivity is measured by the four probe mode and the simplified schematic of working principle is displayed in Fig. 3.10, where two platinum electrodes attached to the upper and lower blocks in Fig. 3.9 can be regarded as the two outermost probes and the probes touching the sample surface are exactly the two inner probes. Therefore, the electrical resistivity (**ρ**) at different temperatures can be calculated from Equation (3.15):

$$\rho = \frac{SR}{L} = \frac{VS}{IL} \tag{3.15}$$

where **S** is the cross-sectional dimension of the sample, **R** is the electrical resistance, **L** is the length between the two inner probes, **V** is the potential difference between the two outermost probes, and **I** is the provided current intensity.

As the electrical conductivity (**σ**) is the reciprocal of the electrical resistivity (**ρ**), it can be described as Equation (3.16):

$$\sigma = \frac{1}{\rho} = \frac{IL}{VS} \tag{3.16}$$

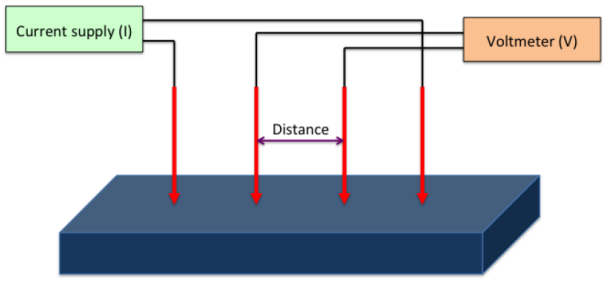

Fig. 3.10 Schematic representation of the four probe mode, taken from Hasegawa et al. [18]

3.10.2 Seebeck Coefficient Measurement

The Seebeck coefficient is defined as the ratio between the voltage difference (Δ**V**) and the temperature difference (Δ**T**), the unit of which is usually converted into μV/K. The Ulvac ZEM-III can also be used to measure the Seebeck coefficient in a Helium atmosphere under a pressure of 0.1 bar using the differential method.

At first, the system is required to be in a steady state, where the current density should be regarded as zero. After a stable temperature environment is created with a constant electrical current, the baseline can be plotted using the ZEM software. In the progress of measurement, the voltage gradient (Δ**V**) test for Seebeck coefficient is simultaneously conducted via the same probes mentioned in Fig. 3.10. In order to improve the accuracy, the voltage drop is calculated on the basis of small ΔV with different values (more than two). A small thermal gradient (Δ**T**) is measured between the inner probes when the temperature becomes stable at each heating stage. Therefore, the Seebeck coefficient can be eventually obtained through dividing Δ**V** by Δ**T**.

Samples used for electrical transport properties measurement were cut from sintered ceramics as bars with dimensions of 3 mm × 3 mm × 8 mm and then ground with 1200 SiC paper to obtain flat surfaces. After ensuring that the sample was conductive at room temperature, using an Avometer, it was tested in the Ulvac ZEM-III machine within the temperature range of 298-823 K in steps of 50 K, the uncertainty of which is around ± 3 %. Three temperature differences of 2, 3 and 4 K were applied to measure the Seebeck coefficient at the same time. The uncertainty is suggested to be ± 5 % by the operation manual, assuming all contacts are in good condition.

3.11 Thermal Conductivity Measurement

Thermal conductivity is a measure of the ability of a material to transfer the heat in a thermal gradient, which can be described by Equation (3.17):

$$\boldsymbol{\kappa = \alpha \rho C_p} \qquad \textbf{(3.17)}$$

where **κ** is the thermal conductivity, **α** is the thermal diffusivity, **ρ** is the sample density and $\mathbf{C_p}$ is the specific heat capacity.

3.11.1 Specific Heat Capacity Measurement

The specific heat capacity is defined as the ratio between the energy needed for increasing the temperature of a material and the heat given when the pressure condition is constant, shown as Equation (3.18):

$$\mathbf{C_p = \left(\frac{dH}{dT}\right)_p} \qquad \textbf{(3.18)}$$

where **dH** is the amount of energy required to increase the temperature by **dT**.

Commonly, the specific heat capacity is measured by a differential scanning calorimeter (DSC) through comparing the DSC curve of candidate sample with that of a reference standard with a known $\mathbf{C_p}$. According to the calculation method described in Fig. 3.11, the ratio between the $\mathbf{C_{p(sample)}}$ and $\mathbf{C_{p(reference)}}$ is proportional to the ratio between the $\mathbf{m_{(reference)}}$ (mass of the reference sample) and $\mathbf{m_{(sample)}}$ (mass of the synthesized sample), where the proportionality coefficient is **y/y'**, if the temperature rises linearly. The baseline mentioned in Fig. 3.11 is established by monitoring the DSC curve of an empty sample holder. In order

to reduce the uncertainty of the result, several measurements are performed, and the obtained values are averaged.

A Netzsch STA 449 C differential scanning calorimeter was utilised to determine the specific heat capacity in this work. The sample for the test was shaped into a disc of 4 mm in diameter and 1 mm in thickness. An empty Pt holder was used for obtaining the baseline and a sapphire disc is selected as the standard reference. In order to monitor the DSC curves of the crucible, sapphire disc and the candidate materials, the machine runs with the heating rate of 20 K/min within the temperature ranges of 298-873 K in an Ar atmosphere. The uncertainty of the specific heat capacity measurements is about 3 % according to the operation manual.

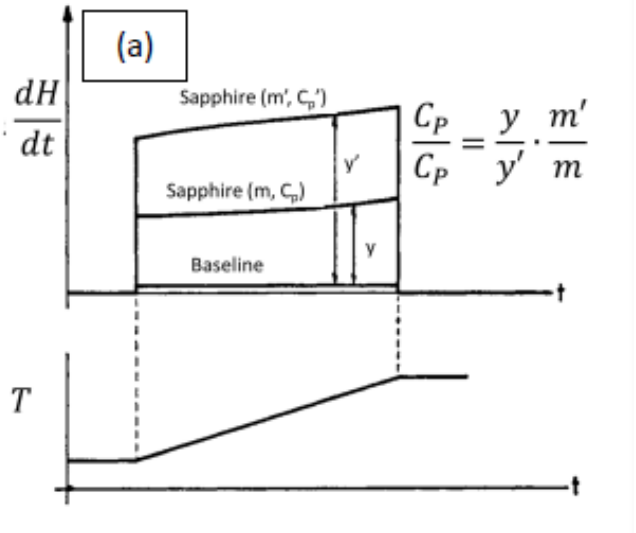

Fig. 3.11 The specific heat capacity ($\mathbf{C_p}$) calculation using the ratio method, taken from O'Neill [19]

3.11.2 Thermal Diffusivity Measurement

The lasher flash technique is extensively used for thermal diffusivity measurement; the concept was firstly proposed by Parker et al. [20]. During the test, a short pulse of laser light is directed onto the front side of an "adiabatically insulated infinite plate", after which the temperature of the rear side is measured, shown in Fig. 3.12. The thermal diffusivity therefore can be calculated from Equation (3.19):

$$\boldsymbol{\alpha = \frac{1.38L^2}{\pi^2 t_{0.5}}} \qquad \textbf{(3.19)}$$

where $\boldsymbol{\alpha}$ is the thermal diffusivity, $\mathbf{L}$ is the thickness of the sample and $\mathbf{t_{0.5}}$ is the time required for the temperature of the rear side reaching half of the maximum temperature rise. In fact,

Parker's principle is established assuming that there is no heat loss. However, the thermal contact and finite pulse time effects give rise to certain heat loss in the system. Therefore, the convergence method and instrument setup were later corrected and calibrated by Cowan [21] and Taylor [22].

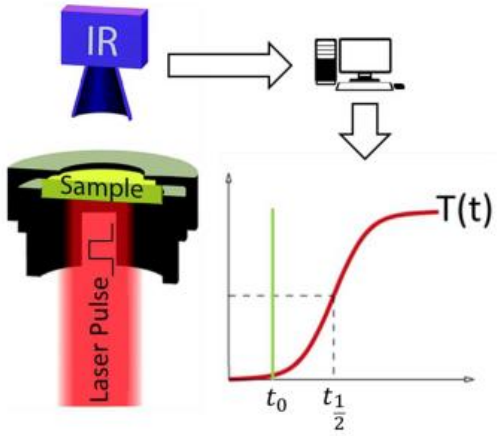

Fig. 3.12 Schematic diagram of laser flash technique, taken from Borup et al. [23]

The thermal diffusivity measurements in this study employed a Netzsch LFA 427 Laser Flash Analyser equipped with a high-energy Nd: YAG solid state laser source (1064 nm in the wavelength and 0.6 s in the pulse width). Prior to the measurement, the sample surface was polished to be flat with a diameter of 6 or 10 mm and a thickness of about 1 mm. Then the sample was placed into a graphite holder, the surface of which was exposed to the high-energy laser during the measurement. Ar atmosphere was used to protect the holder from oxidation. An InSb IR detector with Ge lens was utilised to determine the temperature rise. The temperature of the sample was determined by a thermocouple installed parallel to the holder. A computer with dedicated software was employed to track progress and collect the data. The uncertainty of the thermal diffusivity measurement is taken to be 10-15 % (from instrument operation manual).

References

[1] ASTM International, Standard Test Methods for Density of Compacted or Sintered Powder Metallurgy (PM) Products Using Archimedes' Principle, ASTM Int. (2013).

[2] B.D. Cullity, S.R. Stock, S. Stock, Elements of X-ray Diffraction, 3rd editionPrentice Hall, New York (2001).

[3] L. Bocher, Synthesis, structure, microstructure and thermoelectric properties of perovskite-type manganate phases, Ph. D. Thesis, University of Augsberg (Augsburg), 2009.

[4] J.L. Jones, E.B. Slamovich, K.J. Bowman, Critical evaluation of the Lotgering degree of orientation texture indicator, J. Mater. Res. 19 (2004) 3414–3422.

[5] R. Shimonishi, M. Hagiwara, S. Fujihara, Fabrication of highly textured $Ca_3Co_4O_9$ ceramics with controlled density and high thermoelectric power factors, J. Eur. Ceram. Soc. 40 (2020) 1338–1343.

[6] A. Le Bail, Whole powder pattern decomposition methods and applications: A retrospection, Powder Diffr. 20 (2005) 316–326.

[7] A. Le Bail, Lachlan MD Cranswick, and Ian Madsen. Powder diffraction: theory and practice. Royal Society of Chemistry, (2008).

[8] W. Zhou, R. Apkarian, Z.L. Wang, D. Joy, Fundamentals of scanning electron microscopy (SEM), Scanning Microsc. Nanotechnol. Tech. Appl. (2007) 1–40.

[9] B.J. Inkson, Scanning Electron Microscopy (SEM) and Transmission Electron Microscopy (TEM) for Materials Characterization, in 'Materials Chatateriza tion Using Non-destructive Evaluation (NDE) Methods', Eds G.Hübschen, I. Altpeter, R. Tschuncky, H. G. Herrmann, Woodhead Publishing, (2016) 17-43.

[10] A. Sotelo, S. Rasekh, E. Guilmeau, M.A. Madre, M.A. Torres, S. Marinel, J.C. Diez, Improved thermoelectric properties in directionally grown $Bi_2Sr_2Co_{1.8}O_y$ ceramics by Pb for Bi substitution, Mater. Res. Bull. 46 (2011) 2537–2542.

[11] ASTM, ASTM E112-13: Standard test methods for determining average grain size, ASTM Int. (2013).

[12] M.I. Mendelson, Average Grain Size in Polycrystalline Ceramics, J. Am. Ceram. Soc. 52 (1969) 443–446.

[13] R.E. Fryxell, B.A. Chandler, Creep, Strength, Expansion, and Elastic Moduli of Sintered BeO As a Function of Grain Size, Porosity, and Grain Orientation, J. Am. Ceram. Soc. 47 (1964) 283-291.

[14] C.B. Carter, D.B. Williams, Transmission electron microscopy: Diffraction, imaging, and spectrometry, Springer, (2016).

[15] S. Hofmann, Auger-and X-Ray Photoelectron Spectroscopy in Materials Science, Springer Science & Business Media, (2012).

[16] M. Sardela, Practical materials characterization, Pract. Mater. Charact. (2014) 1–237.

[17] Thermal Property Measuring Systems. ULVAC, p. 800.

[18] S. Hasegawa, I. Shiraki, F. Tanabe, R. Hobara, Transport at surface nanostructures measured by four-tip STM, Curr. Appl. Phys. 2 (2002) 465–471.

[19] M.J. O'Neill, Measurement of Specific Heat Functions by Differential Scanning Calorimetry, Anal. Chem. 38 (1966) 1331–1336.

[20] W.J. Parker, R.J. Jenkins, C.P. Butler, G.L. Abbott, Flash method of determining thermal diffusivity, heat capacity, and thermal conductivity, J. Appl. Phys. 32 (1961) 1679–1684.

[21] R.D. Cowan, Pulse method of measuring thermal diffusivity at high temperatures, J. Appl. Phys. 34 (1963) 926–927.

[22] R. Taylor, Construction of apparatus for heat pulse thermal diffusivity measurements from 300-3000K, J. Phys. E. 13 (1980) 1193–1199.

[23] K.A. Borup, J. De Boor, H. Wang, F. Drymiotis, F. Gascoin, X. Shi, L. Chen, M.I. Fedorov, E. Müller, B.B. Iversen, G.J. Snyder, Measuring thermoelectric transport properties of materials, Energy Environ. Sci. 8 (2015) 423–435.

4. Modulation of Electrical Transport in Calcium Cobaltite Ceramics and Thick Films

4.1 Introduction

The intrinsically low thermal conductivity arising from the layered misfit structure composed of an alternating sequence of conductive [CoO_2] layers and insulating rock salt layers along the *c* axis renders calcium cobaltite ($Ca_3Co_4O_9$) a promising p-type thermoelectric oxide [1]. Therefore, maximising the power factor ($PF = \sigma S^2$) is the main target for electrical transport modulation of calcium cobaltite. In general, elemental doping is one of the most commonly adopted strategies for modifying PF. For example, through substituting 1.7 at.% Ca^{2+} by Bi^{3+} in the lattice of calcium cobaltite, the PF was increased to 0.39 $mWm^{-1}K^{-2}$ at 873 K, showing about 30 % enhancement compared with that of the undoped control group [2]. Moser et al. [3] and Boyle et al. [4] further optimised the bismuth substitution in calcium cobaltite via spark plasma sintering and high-pressure synthesis and confined the optimal doping concentration to within the range of 6.6-13.3 at.% at Ca sites, where the highest PF could reach 0.8 $mWm^{-1}K^{-2}$ at 873 K. Another challenge for enhancing transport properties lies in the suppression of poorly conducting secondary phases in the calcium cobaltite matrix during sintering. It was reported that the Co-containing phases like Co_3O_4 and $Ca_3Co_2O_6$ frequently form in solid state synthesis of calcium cobaltite and lower the overall electrical conductivity [5–7]. In an earlier study, Miyazaki et al. [8] proposed a general formula of $[Ca_2CoO_3]_{0.62}CoO_2$ for calcium cobaltite based on TEM and XRD investigations. Different from the chemical formula $Ca_3Co_4O_9$, this general formula can be described as $Ca_3Co_{3.92}O_{9.34}$, indicating that lower cobalt contents ($3.92 < Co < 4.0$) can still meet the requirements of achieving the layered misfit structure and thereby provide a possible approach to reducing Co-containing secondary phases via increasing the cobalt deficiency.

Integrated micro-thermoelectric modules for energy harvesting or active cooling consisting of both n-type and p-type materials usually show advantages of higher heat fluxes, faster response time and higher thermal voltage [9] compared to traditional bulk counterparts. Thick film technologies are developing rapidly and are extensively utilised in applications of hybrid circuits and silicon solar cells [10], providing opportunities for commercial production of micro-devices. In contrast to thin films, thick films show large potential for automatic large scale production [11] mainly due to lower cost and simpler processing.

Furthermore, higher ZT values can be achieved in thick films, due to the small thickness and possibility to modify grain boundaries, in comparison to bulk materials [12].

Although there have only been a few investigations on calcium cobaltite thick films, some attempts have been made using different preparation techniques such as hot uniaxial pressing [13], aerosol deposition [12,14] and screen printing [11,15,16]. However, these works mainly concentrated on the effects of dopants, substrates and coupling of TE modules on the thermoelectric response. In this chapter, with use of 10.0 at.% Bi^{3+} substitution for Ca^{2+}, the effects of cobalt deficiency on electrical transport properties of $Ca_{2.7}Bi_{0.3}Co_yO_{9+\delta}$ (y = 3.92, 3.96 and 4.0) ceramics prepared by solid state reaction were studied. Based on the selected optimal composition, the effects of sintering conditions on thermoelectric performance of screen-printed calcium cobaltite thick films were investigated in detail. Here, bismuth was chosen as the dopant with the aim of promoting densification by inducing liquid phase sintering [17] and enhancing carrier mobility via Ca-site substitution [18]. The formation of Co-containing secondary phases was expected to be controlled by increasing cobalt deficiency. For calcium cobaltite thin films, the optimised heat-treatment proved to be an efficient way to tailor the microstructure [19,20]. It was therefore anticipated that the phase evolution in as-deposited thick films could be controlled through optimising the sintering conditions. Good quality calcium cobaltite ceramics and thick films were prepared by solid state reaction and screen printing, respectively. The enhanced power factor was confirmed to result from the controlled grain growth and microstructural evolution.

4.2 Characterisation of Raw Materials

4.2.1 XRD Analysis

The starting materials including $CaCO_3$, Co_3O_4 and Bi_2O_3 were examined by powder X-ray diffraction. As Fig. 4.1 shows, the corresponding XRD patterns are successfully indexed as $CaCO_3$ (hexagonal, R-3c), Co_3O_4 (cubic, Fd-3m) and Bi_2O_3 (monoclinic, P21/c), using JCPDS: # 47-1743, JCPDS: # 47-1743 and JCPDS: # 41-1449, respectively. All starting powders are well crystallised, and no traces of impurities are detected. The elevation of the background base line at higher angles in Fig. 4.1(b) is attributed to the fluorescent scattering caused by cobalt.

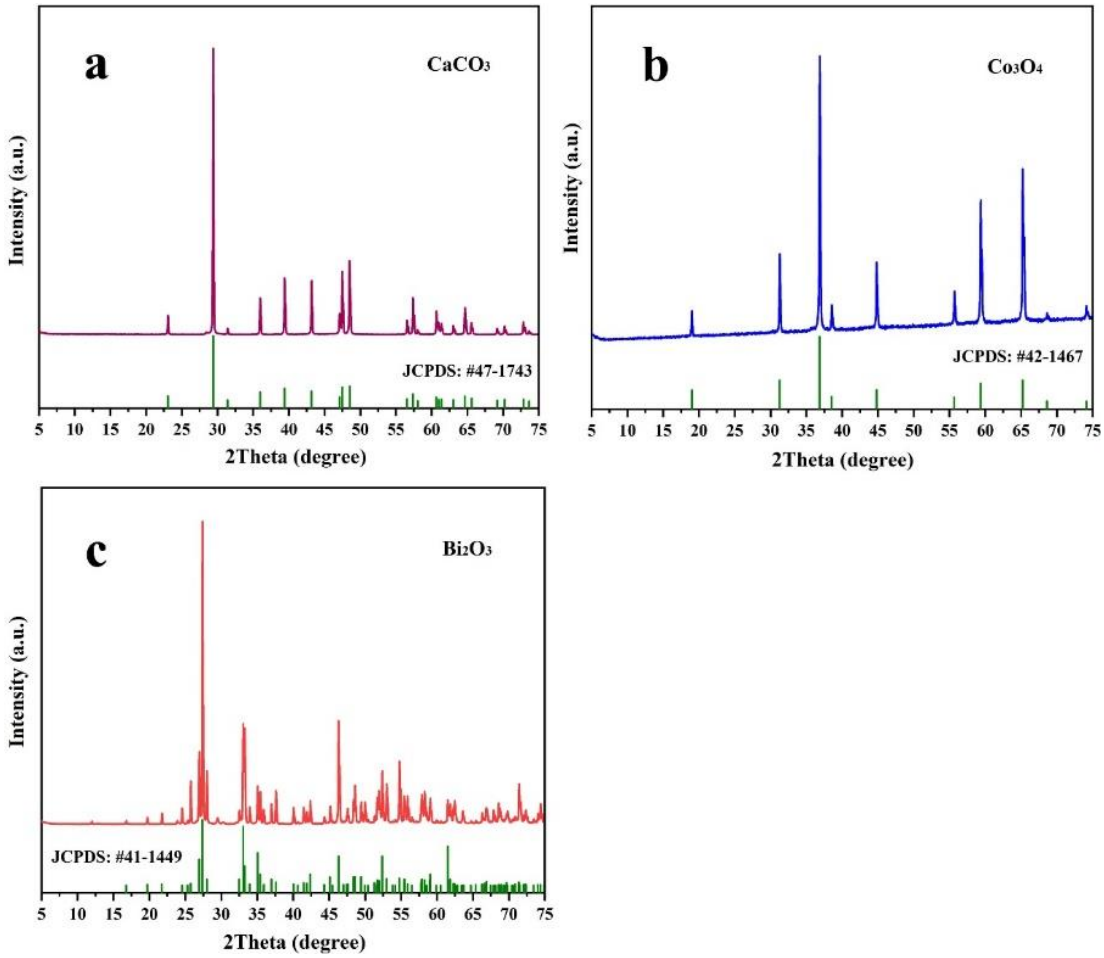

Fig. 4.1 XRD patterns of the raw materials (a. $CaCO_3$; b. Co_3O_4; c. Bi_2O_3)

4.2.2 SEM Analysis

Fig. 4.2 presents both secondary electron (SE: a, c, e) and back scattered electron (BSE: b, d, f) SEM images of the raw materials. As Fig. 4.2(a, b) show, the average grain size of randomly distributed $CaCO_3$ grains is about 10.0 μm. The Co_3O_4 grains in Fig. 4.2(c, d) show obvious agglomerations with the largest particle sizes of about 4.0 μm. In Fig. 4.2(e, f), the micro-sized irregular shaped Bi_2O_3 grains are also agglomerated and the largest particle sizes are estimated to be 10.0 μm. Through comparison of the SE SEM images with the corresponding BSE ones, it is clear that the raw materials are all free of impurities, matching well with the XRD results in Fig. 4.1.

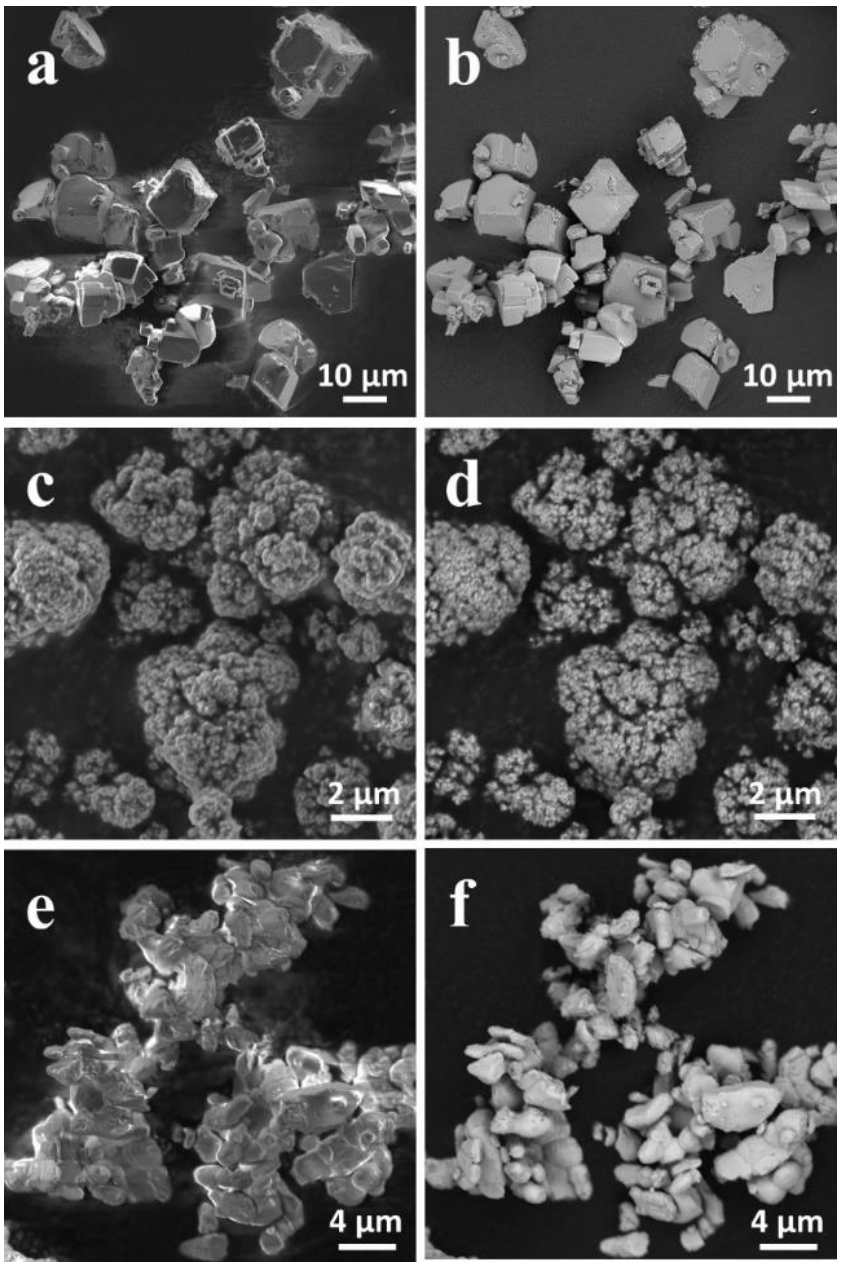

Fig. 4.2 SE (a, c, e) and BSE (b, d, f) SEM images of the raw materials (a,b: $CaCO_3$; c.d: Co_3O_4; e,f: Bi_2O_3)

4.3 Characterisation of Calcined Powders

4.3.1 XRD Analysis

XRD patterns of $Ca_{2.7}Bi_{0.3}Co_yO_{9+\delta}$ (y = 3.92, 3.96 and 4.0) powders calcined at 1203 K for 12 h are presented in Fig. 4.3. It is obvious that the dominant phase with the strongest peak intensity indexed as $Ca_3Co_{3.744}O_{9.176}$ (JCPDS: # 05-001-0461) can be detected in all compositions. Meanwhile, traces of secondary phases including $Bi_2Ca_3Co_2O_9$ (JCPDS: # 52-0125), $Ca_3Co_2O_6$ (JCPDS: # 51-0311) and Co_3O_4 (JCPDS: # 42-0461) are still observed,

suggesting that the current sintering condition (calcination at 1203 K for 12 h) cannot guarantee the formation of single-phase calcium cobaltite. In Fig. 4.3(b), the region within 2θ of 24.0-25.5 degrees in Fig.4.3(a) is enlarged, and the (003) reflection peaks of $Ca_{2.7}Bi_{0.3}Co_yO_{9+\delta}$ samples all shift to a lower angle compared to the standard PDF card (at 24.83 degrees). According to the Bragg law, it is inferred that there is an increase in the interplanar crystal spacing, indicating that bismuth can be doped into the lattice of calcium cobaltite after calcination in spite of formation of Bi-containing secondary phases.

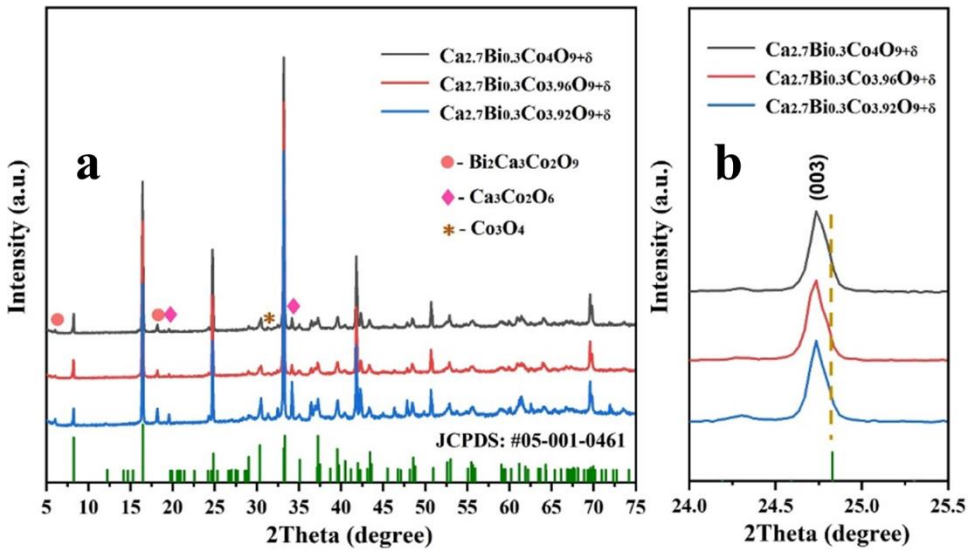

Fig. 4.3 XRD patterns of $Ca_{2.7}Bi_{0.3}Co_yO_{9+\delta}$ powders calcined at 1203 K for 12 h (a. overall view, b. enlarged region)

4.3.2 SEM-EDS Analysis

Fig. 4.4 shows both SE and BSE SEM images of $Ca_{2.7}Bi_{0.3}Co_yO_{9+\delta}$ (y = 3.92, 3.96 and 4.0) powders calcined at 1203 K for 12 h. It is apparent that randomly distributed plate-like grains are present in all compositions. However, small-scale aggregation of grains with maximum particle sizes of about 50.0 µm is revealed, suggesting that an additional milling process is required to achieve a uniform particle size distribution. The BSE images show a minor amount of bright secondary phases among the primary phase in all compositions. In addition, the formation of the bright phase (Fig. 4.4: sites 1-3 in red colour) seems insensitive to the cobalt deficiency; the EDS point analyses in Table 4.1 show that the chemical composition of these bright phase grains are all close to $Bi_2Ca_3Co_2O_9$.

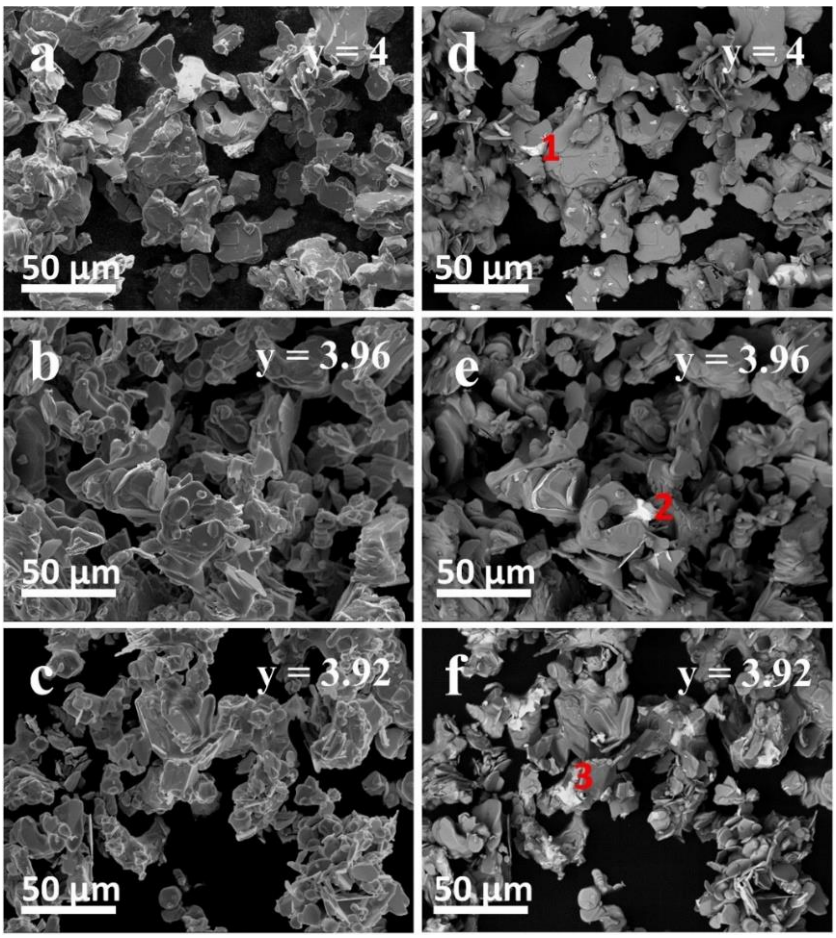

Fig. 4.4 SE (a-c) and BSE (d-f) SEM images of $Ca_{2.7}Bi_{0.3}Co_yO_{9+\delta}$ powders calcined at 1203 K for 12 h

Table 4.1 EDS point analyses for sites 1-3 in Fig. 4.4

Sites	Elements				Calculated Compositions
	Ca (at.%)	Bi (at.%)	Co (at.%)	O (at.%)	
1	15.9	11.0	17.4	55.7	$Ca_3Bi_2Co_3O_{11}$
2	17.1	14.3	20.2	48.4	$Ca_3Bi_{2.5}Co_{3.5}O_9$
3	11.6	9.2	11.2	68.0	$Ca_3Bi_2Co_3O_{17}$

4.4 Calcium Cobaltite Ceramics Prepared by Solid State Reaction

4.4.1 Density and Porosity

The density and porosity dependence of cobalt deficiency for $Ca_{2.7}Bi_{0.3}Co_yO_{9+\delta}$ (y = 3.92, 3.96 and 4.0) ceramics sintered at 1203 K for 12 h is illustrated in Fig. 4.5. All samples prepared by solid state reaction possess low bulk densities (3.0-3.28 g/cm^3), varying from 64.2 % to 70.2 % theoretical, which indicates low densification (Fig. 4.5(a)). Notably, when

the cobalt deficiency increases to 0.04, there is a slight drop in the bulk density to 3.0 g/cm^3 (the lowest: 64.2 % theoretical); this is probably related to the formation of secondary phases and differences in porosity. Fig. 4.5(b) shows the highest and lowest porosity of 38.7 % and 25.7 % for the samples with y = 3.96 and y = 3.92, respectively, matching well with the trend for density data.

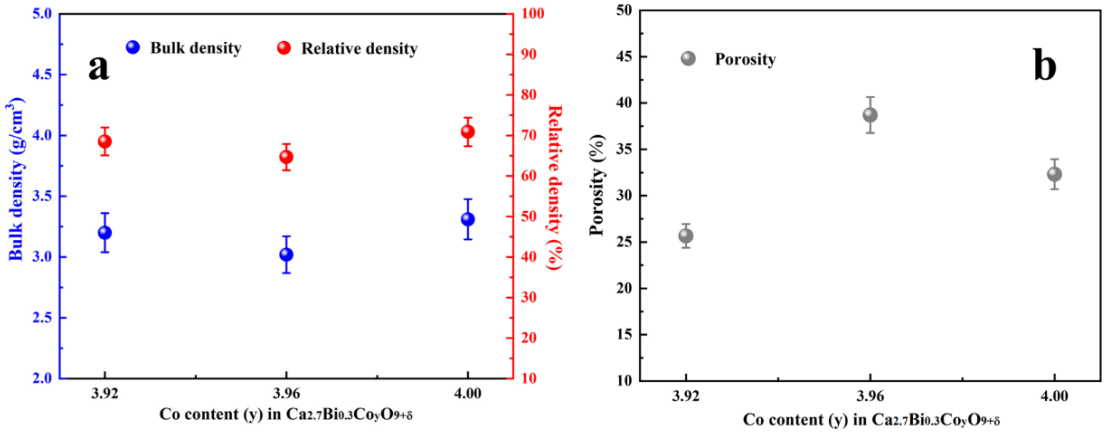

Fig. 4.5 Bulk density (a) and porosity (b) of $Ca_{2.7}Bi_{0.3}Co_yO_{9+\delta}$ (y = 3.92, 3.96 and 4.0) ceramics prepared by solid state reaction as a function of cobalt content

4.4.2 XRD Analysis

Fig. 4.6 shows XRD patterns of $Ca_{2.7}Bi_{0.3}Co_yO_{9+\delta}$ (y = 3.92, 3.96 and 4.0) ceramics sintered at 1203 K for 12 h. The reflection peaks in all compositions are indexed as monoclinic $Ca_3Co_{3.744}O_{9.176}$ (JCPDS: #05-001-0461) as expected (Fig. 4.6(a)). It is clear that the secondary phases are efficiently reduced after pressure-less sintering and X-ray pure calcium cobaltite is successfully prepared. Interestingly, the shift of (003) reflection peaks for different compositions is independent of cobalt deficiency; the (003) reflection peak of $Ca_{2.7}Bi_{0.3}Co_{3.92}O_{9+\delta}$ (at 24.7 degrees) shows the maximum shift, whereas only the slightest change is observed for $Ca_{2.7}Bi_{0.3}Co_{3.92}O_{9+\delta}$ (at 24.8 degrees) (Fig. 4.6(b)).

The relationship between the interplanar crystal spacing and lattice parameter for the monoclinic structure can be described using Equation (4.1):

$$1/d^2 = h^2/(a^2\sin^2\beta) + k^2/b^2 + l^2/(c^2\sin^2\beta) - 2hl\cos\beta/(ac\sin^2\beta) \quad (4.1)$$

where *d* is the interplanar crystal spacing, (*hkl*) is the reflection peak, a, b and c are the lattice parameters and β is the angle between *a* and *c*. The peak position (003) is independent of lattice parameter *a* and *b*. Therefore, the shift of (003) peak mainly reflects the changes in *c*

values. Based on the Bragg law, it is inferred that the largest expansion of *c* occurred in $Ca_{2.7}Bi_{0.3}Co_{3.92}O_{9+\delta}$ samples.

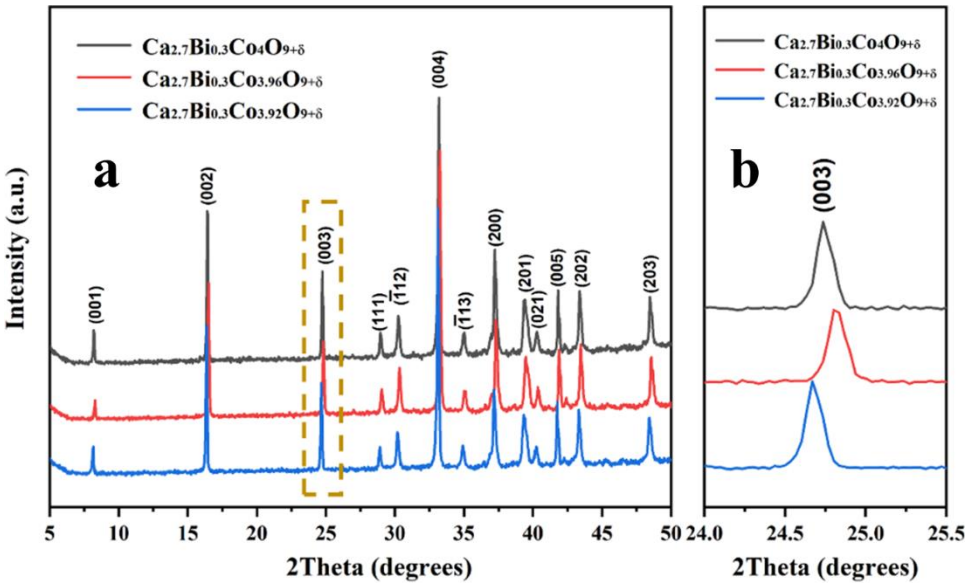

Fig. 4.6 XRD patterns of $Ca_{2.7}Bi_{0.3}Co_yO_{9+\delta}$ (y = 3.92, 3.96 and 4.0) ceramics prepared by solid state reaction (a. overall view, b. enlarged region)

In order to verify this variation trend, the lattice parameters of $Ca_{2.7}Bi_{0.3}Co_yO_{9+\delta}$ (y = 3.92, 3.96 and 4.0) ceramics were refined by Le Bail fitting, using the modulated misfit structure ($[Ca_2CoO_3][CoO_2]_{1.62}$) reported by Grebille et al. [21]. The refined plots of all compositions are shown in Fig. 4.7. It can be seen that there is a good fit (R_{wp}: 9.08-11.52; GoF: 2.59-3.24) between observed and calculated data for all compositions, ensuring the reliability of refined lattice parameters.

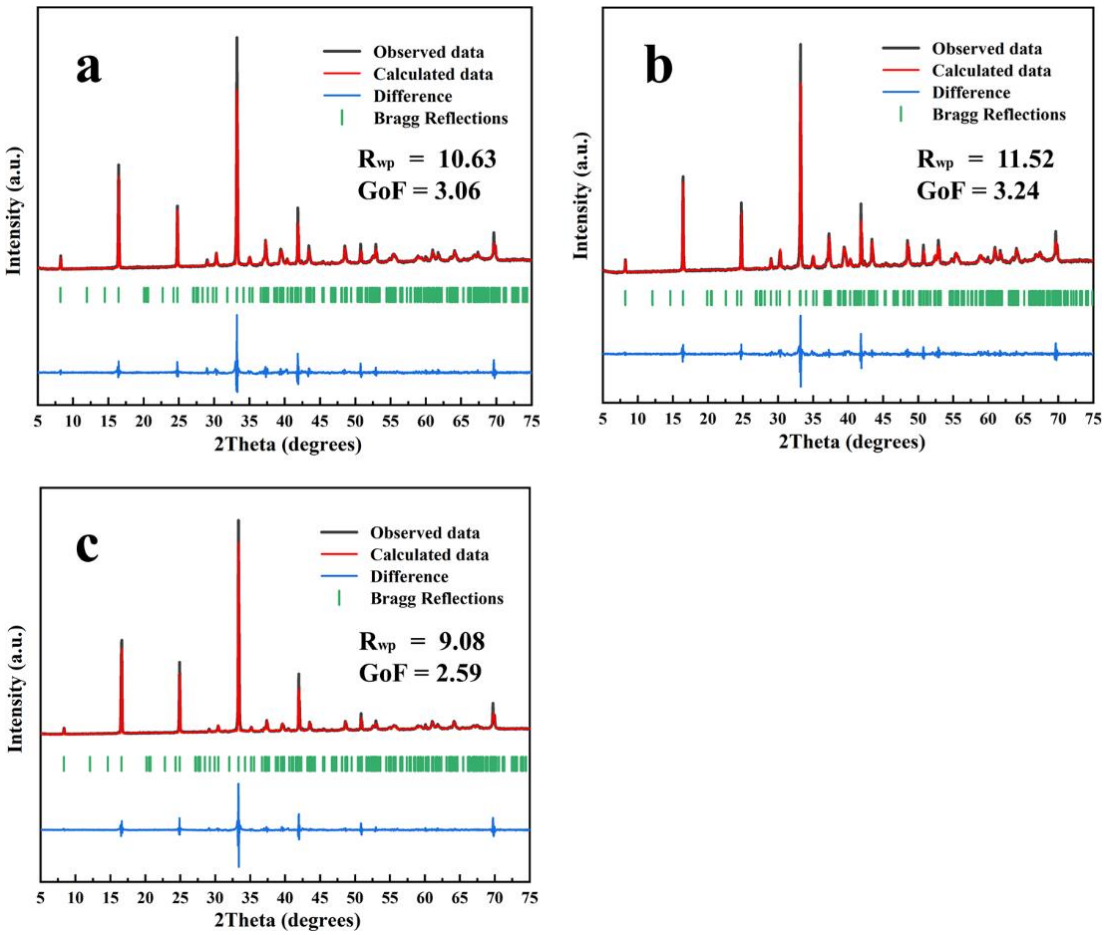

Fig. 4.7 Le Bail refinement data for $Ca_{2.7}Bi_{0.3}Co_yO_{9+\delta}$ ceramics (a. y = 4.0, b. y = 3.96, c. y = 3.92)

Fig. 4.8 shows the refined lattice parameters for $Ca_{2.7}Bi_{0.3}Co_yO_{9+\delta}$ (y = 3.92, 3.96 and 4.0) ceramics sintered at 1203 K for 12 h. Considering the estimated standard deviations, it is clearly seen that the minimum values for the lattice parameter *a*, b_{CoO2} and *c* are obtained for the sample with y = 3.96, whereas those of the samples with x = 3.92 and 4.0 are quite similar. In contrast to the lattice parameters of $[Ca_2CoO_3][CoO_2]_{1.62}$ reported by Grebille et al. (*a* = 4.83 Å; b_{RS} = 4.56 Å; b_{CoO2} = 2.82 Å; *c* = 10.83 Å) [21], the present *a* and *c* values show an obvious increase for the samples with x = 3.92 and 4.0, indicating that bismuth has been successfully doped into the lattice of calcium cobaltite. By contrast, no obvious lattice distortion is observed for the sample with y = 3.96, suggesting that Bi does not enter the crystal lattice. This could be ascribed to the pronounced stoichiometric deviation from the theoretical <349> structure due to complicated phase assemblage (Fig. 4.9(b)). The refined lattice parameter b_{CoO2} (2.81 Å) even shows a small shrinkage compared to the undoped sample (b_{CoO2}: 2.82Å), which could serve as partial evidence for the nonstoichiometry. This nonstoichiometry could lead to less Bi solubility in the main phase, and thus most of the Bi

is consumed in forming the Bi-rich phase rather than performing as a dopant in the lattice. β shares the similar variation trend with lattice parameter a, b_{CoO2} and c. Nevertheless, the refined lattice parameters for all compositions (Fig. 4.8) are in broad agreement with published data for bismuth doped calcium cobaltite [3,4,22].

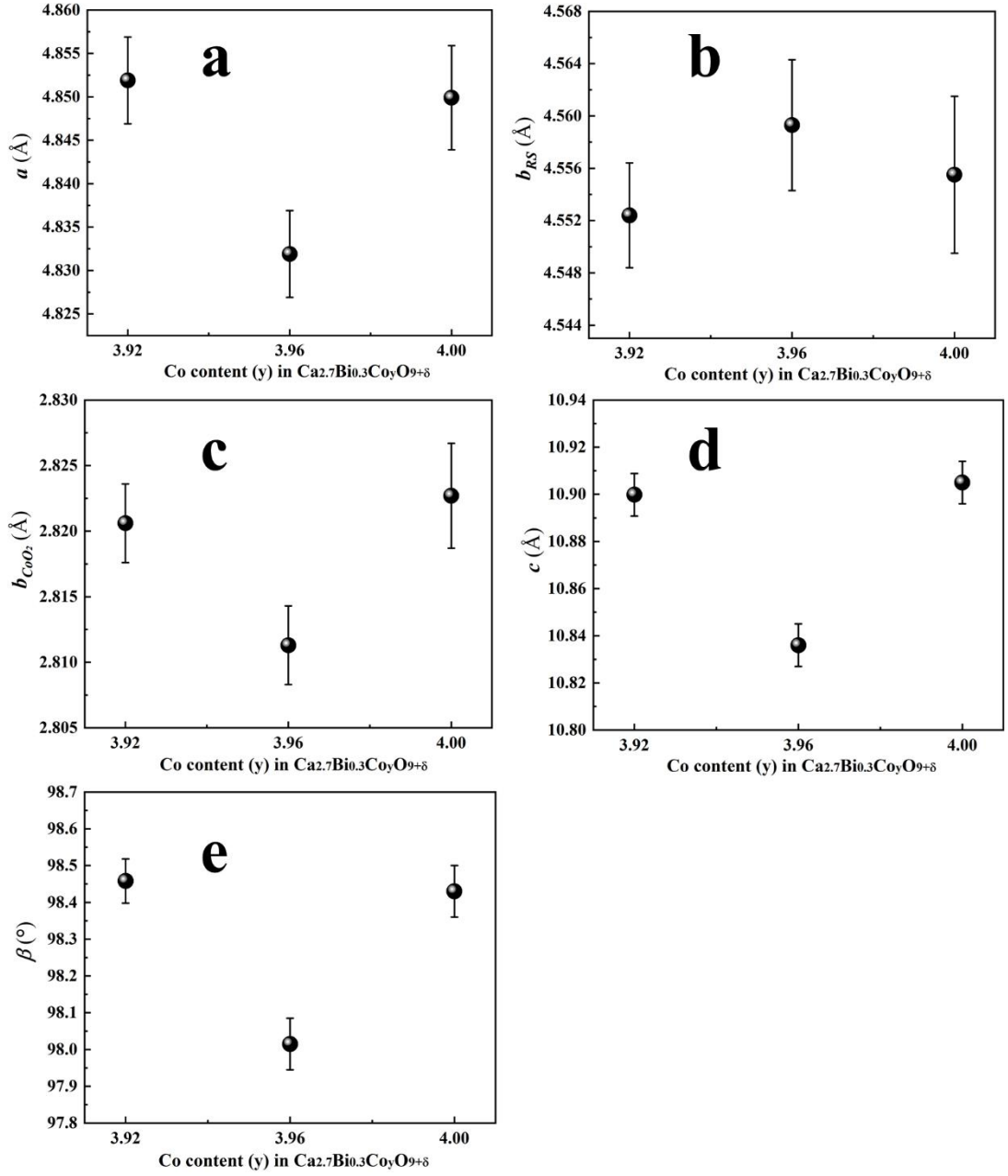

Fig. 4.8 Refined lattice parameters for $Ca_{2.7}Bi_{0.3}Co_yO_{9+\delta}$ ceramics prepared by solid state reaction

4.4.3 SEM-EDS Analysis

As the low-density solid samples cannot be polished adequately, the BSE SEM images of sintered surfaces for $Ca_{2.7}Bi_{0.3}Co_yO_{9+\delta}$ (y = 3.92, 3.96 and 4.0) ceramics sintered at 1203 K

for 12 h were collected for phase analysis (Fig. 4.9). Typical plate-like grains with a random distribution of grains are presented in all compositions, the average size of which increases from 8.8 μm to 10.3 μm as cobalt deficiency increases to 0.08. The loose connection between grains and the presence of pores can serve as a confirmation of the low density data in Fig. 4.5. In addition to the primary phase, there are two kind of secondary phases in the synthesized samples. The formation of bright phases (sites 1, 2 and 4 in Fig. 4.9) seems independent of cobalt deficiency, whereas a small amounts of the dark phase (site 3 in the insert of Fig. 4.9(b)) is only detected for the sample with y = 3.96.

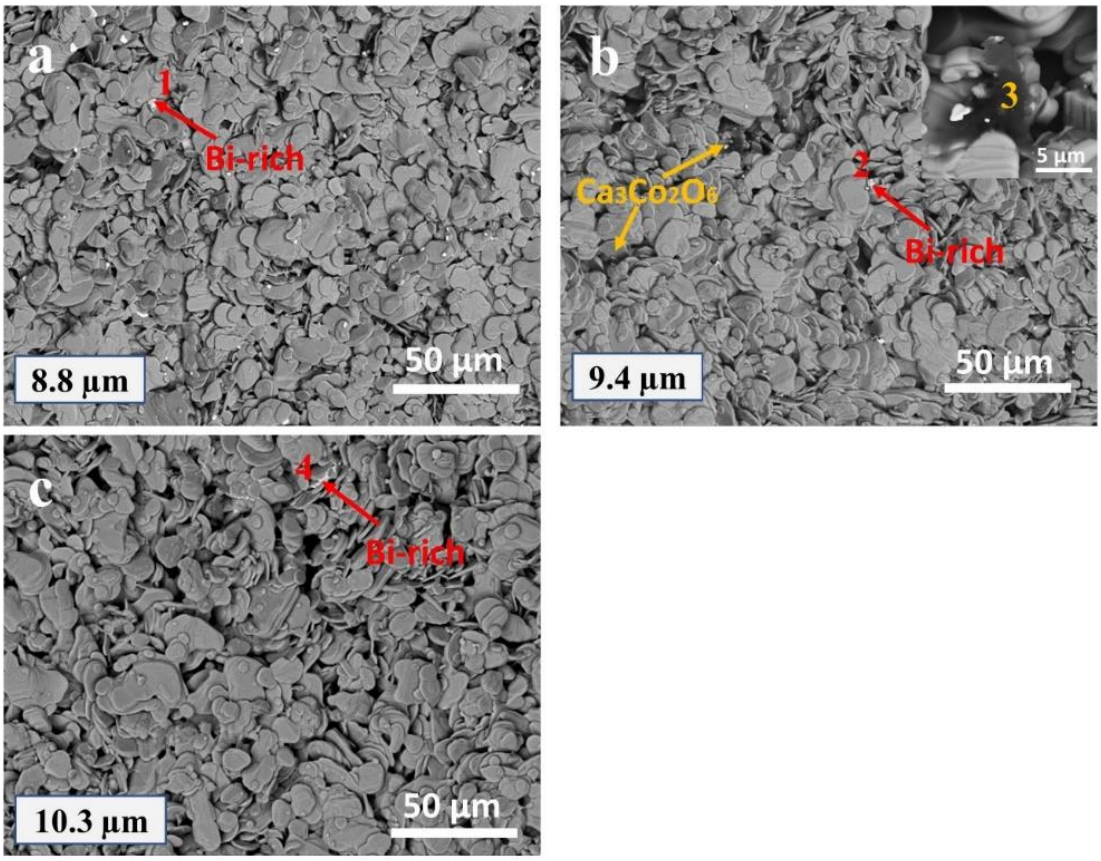

Fig. 4.9 BSE SEM images of sintered surfaces for $Ca_{2.7}Bi_{0.3}Co_yO_{9+\delta}$ ceramics prepared by solid state reaction (a. y = 4.0; b. y = 3.96; c. y = 3.92)

The chemical composition of secondary phases at different sites in Fig. 4.9 was determined by EDS point analysis, and is shown in Table 4.2. The bright phases at sites 1, 2 and 4 are confirmed to be composed of Ca, Bi, Co and O, where the ratio of Bi/Ca is around 2/3. As these secondary phases show higher Bi atomic fractions compared to the primary phase ($Ca_3Co_4O_9$), they are hereafter noted as the Bi-rich phase, highlighted by red arrows in Fig. 4.9. Although the dark phases highlighted by the orange arrows consist of the same four elements as the bright phases, they were eventually indexed as $Ca_3Co_2O_6$ with limited

solubility of Bi. In general, the presence of Bi-rich phases and $Ca_3Co_2O_6$ secondary phases are common for calcium cobaltite prepared by solid state reaction [5,22,23]. Interestingly, $Ca_3Co_2O_6$ is only found for samples with y = 3.96. It could be related to intimate mixing in the initial powders or the selective leaching of the calcium cations by the liquid phase induced by bismuth oxide [24,25].

Table 4.2 EDS point analyses of different sites (sites 1-4) on SEM images in Fig. 4.9

Sites	Elements				Calculated Compositions
	Ca (at.%)	Bi (at.%)	Co (at.%)	O (at.%)	
1	14.5	9.8	6.5	69.3	$Ca_3Bi_2Co_{1.4}O_{14}$
2	15.5	10.9	6.5	67.1	$Ca_3Bi_2Co_{1.3}O_{13}$
3	23.0	0.8	15.9	60.3	$(Ca,Bi)_3Co_2O_7$
4	18.6	13.2	6.0	62.2	$Ca_3Bi_2CoO_{10}$

EDS line and point analyses were performed on the fracture surface of the sample with y = 3.96 to verify the trend for lattice parameters. As Fig. 4.10 shows that four elements including Ca, Bi Co and O were detected in the line scan, with the content of Bi the lowest. The EDS point analyses (Fig. 4.11) yield the chemical compositions of three grains (main phase). It is clear that there is negligible bismuth solubility in calcium cobaltite, which supports the concept of bismuth not entering the crystal lattice, consistent with the XRD refinement results in Fig. 4.8.

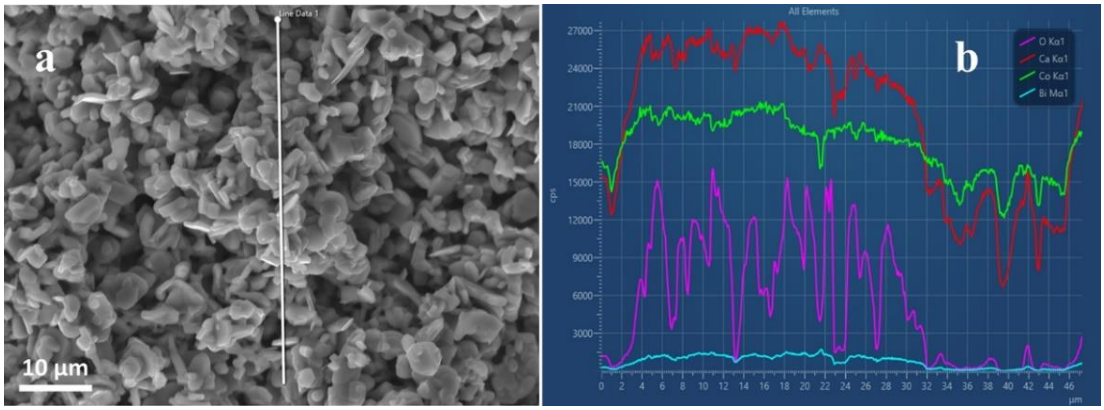

Fig. 4.10 (a) SEM image of the fracture surface of $Ca_{2.7}Bi_{0.3}Co_{3.96}O_{9+\delta}$ bulk ceramic and (b) the corresponding EDS line analysis

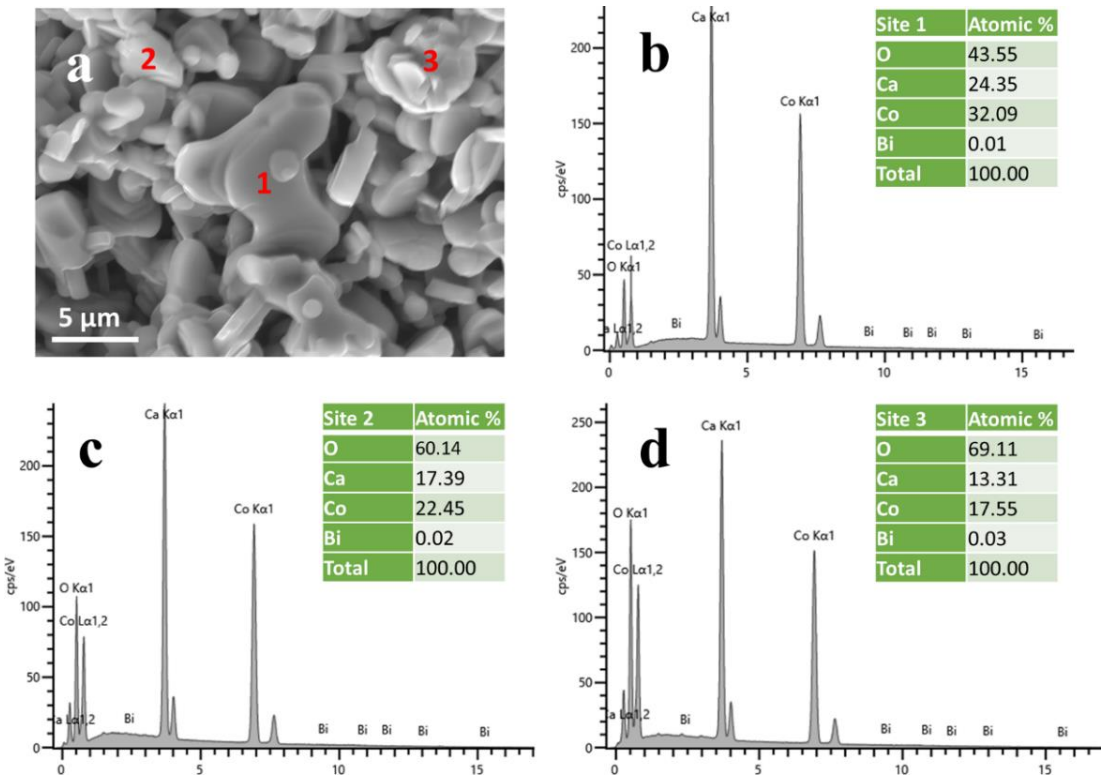

Fig. 4.11 (a) SEM image of the fracture surface of $Ca_{2.7}Bi_{0.3}Co_{3.96}O_{9+\delta}$ bulk ceramic and (b-d) the corresponding EDS point analyses at sites 1-3

4.4.4 TEM Analysis

To examine the crystal structure of synthesized calcium cobaltite in more detail, TEM data for $Ca_{2.7}Bi_{0.3}Co_{3.92}O_{9+\delta}$ ceramic sintered at 1203 K for 12 h were collected. Fig. 4.12(a) shows a bright field image of a grain with plate-like features. The bright areas in the dark field image (Fig. 4.12(b)), in contrast to the corresponding regions in Fig. 4.12(a), indicate the presence of crystalline defects. Although the detailed mechanism for the formation of high-density crystalline defects in the $Ca_{2.7}Bi_{0.3}Co_{3.92}O_{9+\delta}$ sample is unclear, the computational study of Demchenko et al. [26] shows that cobalt vacancies can be introduced in the layered cobaltite Na_xCoO_2 by increasing the cobalt deficiency to 10 at.%. From Fig. 4.12(c,d), the interplanar crystal spacing were determined to be about 1.07 nm and 0.24 nm, matching well with (001) and (200) crystal planes of $Ca_3Co_4O_9$, respectively. Therefore, the fabrication process gave rise to calcium cobaltite grains with different orientations. By examining the circular region in Fig. 4.12(a) along the [001] zone axis, a misfit structure for calcium cobaltite was confirmed, as shown in Fig. 4.12(e); the (020) reflections belonging to CdI_2 type $[CoO_2]$ layers and NaCl type $[Ca_2CoO_3]$ rock salt layers are highlighted in

orange and red colours, in good agreement with SAED patterns reported by Seo et al. [27] and Yubuta et al. [28].

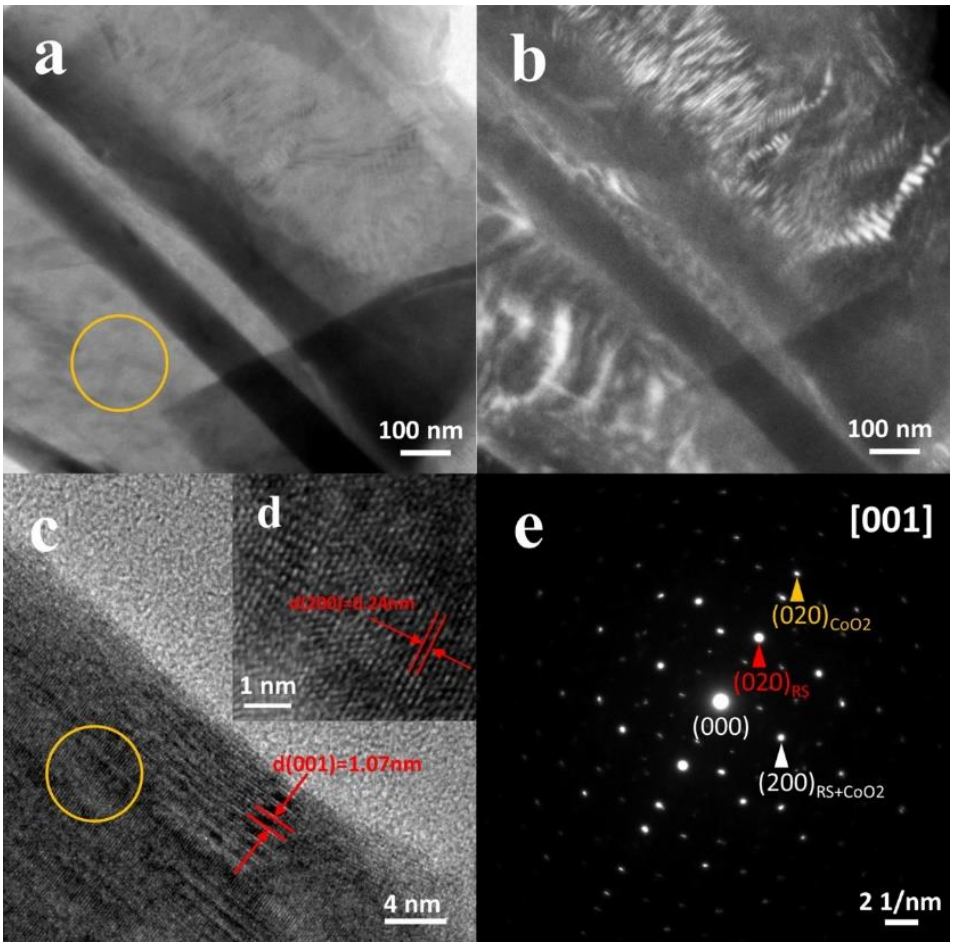

Fig. 4.12 TEM data for $Ca_{2.7}Bi_{0.3}Co_{3.92}O_{9+\delta}$ ceramic sintered at 1203 K for 12 h (a. bright field TEM image; b. dark field TEM image; c. HRTEM image; d. high magnification of the circular region in Fig. 4.4.3(c); e. [001] SAED patterns)

4.4.5 Electrical Transport

Fig. 4.13 displays the electrical transport properties of $Ca_{2.7}Bi_{0.3}Co_yO_{9+\delta}$ (y = 3.92, 3.96 and 4.0) ceramics sintered at 1203 K for 12 h. It is apparent that the electrical conductivity (σ) of all sintered samples (Fig. 4.13(a)) shows an upward trend with increasing temperature, illustrating semiconducting behaviour. The overall σ varies from 13.0 to 40.0 S/cm within the temperature range 298-823 K, showing about 20 % enhancement compared to data for bismuth doped calcium cobaltite prepared by solid state reaction (5.0-32.0 S/cm) reported by Matsukevich et al. [22]. Notably, the present data show σ is not linearly correlated with the cobalt deficiency; the values for the sample with y = 3.92 are almost tripled compared to the data for the sample with y = 3.96, whereas a moderate level is retained for

$Ca_{2.7}Bi_{0.3}Co_4O_{9+\delta}$. These differences are related to differences in density and phase compositions in the different samples.

The Seebeck coefficients (S) for all samples (Fig. 4.13(b)) are almost the same, rising from approximately 130.0 to 160.0 μV/K; this is in agreement with published data (120.0-170 μV/K) for calcium cobaltite [2,29,30]. Meanwhile, the positive thermopower data confirm the p-type conduction behaviour for bismuth doped calcium cobaltite.

The calculated power factor (PF) (Fig. 4.13(c)) follows the expected trend, increasing with increasing temperature. The PF as a function of cobalt deficiency is in accordance with the trend for σ, where the highest value of 98.0 $\mu Wm^{-1}K^{-2}$ is achieved for the sample with y = 3.92 at 823 K while the lowest value of 44.0 $\mu Wm^{-1}K^{-2}$ is obtained for the sample with y = 3.96 at 823 K. The PF data for 298-823 K may be compared with related published work. Matsukevich et al. [22] reported values of 15.0-60.0 $\mu Wm^{-1}K^{-2}$ for $Ca_{2.7}Bi_{0.3}Co_4O_{9+\delta}$ samples. Hao et al. [31] fabricated $Ca_3Co_4O_9$ with the power factor ranging from 15.0 to 60.0 $\mu Wm^{-1}K^{-2}$. Sotelo et al. [32] also reported values of 30.0-70.0 $\mu Wm^{-1}K^{-2}$ for $Ca_3Co_4O_9$ samples prepared by the mixed oxide route. In conclusion, the PF values in this study show at least 20 % enhancement compared to published data.

In order to better understand the electrical transport behaviour, ln(σT) was plotted against reciprocal temperature and the calculated activation energies were also summarised (Fig. 4.14). The plot data over 573 K in Fig. 4.14(a) shows a linear correlation with reciprocal of temperatures, matching well with the small polaron hopping conduction (SPHC) model, which can be described by Equation (2.25).

The activation energy (E_h) derived from the slope of fitted data (Fig. 4.14(b)) has a maximum E_h of 90.9 meV for samples with y = 3.96, being about 10 meV higher for the rest of the samples. Meanwhile, the values for samples with y = 3.92 (82.6 meV) and 4.0 (80.8 meV) are quite similar. The relatively higher E_h for the sample with y = 3.96 probably results from the highest porosity among all compositions (Fig. 4.5). Essentially, the pores and poorly conducting secondary phases in solid samples can block the transport path of carriers, and thereby higher energy barriers need to be overcome during transport processes. It has been reported that high-density grain boundaries caused by smaller grain size and interfaces are able to filter low-energy carriers, thereby increasing E_h [33,34].

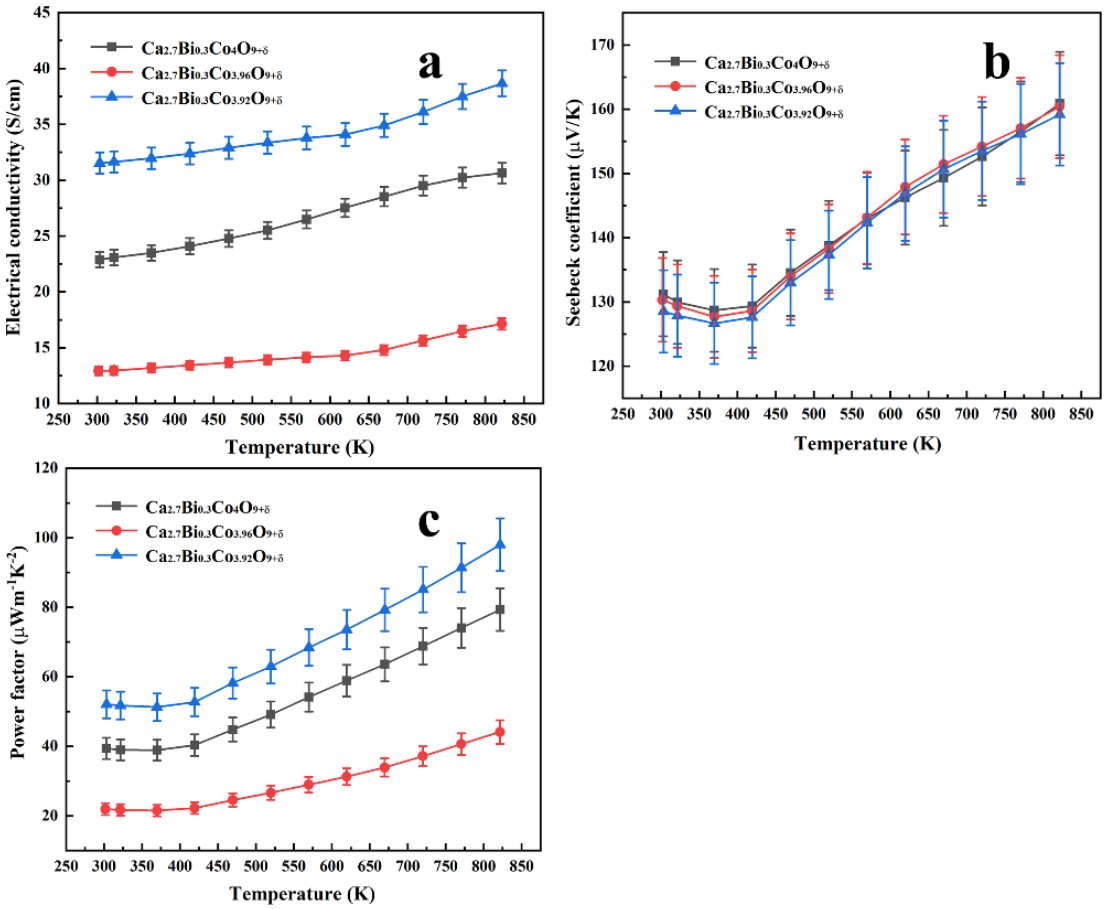

Fig. 4.13 Electrical transport properties of $Ca_{2.7}Bi_{0.3}Co_yO_{9+\delta}$ ceramics as a function of temperature (a. electrical conductivity; b. Seebeck coefficient; c. power factor)

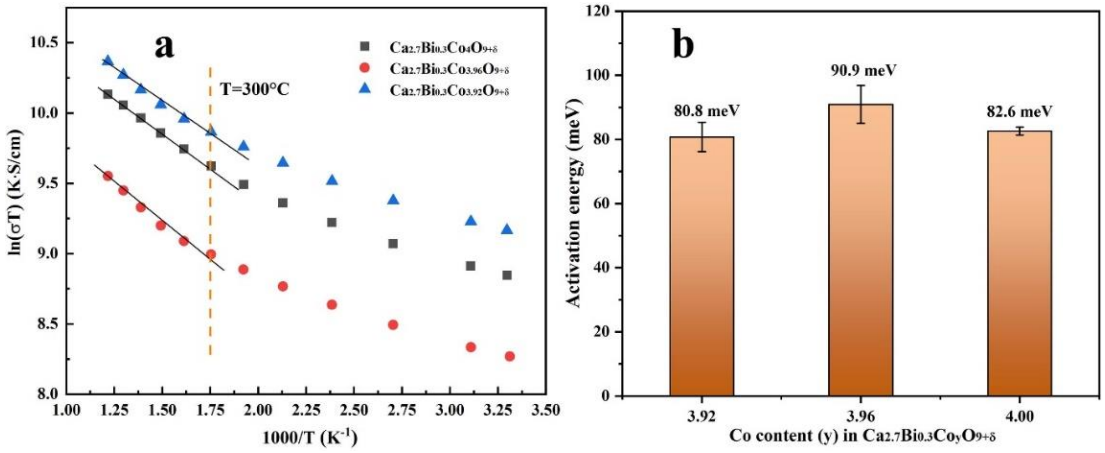

Fig. 4.14 ln(σT) as a function of reciprocal temperature (a) and calculated activation energy (b) for $Ca_{2.7}Bi_{0.3}Co_yO_{9+\delta}$ ceramics prepared by solid state reaction (the lines are linearly fitted by a least-square method)

In order to understand the contributions from different factors to σ, the data for σ at 300 K and 823 K were plotted as a function of (i) the grain size, (ii) the lattice parameter *c* and (iii)

porosity. In Fig. 4.15(a) it can be seen that σ shows a strong inverse relationship with porosity; σ increases with decreasing porosity. Although the grain size and lattice parameter *c* also show some influence (Fig. 4.15(b, c)), the porosity is expected to have a dominant role on changes in σ. Although it is difficult to determine via XRD refinement the fractions of poorly conducting secondary phases with any reliability, it can be clearly seen that the secondary phases in the sample with y = 3.92 are almost absent (Fig. 4.9(c)), whilst the most complicated phase assemblage, comprising both dark and bright phases, is observed in the sample with y = 3.96 (Fig. 4.9(b)). It can be therefore inferred that the impurities should have the minimum effect on carrier mobility for the sample with y = 3.92, and will not reduce the high carrier mobility caused by the lowest porosity. Consequently, the highest σ is achieved for $Ca_{2.7}Bi_{0.3}Co_{3.92}O_{9+\delta}$ ceramics, as noted in Fig. 4.13.

The variation trend of the carrier concentration (n) can be roughly estimated by the Mott formula Equation (2.4). It is acknowledged that the simple Drude model (C_e/n), the first term in Equation (2.4), dominates the changes to Seebeck coefficients [35–37]. As the electronic specific heat is fixed, the variation of carrier concentration can be deduced from values of the Seebeck coefficient. As there are only slight variations in thermopower between the synthesized calcium cobaltite samples, a similar n is inferred according to the Drude model.

In order to verify the relationship between electrical transport properties and cobalt deficiency, the carrier concentration (n) and carrier mobility (μ) were calculated from Equations (2.10) and (2.23) [38,39] based on room temperature data. Fig. 4.16 shows that n is not dependent of cobalt deficiency; the values for all samples are stable at around 6.0×10^{20} cm^{-3}, which is consistent with the analysis results based on Drude model. By contrast, the μ shows a maximum value of 0.33 $cm^2V^{-1}s^{-1}$, followed by a sharp decrease to about 0.13 $cm^2V^{-1}s^{-1}$ when the cobalt content increases from 3.92 to 3.96. This helps to confirm that a higher energy barrier at grain boundaries for carrier transportation is achieved in $Ca_{2.7}Bi_{0.3}Co_{3.96}O_{9+\delta}$. The calculated n and μ are in broad agreement with published data determined by the Hall effect [40,41].

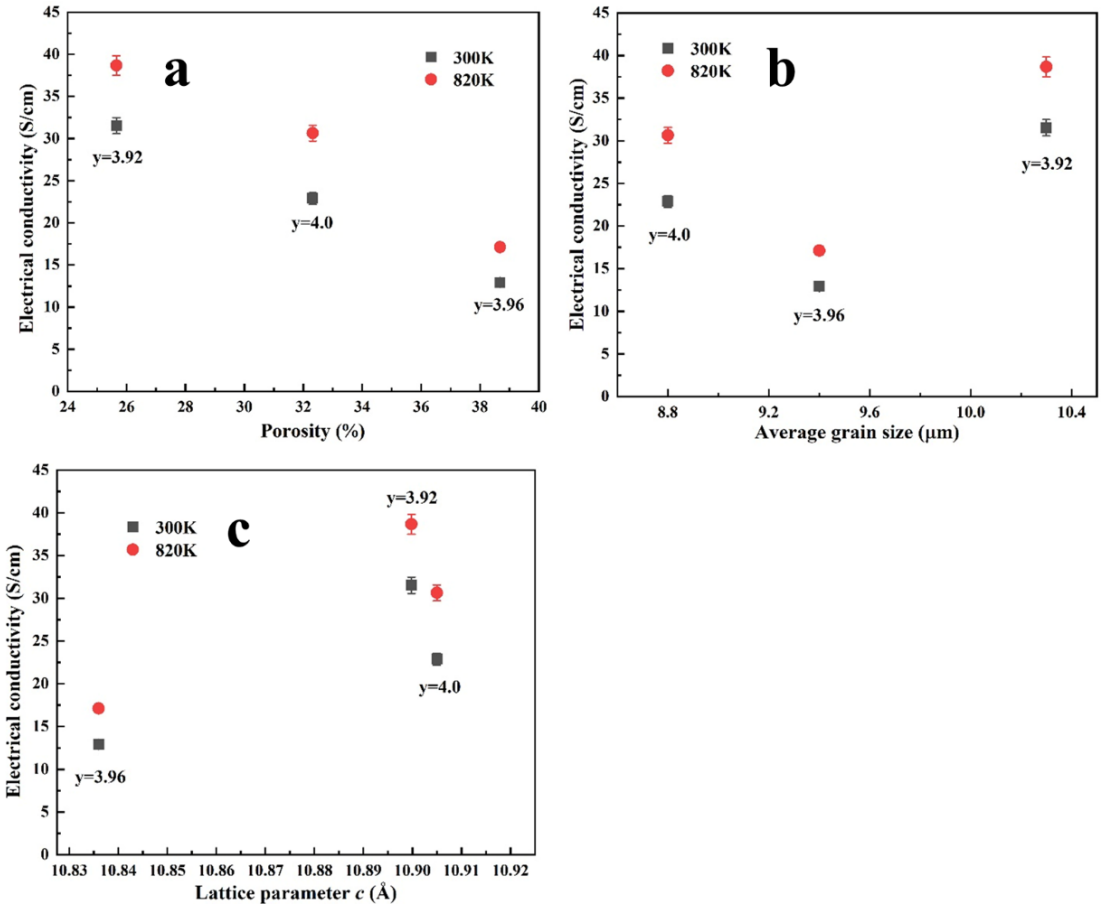

Fig. 4.15 The electrical conductivity of $Ca_{2.7}Bi_{0.3}Co_yO_{9+\delta}$ (y = 3.92, 3.96 and 4.0) ceramics as a function of porosity (a), average grain size (b) and lattice parameter *c* (c)

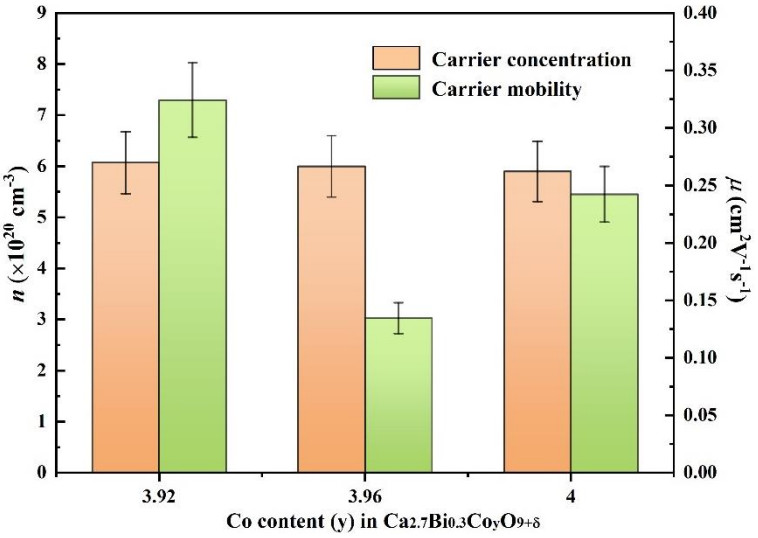

Fig. 4.16 Calculated carrier concentration and carrier mobility for $Ca_{2.7}Bi_{0.3}Co_yO_{9+\delta}$ ceramics prepared by solid state reaction

4.5 Calcium Cobaltite Thick Films Prepared by Screen Printing

4.5.1 XRD Analysis

Fig. 4.17 shows XRD patterns of the original $Ca_{2.7}Bi_{0.3}Co_{3.92}O_{9+\delta}$ thick films (denoted as as-received because they were screen-printed at University of Surrey) and $Ca_{2.7}Bi_{0.3}Co_{3.92}O_{9+\delta}$ thick films which had been sintered at 1153 and 1203 K for 4, 8 and 12 h. As expected, the main phase in all samples is indexed as $Ca_3Co_{3.744}O_{9.176}$ (JCPDS: # 05-001-0461). Traces of secondary phases, including $Bi_2Ca_3Co_2O_9$ and $Ca_3Co_2O_6$, are observed for as-received thick films, basically matching with XRD analyses for calcined $Ca_{2.7}Bi_{0.3}Co_{3.92}O_{9+\delta}$ powders (Fig. 4.3). By comparing the XRD data of as-received samples with sintered samples, it is found that the secondary phases can be eliminated by sintering at 1153 or 1203 K for 4-12 h, which means that X-ray pure calcium cobaltite thick films can be fabricated by controlling sintering conditions. Different from the XRD patterns of $Ca_{2.7}Bi_{0.3}Co_{3.92}O_{9+\delta}$ samples prepared by solid state reaction (Fig. 4.6), high-intensity reflection peaks of (00l) family are detected in contrast for films (whilst all other peals are smaller), indicating that all sintered films are highly orientated in the c axis; this preferred (00l) orientation was reported by Zhu et al. [42] for calcium cobaltite thin films, but the effect seemed to result from the substrate nucleated templated crystallisation. The comparison between Fig 4.17(a) and (b) show that the reflection peaks not belonging to (00l) family become even weaker as the sintering temperature increases from 1153 K to 1203 K, whilst the effects of sintering time are not pronounced when the sintering temperature is fixed.

Lotgering factors were calculated from the XRD patterns in Fig. 4.17 (with the aid of PDF card: JCPDS: # 05-001-0461) to characterise the grain orientation for the sintered thick films; results are shown in Fig. 4.18. It is apparent that the Lotgering factors for thick films sintered at 1153 K and 1203 K are stable at around 0.86 and 0.96, respectively, indicating that the texture can be enhanced by increasing sintering temperature. This can be ascribed to the further reduction of secondary phases that hinder the alignment of matrix grains, and the greater ability to re-orientate the plate-like grains due to the enhanced surface stresses when subject to a higher temperature. However, the grain orientation seems to be independent of the sintering time, suggesting that the phase evolution and grain growth are more sensitive to sintering temperatures.

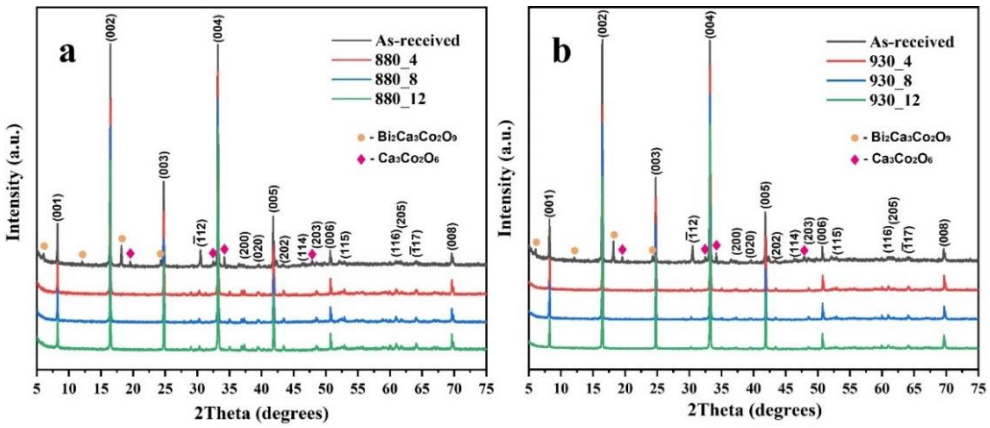

Fig. 4.17 XRD patterns of as-received $Ca_{2.7}Bi_{0.3}Co_{3.92}O_{9+\delta}$ thick films and films sintered at different sintering conditions (a. 1153 K for 4, 8 and 12 h; b. 1203 K for 4, 8 and 12 h)

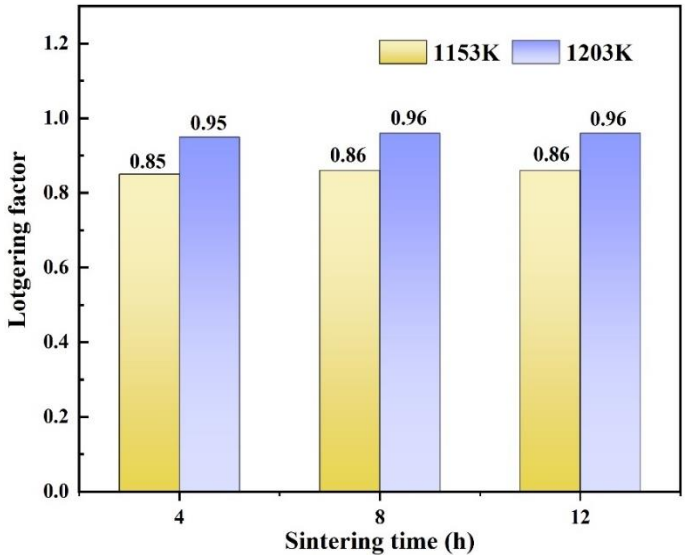

Fig. 4.18 Lotgering factors for $Ca_{2.7}Bi_{0.3}Co_{3.92}O_{9+\delta}$ thick films sintered at 1153 K and 1203 K for 4, 8 and 12 h

In order to investigate the effects of sintering conditions on lattice parameters of $Ca_{2.7}Bi_{0.3}Co_{3.92}O_{9+\delta}$ thick films sintered at 1153 K and 1203 K for 4, 8 and 12 h, XRD data were fitted by Le Bail refinement, using the modulated misfit structure ($[Ca_2CoO_3][CoO_2]_{1.62}$) reported by Grebille et al. [21]. Fig. 4.19(a-c) show that the refined data of thick films sintered at 1153 K exhibit reasonable R_{wp} and GoF values within the ranges of 14.87-15.13 and 1.68-1.70, respectively. By contrast, for thick films sintered at 1203 K (Fig. 4.19(d-f)), R_{wp} values are slightly higher (16.85-17.08) although GoF values of 1.93-2.04 still show a good fit. The higher R_{wp} values could be attributed to higher R_{exp} values, which indicate that there is room for improvement in the quality of the collected XRD data. It was reported that screen printing technology is likely to introduce texture [43,44] and a high aspect ratio (*a*-

b/c) planes was naturally found in the layered cobaltite [45]. Therefore, compared with randomly orientated $Ca_{2.7}Bi_{0.3}Co_{3.92}O_{9+\delta}$ samples (Fig. 4.6), the higher R_{wp} values for sintered thick films are also related to the high degree of anisotropy, which is responsible for the mismatch of (00l) family peaks between calculated and observed data.

The refined lattice parameters of $Ca_{2.7}Bi_{0.3}Co_yO_{9+\delta}$ thick films sintered at 1153 K and 1203 K for 4, 8 and 12 h are shown in Fig. 4.20. Within the margin of uncertainties, the effects of sintering time on lattice parameters of thick films sintered at 1153 K are not pronounced except for the lattice parameter *a*. The increase in *a* values for the sample sintered at 1153 K for 12 h (Fig. 4.20(a, e)) is probably due to pronounced bismuth doping effects induced by extended reaction time. When short sintering times are employed (4 or 8 hours), it is found that a higher sintering temperature leads to higher *a* values, whilst only slight changes are observed in other lattice parameters. Although the detailed mechanisms for the partial lattice distortion needs further exploration, the *a* values currently seem more sensitive to sintering time; a longer sintering time probably contributes to larger Bi solubility in calcium cobaltite.

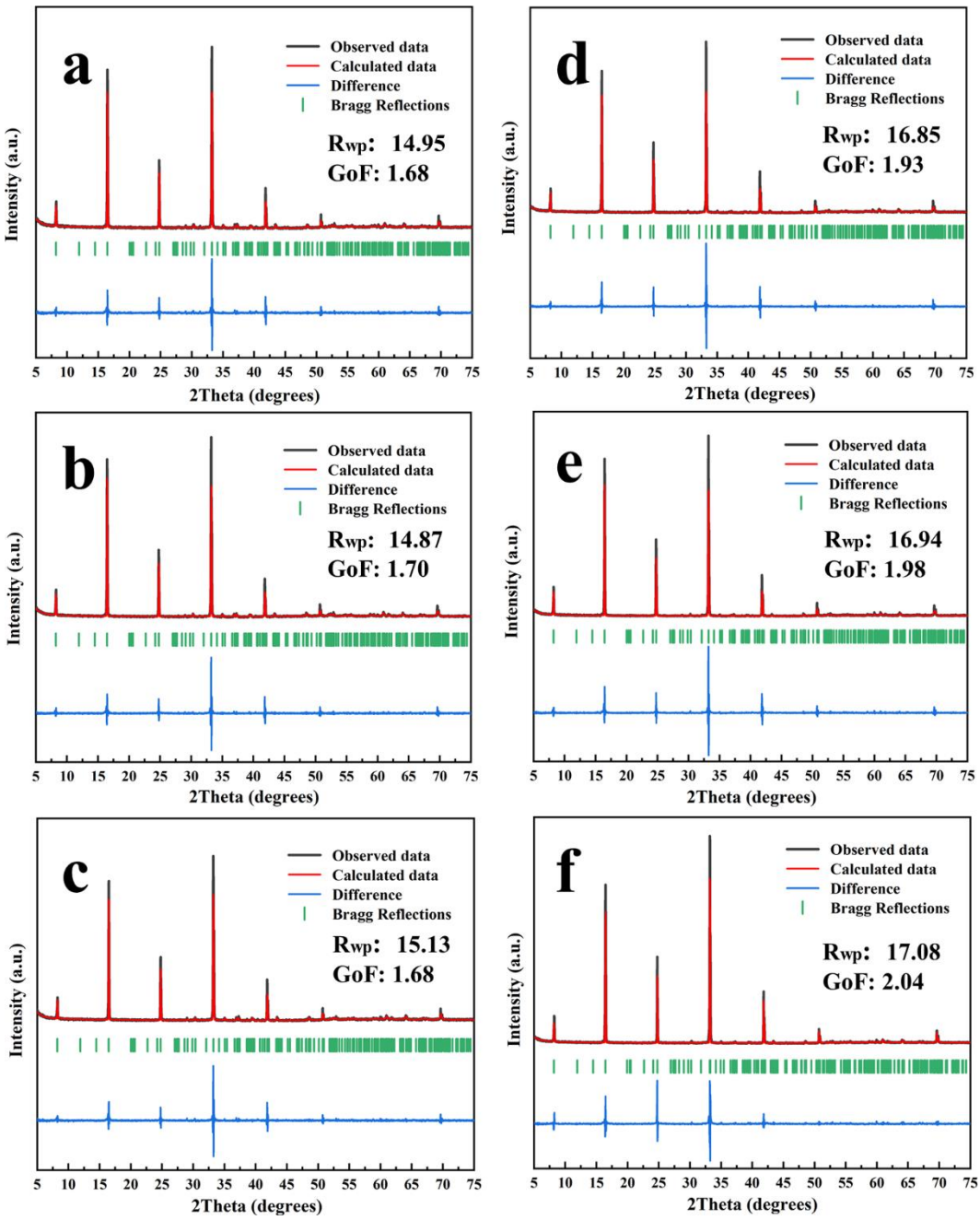

Fig. 4.19 Le Bail refinement data for sintered $Ca_{2.7}Bi_{0.3}Co_{3.92}O_{9+\delta}$ thick films (a. 1153 K_4 h, b. 1153 K_8 h, c. 1153 K_12 h, d. 1203 K_4 h, e. 1203 K_8 h, f. 1203 K_12 h)

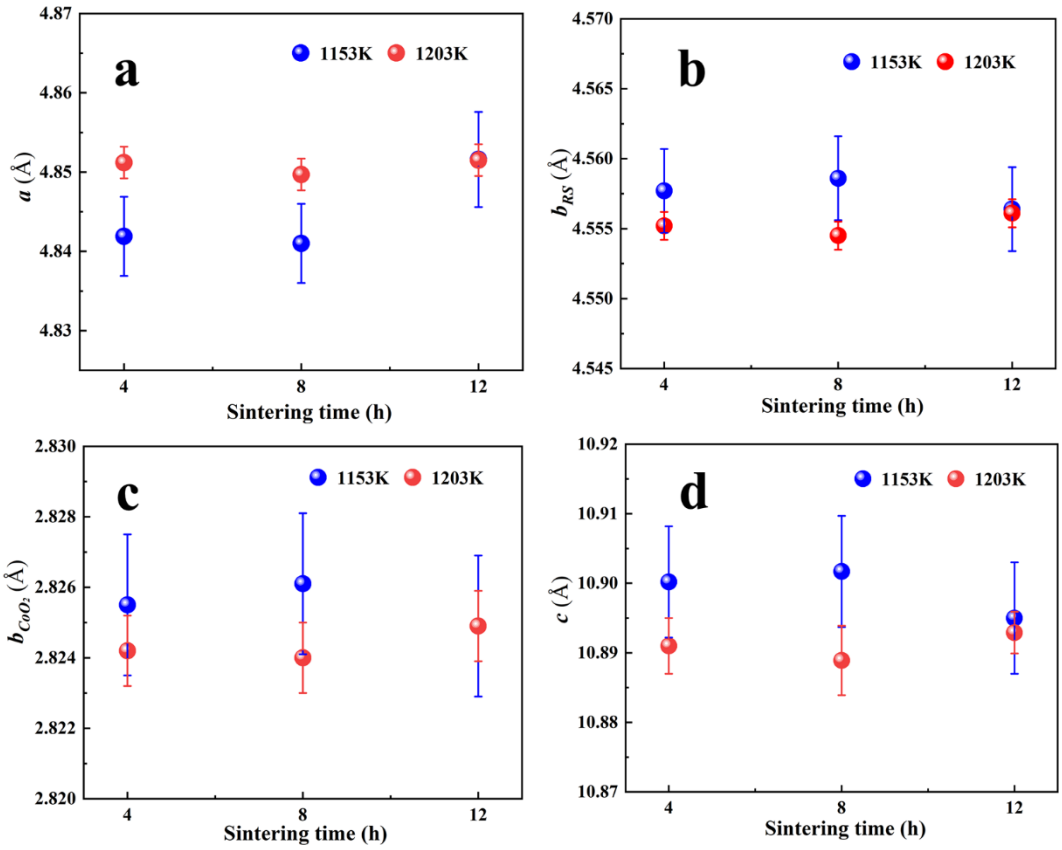

Fig. 4.20 Refined lattice parameters for $Ca_{2.7}Bi_{0.3}Co_yO_{9+\delta}$ thick films sintered at 1153 K and 1203 K for 4, 8 and 12 h

4.5.2 SEM-EDS Analysis

Fig. 4.21 shows BSE SEM images of $Ca_{2.7}Bi_{0.3}Co_yO_{9+\delta}$ thick films sintered at 1153 K and 1203 K for 4, 8 and 12 h. Overall, the plate-like grains with an average grain size over 10.0 μm are presented in all samples. It is noticeable that the grain size shows slight variations with increasing holding time but increases with increasing temperature, indicating that the sintering temperature takes a dominating role in grain growth. Compared to samples prepared by solid state reaction (Fig. 4.9), an increasing number of pores can be observed on the sintered surfaces for thick films. Furthermore, bright secondary phases can be detected in most thick film samples (Fig. 4.21(a-c, f)) except the ones sintered at 1203 K for 4 and 8 h (Fig. 4.21(d, e)). By contrast, the trace of the grey phase is only observed for the films sintered at 1203 K for 4 h. In general, the fraction of the bright phase tends to decrease with increasing holding time when sintered at 1153 K. However, the phase evolution in the films sintered at 1203 K is more complicated; the grey phase is eliminated when the holding time increases from 4 to 8 h, followed by development of the newly formed bright phase when

the holding time further increases to 12 h. In summary, single-phase $Ca_{2.7}Bi_{0.3}Co_yO_{9+\delta}$ thick films can be successfully fabricated when sintered at 1203 K for 8 h.

Table 4.3 presents the EDS point analyses for sites (1-6) in Fig. 4.21. The chemical composition of bright phases highlighted in red colour at sites 1-3 (Fig. 4.21(a-c)) approaches $Bi_2Ca_3Co_2O_9$, similar to the one in Fig. 4.9. However, the atomic ratio of Ca/Bi (1/2) for the bright phase at site 6 (Fig. 4.21(f)) is significantly lower than 3/2, confirming the formation of a new Bi-rich secondary phase. This could be related to different chemical reactions occurring at different temperatures. The chemical composition of the grey phase marked in orange colour in Fig. 4.21(e) basically matches with CoO phase. As expected, the primary phase (site 5) is bismuth doped calcium cobaltite. Notably, no trace of $Ca_3Co_2O_6$ phase is detected in the sintered thick films; this could be because heat conduction tends to be more uniform in thick films compared to sintered ceramics due to the smaller thickness and hence adequate energy is provided to ensure complete reactions of forming calcium cobaltite. Such Co-rich phases are also probably related to the loss of the less refractory elements as a result of evaporation and diffusion into the substrate [46].

Table 4.3 EDS point analyses at different sites (sites 1-6) shown in SEM images of thick films (Fig. 4.21)

Sites	**Elements**				**Calculated Compositions**
	Ca (at.%)	**Bi (at.%)**	**Co (at.%)**	**O (at.%)**	
1	16.2	10.9	7.9	65.0	$Ca_3Bi_2Co_2O_{12}$
2	14.4	8.9	7.1	69.6	$Ca_3Bi_{1.9}Co_{1.5}O_{15}$
3	20.7	9.4	14.3	55.6	$Ca_3Bi_2Co_2O_8$
4	1.9	0.2	48.7	49.2	(Ca,Bi,Co)O
5	17.8	1.9	19.4	50.9	$Ca_{2.7}Bi_{0.3}Co_3O_8$
6	5.7	12.0	25.4	56.9	$CaBi_2Co_5O_{10}$

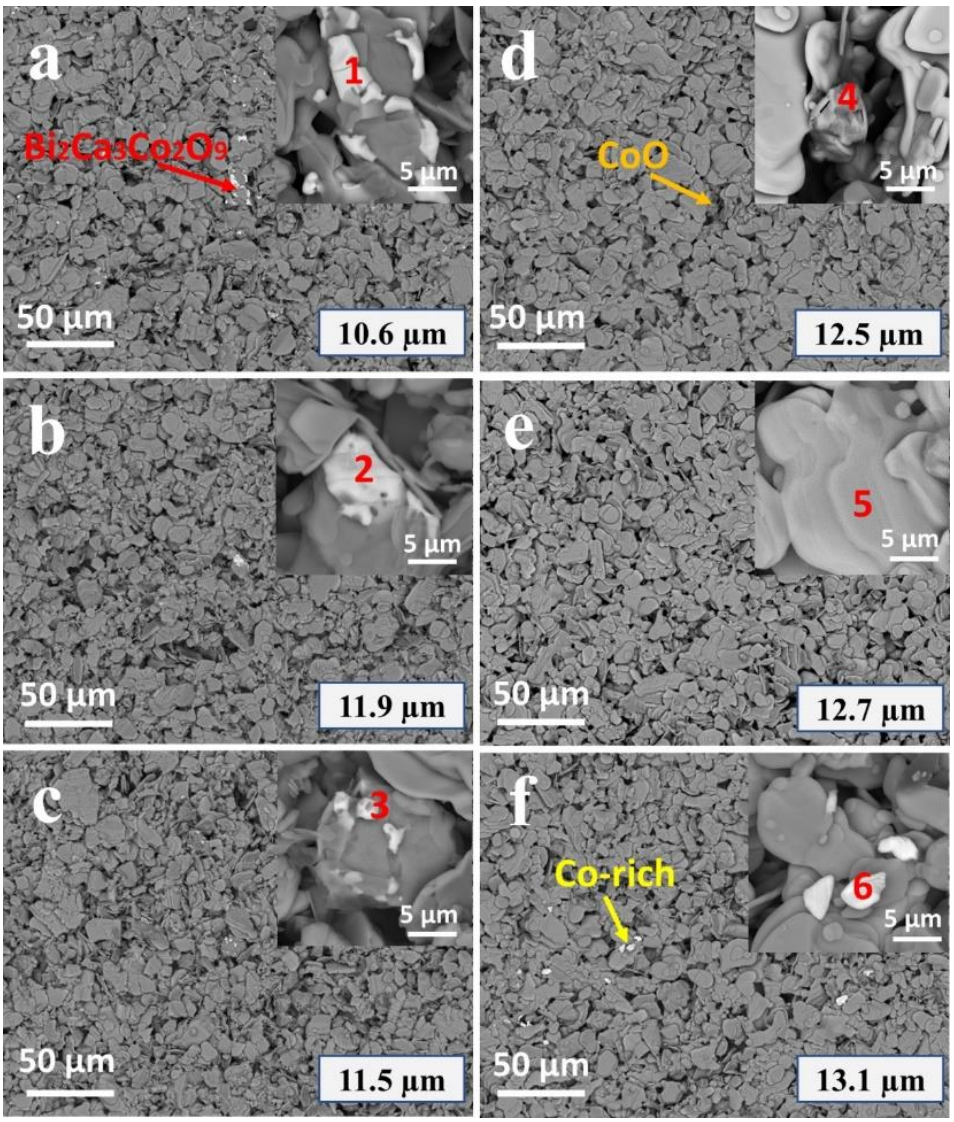

Fig. 4.21 BSE SEM images of $Ca_{2.7}Bi_{0.3}Co_yO_{9+\delta}$ thick films sintered under the following conditions: a-c: 1153 K for 4, 8 and 12 h; e-f: 1203 K for 4, 8 and 12 h

Fig. 4.22 shows SE SEM images of fracture surfaces for $Ca_{2.7}Bi_{0.3}Co_yO_{9+\delta}$ thick films sintered at 1203 K for 8 h. In Fig. 4.22(a, b), it is clear that relatively unconsolidated calcium cobaltite (CCO) film has been deposited onto the rigid alumina substrate, with thickness of 52.6 µm and 699.1 µm, respectively. In the region near the top surface of the thick film (Area 1 in Fig. 4.22(c)), the CCO grains shows a better alignment with a tendency for growth along the ab planes. Shi et al. [47] and Yu et al. [18] also reported this type of textured structure for calcium cobaltite based materials prepared by tape-casting and SPS methods. By marked contrast, in the region near the interface (Area 2 in Fig. 4.22(d)), the CCO grains are disordered and show a loose connection with the substrate. The order-disorder structural transition between Area 1 and Area 2 is summarised in Fig. 4.22(e); this transition should be strongly correlated with the interface. Basically, the calcined $Ca_{2.7}Bi_{0.3}Co_yO_{9+\delta}$ powders

contain multiple phases including the primary phase (CCO) and intermediate phases (Fig. 4.4(f)), which can be regarded as the precursor mixture. Here, the intermediate phases and uncrystallised grains perform as the matrix powders and the plate-like CCO grains act as the platelet template seeds [47]. Distant from the substrate, Area 1 is free of the effects of the interface. The grains here are able to re-orientate themselves to reduce stresses caused by differential shrinkage of the film with respect to the rigid substrate during drying and sintering. Furthermore, the growth of CCO grains are also driven by the low surface free energies [48] and thus the arrangement of grains along the ab planes of the platelet template seeds develops. However, the stress arising from different coefficients of thermal expansion between the film and substrate tends to be pronounced during the cooling stage. With a significantly higher average coefficient of thermal expansion (12.6 $ppmK^{-1}$) [30] than alumina (7.3 $ppmK^{-1}$) [49], the shrinkage of CCO layer is more obvious than the alumina layer and leads to a tensile stress as a result. There are limited chances for grains to re-orientate themselves during this stage compared to the drying and sintering stages because the individual grains are expected to be more strongly fused together as a result of sintering. Consequently, Area 2 is subject to the constrained sintering [50] owing to the overall tensile surface stress; the flow of matter and the mobility of the grain boundaries are dramatically decreased because of the grain necks in the direction parallel to the stress [51]. In addition, grain growth in Area 2 could be related to the difference between the surface free energies and surface stress. Ibach et al. [52] reported that a symmetry-breaking reconstruction resulting from this difference enabled unfavorable bonding positions of atoms in the surface layer, thereby modifying the steady grain growth along the original orientation.

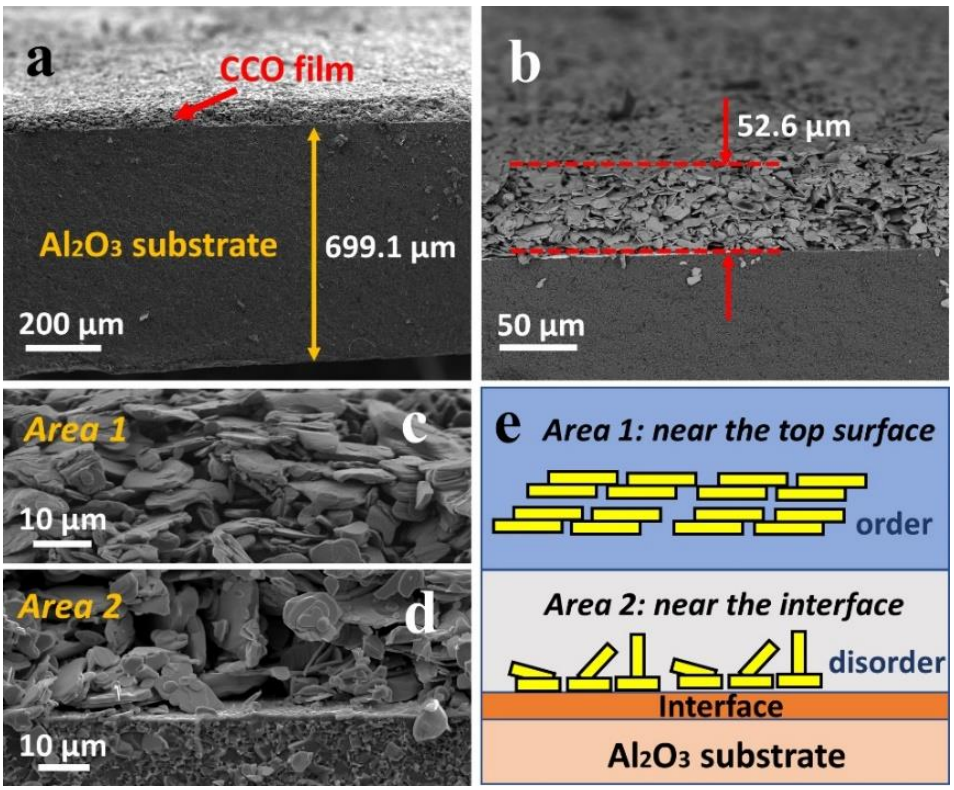

Fig. 4.22 SE SEM images for the fracture surface of $Ca_{2.7}Bi_{0.3}Co_yO_{9+\delta}$ thick films sintered at 1203 K for 8 h (a. thickness of Al_2O_3 substrate, b. thickness of CCO film, c. morphology near the top surface, d. morphology near the interface, e. schematic diagram for grain distributions in the order-disorder regions)

4.5.3 XPS Analysis

The high-resolution XPS spectra of Co 2p 3/2 for $Ca_{2.7}Bi_{0.3}Co_{3.92}O_{9+\delta}$ thick films sintered under different conditions are displayed in Fig. 4.23. The Co 2p 3/2 spectra for all samples within 776.5-785.5 eV can be divided into three peaks, where the first peaks at 778.9-779.1 eV correspond to Co^{3+}, the second peaks at 779.8-780.1 eV are assigned to Co^{2+} and the third peaks at 781.6-781.9 eV are ascribed to Co^{4+}. These results match well with published XPS data in earlier investigations [53–55] and also confirm the existence of three species of cobalt ions (Co^{2+}, Co^{3+} and Co^{4+}) in the synthesized materials. The fractions of different cobalt ions were calculated from the plot XPS data in Fig. 4.23 and the results are present in Table 4.4. For thick films sintered at 1153K, the fractions of Co^{2+}, Co^{3+} and Co^{4+} are quite similar, and stable at 45.2-47.6 %, 30.0-32.2 % and 22.2-22.6 %, respectively. When the sintering temperature is increased to 1203 K, the concentration of Co^{4+} in the thick film sintered for 8 h shows an increase as a natural result of the absence of secondary phases (Fig. 4.21(e)) and the removal of the more volatile elements. The decrease in fractions of Co^{4+} for thick films sintered for 4 and 12 h can be attributed to the newly formed Co-containing

phases (Fig. 4.21(d,f)). Consequently, the maximum fractions of $Co^{4+}/(Co^{3+}+Co^{4+})$ (54.3 %) is achieved for the thick film sintered at 1203 K for 8 h mainly due to the controlled phase evolution.

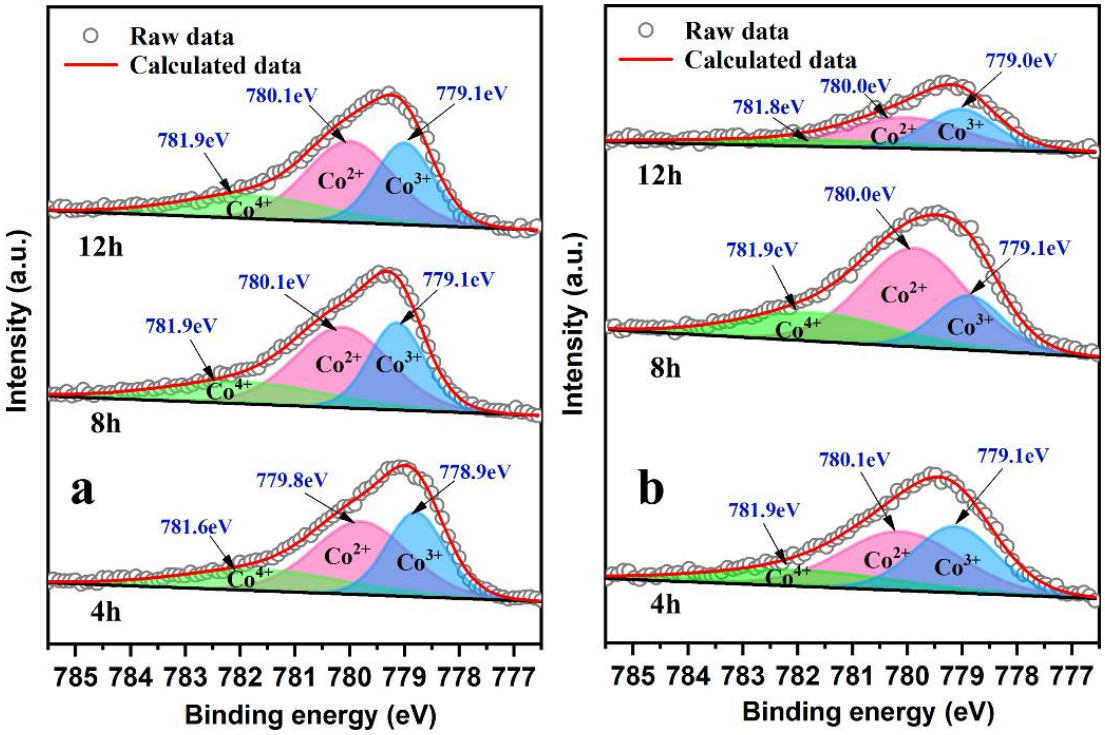

Fig. 4.23 High-resolution XPS spectra of Co 2p 3/2 for $Ca_{2.7}Bi_{0.3}Co_{3.92}O_{9+\delta}$ thick films sintered at different temperatures (a. 1153 K; b. 1203 K) for 4, 8 and 12 h

Table 4.4 Fractions of cobalt ions in $Ca_{2.7}Bi_{0.3}Co_{3.92}O_{9+\delta}$ thick films sintered at 1153 K and 1203 K for 4, 8 and 12 h

T (K)	Time (h)	Co^{3+} (%)	Co^{2+} (%)	Co^{4+} (%)	$Co^{4+}/(Co^{3+}+Co^{4+})$ (%)
1153	4	32.2	45.2	22.6	41.3
1153	8	30.0	47.6	22.4	42.7
1153	12	31.3	46.5	22.2	41.4
1203	4	35.0	44.8	20.2	36.6
1203	8	20.1	56.0	23.9	54.3
1203	12	34.8	47.0	18.2	34.3

4.5.4 Electrical Transport

The effects of sintering conditions on electrical transport properties of sintered $Ca_{2.7}Bi_{0.3}Co_yO_{9+\delta}$ thick films are presented in Fig. 4.24. There are only slight variations in σ (Fig. 4.24(a)) for thick films sintered at 1153 K for 4-12 h (5.5-10.3 S/cm) within the temperature range of 323-673 K. By contrast, for thick films sintered at 1203 K, σ varies from 10.5 to 19.7 S/cm when sintered for 4 h, and then shows a slight enhancement (13.0 to 21.3 S/cm) with the holding time increasing to 8 h, followed by a sharp drop (7.0 to 12.0 S/cm) when the hold time is extended to 12 h. This behaviour could be attributed to the phase evolution with increasing holding time, shown as Fig. 4.21(d-f), which indicates that the presence of CoO and Co-rich phases degrade σ. Moreover, it is evident that σ is enhanced by increasing sintering temperature from 1153 K to 1203 K. Essentially, σ is mainly determined by carrier concentration (n) and carrier mobility (μ). Here, n is reflected by the ratio of $Co^{4+}/(Co^{3+}+Co^{4+})$ (x) in the crystal lattice of $Ca_3Co_4O_9$ [18]. As Table 4.4 shows, x is stable at about 42.0 % for thick films sintered at 1153 K, indicating a similar level of n. By contrast, x shows a decrease (~35 %) for thick films sintered at 1203 K for 4 and 12 h, but shows an increase (54.3 %) when the sintering time is fixed at 8 h. This confirms that the n can be controlled by optimising sintering conditions. In spite of a lower n, the thick films sintered at 1203 K for 4 and 12 h still exhibit enhanced σ, suggesting that the corresponding μ is increased (Equation (2.23)). According to Equations (2.23) and (2.24), the relaxation time τ dominates μ. Here, the factors affecting τ are equally complex, including porosity, grain size, texture, and secondary phases. Due to improved densification brought about by enhanced sintering, the increased grain boundary area leads to increased conduction. However, the in-plane grain boundary density can be reduced by enlarging the grain size and improving the texture, thereby resulting in smaller energy barriers at grain boundaries [33,34] and hence a larger τ. The larger grain size (Fig. 4.21) and stronger texture (Fig. 4.18) at higher temperatures should take a dominant role in decreasing the energy barrier despite the partial offset effects caused by the presence of poorly conducting phases. As a result, the maximum σ of 21.3 S/cm at 673 K is obtained for the thick film sintered at 1203 K for 8 h, which is comparable to the value for for screen printed Sr-doped calcium cobaltite with 57.67 wt.% solid loading (26.0 S/cm) reported by Torres et al. [11]. However, this value is still lower than values (30.0 to 71.4 S/cm) reported by Markowski et al. [15] and Nong et al. [16]. This can be ascribed to a lower μ caused by the observable pores on the surface of sintered thick films (Fig. 4.21) as a result of the pyrolysis of organic binders and the pronounced packing near the interface. Torres et al. reported that σ could be

enhanced by reducing porosity through increasing $Ca_3Co_4O_9$ solid content in the ink [11], providing a possible route to cope with this technical problem.

Fig. 4.24(b) exhibits the variations in the Seebeck coefficient for thick films. The Seebeck coefficients increase from 134.0 to 165.0 μV/K, with a distinguishable difference (ΔS = 15.0-20.0 μV/K) between the samples sintered at 1153 K and 1203 K for 8 h. As the thick films exhibit strong texture, carrier scattering effects need to be taken into consideration and thus the Seebeck coefficient can be alternatively described by Equations (2.5) and (2.7) [56].

Here, the scattering factor (γ) reflects the energy filtering effect caused by the interfaces and grain boundaries. Complex interface or grain boundaries are able to filter the low-energy carriers, thereby increasing the Seebeck coefficient. When sintered at 1203 K for 8 h, the thick film shows larger grain size, stronger texture and low content of secondary phases, thereby leading to a lower energy barrier and hence a smaller γ. In addition, n is higher than that of sample sintered at 1153 K for 8 h, and thus a relatively smaller S is achieved according to Equation (2.7). However, the decrease in S resulting from grain growth and texture development compensates for the increase brought about by presence of poorly conducting phases and lower n, so there are only slight variations for the remaining samples. The S values of synthesized samples basically match with earlier studies (135.0-170.0 μV/K between 298 K and 673 K) for calcium cobaltite thick films [12–14] and data for the sintered calcium cobaltite ceramics (Fig. 4.13).

Fig. 4.24(c) shows the temperature dependence of power factor for thick films sintered under different conditions. It is clear that the highest power factor of 55.5 $\mu Wm^{-1}K^{-2}$ at 673 K was obtained for $Ca_{2.7}Bi_{0.3}Co_{3.92}O_{9+\delta}$ thick films sintered at 1203 K for 8 h; this value is consistent with published data for screen-printed Sr-doped calcium cobaltite thick film (50.0 $\mu Wm^{-1}K^{-2}$ at 673 K) [11]. Although further improvements in the power factor are required, our work established the ground rules for the processing-microstructure relationships for calcium cobaltite thick films.

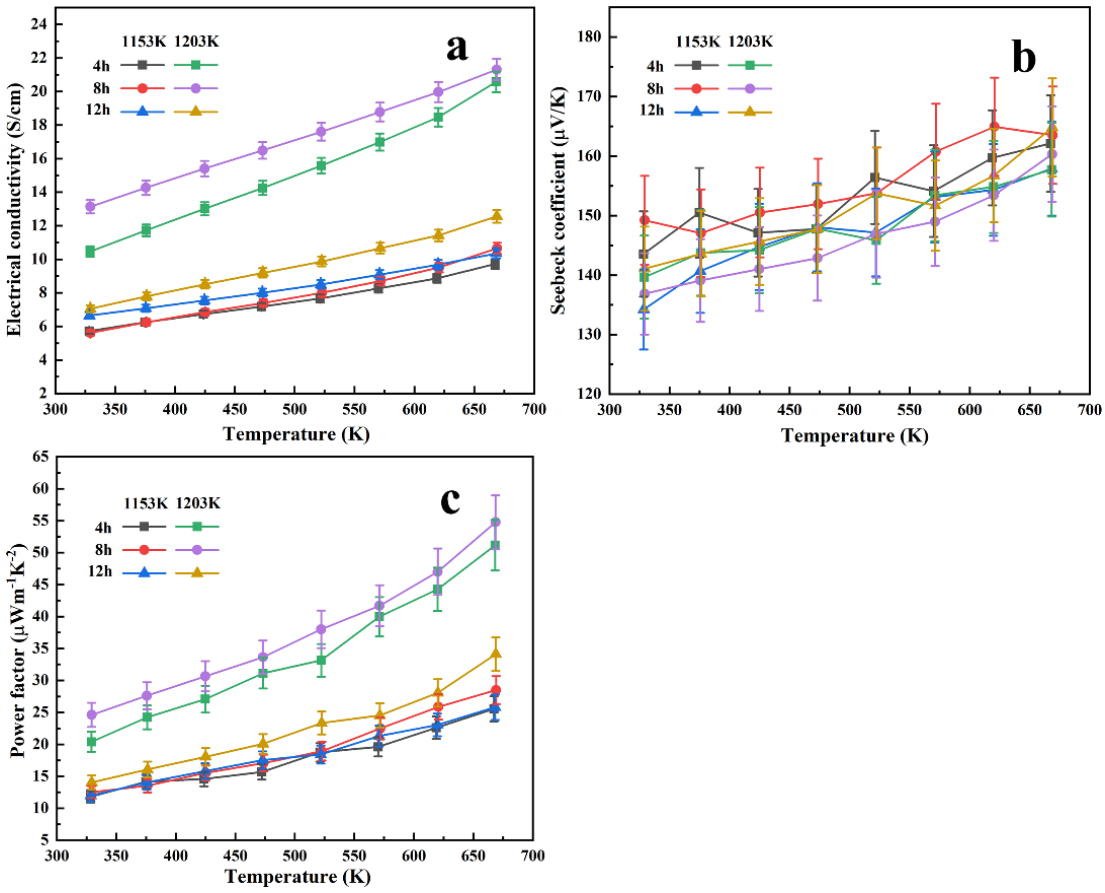

Fig. 4.24 Electrical conductivity (a), Seebeck coefficient (b) and power factor (c) of $Ca_{2.7}Bi_{0.3}Co_yO_{9+\delta}$ thick films sintered at 1153 and 1203 K for 4-12 h as a function of temperature

Fig. 4.25 shows the electrical conductivity (σ) and Seebeck coefficient (S) at 323K for $Ca_{2.7}Bi_{0.3}Co_yO_{9+\delta}$ thick films sintered at different temperatures as a function of dwelling time. It is clear that σ for samples sintered at 1153 K slightly increases with increasing dwelling time. By contrast, σ peaks in the sample sintered at 1203 K for 8 h, followed by an obvious decrease with the dwelling time up to 12 h. The S values are quite similar except for the samples sintered for 8 h. The enhancement in σ and decrease in S for the sample sintered at 1203 K for 8 h should be mainly ascribed to the suppression of the secondary phases, which increases the fractions of calcium cobaltite and decreases the energy barriers at grain boundaries.

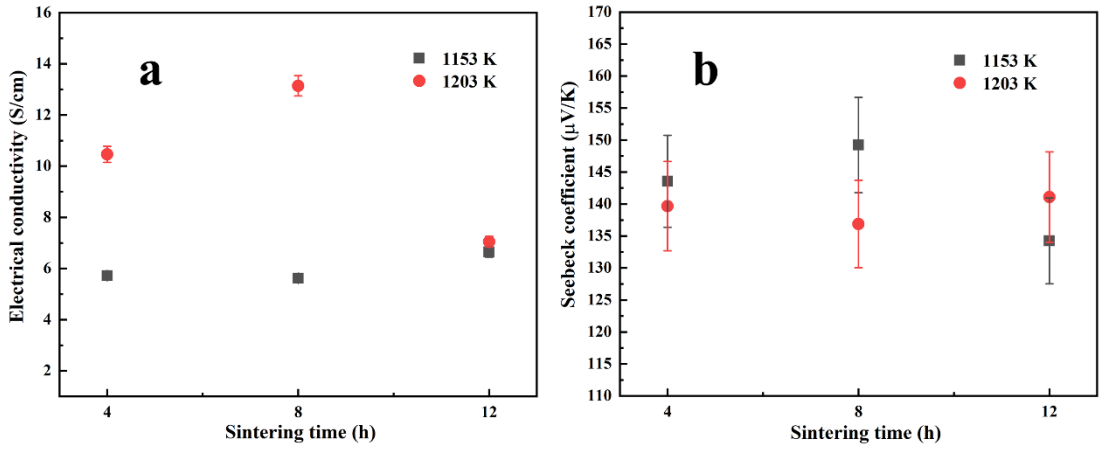

Fig. 4.25 Electrical conductivity (a) and Seebeck coefficient (b) at 323 K for $Ca_{2.7}Bi_{0.3}Co_yO_{9+\delta}$ thick films sintered at different temperature as a function of dwelling time

4.6 Summary

In this chapter, the effects of cobalt deficiency on electrical transport properties of $Ca_{2.7}Bi_{0.3}Co_yO_{9+\delta}$ (y = 3.92, 3.96 and 4.0) ceramics prepared by solid state reaction were studied and then the influence of sintering conditions on electrical transport properties of the screen printed thick films prepared with the optimal composition ($Ca_{2.7}Bi_{0.3}Co_{3.92}O_{9+\delta}$) was investigated. This work provides a practical approach to modulating electrical transport by optimising the sintering conditions for thick film preparation.

For sintered calcium cobaltite ceramics, it was found that by 10.0 at.% substitution of Ca^{2+} by Bi^{3+}, the lattice parameters were increased. By introducing 2.0 at.% cobalt deficiency, the poorly conducting secondary phases were efficiently reduced. Overall, the carrier mobility was significantly increased mainly due to the decrease of porosity and limited content of secondary phases. The highest power factor of 98.0 $\mu Wm^{-1}K^{-2}$ was achieved for $Ca_{2.7}Bi_{0.3}Co_{3.92}O_{9+\delta}$ ceramics at 823 K because of the enhanced electrical conductivity, showing about 20.0 % enhancement over previous studies regarding calcium cobaltite prepared by solid state reaction.

For sintered $Ca_{2.7}Bi_{0.3}Co_{3.92}O_{9+\delta}$ thick films, the single-phase samples sintered at 1203 K for 8 h show the highest volume fractions of the primary phase (calcium cobaltite), thereby providing best electrical conduction. Meanwhile, the strong texture, along with larger grain size, helped to reduce the energy barriers at grain boundaries, thereby increasing carrier mobility. The investigation on the fracture surface morphology showed an order-disorder structural transition near the interface between the film and substrate. A grain growth

mechanism was proposed to explain constrained sintering effects brought by the tensile stresses from the substrate. As a result, the highest power factor of 55.5 $\mu Wm^{-1}K^{-2}$ was achieved for $Ca_{2.7}Bi_{0.3}Co_{3.92}O_{9+\delta}$ thick films at 673 K by the control of microstructure.

References

[1] C.H. Lim, W.S. Seo, S. Lee, Y.S. Lim, J.Y. Kim, H.H. Park, S.M. Choi, K.H. Lee, K. Park, Anisotropy of the thermoelectric figure of merit (ZT) in textured $Ca_3Co_4O_9$ ceramics prepared by using a spark plasma sintering process, J. Korean Phys. Soc. 66 (2015) 794–799.

[2] J.Y. Cho, O.J. Kwon, Y.K. Chung, J.S. Kim, W.S. Kim, K.J. Song, C. Park, Effect of Trivalent Bi Doping on the Seebeck Coefficientand Electrical Resistivity of $Ca_3Co_4O_9$, J. Electron. Mater. 44 (2015) 3621–3626.

[3] D. Moser, L. Karvonen, S. Populoh, M. Trottmann, A. Weidenkaff, Influence of the oxygen content on thermoelectric properties of $Ca_{3-x}Bi_xCo_4O_{9+\delta}$ system, Solid State Sci. 13 (2011) 2160–2164.

[4] C. Boyle, P. Carvillo, Y. Chen, E.J. Barbero, D. Mcintyre, X. Song, Grain boundary segregation and thermoelectric performance enhancement of bismuth doped calcium cobaltite, J. Eur. Ceram. Soc. 36 (2016) 601–607.

[5] G. Constantinescu, S. Rasekh, M.A. Torres, J.C. Diez, M.A. Madre, A. Sotelo, Effect of Sr substitution for Ca on the $Ca_3Co_4O_9$ thermoelectric properties, J. Alloys Compd. 577 (2013) 511–515.

[6] F. Delorme, C.F. Martin, P. Marudhachalam, D. Ovono Ovono, G. Guzman, Effect of Ca substitution by Sr on the thermoelectric properties of $Ca_3Co_4O_9$ ceramics, J. Alloys Compd. 509 (2011) 2311–2315.

[7] Y. Liu, Y. Lin, Z. Shi, C.W. Nan, Z. Shen, Preparation of $Ca_3Co_4O_9$ and Improvement of its Thermoelectric Properties by Spark Plasma Sintering, J. Am. Ceram. Soc. 88 (2005) 1337–1340.

[8] Y. Miyazaki, M. Onoda, T. Oku, M. Kikuchi, Y. Ishii, Y. Ono, Y. Morii, T. Kajitani, Modulated Structure of the Thermoelectric Compound $[Ca_2CoO_3]_{0.62}CoO_2$, J. Phys. Soc. Japan. 71 (2002) 491–497.

[9] J. Fleurial, G.J. Snyder, J.A. Herman, P.H. Giauque, W.M. Phillips, M.A. Ryan, P. Shakkottai, E.A. Kolawa, M.A. Nicolet, Thick-film thermoelectric microdevices, in: Eighteenth Int. Conf. Thermoelectr. Proceedings, ICT'99 (Cat. No.99TH8407) (1999) 294–300.

[10] G.C. Dubey, Application of thick film techniques to the manufacture of solar cells, Sol. Cells. 15 (1985) 1–25.

[11] M.A. Torres, M. Mora, H. Amaveda, M.A. Madre, A. Sotelo, Effect of substrate on the microstructure and thermoelectric performances of Sr-doped $Ca_3Co_4O_9$ thick films, Ceram. Int. 45 (2019) 5431–5435.

[12] W.H. Yoon, J. Ryu, J.J. Choi, B.D. Hahn, J.H. Choi, B.K. Lee, J.H. Cho, D.S. Park, Enhanced Thermoelectric Properties of Textured $Ca_3Co_4O_9$ Thick Film by Aerosol Deposition, J. Am. Ceram. Soc. 93 (2010) 2125–2127.

[13] M. Mora, H. Amaveda, M.A. Torres, M.A. Madre, S. Marinel, A. Sotelo, Enhancement of electrical conductivity of $Ca_{2.93}Sr_{0.07}Co_4O_9$ thick films via hot uniaxial pressing, Int. J. Appl. Ceram. Technol. 17 (2020) 1322–1327.

[14] Y. Nakamura, Y. Matsufuji, M. Inoue, Fabrication and properties of thermoelectric oxide thick films deposited with aerosol deposition method, J. Phys. Conf. Ser. 352 (2012) 12026.

[15] R. Rudež, P. Markowski, M. Presečnik, M. Košir, A. Dziedzic, S. Bernik, Development of thick-film thermoelectric microgenerators based on p-type $Ca_3Co_4O_9$ and n-type $(ZnO)_5In_2O_3$ legs, Ceram. Int. 41 (2015) 13201–13209.

[16] N. Van Nong, A.J. Samson, N. Pryds, S. Linderoth, Microstructure and Thermoelectric Properties of Screen-Printed Thick Films of Misfit-Layered Cobalt Oxides with Ag Addition, J. Electron. Mater. 41 (2012) 1280–1285.

[17] Z. Shi, F. Gao, J. Zhu, J. Xu, Y. Zhang, T. Gao, M. Qin, Influence of liquid−phase sintering on microstructure and thermoelectric properties of $Ca_3Co_4O_9$−based ceramics with Bi_2O_3 additive, J. Mater. 5 (2019) 711–720.

[18] J. Yu, K. Chen, F. Azough, D.T. Alvarez-Ruiz, M.J. Reece, R. Freer, Enhancing the Thermoelectric Performance of Calcium Cobaltite Ceramics by Tuning Composition and Processing, ACS Appl. Mater. Interfaces. 12 (2020) 47634–47646.

[19] B. Paul, J.L. Schroeder, S. Kerdsongpanya, N. Van Nong, N. Schell, D. Ostach, J. Lu,

J. Birch, P. Eklund, Mechanism of Formation of the Thermoelectric Layered Cobaltate $Ca_3Co_4O_9$ by Annealing of CaO–CoO Thin Films, Adv. Electron. Mater. 1 (2015) 1400022.

[20] L. Zhang, T.T. Tan, S. Li, The effect of annealing oxygen concentration in the transformation of Ca_xCoO_2 to thermoelectric $Ca_3Co_4O_9$, RSC Adv. 5 (2015) 28158–28162.

[21] D. Grebille, S. Lambert, F. Bouree, V. Petricek, Contribution of powder diffraction for structure refinements of aperiodic misfit cobalt oxides, J. Appl. Crystallogr. 37 (2004) 823–831.

[22] I. V Matsukevich, A.I. Klyndyuk, E.A. Tugova, A.N. Kovalenko, A.A. Marova, N.S. Krasutskaya, Thermoelectric properties of $Ca_{3-x}Bi_xCo_4O_{9+\delta}$ ($0.0 \leqslant x \leqslant 1.5$) ceramics, Inorg. Mater. 52 (2016) 593–599.

[23] J.C. Diez, M.A. Torres, S. Rasekh, G. Constantinescu, M.A. Madre, A. Sotelo, Enhancement of $Ca_3Co_4O_9$ thermoelectric properties by Cr for Co substitution, Ceram. Int. 39 (2013) 6051–6056.

[24] A. Sotelo, F.M. Costa, N.M. Ferreira, A. Kovalevsky, M.C. Ferro, V.S. Amaral, J.S. Amaral, S. Rasekh, M.A. Torres, M.A. Madre, J.C. Diez, Tailoring $Ca_3Co_4O_9$ microstructure and performances using a transient liquid phase sintering additive, J. Eur. Ceram. Soc. 36 (2016) 1025–1032.

[25] A. Sotelo, S. Rasekh, M.A. Torres, P. Bosque, M.A. Madre, J.C. Diez, Effect of synthesis methods on the $Ca_3Co_4O_9$ thermoelectric ceramic performances, J. Solid State Chem. 221 (2015) 247–254.

[26] D.O. Demchenko, D.B. Ameen, Lattice thermal conductivity in bulk and nanosheet Na_xCoO_2, Comput. Mater. Sci. 82 (2014) 219–225.

[27] W. Seo, S. Lee, Y. Lee, M. Lee, Y. Masuda, K. Koumoto, High-resolution transmission electron microscopy study of $Ca_3Co_4O_9$, Microscopy. 53 (2004) 397–401.

[28] K. Yubuta, X. Huang, Y. Miyazaki, T. Kajitani, High-Resolution Electron Microscopy Study of $[(Ca, Bi)_2CoO_3]_{0.62}CoO_2$, J. Phys. Soc. Japan. 77 (2008) 94603.

[29] T. Yin, D. Liu, Y. Ou, F. Ma, S. Xie, J.F. Li, J. Li, Nanocrystalline Thermoelectric $Ca_3Co_4O_9$ Ceramics by Sol−Gel Based Electrospinning and Spark Plasma Sintering,

J. Phys. Chem. C. 114 (2010) 10061–10065.

[30] D. Kenfaui, G. Bonnefont, D. Chateigner, G. Fantozzi, M. Gomina, J.G. Noudem, $Ca_3Co_4O_9$ ceramics consolidated by SPS process: Optimisation of mechanical and thermoelectric properties, Mater. Res. Bull. 45 (2010) 1240–1249.

[31] H. Hao, Q. He, C. Chen, H. Sun, X. Hu, Textured Structure and Anisotropic Thermoelectric Properties of $Ca_{2.7}Bi_{0.3}Co_4O_9$ Oxides Prepared by Conventional Solid-State Reaction, Int. J. Mod. Phys. B. 23 (2009) 87–95.

[32] A. Sotelo, G. Constantinescu, S. Rasekh, M.A. Torres, J.C. Diez, M.A. Madre, Improvement of thermoelectric properties of $Ca_3Co_4O_9$ using soft chemistry synthetic methods, J. Eur. Ceram. Soc. 32 (2012) 2415–2422.

[33] Y. Zhou, I. Matsubara, W. Shin, N. Izu, N. Murayama, Effect of grain size on electric resistivity and thermopower of $(Ca_{2.6}Bi_{0.4})Co_4O_9$ thin films, J. Appl. Phys. 95 (2003) 625–628.

[34] T. Sun, H.H. Hng, Q.Y. Yan, J. Ma, Enhanced high temperature thermoelectric properties of Bi-doped c-axis oriented $Ca_3Co_4O_9$ thin films by pulsed laser deposition, J. Appl. Phys. 108 (2010) 83709.

[35] Y.H. Lin, C.W. Nan, Y. Liu, J. Li, T. Mizokawa, Z. Shen, High-Temperature Electrical Transport and Thermoelectric Power of Partially Substituted $Ca_3Co_4O_9$-Based Ceramics, J. Am. Ceram. Soc. 90 (2007) 132–136.

[36] Y. Wang, Y. Sui, P. Ren, L. Wang, X. Wang, W. Su, H. Fan, Strongly Correlated Properties and Enhanced Thermoelectric Response in $Ca_3Co_{4-x}M_xO_9$ (M = Fe, Mn, and Cu), Chem. Mater. 22 (2010) 1155–1163.

[37] B.C. Zhao, Y.P. Sun, W.J. Lu, X.B. Zhu, W.H. Song, Enhanced spin fluctuations in $Ca_3Co_{4-x}Ti_xO_9$ single crystals, Phys. Rev. B. 74 (2006) 144417.

[38] H. Taguchi, M. Sonoda, M. Nagao, Relationship between Angles for Mn–O–Mn and Electrical Properties of Orthorhombic Perovskite-Type $(Ca_{1-x}Sr_x)MnO_3$, J. Solid State Chem. 137 (1998) 82–86.

[39] D. Srivastava, C. Norman, F. Azough, M.C. Schäfer, E. Guilmeau, D. Kepaptsoglou, Q.M. Ramasse, G. Nicotra, R. Freer, Tuning the thermoelectric properties of A-site deficient $SrTiO_3$ ceramics by vacancies and carrier concentration, Phys. Chem. Chem. Phys. 18 (2016) 26475–26486.

[40] Y. Liu, L. Zhang, S.E. Shirsath, J. Zheng, Y. Liu, C. Ulrich, S. Li, Manipulation of charge carrier concentration and phonon scattering via spin-entropy and size effects: Investigation of thermoelectric transport properties in La-doped $Ca_3Co_4O_9$, J. Alloys Compd. 801 (2019) 60–69.

[41] S. Porokhin, L. Shvanskaya, V. Khovaylo, A. Vasiliev, Effect of NaF doping on the thermoelectric properties of $Ca_3Co_4O_9$, J. Alloys Compd. 695 (2017) 2844–2849.

[42] X. Zhu, D. Shi, S. Dou, Y. Sun, Q. Li, L. Wang, W. Li, W. Yeoh, R. Zheng, Z. Chen, C. Kong, (00l)-oriented $Bi_2Sr_2Co_2O_y$ and $Ca_3Co_4O_9$ films: Self-assembly orientation and growth mechanism by chemical solution deposition, Acta Mater. 58 (2010) 4281–4291.

[43] J. Zeng, Y. Li, Q. Yang, X. Jing, Q. Yin, Grain oriented $CaBi_4Ti_4O_{15}$ piezoceramics prepared by the screen-printing multilayer grain growth technique, J. Eur. Ceram. Soc. 25 (2005) 2727–2730.

[44] Y. Li, C. Hui, M. Wu, Y. Li, Y. Wang, Textured $(K_{0.5}Na_{0.5})NbO_3$ ceramics prepared by screen-printing multilayer grain growth technique, Ceram. Int. 38 (2012) S283–S286.

[45] N. Kulwongwit, P-type, Misfit Layered Structure Cobaltite for Thermoelectric Applications, Ph. D. Thesis, The University of Manchester (United Kingdom), 2017.

[46] E.M. Jakubczyk, A. Mapp, C.C. Chung, C.L. Sansom, J.L. Jones, R.A. Dorey, Enhancing thermoelectric properties of $NaCo_2O_4$ ceramics through Na pre-treatment induced nano-decoration, J. Alloys Compd. 788 (2019) 91–101.

[47] Z. Shi, J. Xu, J. Zhu, Y. Zhang, T. Gao, M. Qin, H. Sun, G. Dong, F. Gao, Effect of platelet template seeds on microstructure and thermoelectric properties of $Ca_3Co_4O_9$ ceramics, Ceram. Int. 45 (2019) 1977–1983.

[48] Z. Shi, T. Su, P. Zhang, Z. Lou, M. Qin, T. Gao, J. Xu, J. Zhu, F. Gao, Enhanced thermoelectric performance of $Ca_3Co_4O_9$ ceramics through grain orientation and interface modulation, J. Mater. Chem. A. 8 (2020) 19561–19572.

[49] S. Skirl, M. Hoffman, K. Bowman, S. Wiederhorn, J. Rödel, Thermal expansion behavior and macrostrain of Al_2O_3/Al composites with interpenetrating networks, Acta Mater. 46 (1998) 2493–2499.

[50] D.J. Green, O. Guillon, J. Rödel, Constrained sintering: A delicate balance of scales,

J. Eur. Ceram. Soc. 28 (2008) 1451–1466.

[51] M. Tillman, J.A. Yeomans, R.A. Dorey, The effect of a constraint on the sintering and stress development in alumina thick films, Ceram. Int. 40 (2014) 9715–9721.

[52] H. Ibach, The role of surface stress in reconstruction, epitaxial growth and stabilization of mesoscopic structures, Surf. Sci. Rep. 29 (1997) 195–263.

[53] Y. Huang, B. Zhao, S. Lin, R. Ang, Y. Sun, Enhanced Thermoelectric Performance Induced by Cr Doping at Ca-Sites in $Ca_3Co_4O_9$ System, J. Am. Ceram. Soc. 97 (2014) 3589–3596.

[54] K. Park, D.A. Hakeem, J.S. Cha, Synthesis and structural properties of thermoelectric $Ca_{3-x}Ag_xCo_4O_{9+\delta}$ powders, Dalt. Trans. 45 (2016) 6990–6997.

[55] H. Liu, G.C. Lin, X.D. Ding, J.X. Zhang, Mechanical relaxation in thermoelectric oxide $Ca_{3-x}Sr_xCo_4O_{9+\delta}$ (x = 0, 0.25, 0.5, 1.0) associated with oxygen vacancies, J. Solid State Chem. 200 (2013) 305–309.

[56] Z.Y. Liu, F.P. Zhang, J.X. Zhang, X. Zhang, Q.M. Lu, X.Y. Yang, Enhanced electrical transport by texture modulation and co-doping for $Ca_3Co_4O_{9+\delta}$ materials, Results Phys. 6 (2016) 203–208.

5. Enhancing Thermoelectric Performance of Calcium Cobaltite Ceramics by Optimising Chemical Composition and the Annealing Process

5.1 Introduction

In Chapter 4, the Co-containing secondary phases in calcium cobaltite prepared by solid state reaction were successfully reduced through increasing cobalt deficiency, whereas minor amounts of Bi-rich phases were still detected in sintered $Ca_{2.7}Bi_{0.3}Co_yO_{9+\delta}$ ceramics, which suggests excessive Bi_2O_3 addition during the sample preparation. Furthermore, the decomposition of $Ca_3Co_4O_9$ will occur above 1203 K, but its eutectic temperature is around 1623 K [1]. This problem in combination with the intrinsically layered structure of calcium cobaltite drastically limits densification, thereby leading to the low density for solid state synthesized samples. Indeed, the investigation of $Ca_{2.7}Bi_{0.3}Co_{3.92}O_{9+\delta}$ thick films demonstrated that texture development enables enhanced carrier mobility by reducing grain boundary density, thereby providing an opportunity to tailor electrical transport by grain boundary engineering.

Currently, many techniques, including laser floating zone melting [2], uniaxial high-pressure synthesis [3], hot pressing [4], and spark plasma sintering (SPS) are employed to fabricate highly dense calcium cobaltite with strong texture. By aligning conducting *ab* planes with the direction of current flow and creating close connection between grains under pressure, the electrical conductivity is significantly improved due to increased carrier mobility. In addition, an annealing process is frequently used to ensure the formation of primary phase ($Ca_3Co_4O_9$) and the chemical homogeneity of the synthesized materials [5–7], thereby modifying the electrical transport properties.

In the present chapter, $Ca_{3-x}Bi_xCo_{3.92}O_{9+\delta}$ (x = 0.1, 0.2, 0.3) and $Ca_{2.7}Bi_{0.3}Co_yO_{9+\delta}$ (y = 3.92, 3.96 and 4.0) ceramics were prepared by spark plasma sintering with the aims of introducing texture and yielding higher density. The effects of chemical compositions and heat-treatment on the thermoelectric performance of calcium cobaltite were studied in detail. Chemical compositions and annealing process were found to take important roles in determining crystal and microstructural evolution. By optimising bismuth substitution, cobalt content and annealing conditions, the power factor was significantly enhanced and the thermal conductivity was reduced.

5.2 $Ca_{3-x}Bi_xCo_yO_{9+\delta}$ Ceramics Prepared by the SPS Route

5.2.1 Density

Fig. 5.1 shows the bulk and relative density of $Ca_{3-x}Bi_xCo_yO_{9+\delta}$ ceramics prepared by the SPS route as a function of bismuth and cobalt content. It can be seen that the bulk density of SPS-processed calcium cobaltite varies slightly from 4.02 to 4.26 g/cm^3 (86.1-91.2 % theoretical) but in spite of uncertainties in the data, there is still about 20 % increase compared to density of calcium cobaltite prepared by solid state reaction (Fig. 4.5(a)). This could be ascribed to higher densification induced by the SPS process involving high pressure and high temperature. In general, the density of calcium cobaltite increases slightly with increasing bismuth content, whilst the effects of the cobalt deficiency are not pronounced. The porosity in all samples is very small (no more than 6 %).

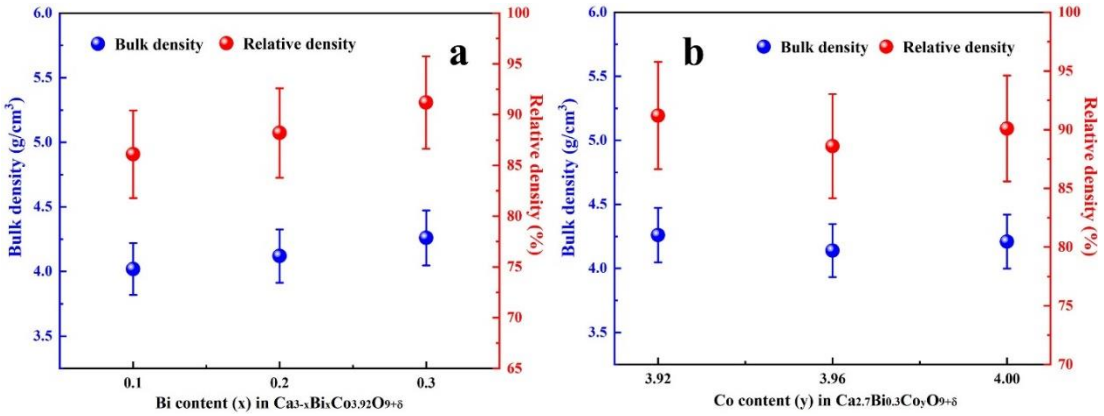

Fig. 5.1 Density of $Ca_{3-x}Bi_xCo_yO_{9+\delta}$ ceramics prepared by the SPS route as a function of (a) bismuth and (b) cobalt content

5.2.2 XRD Analysis

XRD patterns of $Ca_{3-x}Bi_xCo_yO_{9+\delta}$ ceramics prepared by the SPS route are presented in Fig. 5.2; the main phase is indexed as $Ca_3Co_{3.744}O_{9.176}$ (JCPDS: # 05-001-0461). However, traces of minor secondary phases ($Ca_3Co_2O_6$, $Bi_2Ca_3Co_2O_9$ or Co_3O_4) can still be observed in all compositions. These results are in good agreement with earlier studies, where the formation of Ca-rich phase [8,9], Bi-rich phase [10,11] and Co-rich phase [12] were detected in Sr doped, Cr doped and Bi doped calcium cobaltite, respectively. Notably, with the bismuth content rising from 0.1 to 0.3, the normalized intensity of $Bi_2Ca_3Co_2O_9$ phase shows an increase, whilst that of $Ca_3Co_2O_6$ phase shows a decline, which indicates that the formation of secondary phases is more sensitive to the bismuth substitution. The detailed information for (003) reflection peaks in the 2θ range (24.0 to 25.5 degrees; Fig. 5.2(b)) illustrates the

peak shift dependence on bismuth and cobalt content. Different from the behaviour in Fig. 4.6, the position of (003) peaks here shows negligible change with cobalt deficiency, indicating that the SPS method enables greater chemical homogeneity than the classical solid state reaction method. By contrast, the shifts of (003) peaks towards lower angles increases with increasing bismuth content. This is attributed to the expansion of lattice parameter *c* induced by bismuth substitution, according to Equation (4.1).

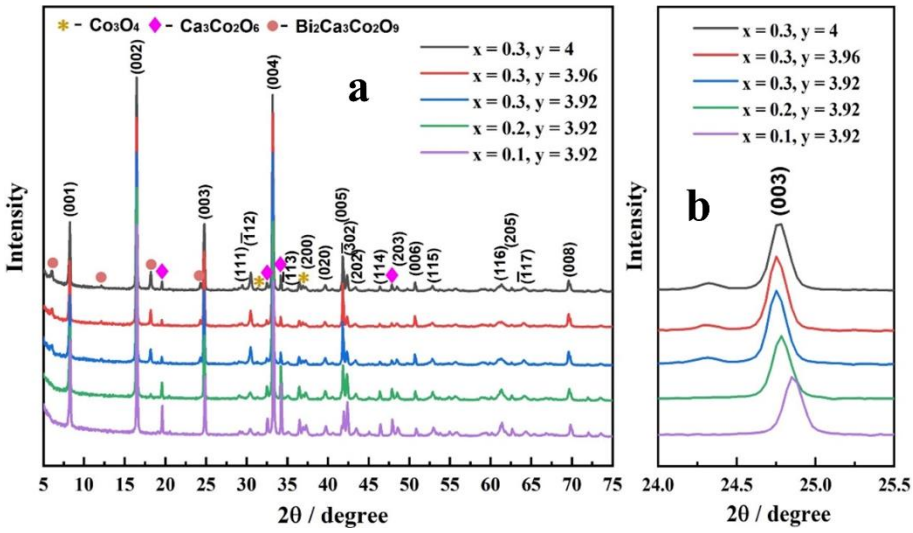

Fig. 5.2 XRD patterns of $Ca_{3-x}Bi_xCo_yO_{9+\delta}$ ceramics prepared by the SPS route (a. overall view, b. enlarged region)

5.2.3 SEM-EDS Analysis

Fig. 5.3 displays backscattered electron SEM images of polished surfaces for $Ca_{3-x}Bi_xCo_yO_{9+\delta}$ ceramics prepared by the SPS route. Based on earlier studies [13,14] and the XRD patterns in Fig. 5.2, most phases can be readily distinguished: (i) plate-like grains (main phase: $Ca_3Co_4O_9$) and (ii) minor irregular shaped grains (bright phases highlighted in red colour: $Bi_2Ca_3Co_2O_9$; dark phases highlighted in orange colour: $Ca_3Co_2O_6$; grey phases highlighted in pink colour: Co_3O_4). The average grain size is almost constant (about 5.5 μm), regardless of cobalt deficiency. However, grain size decreases to 4.3 μm for the lower bismuth content of 0.1, indicating that high fractions of Bi_2O_3 addition help to accelerate grain growth.

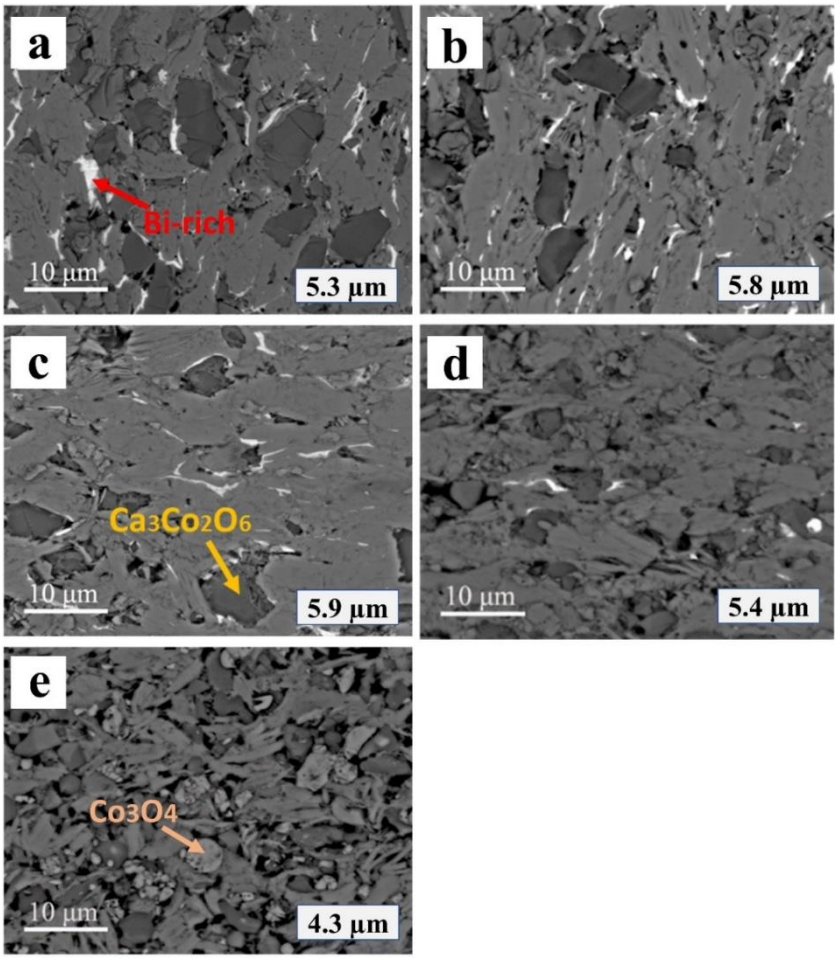

Fig. 5.3 Backscattered electron SEM images of polished surfaces for $Ca_{2.7}Bi_{0.3}Co_yO_{9+\delta}$ ceramics (a-c: y = 4.0, 3.96 and 3.92, respectively) and $Ca_{3-x}Bi_xCo_{3.92}O_{9+\delta}$ ceramics (c-e: x = 0.3, 0.2 and 0.1, respectively) prepared by the SPS route

The volume fractions of the different phases visible in Fig. 5.3 are shown in Table 5.1. Although the content of the primary phase ($Ca_3Co_4O_9$) increases slightly with increasing bismuth content and cobalt deficiency, the value only reaches 46-64 % of the total. The volume fractions of Co-containing secondary phases, including $Ca_3Co_2O_6$ and Co_3O_4, vary from 25-33 % and 7-21 %, respectively, independent of bismuth and cobalt content. By contrast, the fractions of $Bi_2Ca_3Co_2O_9$ tend to increase with the bismuth content; the maximum value of about 6 % is achieved for samples with x = 0.3. Low volume fractions of the primary phase in these samples are attributed to development of considerable amounts of secondary phases in the calcined calcium cobaltite powders (Fig. 4.4). Spark plasma sintering was conducted at 1023 K for 5 min; such sintering conditions are possibly inadequate to achieve complete reaction to form calcium cobaltite. Furthermore, the calcined powders were sealed in a graphite die and subject to a vacuum atmosphere; this reducing atmosphere might give rise to reduction reactions among different chemicals.

Table 5.1 Volume fractions of phases in SPS-processed $Ca_{3-x}Bi_xCo_yO_{9+\delta}$ ceramics

x	y	$Ca_3Co_4O_9$ (vol.%)	$Ca_3Co_2O_6$ (vol.%)	$Bi_2Ca_3Co_2O_9$ (vol.%)	Co_3O_4 (vol.%)
0.1	3.92	46.3	32.8	0	20.9
0.2	3.92	57.3	24.7	1.2	16.8
0.3	3.92	64.2	24.9	3.7	7.2
0.3	3.96	55.1	28.8	5.2	11.9
0.3	4.00	51.8	31.9	6.3	10.0

To determine the chemical compositions of secondary phases, EDS point and mapping analyses were carried out on the polished surface of SPS-processed $Ca_{2.7}Bi_{0.3}Co_{3.92}O_{9+\delta}$ ceramic as a representative of the group. Fig. 5.4 shows compositional distributions of four elements (Ca, Bi, Co and O); three secondary phases (Ca-rich, Bi-rich and Co-rich phases) are distinguished (highlighted by orange arrows), in good agreement with XRD results (Fig. 5.2). The point analyses of different sites (sites 1-3) in Fig. 5.4 are summarised in Table 5.2. The estimated atomic ratio of Ca/Bi/Co for the bright phase (site 1) is 3:2:4, which is close to $Bi_2Ca_3Co_2O_9$. The dark phase (site 2) with Ca/Co ratio of 3:2 is inferred to be $Ca_3Co_2O_6$. The grey phase (site 3) has a Co/O ratio of 3:4, indicating the presence of Co_3O_4. Indeed, the detailed atomic ratio for site 3 indicates that there is limited solubility of Ca in Co_3O_4.

EDS point analyses for the main phase in $Ca_{2.7}Bi_{0.3}Co_{3.92}O_{9+\delta}$ ceramics prepared by the SPS route are displayed in Fig. 5.5; four sites in two different areas were examined. The chemical compositions of all sites are similar: the r Bi/(Ca+Bi) ratio is approximately 10 at.%, which matches well the target chemical composition ($Ca_{2.7}Bi_{0.3}Co_{3.92}O_{9+\delta}$). Furthermore, the presence of large amounts of Bi-rich secondary phases (Fig 5.2 and 5.3), suggests the Bi solubility limit to be about 10 at.% in the original SPS-processed calcium cobaltite samples.

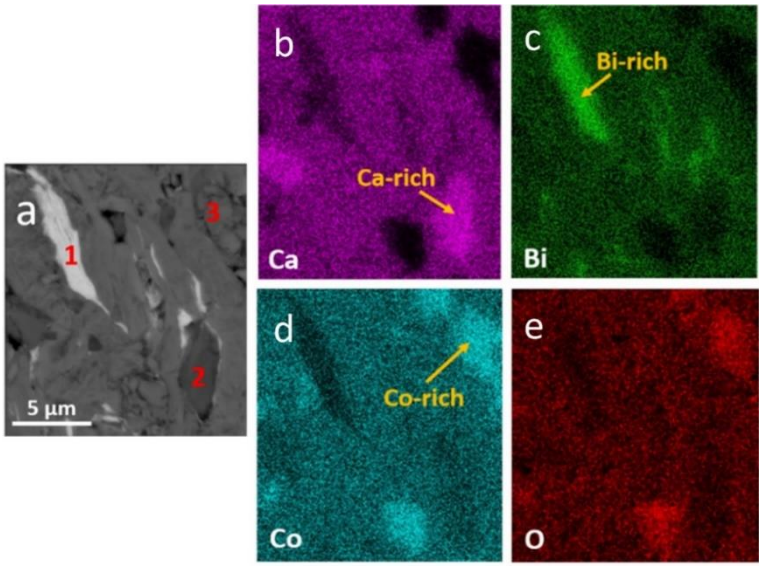

Fig. 5.4 EDS mapping data for the polished surfaces of $Ca_{2.7}Bi_{0.3}Co_{3.92}O_{9+\delta}$ ceramics prepared by the SPS route

Table 5.2 EDS point analysis for sites 1-3 in the surface of $Ca_{2.7}Bi_{0.3}Co_{3.92}O_{9+\delta}$ in the SEM image (Fig. 5.4)

Sites	Elements				Calculated Compositions
	Ca (at.%)	Bi (at.%)	Co (at.%)	O (at.%)	
1	13.0	10.0	16.2	60.8	$Ca_3Bi_2Co_4O_{14}$
2	22.9	0.8	16.3	60.0	$(Ca,Bi)_3Co_2O_7$
3	1.2	0	43.1	55.7	$(Ca,Co)_3O_4$

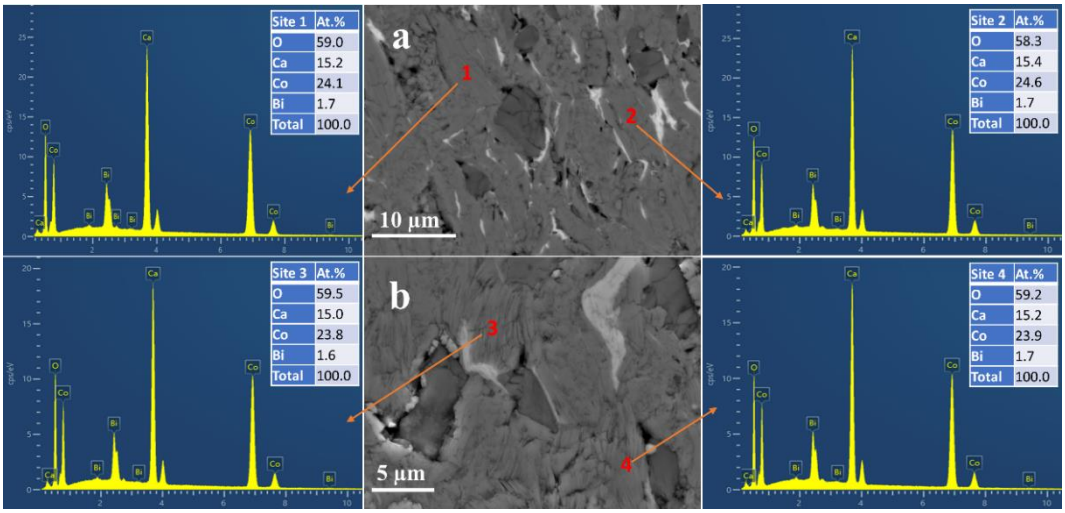

Fig. 5.5 EDS point analyses for the main phase in $Ca_{2.7}Bi_{0.3}Co_{3.92}O_{9+\delta}$ ceramics prepared by the SPS route

5.2.4 XPS Analysis

Fig. 5.6 shows XPS survey spectra for $Ca_{3-x}Bi_xCo_yO_{9+\delta}$ ceramics prepared by the SPS route. It can be seen that peaks belonging to oxidation states of Ca, Bi, Co and O atoms are revealed in addition to the C 1s peak (carbon contamination is commonly encountered in XPS characterisation). The elemental constituents are consistent with target compositions, indicating high elemental purity of sintered ceramics.

The high resolution core-level spectra of Co 2p 3/2 for $Ca_{3-x}Bi_xCo_yO_{9+\delta}$ ceramics prepared by the SPS route are illustrated in Fig. 5.7; the concentrations of Co^{3+} and Co^{4+} calculated from XPS data (Fig. 5.7) are shown in Table 5.3. As Fig. 5.7 shows, the Co 2p 3/2 spectra can be deconvoluted into three peaks, where the peaks at 779.01-779.33 eV (in blue colour) correspond to Co^{3+}, the peaks at 780.01-780.33 eV (in green colour) are assigned to Co^{2+} and those between 781.22 and 782.13 eV (in green colour) can be ascribed to Co^{4+}. These results match well with previous work of Park et al. [15], Zhang et al. [16] and Liu et al. [17]. As seen from Table 5.3, the ratios of $Co^{4+}/(Co^{4+}+Co^{3+})$ are similar (about 38.0 %) for all compositions. Although there is a mixed valence of cobalt ions (+2, +3 and +4) in the lattice of calcium cobaltite [18], the detected oxidation states of cobalt can also come from Co-containing secondary phases including Co_3O_4, $Ca_3Co_2O_6$ and $Bi_2Ca_3Co_2O_9$. Therefore, the ratio of $Co^{4+}/(Co^{4+}+Co^{3+})$ in the primary phase ($Ca_3Co_4O_9$) cannot be unambiguously evaluated from the current XPS data.

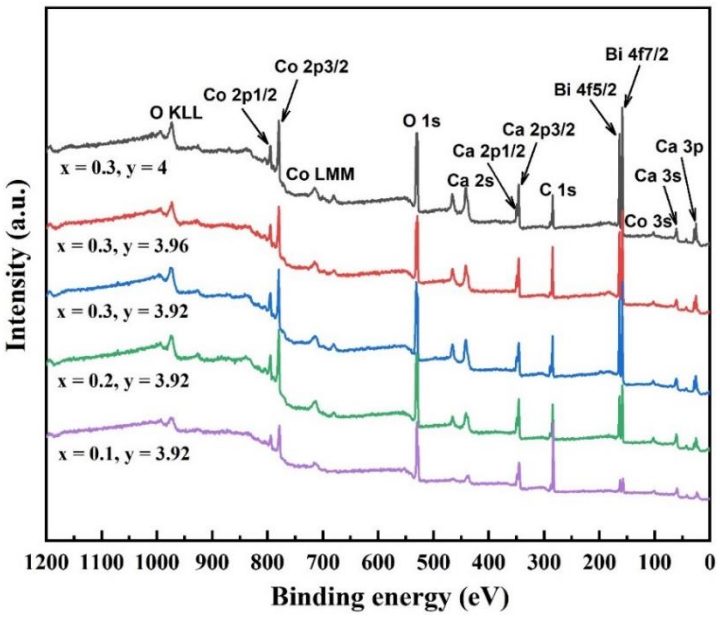

Fig. 5.6 XPS survey spectra for $Ca_{3-x}Bi_xCo_yO_{9+\delta}$ ceramics prepared by the SPS route

Table 5.3 Concentrations of cobalt ions in $Ca_{3-x}Bi_xCo_yO_{9+\delta}$ ceramics prepared by the SPS route

x	y	Co^{3+} (%)	Co^{2+} (%)	Co^{4+} (%)	$Co^{4+}/(Co^{3+}+Co^{4+})$ (%)
0.1	3.92	23.0	63.5	13.5	37.0
0.2	3.92	27.5	55.8	16.7	37.8
0.3	3.92	32.3	46.9	20.8	39.2
0.3	3.96	30.4	49.7	19.9	39.6
0.3	4.00	40.6	33.4	26.0	39.0

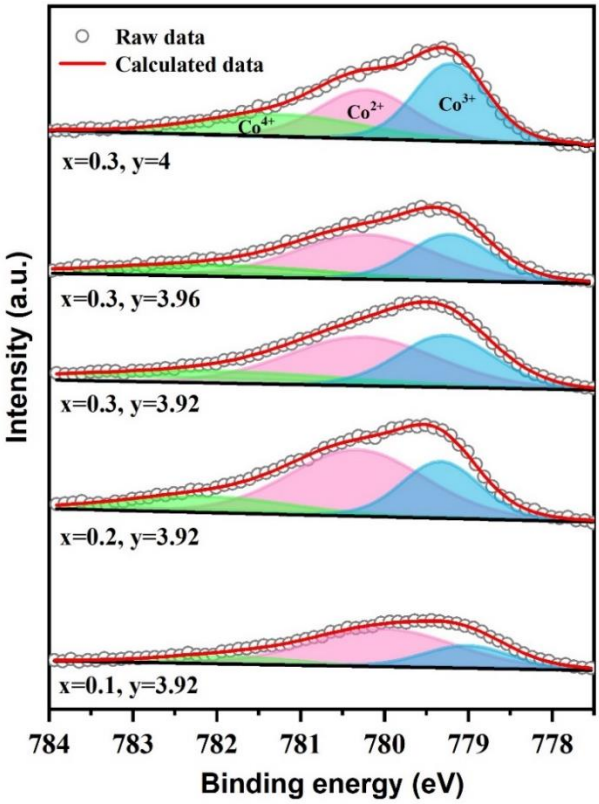

Fig. 5.7 High resolution core-level spectra of Co 2p 3/2 for $Ca_{3-x}Bi_xCo_yO_{9+\delta}$ ceramics prepared by the SPS route

5.2.5 Electrical Transport

Fig. 5.8 demonstrates the electrical transport properties of $Ca_{3-x}Bi_xCo_yO_{9+\delta}$ (x = 0.1-0.3 and y = 3.92-4.0) ceramics prepared by the SPS route. Electrical conductivity (σ) all increases with increasing temperature (Fig. 5.8(a)), indicating semiconducting behaviour. At 823 K σ nearly triples (increases from 15.0 to 47.0 S/cm) as the bismuth content increases from 0.1 to 0.3, whereas σ for 10.0 at.% Bi substituted samples with different cobalt deficiencies show almost no variation (about 47.0 S/cm). This suggests that a higher bismuth substitution gives

rise to higher σ; this increase can be ascribed to the increasing volume fractions of the primary phase ($Ca_3Co_4O_9$) in the matrix (Table 5.1). Bi_2O_3 additions are more likely to induce liquid phase sintering at high temperatures, where the liquid-solid mass transfer mechanism becomes pronounced, which is beneficial to calcium cobaltite formation. When the bismuth content increased from 0.1 to 0.3, the volume fraction of $Ca_3Co_4O_9$ increased from 46.3 % to 64.2 %, whilst fraction of Co_3O_4 fell from 20.9 % to 7.2 %. The room temperature σ follows the sequence: the primary phase (20.0 S/cm [19]) > Bi-rich phase (10.0 S/cm [20]) > Ca-rich phase (7.0 S/cm [21]) > Co_3O_4 (1.0×10^{-4} S/cm [22]). Therefore, a higher volume fraction of the primary phase ($Ca_3Co_4O_9$) enables better conduction [19]. In addition, with enhanced carrier mobility (μ) due to higher density, the σ of highly dense SPS-processed samples (45.0 S/cm at 823 K) does not significantly outperform the solid state synthesized (SSR) samples with high porosity (about 40.0 S/cm at 823 K in Fig. 4.13(a)), which also indicates a lower carrier concentration (n).

The positive values for Seebeck coefficients (S) in all compositions confirm a hole conduction mechanism (Fig. 5.8(b)); S varies from 138.0 to 186.0 μV/K within the temperature range of 323-823 K. Notably, the values for 10 at.% Bi substituted samples with different cobalt deficiencies are stable around 138.0 to 170.0 μV/K. By contrast, S falls from 185.0 to 170.0 μV/K at 823 K with increasing bismuth substitution, suggesting an increased n according to Equation (2.4). Similarly, the overall thermopower values for SPS-processed samples are higher than the values for SSR samples (130.0-160.0 μV/K in Fig. 4.13(b)), confirming that the σ of SPS-processed samples is heavily restricted by the low carrier concentration (n).

As a result, the power factors (Fig. 5.8(c)) increase linearly with increasing bismuth content, reaching the maximum value of 140.0 $\mu Wm^{-1}K^{-2}$ for $Ca_{3-x}Bi_xCo_yO_{9+\delta}$ at 823 K, whereas the effects of changes in cobalt content are negligible. This value of 140.0 $\mu Wm^{-1}K^{-2}$ represents about 40 % enhancement compared to the peak value achieved in $Ca_{3-x}Bi_xCo_yO_{9+\delta}$ ceramic prepared by solid state reaction (98.0 $\mu Wm^{-1}K^{-2}$ at 823 K in Fig. 4.13(c)), mainly due to the higher Seebeck coefficients obtained for the SPS-processed samples.

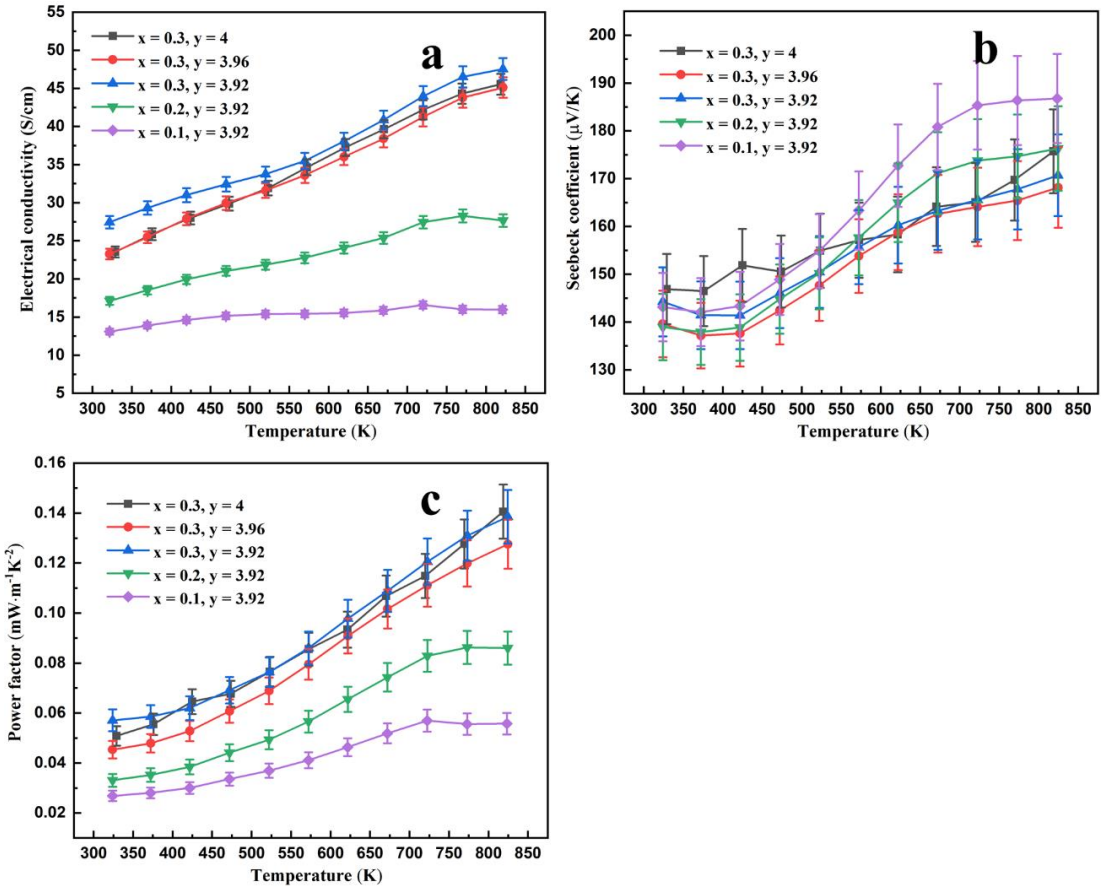

Fig. 5.8 Electrical transport properties of SPS-processed $Ca_{3-x}Bi_xCo_yO_{9+\delta}$ ceramics as a function of temperature (a. electrical conductivity; b. Seebeck coefficient; c. power factor)

Fig. 5.9 shows electrical conductivity (σ) and Seebeck coefficient (S) at 823 K for SPS-processed $Ca_{2.7}Bi_{0.3}Co_yO_{9+\delta}$ ceramics as a function of cobalt content. It is evident that the effects of cobalt deficiency on electrical transport properties of SPS-processed samples are limited. σ only shows a slight increase when the cobalt deficiency increases to 0.08, while S values are quite similar, independent of cobalt content. It is because that the suppression of Co-containing phases caused by increasing cobalt deficiency is not pronounced in original SPS samples.

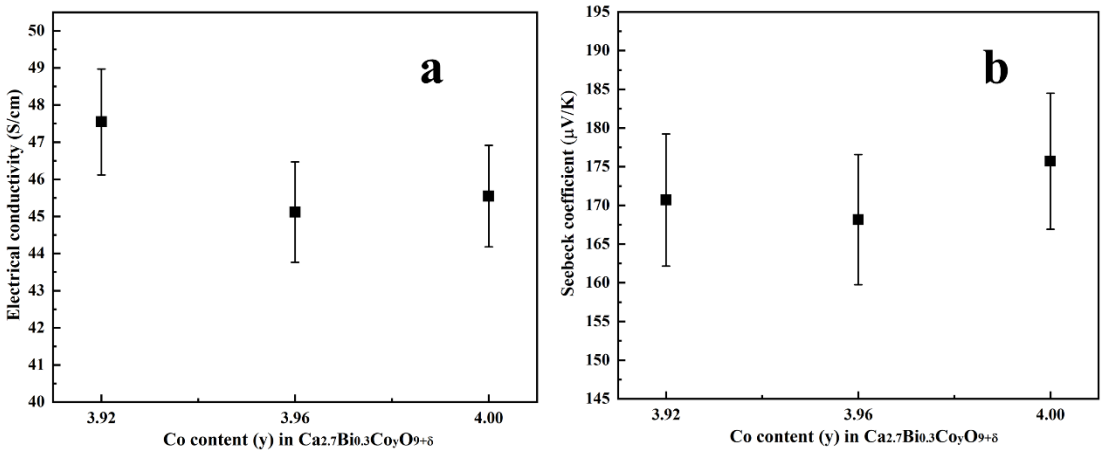

Fig. 5.9 Electrical conductivity (a) and Seebeck coefficient (b) at 823 K for SPS-processed $Ca_{2.7}Bi_{0.3}Co_yO_{9+\delta}$ ceramics as a function of cobalt content

A plot of ln(σT) against reciprocal temperature fitted to the SPHC model according to Equation (2.25) is shown in Fig. 5.10(a). The linear regions above 523 K are consistent with the small polaron hopping conduction mechanism at high temperatures. The calculated activation energies (E_h) (Fig. 5.10(b)) show an increase (66.1-107.9 meV) with increasing bismuth content, while the values for 10 at.% Bi substituted samples are stable at about 107.0 meV, independent of cobalt deficiency. The variation as a function of bismuth content is consistent with data for bismuth doped calcium cobaltite reported by Li et al. [23], which was attributed to the high level of bismuth ions acting as the scattering centres [24].

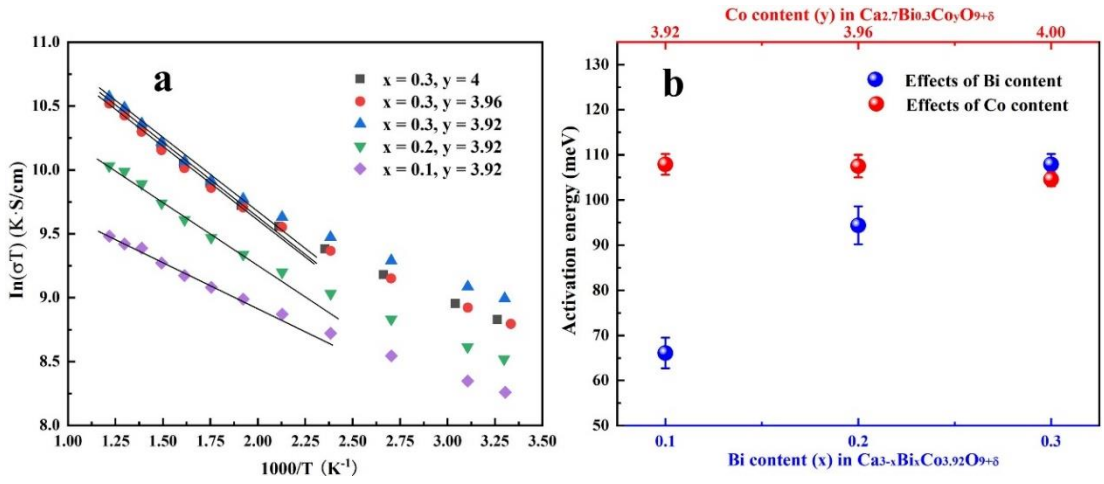

Fig. 5.10 ln(σT) as a function of reciprocal temperature (a) and calculated activation energies (b) for $Ca_{3-x}Bi_xCo_yO_{9+\delta}$ ceramics prepared by the SPS route (The lines are linearly fitted by a least-square method)

5.3 SPS-processed $Ca_{3-x}Bi_xCo_yO_{9+\delta}$ Ceramics Annealed at Different Temperatures

5.3.1 Density

Fig. 5.11 shows the bulk density of SPS-processed $Ca_{3-x}Bi_xCo_yO_{9+\delta}$ ceramics annealed at different temperatures for 12 h. Generally, the SPS-processed samples annealed at 1023 K and 1203 K show bulk densities of 4.11-4.39 g/cm^3 (88.0-93.9 % theoretical) and 4.22-4.51 g/cm^3 (90.4-96.5 % theoretical), respectively. Although densification of the heat-treated ceramics is not significantly influenced by annealing temperature, the densities of samples annealed at 1203 K are higher than the unannealed ones (Fig. 5.1). This is probably related to phase compositional differences and more compact microstructure after heat-treatment. Similar to the density dependence of bismuth and cobalt content for the original SPS-processed samples, the bulk density is positively correlated to bismuth substitution (Fig. 5.1(a)), but is independent of cobalt deficiency (Fig. 5.1(b)).

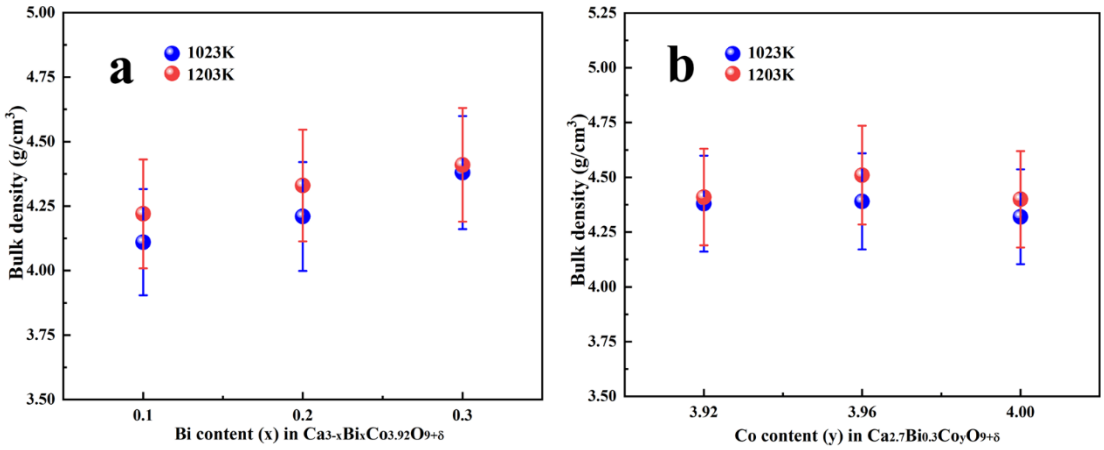

Fig. 5.11 Density of SPS-processed $Ca_{3-x}Bi_xCo_yO_{9+\delta}$ ceramics annealed at different temperatures for 12 h (a. as a function of bismuth content, b. as a function of cobalt content)

5.3.2 XRD Analysis

The XRD patterns of SPS-processed $Ca_{3-x}Bi_xCo_yO_{9+\delta}$ ceramics annealed at different temperatures for 12 h are shown in Fig. 5.12. As expected, the main phase for all annealed samples is indexed as $Ca_3Co_{3.744}O_{9.176}$ (JCPDS: # 05-001-0461). Fig. 5.12(a) shows that traces of secondary phases, including $Ca_3Co_2O_6$, $Bi_2Ca_3Co_2O_9$ and Co_3O_4, are still detected when annealed at 1023 K, although their peak intensities show an obvious decrease compared to the unannealed samples (Fig. 5.2). This suggests that the initial annealing temperature (1023 K) is insufficient for eliminating the secondary phases. By marked

contrast, most secondary phases are absent, except a minor amount of Co_3O_4, when the annealing temperature is increased to 1203 K (Fig. 5.12(b)). A similar phenomenon was reported for pressure-less sintered calcium cobaltite, where $Ca_3Co_2O_6$, CaO, CoO and Co_3O_4 can be transformed into $Ca_3Co_4O_9$ after annealing at 1173 K for 72 h [5]. Hence, it can be concluded that $Ca_3Co_2O_6$ and $Bi_2Ca_3Co_2O_9$ can be efficiently reduced by controlling the annealing temperature.

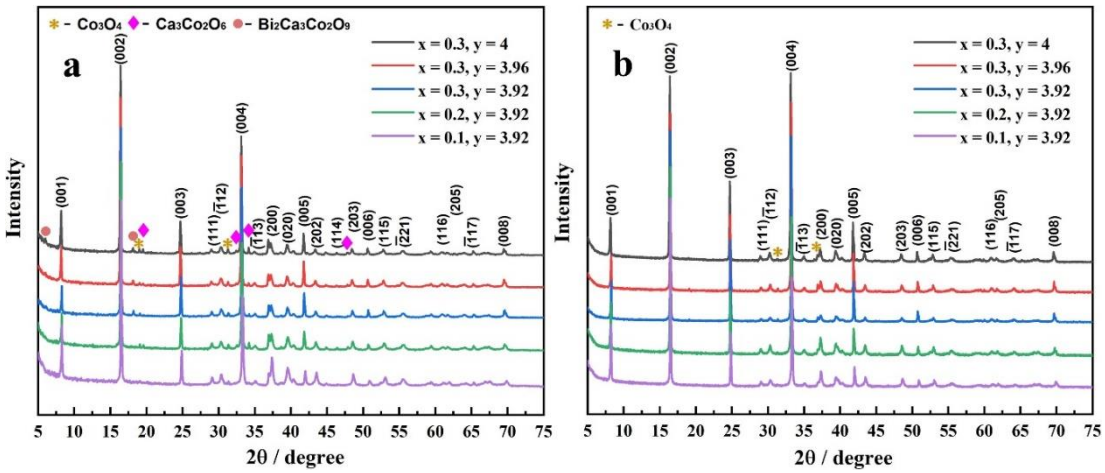

Fig. 5.12 XRD patterns of SPS-processed $Ca_{3-x}Bi_xCo_yO_{9+\delta}$ ceramics annealed for 12 h at temperatures of (a) 1023 K and (b) 1203 K

As XRD patterns of SPS-processed samples annealed at 1203 K exhibit high intensity peaks belonging to (00l) family, similar to XRD data for textured thick films (Fig. 4.17), the Lotgering factors (reflecting the degree of grain orientation) were calculated as a function of bismuth and cobalt content. It is apparent (Fig. 5.13) that by increasing bismuth substitution or cobalt deficiency the Lotgering factor shows an increase to the maximum value of 0.8 for the samples with x = 0.3 and y = 3.92. This enhanced texture could be related to the reduction of Co-containing phases and formation of Bi-rich phases. The grain alignment of plate-like calcium cobaltite can be hindered by large amounts of irregular shaped Co-containing phases. The additive (Bi_2O_3) tends to be soft and even melts at high temperatures, which helps to facilitate grain boundary sliding [25]. Meanwhile, Bi segregation at grain boundaries can reduce the grain boundary energies in ceramics. Therefore, a steady-state distribution of grain boundaries can be finally realised as a result of the reduction of high energy boundaries and the growth of lower energy interfaces [26].

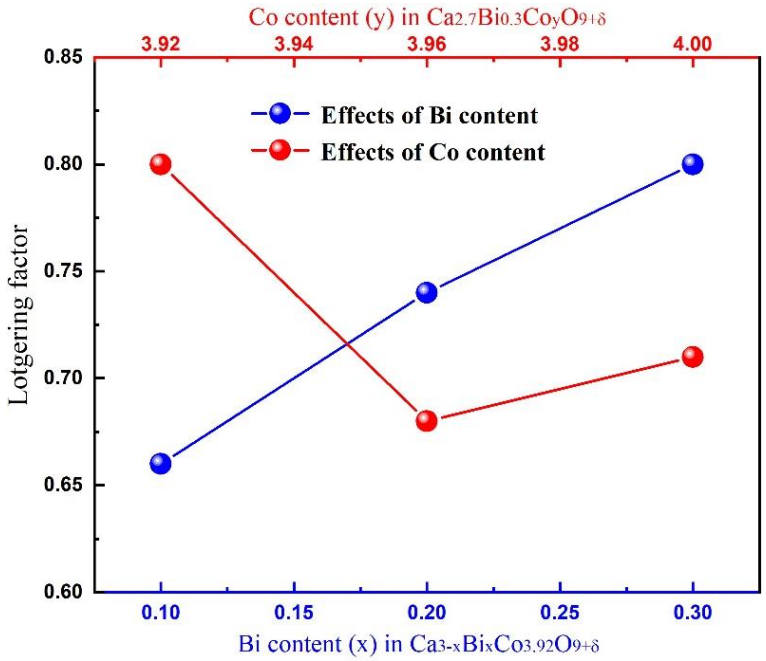

Fig. 5.13 Lotgering factors for SPS-processed $Ca_{3-x}Bi_xCo_yO_{9+\delta}$ ceramics annealed at 1203 K for 12 h as a function of bismuth and cobalt content

In order to examine the lattice distortion for SPS-processed samples annealed at 1203 K, the Le Bail refinement was performed to calculate the lattice parameters based on the modulated misfit structure ($[Ca_2CoO_3][CoO_2]_{1.62}$) reported by Grebille et al. [27]. As Fig. 5.14 shows, there is a good match between the observed and calculated data with the R_{wp} values of 7.96-10.43 and the GoF values of 1.68-2.80 for all compositions. Therefore, the refined lattice parameters are believed to be reliable for subsequent analysis.

Fig. 5.15 shows refined lattice parameters for SPS-processed $Ca_{3-x}Bi_xCo_yO_{9+\delta}$ ceramics annealed at 1203 K for 12 h as a function of bismuth and cobalt content. Within the levels of uncertainty, the effects of cobalt deficiency on lattice distortion are negligible compared to the contributions from bismuth substitution. It is clearly seen that almost all lattice parameters increase with increasing bismuth content, due to the larger atomic radius of Bi^{3+} (1.03 Å) compared to Ca^{2+} (0.99 Å). It is noticeable (Fig. 5.15(d)) that the largest lattice distortion occurs in the c axis, where the *c* length increases from 10.85 Å to 10.90 Å when the bismuth content rises from 0.1 to 0.3. Meanwhile, a more severe lattice expansion of *b* lattice parameter with increasing bismuth content is observed in the rock salt layer (Fig. 5.15(b)) in contrast to the CoO_2 layer (Fig. 5.14(c)), suggesting that the bismuth substitution is more likely to occur in the rock salt layer.

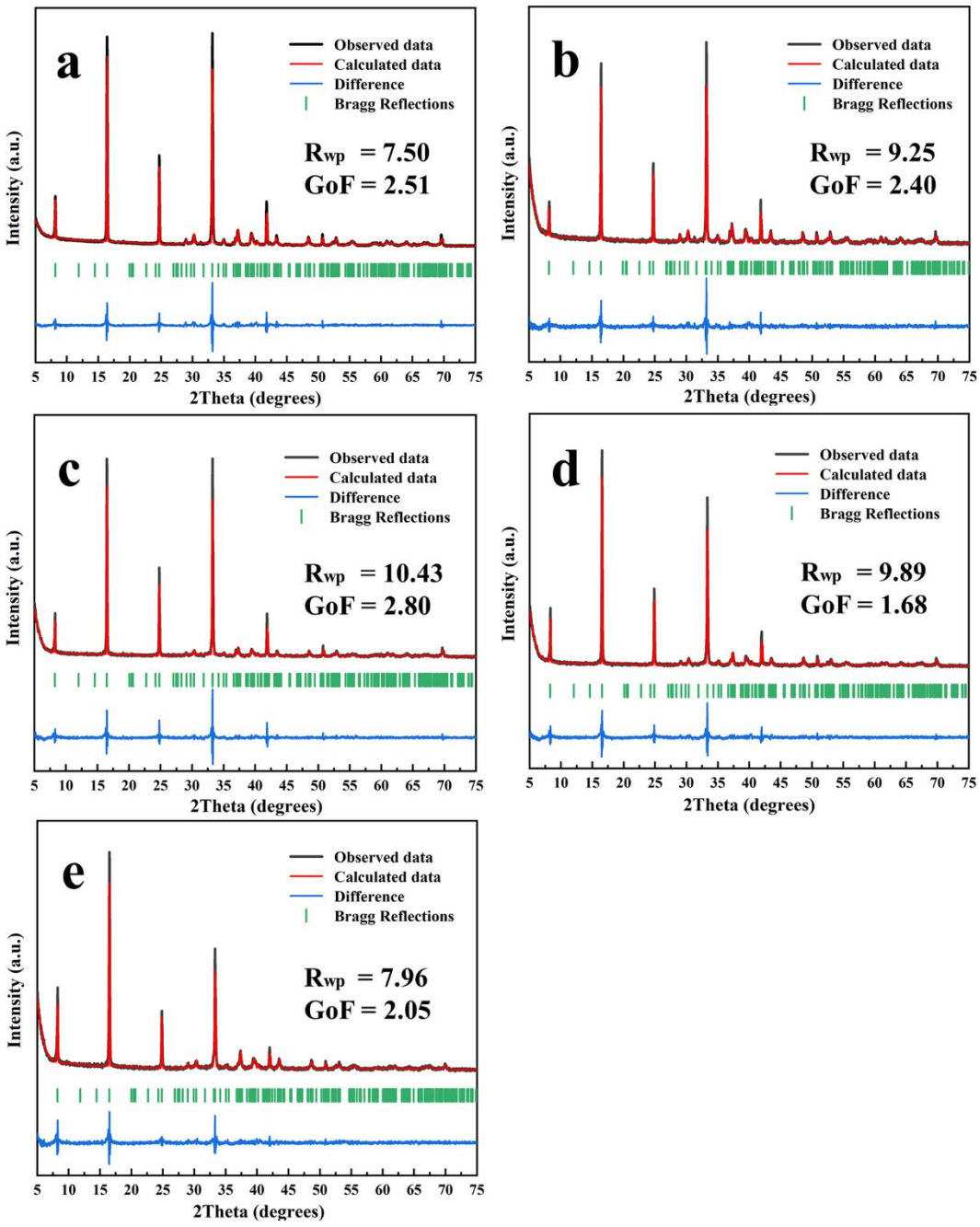

Fig. 5.14 Le Bail refinement data for SPS-processed $Ca_{3-x}Bi_xCo_yO_{9+\delta}$ ceramics annealed at 1203 K for 12 h (a. x = 0.3, y = 4.0; b. x = 0.3, y = 3.96; c. x = 0.3, y = 3.92; d. x = 0.2, y = 3.92; e. x = 0.1, y = 3.92)

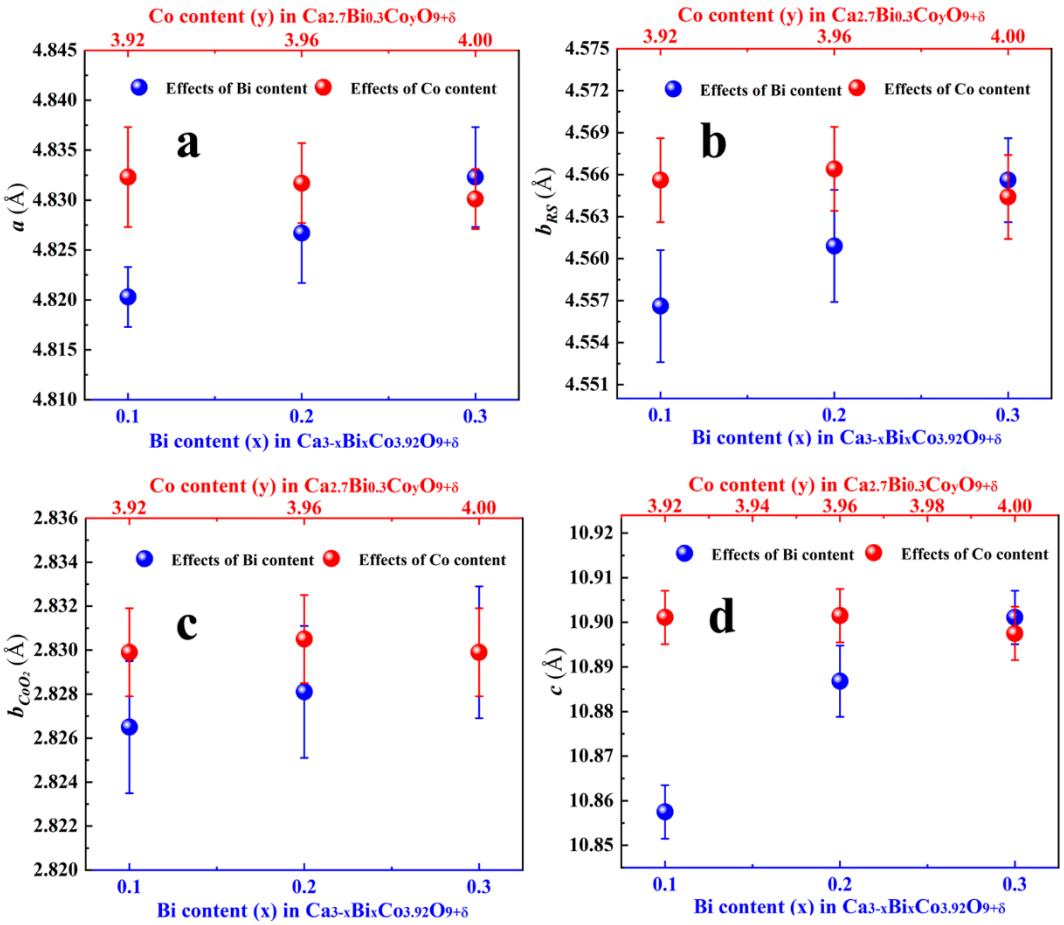

Fig. 5.15 Refined lattice parameters for SPS-processed $Ca_{3-x}Bi_xCo_yO_{9+\delta}$ ceramics annealed at 1203 K for 12 h as a function of bismuth and cobalt content

5.3.3 SEM-EDS Analysis

Fig. 5.16 shows backscattered electron SEM images of polished surfaces for SPS-processed $Ca_{3-x}Bi_xCo_yO_{9+\delta}$ ceramics annealed at 1023 K and 1203 K for 12 h; the volume fractions of different phases are summarised in Table 5.4. The average grain size of annealed samples is larger than that of the original ones (Fig. 5.3), but sizes are heavily influenced by increasing annealing temperature. Based on the analysis of phases in Fig. 5.3, it is found that the irregular shaped secondary phases, including $Bi_2Ca_3Co_2O_9$ (bright phase), $Ca_3Co_2O_6$ (dark phase) and Co_3O_4 (grey phase), still exist among the plate-like calcium cobaltite (primary phase) grains for the SPS-processed samples annealed at 1023 K (Fig. 5.16(a-e)). By increasing the annealing temperature to 1203 K, the volume fraction of the primary phase increases to over 90.0 % (Table 5.4 and Fig. 5.16(f-j)); most secondary phases are efficiently reduced, and $Ca_3Co_2O_6$ in particular is absent. Table 5.4 shows that increased volume fractions of $Bi_2Ca_3Co_2O_9$ are produced with increasing bismuth substitution, whilst a reduction in the content of Co_3O_4 can be observed with increasing cobalt deficiency.

Compared to the phase composition for unannealed SPS-processed samples (Table 5.1), high fractions of the primary phase prove that the annealing process is beneficial to promoting the complete reaction for forming calcium cobaltite and a higher annealing temperature is more helpful to reducing secondary phases.

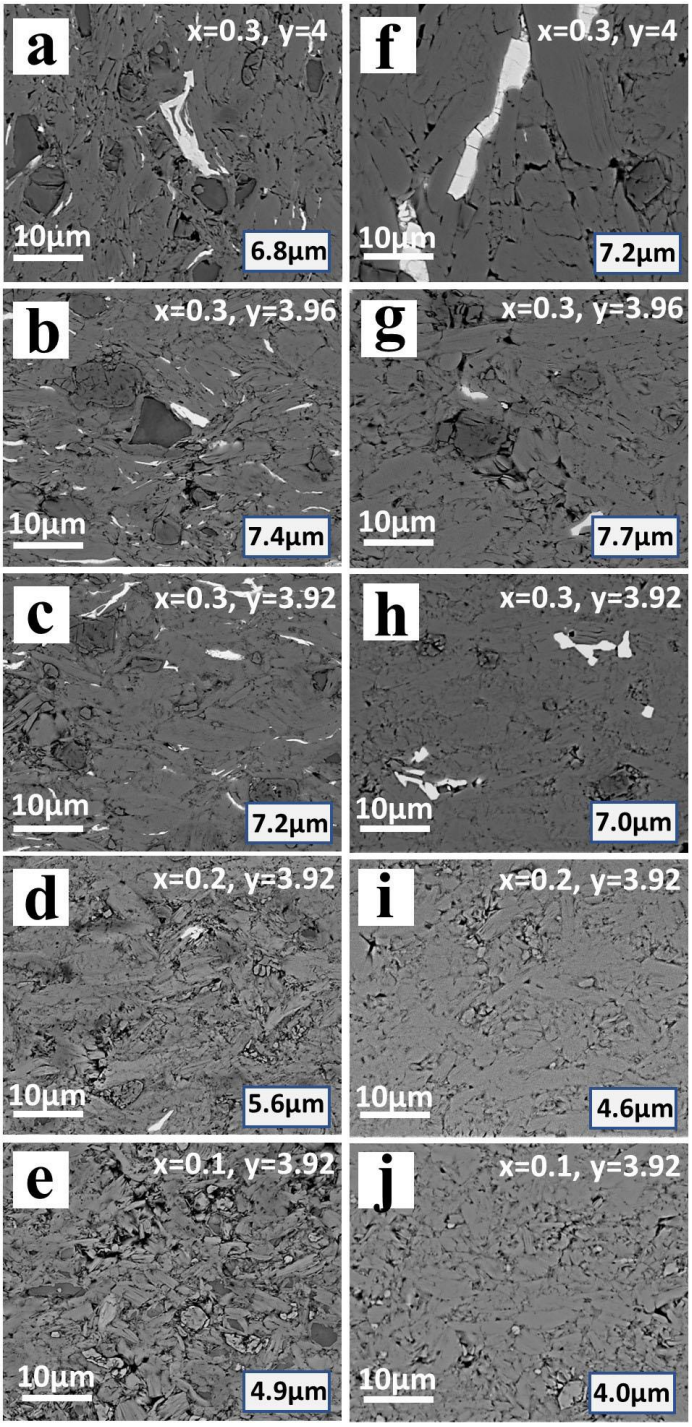

Fig. 5.16 Backscattered electron SEM images of polished surfaces for SPS-processed $Ca_{3-x}Bi_xCo_yO_{9+\delta}$ ceramics annealed at 1023 K (a-e) and 1203 K (f-j)

Table 5.4 Volume fractions of phases in SPS-processed $Ca_{3-x}Bi_xCo_yO_{9+\delta}$ ceramics annealed at different temperatures

x	y	$Ca_3Co_4O_9$ (vol.%)		$Ca_3Co_2O_6$ (vol.%)		$Bi_2Ca_3Co_2O_9$ (vol.%)		Co_3O_4 (vol.%)	
		1023 K	1203 K	1023 K	1203 K	1023 K	1203 K	1023 K	1203 K
0.1	3.92	81.5	90.7	4.6	0	0	0	13.9	9.3
0.2	3.92	78.8	91.8	5.4	0	1.5	0	14.3	8.2
0.3	3.92	76.3	91.2	8.5	0	3.5	3.3	11.7	5.5
0.3	3.96	72.6	88.4	10.5	0	3.8	1.2	13.1	10.4
0.3	4.00	70.2	86.1	12.2	0	5.2	4.8	12.4	9.1

In order to verify the chemical composition of annealed SPS-processed $Ca_{3-x}Bi_xCo_yO_{9+\delta}$ ceramics, EDS point and mapping analyses were performed on polished surfaces of $Ca_{2.7}Bi_{0.3}Co_{3.92}O_{9+\delta}$ ceramic annealed at 1023 K and 1203 K. Fig. 5.17 shows that the compositional distributions of Bi and Co with high contrast in both annealed samples match well with the position of the Bi-rich (sites 1 and 4) and Co-rich (sites 3 and 5) phases, whereas the Ca-rich phase (sites 2) disappears when the annealing temperature increases from 1023 K to 1203 K (Fig. 5.17(b)). The atomic ratios (Table 5.5) confirm that the Bi-rich and Co-rich phases correspond to $Bi_2Ca_3Co_2O_9$ and Co_3O_4, respectively. The absent Ca-rich phase is identified as $Ca_3Co_2O_6$ with limited solubility of Bi. It is therefore concluded that the formation of secondary phases can be heavily suppressed by the annealing process, especially for $Ca_3Co_2O_6$.

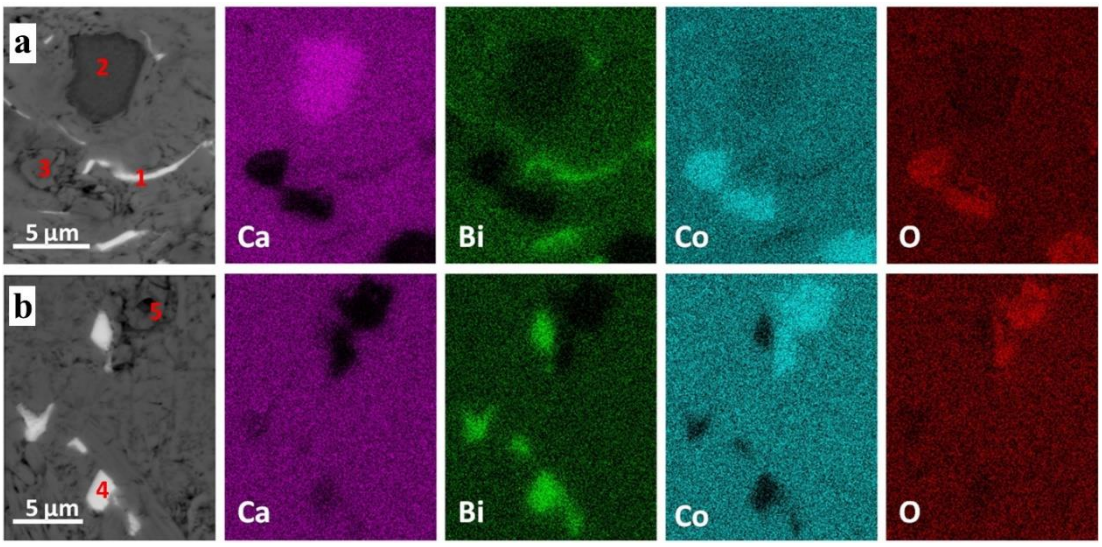

Fig. 5.17 EDS mapping data for polished surfaces of SPS-processed $Ca_{2.7}Bi_{0.3}Co_{3.92}O_{9+\delta}$ ceramics annealed at 1023 K (a) and 1203 K (b)

Table 5.5 EDS point analyses of different sites 1-5 on the SEM image in Fig. 5.16

Sites	Elements				Calculated Compositions
	Ca (at.%)	Bi (at.%)	Co (at.%)	O (at.%)	
1	15.1	10.0	7.3	67.6	$Ca_3Bi_2Co_{1.5}O_{14}$
2	23.1	0.6	18.7	57.6	$(Ca,Bi)_3Co_2O_7$
3	3.4	0	41.7	54.9	$(Co,Ca)_3O_4$
4	16.1	10.4	6.7	66.8	$Ca_3Bi_2Co_2O_{11}$
5	0.4	0	41.9	57.7	$(Co,Ca)_3O_4$

The fracture surfaces for SPS-processed $Ca_{3-x}Bi_xCo_yO_{9+\delta}$ ceramics annealed at 1203 K (Fig. 5.18) were examined by SEM to characterise the texture. The plate-like calcium cobaltite grains can be easily distinguished in all samples and the grain size increases with increasing bismuth content, as noted for Fig. 5.16. Grains in the 10.0 at.% bismuth substituted samples (Fig. 5.18(a-c)) are aligned along *ab* planes, stacking in the *c* axis; this preferred grain orientation plays vital roles in modifying thermoelectric properties. Parallel to the *ab* plane, the electrical conductivity and thermal conductivity will be maximised while the Seebeck coefficient will be minimised [28,29], owing to the reduced grain boundary barriers; the case for the direction perpendicular to the *ab* plane is opposite. It is also clear that the texture development is highly dependent upon the bismuth substitution; the strongest texture occurs for samples with x = 0.3. These results match well with the variational trend for Lotgering factors (Fig. 5.13).

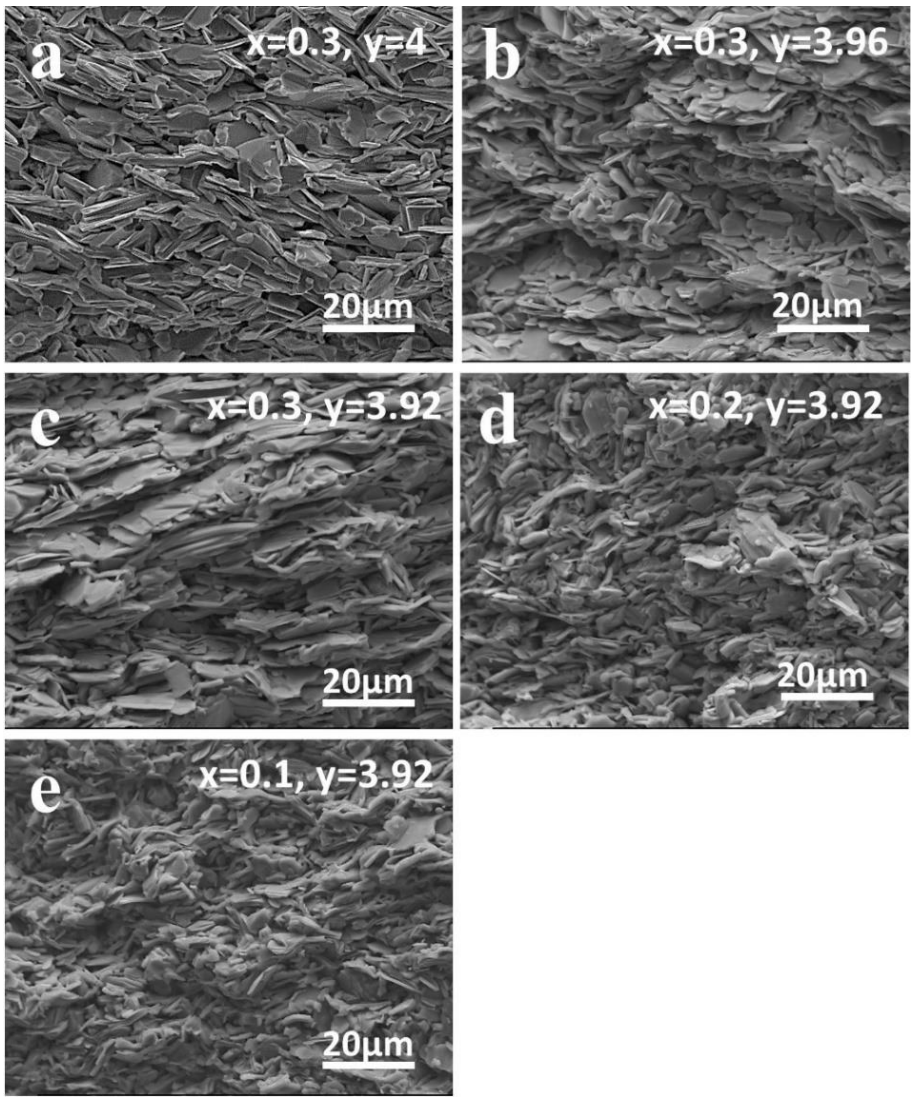

Fig. 5.18 Secondary electron SEM images of fracture surfaces for SPS-processed $Ca_{3-x}Bi_xCo_yO_{9+\delta}$ ceramics annealed at 1203 K

5.3.4 TEM Analysis

TEM data for SPS-processed $Ca_{2.7}Bi_{0.3}Co_{3.92}O_{9+\delta}$ ceramics annealed at 1203 K prepared by Focused Ion Beam show evidence of a plate-like grain with the presence of minor amounts of dislocations (distinguished by regions of dark contrast) in bright field TEM images at low magnification (Fig. 5.19(a)). A high-resolution image, corresponding to the red rectangular region in Fig. 5.19(a), reveals a d-spacing of 0.294 nm, matching with the (-112) crystal plane of calcium cobaltite (Fig. 5.19(b)). The corresponding SAED patterns (Fig. 5.19(c)) confirm well indexed (000), (11-2), (-113) and (021) crystal planes, based on the PDF card (JCPDS: # 05-001-0461).

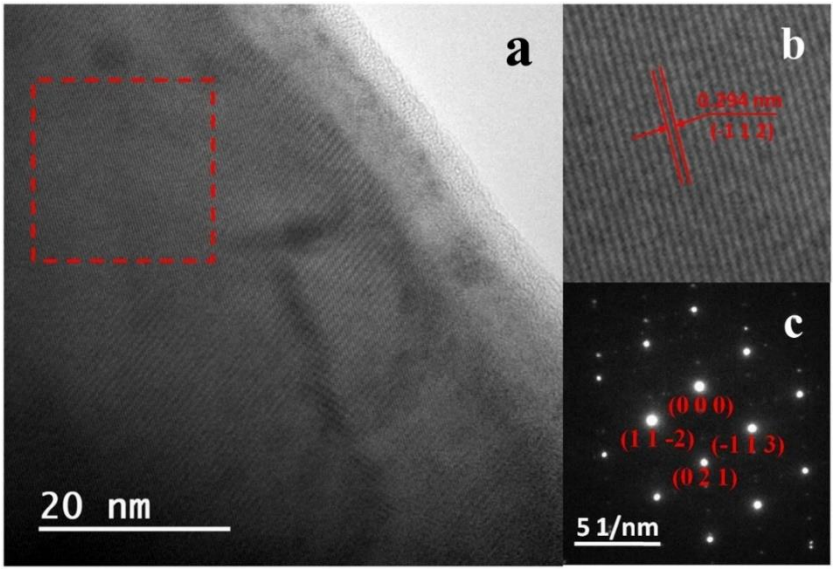

Fig. 5.19 TEM data for SPS-processed $Ca_{2.7}Bi_{0.3}Co_{3.92}O_{9+\delta}$ ceramics annealed at 1203 K; sample prepared by FIB method (a. low magnification; b. high-resolution; c. SAED patterns)

In order to further investigate the microstructure and crystal structure of SPS-processed $Ca_{2.7}Bi_{0.3}Co_{3.92}O_{9+\delta}$ ceramics annealed at 1203 K, a thinner TEM sample was fabricated using the standard crushing method. By tilting the incident electron beam along the [001] zone axis, the SAED patterns of calcium cobaltite are revealed in Fig. 5.20(a), where two distinct sets of diffraction spots arise from the rock salt (red arrow) and CoO_2 (orange arrow) sublayers; this shows the sublattices with an identical *a* lattice parameter and different *b* lattice parameters. Our [001] SAED patterns match well with data reported by Seo et al. [30] and Yubuta et al. [31]. The corresponding [001] HRTEM image is displayed in Fig. 5.20(b). This defect-free structure indicates good crystallinity for our annealed SPS-processed sample.

The [100] TEM data of SPS-processed $Ca_{2.7}Bi_{0.3}Co_{3.92}O_{9+\delta}$ ceramics annealed at 1203 K are shown in Fig. 5.20. The low magnification TEM image (Fig. 5.21(a)) presents plate-like grains with sub-grain features appearing as dark and bright contrast. The [100] HRTEM and corresponding FFT images are shown in Fig. 5.21(b, c). The d-spacing of the crystal planes (highlighted in red) was determined to be around 1.07 nm, which can be indexed as the (001) plane of calcium cobaltite, approaching the *c* lattice parameter of $Ca_{2.7}Bi_{0.3}Co_{3.92}O_{9+\delta}$ ceramic annealed at 1203 K as shown in Fig. 5.15. This helps to confirm that this misfit layered structure is built upon stacking sheets of alternating layers of CoO_2 and rock salt Ca_2CoO_3(-CaO-CoO-CaO-sequence) along the *c* axis. By contrast, there is a small amount

of stacking faults amongst the normal misfit $Ca_3Co_4O_9$ (CCO) structure in the rectangular region (highlighted in orange); the angle (about 4 .0 degrees) between the different planes can be distinguished in the corresponding inverse FFT image (Fig. 5.21(d)). A similar finding was also reported by Sun et al. [32,33] for calcium cobaltite films. Nevertheless, the data in Fig. 5.18 and 5.19 suggest that high-quality layer-structured calcium cobaltite has been successfully prepared.

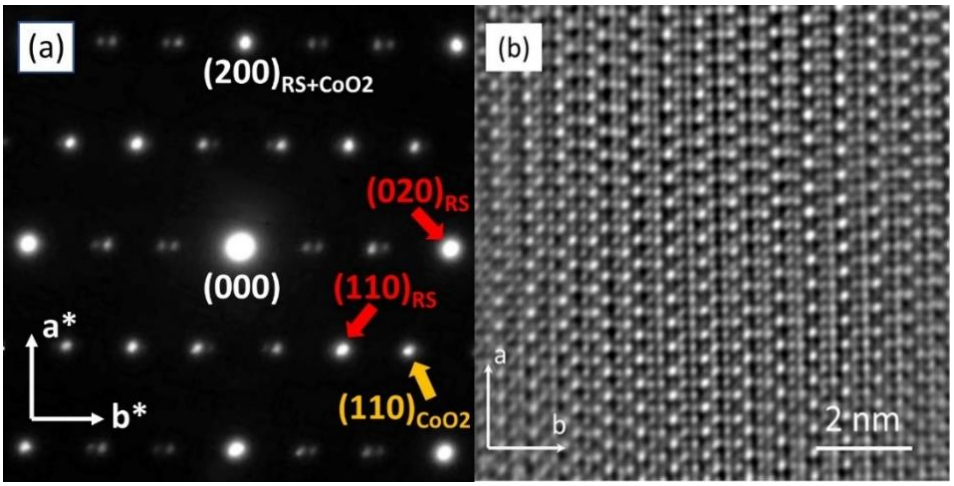

Fig. 5.20 TEM data for SPS-processed $Ca_{2.7}Bi_{0.3}Co_{3.92}O_{9+\delta}$ ceramics annealed at 1203 K prepared by the standard crushing method (a. SAED pattern in [001] zone axis; b. corresponding HRTEM image)

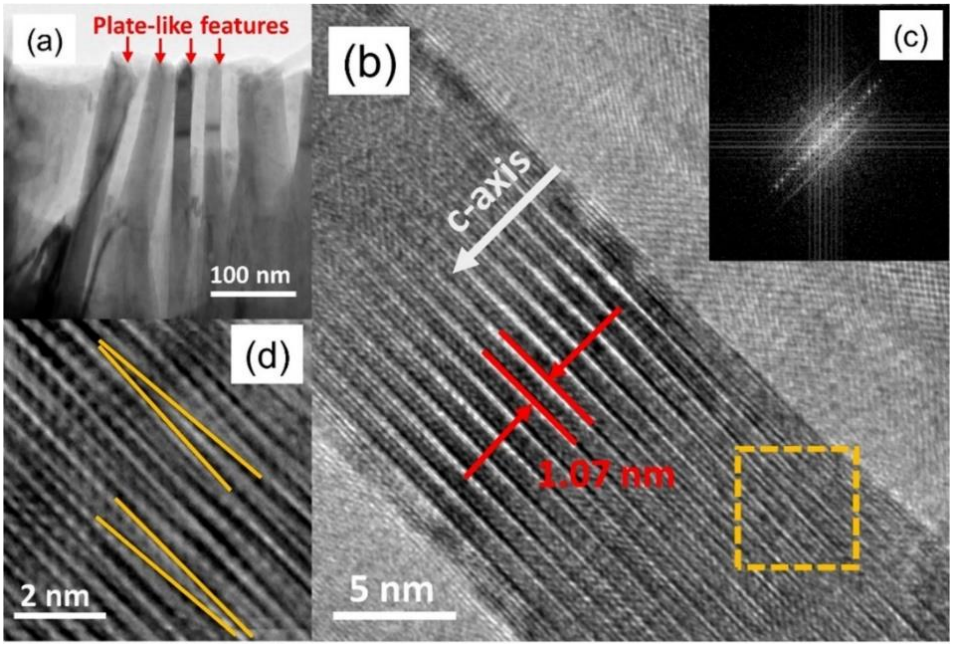

Fig. 5.21 TEM data for SPS-processed $Ca_{2.7}Bi_{0.3}Co_{3.92}O_{9+\delta}$ ceramics annealed at 1203 K prepared by the standard crushing method (a: low magnification ; b: [100] HRTEM image; c: the corresponding FFT image in [100] zone axis; d: the inverse FFT image of the rectangular region)

5.3.5 XPS Analysis

High-resolution XPS spectra of Ca 2p for SPS-processed $Ca_{3-x}Bi_xCo_yO_{9+\delta}$ (x = 0.1-0.3; y = 3.92) ceramics annealed at 1203 K were collected to examine the bismuth doping site (Fig. 5.22). In the annealed samples, the Ca-containing secondary phases were almost eliminated, thereby mitigating the interference of calcium in the impurity phase. In contrast to the two single peaks for Ca 2p in the standard XPS spectra for $CaCO_3$ in the XPS handbook [34], a pair of doublets are revealed in our Ca 2p spectra. It is found that the doublets can be divided into two sets of spin-orbit coupling peaks for Ca 2p 3/2 and Ca 2p 1/2, respectively; the first set is located at 345.28-345.39 eV and 348.82-348.94 eV, and the other lies at 346.67-348.89 eV and 350.22-350.43 eV. For the samples with x = 0.1, 0.2 and 0.3, the full width at half-maximum (FWHM) of the first set is 1.02, 1.11 and 1.23 eV, whilst that of the second set is 1.62, 1.60 and 1.67 eV, respectively. It is clear that the FWHM of the second set is broader than the first one, but a similar spin-orbit splitting δ (Ca 2p 1/2-Ca 2p 3/2) of about 3.5 eV is commonly observed for both sets. This suggests that the calcium in the annealed SPS-processed samples is subject to two different chemical environments [35]. In addition, all the Ca 2p peaks are found to shift towards a lower binding energy ($\Delta BE \approx 1.6$ eV) compared to the Ca 2p spectra for undoped $Ca_3O_4O_9$, indicating partial element substitution at the Ca site. The changes in the binding energy can be ascribed to Bi^{3+} substitution for Ca^{2+}, which donates the electron and thereby lowers the binding energy. It is therefore inferred, in combination with the refined lattice parameters (Fig. 5.15), that the bismuth is successfully doped into the Ca site.

The high-resolution XPS spectra of Co 2p 3/2 for SPS-processed $Ca_{3-x}Bi_xCo_yO_{9+\delta}$ (x = 0.1-0.3; y = 3.92-4.0) ceramics annealed at 1203 K were collected to examine the cobalt species (Fig. 5.23). It is acknowledged that there are three types of Co ionic valences in the crystal lattice of $Ca_3Co_4O_9$: Co^{2+} existing in the rock salt layers while Co^{3+} and Co^{4+} coexisting in the CoO_2 layers [18]. The Co 2p 3/2 spectra are thus deconvoluted into three peaks, where the peaks at 779.26-779.30 eV, 780.26-780.30 eV and 782.06-782.10 eV are assigned to Co^{3+} , Co^{2+} and Co^{4+}, respectively. These results are similar with Co 2p XPS data reported by Park et al. [15], Zhang et al. [16] and Liu et al. [17], and confirm a mixed valance of cobalt (+2, +3, and +4) in the lattice of calcium cobaltite.

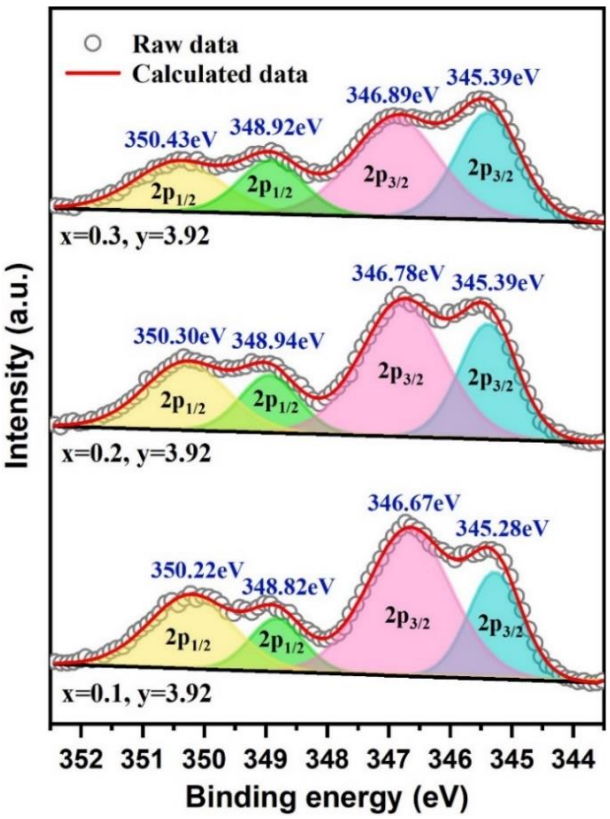

Fig. 5.22 High-resolution XPS spectra of Ca 2p for SPS-processed $Ca_{3-x}Bi_xCo_yO_{9+\delta}$ ceramics annealed at 1203 K

The fractions for each cobalt ion determined from the Co 2p 3/2 data (Fig. 5.22) are displayed in Table 5.6. Compared to the original SPS-processed samples (Table 5.3), the fraction of Co^{3+} significantly decreases whilst that of Co^{4+} increases as a natural consequence of the annealing process. The ratios of $Co^{4+}/(Co^{3+}+Co^{4+})$ in the annealed samples fluctuates around 45 %, independent of bismuth content, showing about 20 % increase after the heat-treatment. Interestingly, a decrease in the ratios of $Co^{4+}/(Co^{3+}+Co^{4+})$ with increasing bismuth content is usually expected because Ca^{2+} substitution by Bi^{3+} can lower the average valence of cobalt according to the neutralization principle. The contradictory results in our study could be due to the diffusion of oxygen into the cobaltite lattice during annealing, which helps to increase the ratio of Co^{4+} in CoO_2 layers and thus generates more hole carriers to compensate for the reduction in the ratio of $Co^{4+}/(Co^{3+}+Co^{4+})$ [36].

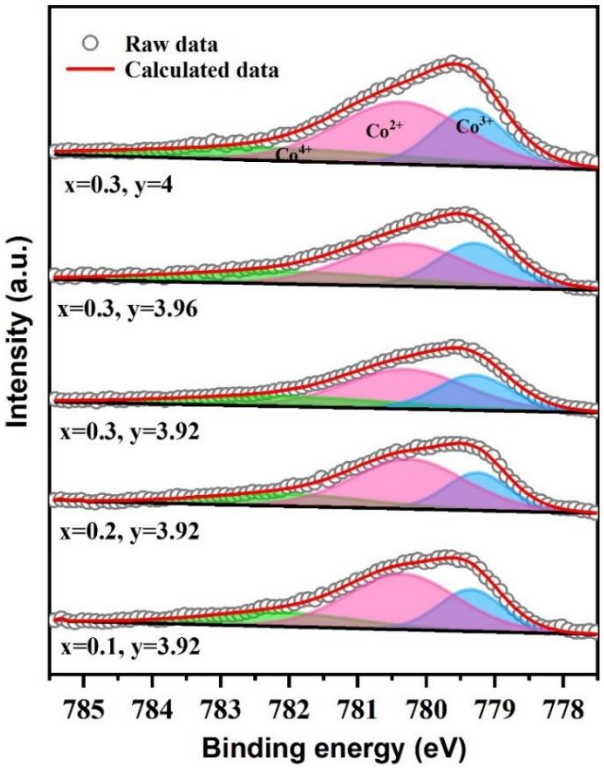

Fig. 5.23 High-resolution XPS spectra of Co 2p 3/2 for SPS-processed $Ca_{3-x}Bi_xCo_yO_{9+\delta}$ ceramics annealed at 1203 K

Table 5.6 Concentrations of cobalt ions in SPS-processed $Ca_{3-x}Bi_xCo_yO_{9+\delta}$ ceramics annealed at 1203 K

x	y	Co^{3+} (%)	Co^{2+} (%)	Co^{4+} (%)	$Co^{4+}/(Co^{3+}+Co^{4+})$ (%)
0.1	3.92	24.5	55.5	20.0	44.9
0.2	3.92	23.9	55.8	20.3	45.9
0.3	3.92	27.2	49.7	23.1	45.9
0.3	3.96	29.3	45.1	25.6	46.6
0.3	4.00	26.5	51.4	22.1	45.5

High-resolution XPS spectra of O 1s for SPS-processed $Ca_{3-x}Bi_xCo_{3.92}O_{9+\delta}$ (x = 0.1, 0.2, 0.3) ceramics annealed at 1203 K were collected to identify variations in lattice oxygen (Fig. 5.24). There are three kinds of identical deconvoluted peaks at 528.94-529.00 eV, 531.11-531.13 eV and 533.14-533.20 eV, corresponding to the CoO_2 surfaces, CaO surfaces and abs. O (adsorbed water or surface degradation) [17,35,37,38], respectively. It is also clear that fractions of different oxygen species in all compositions follow the order: Ca-O > Co-O > abs. O. The oxygen concentrations derived from Fig. 5.23 are summarised in Table 5.7.

It is evident that the fractions of Co-O bonding increase from 28.0 % to 33.9 % as the bismuth content increases from 0.1 to 0.3. This variational trend confirms that with increasing bismuth content an increasing amount of oxygen enters the crystal lattice to coordinate with cobalt, thereby counteracting the reduction of Co^{4+} caused by bismuth substitution.

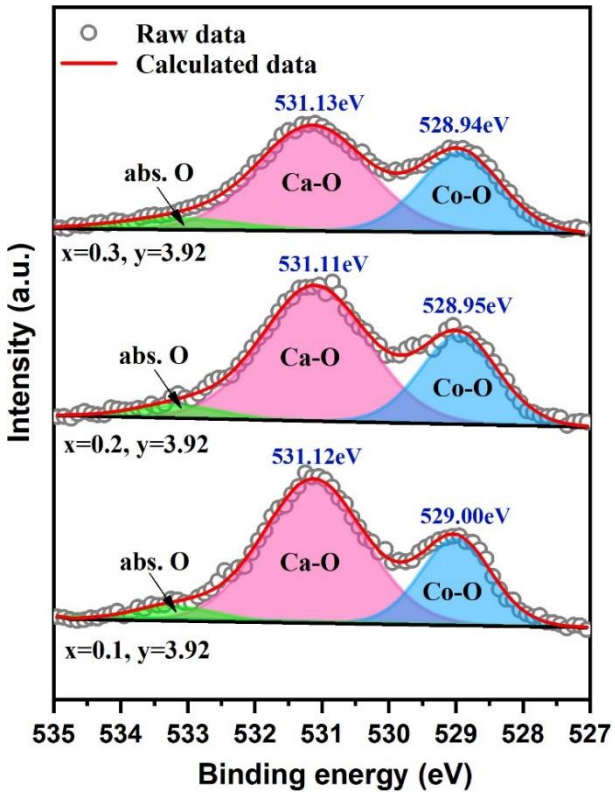

Fig. 5.24 High-resolution XPS spectra of O 1s for SPS-processed $Ca_{3-x}Bi_xCo_yO_{9+\delta}$ ceramics annealed at 1203 K

Table 5.7 Oxygen concentrations in SPS-processed $Ca_{3-x}Bi_xCo_yO_{9+\delta}$ samples annealed at 1203 K

x	y	O 1s (1) Co-O (%)	O 1s (2) Ca-O (%)	O 1s (2) abs. O (%)
0.1	3.92	28.0	66.5	5.5
0.2	3.92	31.0	64.0	5.0
0.3	3.92	33.9	58.9	7.2

5.3.6 Electrical Transport

The electrical transport properties of SPS-processed $Ca_{3-x}Bi_xCo_yO_{9+\delta}$ ceramics annealed at 1023 K and 1203 K are shown in Fig. 5.25. The electrical conductivity (σ) parallel to the *ab*

plane for the annealed samples increases with increasing temperature (1023 K: 53.0-67.0 S/cm; 1203 K: 70.0-125.0 S/cm), showing the semiconducting behaviour and a 20 % enhancement compared to earlier studies (20.0-100.0 S/cm) [39–43]. It is clear that σ nearly doubles and then triples by annealing the original samples (Fig. 5.8) at 1023 K and 1203 K, respectively. Notably, σ for samples annealed at 1023 K decreases with increasing bismuth substitution, whereas the value for samples annealed at 1203 K shows a positive correlation. Interestingly, σ is enhanced for the cobalt deficiencies up to 2.0 at.%; smaller cobalt deficiencies (< 1.0 at.%) do not give rise to any significant changes in σ.

The Seebeck coefficient (S) parallel to the *ab* plane, increases with increasing temperature (1023 K: 120.0-168.0 μV/K; 1203 K: 130.0-165.0 μV/K), consistent with previously reported work (120.0-170.0 μV/K) [39,41,42,44,45], confirming a conduction mechanism governed by holes as carriers. The thermopower for annealed SPS-processed samples is about 10 % lower than the original ones (Fig. 5.8). S values for the SPS-processed samples annealed at 1023 K increase with increasing bismuth substitution, but are almost constant for the samples annealed at 1203 K.

According to the simple Drude model, (C_e/n) in Equation (2.4), S is dominated by the carrier concentration (n). As annealed SPS-processed samples show lower thermopower values than the original ones, it is inferred that n in the annealed samples is higher than in the unannealed samples. It is also evident that the fractions of calcium cobaltite significantly increase after the heat-treatment and slightly increase with increasing annealing temperatures (original: 46-64 % in Table 5.1; annealed at 1023 K and 1203 K: 70-82 % and 86-92 % in Table 5.4), thereby resulting in higher σ for SPS-processed samples annealed at 1203 K. However, the enhanced σ at the higher annealing temperature is mainly ascribed to the increase in carrier mobility (μ), because only a slight drop in the thermopower is observed when the annealing temperature increases from 1023 K to 1203 K.

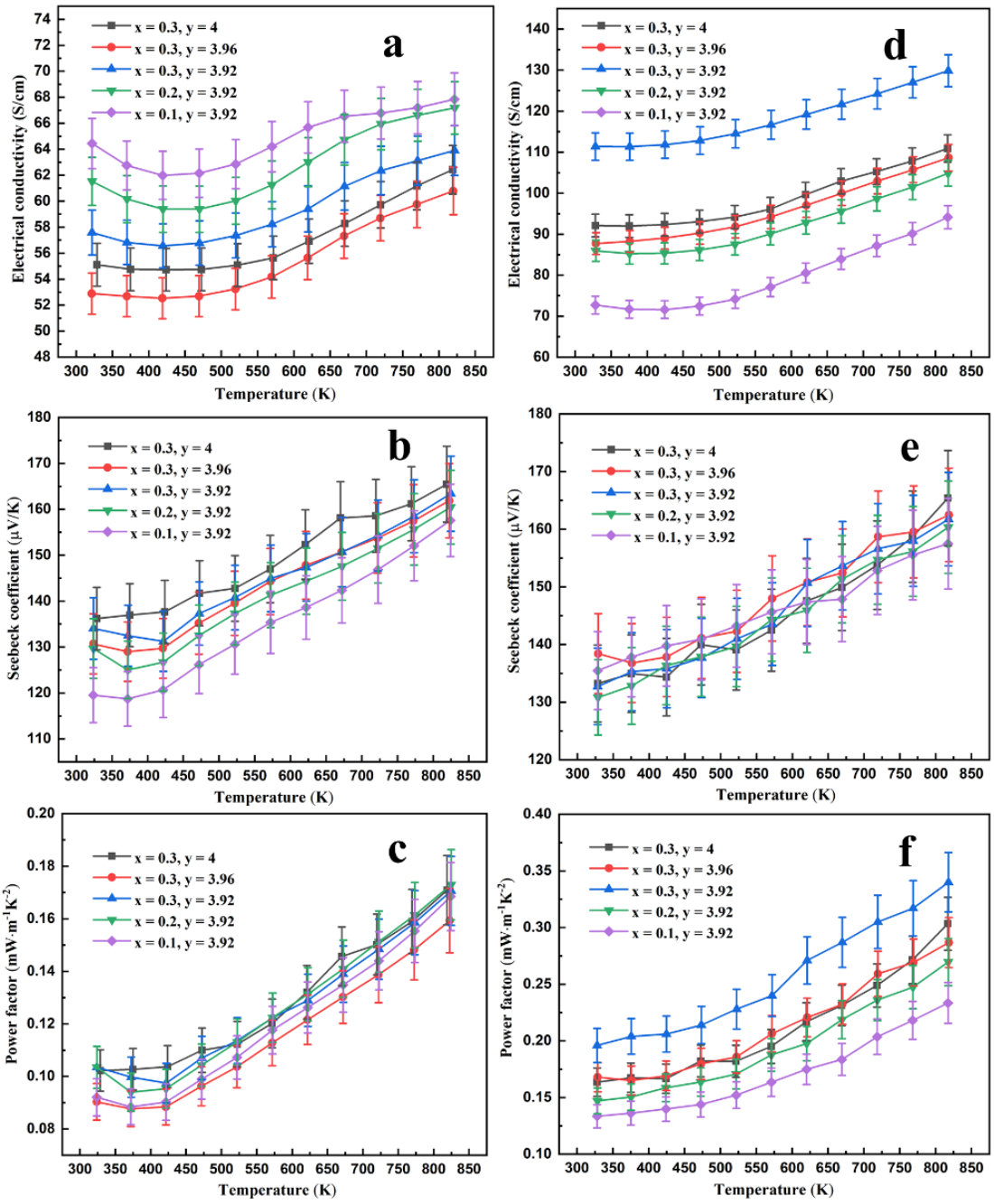

Fig. 5.25 Electrical transport properties of SPS-processed $Ca_{3-x}Bi_xCo_yO_{9+\delta}$ ceramics annealed at 1023 K (a-c) and 1203 K (d-f)

Similarly, the variation in σ with chemical compositions is mainly related to the changes in fractions of the primary phase (Table 5.4) for SPS-processed samples annealed at 1023 K. For SPS-processed samples annealed at 1203 K, having similar fractions of the primary phase (about 90 %), the increased σ with increasing bismuth substitution is attributed to the enhanced μ according to Equation (2.23). Notably, the increased μ should be related to the phase evolution, texture development and oxygen diffusion. The low fractions of secondary phases after annealing (Table 5.4), indicates a reduction of secondary phases in the matrix,

thereby increasing the connections between calcium cobaltite grains. By aligning the grains parallel to the *ab* plane, the in-plane grain boundary density is efficiently reduced, thereby decreasing the carrier scattering. In addition, the oxygen diffusion into CoO_2 sublayers offsets the reduction of Co^{4+} caused by bismuth substitution [36], thereby maintaining a high level of n.

The S can be alternatively evaluated by the modified Heikes formula (Equation (2.11)). The presence of Co^{4+} amongst Co^{3+} is responsible for regulating the carrier concentration which is reflected by the value of x. As Table Table 5.6 shows, x is consistent at around 45 %, indicating negligible differences in carrier concentration for all compositions. According to Equation (2.11), S is almost constant, matching well with phase compositional changes in Table 5.4 and the thermopower data in Fig. 5.24(e).

Fig. 5.26 shows electrical conductivity (σ) and Seebeck coefficient (S) at 323 K for annealed SPS-processed $Ca_{3-x}Bi_xCo_yO_{9+\delta}$ ceramics as a function of bismuth content and cobalt content. It is clear that the σ for SPS-processed samples annealed at 1023 K and 1203 K show a decrease and an increase with increasing bismuth substitution, respectively (Fig. 5.26(a)). As the similar S values achieved in samples annealed at 1203 K (Fig. 5.26(b)), independent of bismuth substitution, suggest a similar carrier concentration, the increased σ is attributed to the enhanced carrier mobility with increasing bismuth substitution. By contrast, the S values for samples annealed at 1023 K show a slight upward trend when the bismuth content increases (Fig. 5.26(b)), opposite to the variation of σ, which indicates a small reduction in carrier concentration due to the different phase evolution. However, the S values for samples annealed at 1023 K and 1203 K are almost constant with the cobalt deficiency varying (Fig. 5.26(d)), suggesting that the carrier concentration is less influenced by the cobalt deficiency. The enhanced σ for the samples annealed at 1203 K in contrast to those annealed at 1023 K (Fig. 5.26(c)) is ascribed to the higher fractions of the main phase (calcium cobaltite), which provides better conduction.

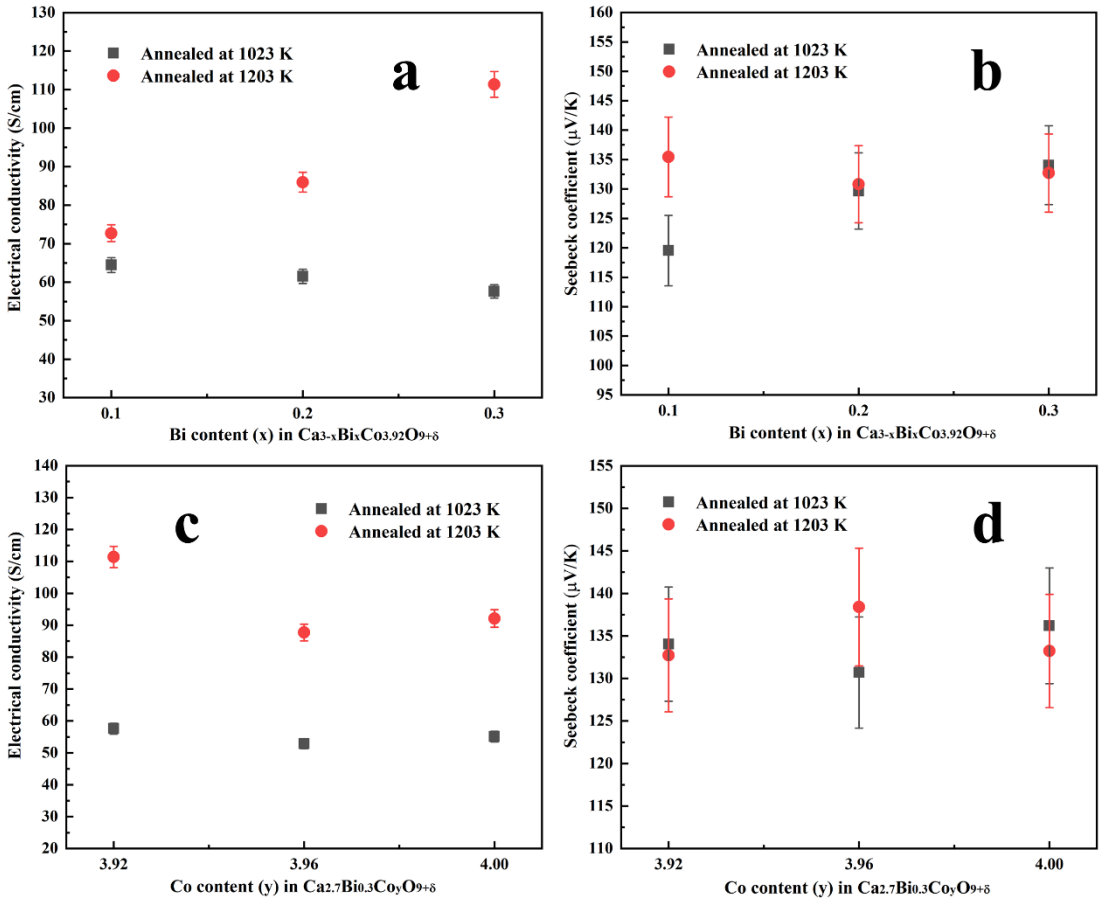

Fig. 5.26 Electrical conductivity and Seebeck coefficient at 323 K for annealed SPS-processed $Ca_{3-x}Bi_xCo_yO_{9+\delta}$ ceramics as a function of bismuth content (a, b) and cobalt content (c, d)

The activation energies (E_h) derived from reciprocal Arrhenius plots (Fig. 5.27) show strong linear regions above 500 K (Fig. 5.27(a)), fitting well to the SPHC model (Equation (2.25)), indicating a small polaron hopping conduction mechanism. As seen in Fig. 5.27(b), the calculated E_h for annealed samples with x = 0.1, 0.2 and 0.3 are 90.5, 83.1 and 77.6 meV, showing a reverse trend compared to the original SPS-processed samples (Fig. 5.10). Despite the enhanced scattering effects with increasing bismuth content, the improved texture (Fig. 5.13) and increased grain size (Fig. 5.16) can result in smaller amounts of grain boundaries and interfaces [47], thereby reducing the activation energy [46]. By contrast, the cobalt deficiency has less influence; only a slight drop from 81.3 meV to 77.6 emV is observed with the cobalt content decreasing to 3.92. As a result, the power factor increases significantly with increasing bismuth content, with the maximum value of 0.34 $mWm^{-1}K^{-2}$ at 823 K obtained for $Ca_{2.7}Bi_{0.3}Co_{3.92}O_{9+\delta}$ ceramic annealed at 1203 K, showing at least about 25 % increase compared to previous studies [9,14,36,39,48,49].

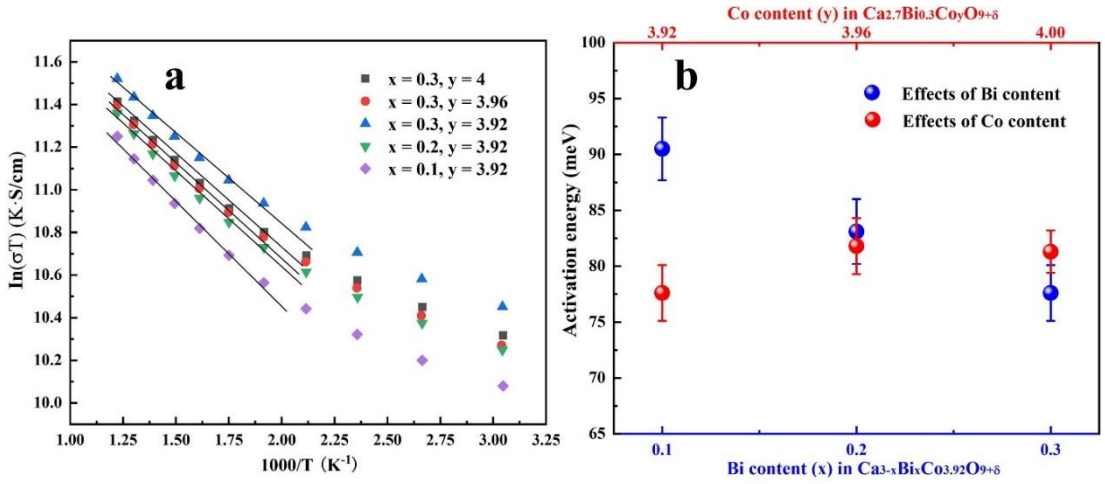

Fig. 5.27 ln(σT) versus as a function of reciprocal temperature (a) and calculated activation energy (b) for SPS-processed $Ca_{3-x}Bi_xCo_yO_{9+\delta}$ ceramics annealed at 1203 K (The lines are linearly fitted by a least-square method)

Carrier concentration (n) and mobility (μ) of SPS-processed $Ca_{3-x}Bi_xCo_yO_{9+\delta}$ ceramics annealed at 1203 K calculated from Equations (2.10) and (2.23) are shown in Fig. 5.28. It is found that n (consistent at about 5.5×10^{20} cm^{-3}) is independent of bismuth and cobalt content; this basically matches with the data for calcium cobaltite prepared by solid state reaction (Fig. 4.17), indicating that n cannot be significantly modified by changing preparation routes. By marked contrast, μ increases with increasing bismuth content and cobalt deficiency, peaking at 1.19 $cm^2V^{-1}s^{-1}$ for the sample with x = 0.3 and y = 3.92.

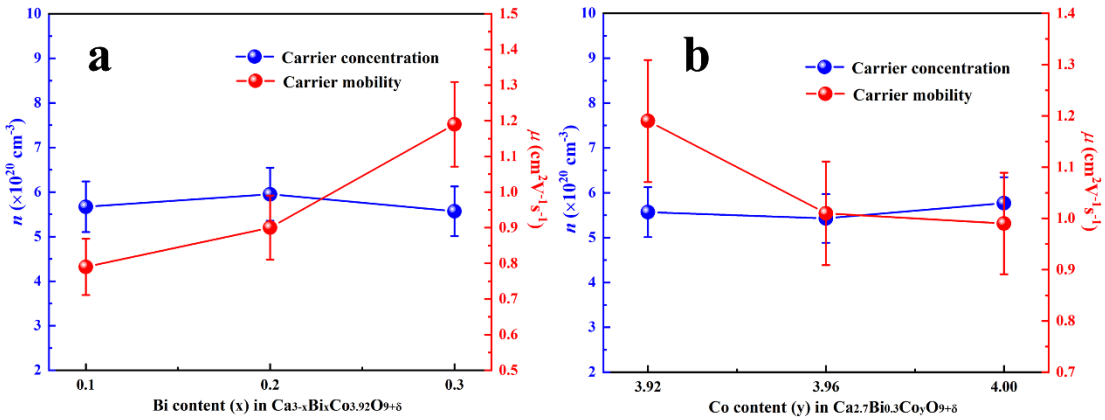

Fig. 5.28 Calculated carrier concentration and mobility for SPS-processed $Ca_{3-x}Bi_xCo_yO_{9+\delta}$ ceramics annealed at 1203 K as a function of bismuth content (a) and cobalt content (b)

5.3.7 Thermal Transport

The total thermal conductivity (κ) perpendicular to the *ab* plane for SPS-processed $Ca_{2.7}Bi_{0.3}Co_yO_{9+\delta}$ ceramics annealed at 1203 K is displayed in Fig. 5.29(a). It is clearly seen that κ decreases with increasing temperature (1.56-1.03 $Wm^{-1}K^{-1}$ between 323 K and 823 K), which can be ascribed to enhanced phonon-phonon interactions at high temperatures; the lowest value shows at least 20 % reduction compared to the undoped calcium cobaltite prepared by the SPS route [28,50–52]. Notably, κ at 823 K shows a drop from 1.27 $Wm^{-1}K^{-1}$ to 1.03 $Wm^{-1}K^{-1}$ when the bismuth content increases from 0.1 to 0.3. However, by increasing the cobalt deficiency to 0.08, κ decreases slightly from 1.26 $Wm^{-1}K^{-1}$ to 1.23 $Wm^{-1}K^{-1}$, followed by an obvious decline to 1.03 $Wm^{-1}K^{-1}$.

The contributions from the lattice ($\kappa_{lattice}$) and electronic ($\kappa_{electronic}$) components to the total κ were derived the Wiedemnn-Franz law (Equations (2.28) and (2.29)). As Fig. 5.29(b) shows, $\kappa_{electronic}$ increases slightly from 0.05 $Wm^{-1}K^{-1}$ to 0.3 $Wm^{-1}K^{-1}$ with increasing temperature; this value is almost constant among different compositions, indicating that the compositional changes has limited influence on $\kappa_{electronic}$. By marked contrast, $\kappa_{lattice}$ decreases significantly from 1.5 $Wm^{-1}K^{-1}$ to 0.8 $Wm^{-1}K^{-1}$. With maximum lattice contribution of 95 % of the total at 323 K and ~75 % at high temperatures, the lattice component appears to take a dominating role in thermal conduction.

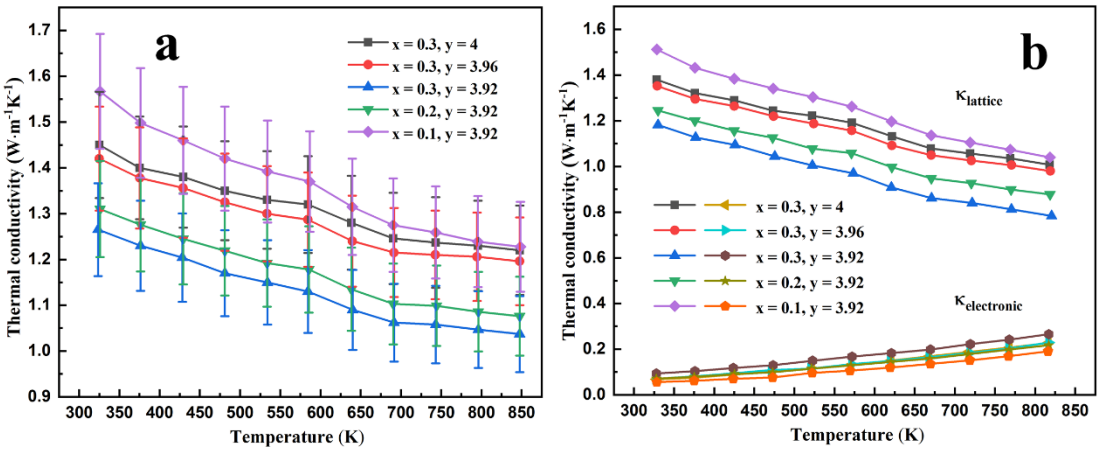

Fig. 5.29 (a) Total κ (⊥ *ab*) and (b) lattice and electronic κ (⊥ *ab*) for SPS-processed $Ca_{3-x}Bi_xCo_yO_{9+\delta}$ ceramics annealed at 1203 K

In order to provide a clear insight into the thermal transport behaviour, $\kappa_{lattice}$ was replotted against the reciprocal temperature [53,54], and is shown in Fig. 5.30(a). It is apparent that above 573 K all samples show a strong linear dependence, in agreement with the Umklapp

process, indicating that phonon-phonon interactions take a dominating role at higher temperatures. Interface scattering and grain boundary scattering are believed to be responsible for the behaviour below 573 K. The transition temperature of 573 K highlighted in orange colour in Fig. 5.30(a) is consistent with the calculated Debye temperature (572 K) for calcium cobaltite reported by Wu et al. [55].

The mean free path of phonons at 573 K was calculated from Equation (2.31) to understand the mechanism for thermal conduction, where velocity of sound is derived from the Debye temperature [56,57]. Fig. 5.30(b) shows l_{ph} as a function of bismuth and cobalt content. It is evident that l_{ph} of samples with x = 0.1 and y = 3.92 is about 8.9 Å, which is lower than the *c* lattice parameter (10.8 Å) in Fig. 5.14. The value is further reduced to 6.6 Å when the bismuth content increases to 0.3; this reduction in $\kappa_{lattice}$ with bismuth substitution matches well with investigations of Boyle et al. [26] and Li et al. [23]. Although l_{ph} is suspected to be enlarged due to smaller amounts of grain boundaries and interfaces caused by the increased grain size and enhanced texture [58], the decrease in $\kappa_{lattice}$ can still be explained by Equation (2.36). Because of the larger atomic mass differences between Bi (208.98) and Ca (40.08), the atom mass difference caused by substitution of Bi^{3+} for Ca^{2+} plays an important part in determining l_{ph} according to Equation (2.36). Higher bismuth substitution level means larger values of $\delta M/M$, resulting in a reduction in l_{ph} and hence enhanced phonon scattering. Interestingly, for samples with x = 0.3, when the cobalt content decreases from 4.0 to 3.96 l_{ph} is found to be around 7.9 Å within the level of uncertainty, and then falls sharply to 6.6 Å with the cobalt deficiency increasing to 0.08. Due to the similar bismuth doping level and average grain size (Fig. 5.16), the decrease in l_{ph} can be ascribed to the effects of crystalline defect scattering. Based on computational modelling, Demchenko et al. [59] reported that cobalt vacancies could be introduced by large cobalt deficiencies in cobaltites. Furthermore, the TEM data (Fig. 5.21) demonstrate small amounts of stacking faults in the $Ca_{2.7}Bi_{0.3}Co_{3.92}O_{9+\delta}$ ceramics annealed at 1203 K for 12 h. These crystalline defects are able to act as the scattering centres, thereby leading to a decrease in l_{ph} and $\kappa_{lattice}$ in turn.

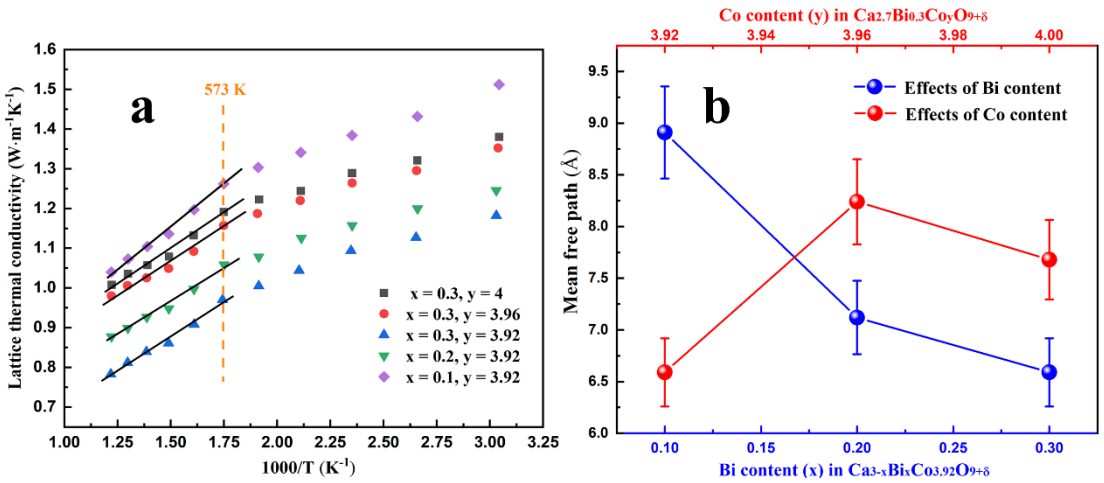

Fig. 5.30 (a) $\kappa_{lattice}$ as a function of the reciprocal temperature and (b) the phonon mean free path as a function of bismuth and cobalt content

Due to the thickness limitation (< 6 mm) for SPS-processed samples, the standard thermal conductivity measurement cannot be undertaken parallel to the *ab* plane. Therefore, κ parallel to the *ab* plane (κ//ab) for SPS-processed $Ca_{3-x}Bi_xCo_yO_{9+\delta}$ ceramics annealed at 1203 K was estimated using the data perpendicular to the *ab* plane (κ ⊥ ab). In order to understand the relationship between κ//ab and κ ⊥ ab for calcium cobaltite based ceramics prepared by the SPS route [28,50–52,60], the ratio of (κ//ab) /(κ ⊥ ab) was extracted from κ value data in earlier studies (Fig. 5.31(a)). It is evident that the values of (κ//ab) /(κ ⊥ ab) tend to approach a constant (1.4 to 2.75) with increasing temperature, mainly due to different degrees of the grain orientation caused by different experimental conditions used for SPS processing. The ratio of (κ//ab) /(κ ⊥ ab) seems insensitive to the heavy element doping when the fabrication route consistent [67]. Therefore, our textured calcium cobaltite is expected to behave the same way and have (κ//ab) /(κ ⊥ ab) ratio in the range 1.4-2.75. In principle, κ//ab values can be estimated using the κ (⊥ ab) data once a reliable ratio of (κ//ab) /(κ ⊥ ab) is obtained.

The κ//ab data of textured $Ca_{2.7}Bi_{0.3}Co_4O_9$ ceramics in earlier investigations [26,61] were used as the reference to calibrate the (κ//ab) /(κ ⊥ ab) ratio. As Fig. 5.31(b) shows, the κ//ab data for the annealed SPS-processed $Ca_{2.7}Bi_{0.3}Co_4O_{9+\delta}$ ceramic in the current work (red colour) are basically consistent with reported values for the same composition (blue and grey colours), when the (κ//ab) /(κ ⊥ ab) ratio is about 1.7. Therefore, the κ//ab data for the remaining compositions in our work were calculated using this (κ//ab) /(κ ⊥ ab) ratio accordingly.

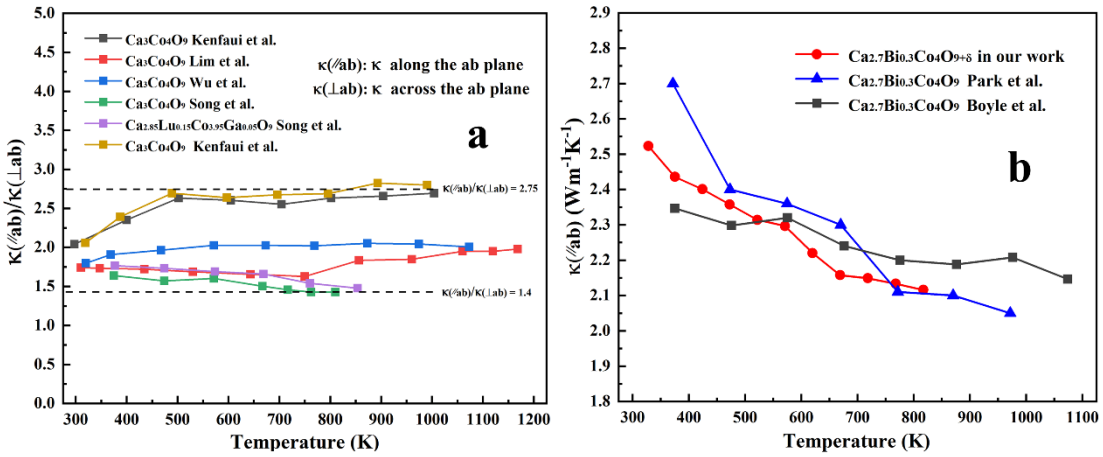

Fig. 5.31 (a) (κ//ab) /(κ ⊥ ab) ratios for $Ca_3Co_4O_9$ based ceramics prepared by the SPS route; (b) κ(//ab) for textured $Ca_{2.7}Bi_{0.3}Co_4O_{9+\delta}$ ceramics in our work and previous studies

The total κ values parallel and perpendicular to the *ab* plane for SPS-processed $Ca_{3-x}Bi_xCo_yO_{9+\delta}$ ceramics annealed at 1203 K are shown in Fig. 5.32. It is clear that the temperature dependences are similar in both directions: decreasing with increasing temperature. The lowest κ//ab value of 1.79 $mW^{-1}K^{-1}$ at 823 K was achieved for the sample with x = 0.3 and y = 3.92. The κ ⊥ ab values for all samples are about 1.7 times that of the κ//ab values, which is attributed to enhanced phonon scattering across the *ab* plane caused by both the layered crystal structure of calcium cobaltite and the preferred grain orientation along *ab* planes [50].

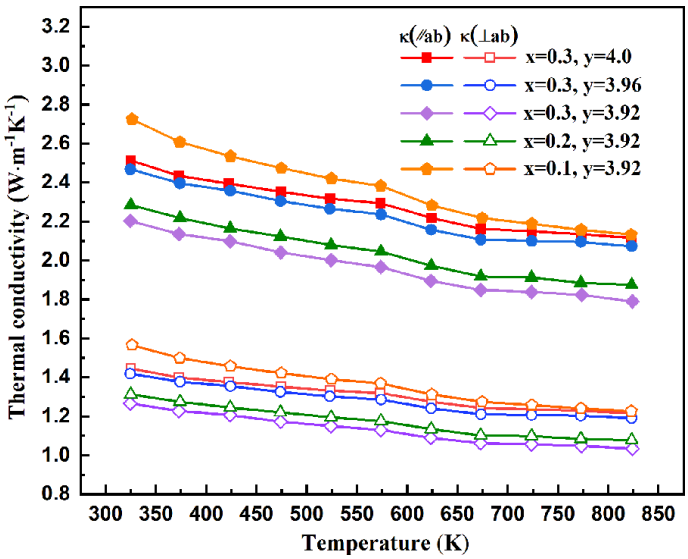

Fig. 5.32 Temperature dependence of total κ parallel (κ//ab) and perpendicular (κ ⊥ ab) to the *ab* plane for SPS-processed $Ca_{3-x}Bi_xCo_yO_{9+\delta}$ ceramics annealed at 1203 K (estimated using the optimised (κ//ab) /(κ ⊥ ab) ratio)

5.3.8 Thermoelectric Figure of Merit (ZT)

Highly textured samples (Fig. 5.18) were fabricated after annealing at 1203 K, thereby leading to strong anisotropy. It was reported that for textured calcium cobaltite, the ZT values perpendicular to the *ab* plane only reached half of the value parallel to the *ab* plane [28,50–52]. Therefore, the data parallel to the *ab* plane (ZT//ab) are used for evaluating the thermoelectric performance in this work. Fig. 5.33 illustrates the temperature dependence of ZT//ab values for SPS-processed $Ca_{3-x}Bi_xCo_yO_{9+\delta}$ ceramics annealed at 1203 K. It is clear that the ZT//ab for all samples increases with increasing temperature. At the same time, the values increase with increasing bismuth content and cobalt deficiency; the maximum ZT//ab of about 0.16 at 823 K is obtained for the sample with x = 0.3 and y = 3.92. Compared to ZT//ab values at 823 K for SPS-processed calcium cobaltite based materials in earlier studies [11,28,36,43,50–52,60,62–66], it is apparent that the maximum ZT//ab in this work outperforms the values (< 0.16) of most previous investigations. Although still higher ZT values can be achieved by either the toxic Cd doping [62] or the development of interface modulation via the complex processing [60], this work is still competitive due to the environmentally friendly chemical composition and simple fabrication process.

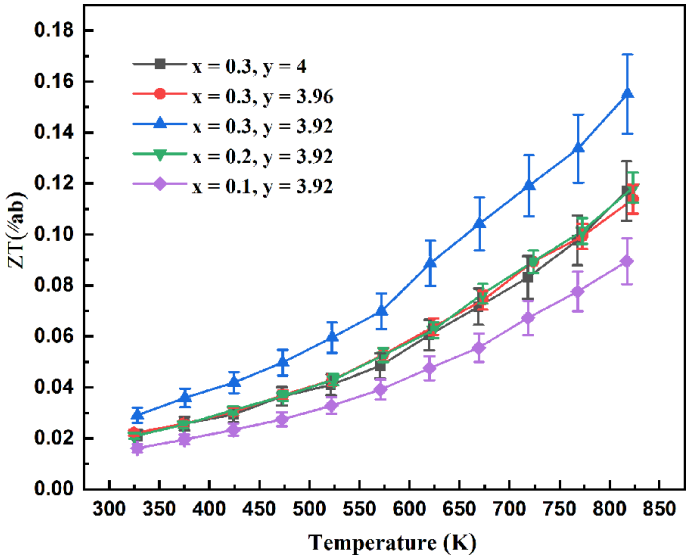

Fig. 5.33 Temperature dependence of ZT//ab values (calculated using the estimated thermal conductivity) of SPS-processed samples annealed at 1203 K

5.4 Summary

This chapter demonstrates a simple processing route to enhance thermoelectric properties of calcium cobaltite by controlling the microstructural evolution through tuning the chemical composition and annealing conditions. By air-annealing at 1203 K for 12 h, high-quality

$Ca_{3-x}Bi_xCo_yO_{9+\delta}$ (x = 0.1-0.3; y = 3.92-4.0) ceramics with minor amounts of Co_3O_4 were successfully fabricated via liquid-phase assisted spark plasma sintering.

The original SPS-processed samples were found to contain high volume fractions of poorly conducting secondary phases, including $Bi_2Ca_3Co_2O_9$, $Ca_3Co_2O_6$ and Co_3O_4, thereby reducing the overall electrical conductivity. After annealing at 1203 K in air, the reduction or elimination of the secondary phase (especially $Ca_3Co_2O_6$) was observed, thereby increasing the volume fractions of the primary phase ($Ca_3Co_4O_9$) and enhancing the overall electrical conductivity.

When Ca^{2+} in the rock salt layer of calcium cobaltite is substituted by Bi^{3+}, the introduction of oxygen into $Ca_3Co_4O_9$ lattice during the air-annealing efficiently suppresses the reduction of Co^{4+} caused by the bismuth substitution, thereby maintaining a high-level carrier concentration. The enhanced texture and increased grain size as a result of increasing bismuth substitution led to a decrease in the amounts of grain boundaries and interfaces, thereby improving the carrier mobility. The decrease in thermal conductivity with increasing bismuth substitution and cobalt deficiency is mainly due to the enhanced phonon scattering resulting from the 'heavy' bismuth doping at calcium sites and the presence of crystalline defects such as the stacking faults and point defects. As a result, a 25 % increase in power factor parallel to the *ab* plane and a 20 % decrease in thermal conductivity perpendicular to the *ab* plane were obtained for $Ca_{2.7}Bi_{0.3}Co_{3.92}O_{9+\delta}$ ceramics compared to most previous studies, leading to a completive ZT value (parallel to the *ab* plane) of 0.16 at 823 K.

References

[1] D. Sedmidubský, V. Jakeš, O. Jankovský, J. Leitner, Z. Sofer, J. Hejtmánek, Phase equilibria in Ca–Co–O system, J. Solid State Chem. 194 (2012) 199–205.

[2] J.C. Diez, S.H. Rasekh, M.A. Madre, E. Guilmeau, S. Marinel, A. Sotelo, Improved Thermoelectric Properties of Bi-M-Co-O (M = Sr, Ca) Misfit Compounds by Laser Directional Solidification, J. Electron. Mater. 39 (2010) 1601–1605.

[3] P. Carvillo, Y. Chen, C. Boyle, P.N. Barnes, X. Song, Thermoelectric Performance Enhancement of Calcium Cobaltite through Barium Grain Boundary Segregation, Inorg. Chem. 54 (2015) 9027–9032.

[4] H. Wang, X. Sun, X. Yan, D. Huo, X. Li, J.-G. Li, X. Ding, Fabrication and thermoelectric properties of highly textured $Ca_9Co_{12}O_{28}$ ceramic, J. Alloys Compd.

582 (2014) 294–298.

[5] T. Schulz, J. Töpfer, Thermoelectric properties of $Ca_3Co_4O_9$ ceramics prepared by an alternative pressure-less sintering/annealing method, J. Alloys Compd. 659 (2016) 122–126.

[6] B. Paul, J.L. Schroeder, S. Kerdsongpanya, N. Van Nong, N. Schell, D. Ostach, J. Lu, J. Birch, P. Eklund, Mechanism of Formation of the Thermoelectric Layered Cobaltate $Ca_3Co_4O_9$ by Annealing of CaO–CoO Thin Films, Adv. Electron. Mater. 1 (2015) 1400022.

[7] L. Zhang, T.T. Tan, S. Li, The effect of annealing oxygen concentration in the transformation of Ca_xCoO_2 to thermoelectric $Ca_3Co_4O_9$, RSC Adv. 5 (2015) 28158–28162.

[8] G. Constantinescu, S. Rasekh, M.A. Torres, J.C. Diez, M.A. Madre, A. Sotelo, Effect of Sr substitution for Ca on the $Ca_3Co_4O_9$ thermoelectric properties, J. Alloys Compd. 577 (2013) 511–515.

[9] J.C. Diez, M.A. Torres, S. Rasekh, G. Constantinescu, M.A. Madre, A. Sotelo, Enhancement of $Ca_3Co_4O_9$ thermoelectric properties by Cr for Co substitution, Ceram. Int. 39 (2013) 6051–6056.

[10] S. Li, R. Funahashi, I. Matsubara, K. Ueno, S. Sodeoka, H. Yamada, Synthesis and Thermoelectric Properties of the New Oxide Materials $Ca_{3-x}Bi_xCo_4O_{9+\delta}$ ($0.0 < x < 0.75$), Chem. Mater. 12 (2000) 2424–2427.

[11] Y. Liu, Y. Lin, L. Jiang, C.-W. Nan, Z. Shen, Thermoelectric properties of Bi^{3+} substituted Co-based misfit-layered oxides, J. Electroceramics. 21 (2008) 748–751.

[12] I. V Matsukevich, A.I. Klyndyuk, E.A. Tugova, M. V Tomkovich, N.S. Krasutskaya, V. V Gusarov, Synthesis and properties of materials based on layered calcium and bismuth cobaltites, Russ. J. Appl. Chem. 88 (2015) 1241–1247.

[13] M.A. Madre, F.M. Costa, N.M. Ferreira, A. Sotelo, M.A. Torres, G. Constantinescu, S. Rasekh, J.C. Diez, Preparation of high-performance $Ca_3Co_4O_9$ thermoelectric ceramics produced by a new two-step method, J. Eur. Ceram. Soc. 33 (2013) 1747–1754.

[14] A. Sotelo, G. Constantinescu, S. Rasekh, M.A. Torres, J.C. Diez, M.A. Madre, Improvement of thermoelectric properties of $Ca_3Co_4O_9$ using soft chemistry synthetic

methods, J. Eur. Ceram. Soc. 32 (2012) 2415–2422.

[15] K. Park, D.A. Hakeem, J.S. Cha, Synthesis and structural properties of thermoelectric $Ca_{3-x}Ag_xCo_4O_{9+\delta}$ powders, Dalt. Trans. 45 (2016) 6990–6997.

[16] R. Zhang, Y. Lu, L. Wei, Z. Fang, C. Lu, Y. Ni, Z. Xu, S. Tao, P. Li, Synthesis and conductivity properties of $Gd_{0.8}Ca_{0.2}BaCo_2O_{5+\delta}$ double perovskite by sol–gel combustion, J. Mater. Sci. Mater. Electron. 26 (2015) 9941–9948.

[17] H. Liu, G.C. Lin, X.D. Ding, J.X. Zhang, Mechanical relaxation in thermoelectric oxide $Ca_{3-x}Sr_xCo_4O_{9+\delta}$ (x = 0, 0.25, 0.5, 1.0) associated with oxygen vacancies, J. Solid State Chem. 200 (2013) 305–309.

[18] Y. Huang, B. Zhao, S. Lin, R. Ang, Y. Sun, Enhanced Thermoelectric Performance Induced by Cr Doping at Ca-Sites in $Ca_3Co_4O_9$ System, J. Am. Ceram. Soc. 97 (2014) 3589–3596.

[19] I. V Matsukevich, A.I. Klyndyuk, E.A. Tugova, A.N. Kovalenko, A.A. Marova, N.S. Krasutskaya, Thermoelectric properties of $Ca_{3-x}Bi_xCo_4O_{9+\delta}$ ($0.0 \leqslant x \leqslant 1.5$) ceramics, Inorg. Mater. 52 (2016) 593–599.

[20] A. Sotelo, S. Rasekh, M.A. Madre, E. Guilmeau, S. Marinel, J.C. Diez, Solution-based synthesis routes to thermoelectric $Bi_2Ca_2Co_{1.7}O_x$, J. Eur. Ceram. Soc. 31 (2011) 1763–1769.

[21] D. Lu, G. Chen, J. Pei, X. Yang, H. Xian, Effect of erbium substitution on thermoelectric properties of complex oxide $Ca_3Co_2O_6$ at high temperatures, J. Rare Earths. 26 (2008) 168–172.

[22] P. Vikas, J. Pradeep, C. Manik, S. Shashwati, Synthesis and characterization of Co_3O_4 thin film, Soft Nanosci. Lett. 2012 (2011).

[23] S. Li, R. Funahashi, I. Matsubara, K. Ueno, S. Sodeoka, H. Yamada, Thermoelectric properties of oxides $Ca_2Co_2O_5$ with Bi substitution, J. Mater. Sci. Lett. 19 (2000) 1339–1341.

[24] Y. Wang, Y. Sui, X. Wang, W. Su, X. Liu, Enhanced high temperature thermoelectric characteristics of transition metals doped $Ca_3Co_4O_{9+\delta}$ by cold high-pressure fabrication, J. Appl. Phys. 107 (2010) 33708.

[25] P.H. Xiang, Y. Kinemuchi, H. Kaga, K. Watari, Fabrication and thermoelectric

properties of $Ca_3Co_4O_9$/Ag composites, J. Alloys Compd. 454 (2008) 364–369.

[26] C. Boyle, P. Carvillo, Y. Chen, E.J. Barbero, D. Mcintyre, X. Song, Grain boundary segregation and thermoelectric performance enhancement of bismuth doped calcium cobaltite, J. Eur. Ceram. Soc. 36 (2016) 601–607.

[27] D. Grebille, S. Lambert, F. Bouree, V. Petricek, Contribution of powder diffraction for structure refinements of aperiodic misfit cobalt oxides, J. Appl. Crystallogr. 37 (2004) 823–831.

[28] N. Wu, T.C. Holgate, N. Van Nong, N. Pryds, S. Linderoth, High temperature thermoelectric properties of $Ca_3Co_4O_{9+\delta}$ by auto-combustion synthesis and spark plasma sintering, J. Eur. Ceram. Soc. 34 (2014) 925–931.

[29] D. Srivastava, C. Norman, F. Azough, D. Ekren, K. Chen, M.J. Reece, I.A. Kinloch, R. Freer, Anisotropy and enhancement of thermoelectric performance of $Sr_{0.8}La_{0.067}Ti_{0.8}Nb_{0.2}O_{3-\delta}$ ceramics by graphene additions, J. Mater. Chem. A. 7 (2019) 24602–24613.

[30] W. Seo, S. Lee, Y. Lee, M. Lee, Y. Masuda, K. Koumoto, High-resolution transmission electron microscopy study of $Ca_3Co_4O_9$, Microscopy. 53 (2004) 397–401.

[31] K. Yubuta, X. Huang, Y. Miyazaki, T. Kajitani, High-Resolution Electron Microscopy Study of $[(Ca, Bi)_2CoO_3]_{0.62}CoO_2$, J. Phys. Soc. Japan. 77 (2008) 94603.

[32] T. Sun, H.H. Hng, Q. Yan, J. Ma, Effects of Pulsed Laser Deposition Conditions on the Microstructure of $Ca_3Co_4O_9$ Thin Films, J. Electron. Mater. 39 (2010) 1611–1615.

[33] T. Sun, J. Ma, Q.Y. Yan, Y.Z. Huang, J.L. Wang, H.H. Hng, Influence of pulsed laser deposition rate on the microstructure and thermoelectric properties of $Ca_3Co_4O_9$ thin films, J. Cryst. Growth. 311 (2009) 4123–4128.

[34] J. Chastain, Handbook of X-ray photoelectron spectroscopy, Perkin-Elmer Corp. 40 (1992) 221.

[35] C.S. Lim, C.K. Chua, Z. Sofer, O. Jankovský, M. Pumera, Alternating Misfit Layered Transition/Alkaline Earth Metal Chalcogenide $Ca_3Co_4O_9$ as a New Class of Chalcogenide Materials for Hydrogen Evolution, Chem. Mater. 26 (2014) 4130–4136.

[36] D. Moser, L. Karvonen, S. Populoh, M. Trottmann, A. Weidenkaff, Influence of the

oxygen content on thermoelectric properties of $Ca_{3-x}Bi_xCo_4O_{9+\delta}$ system, Solid State Sci. 13 (2011) 2160–2164.

[37] Y. Yin, S. Saini, D. Magginetti, K. Tian, A. Tiwari, Thermoelectric response of porous $Ca_3Co_4O_9$ prepared by an eco-friendly technique, Ceram. Int. 43 (2017) 9505–9511.

[38] Y. Wakisaka, S. Hirata, T. Mizokawa, Y. Suzuki, Y. Miyazaki, T. Kajitani, Electronic structure of $Ca_3Co_4O_9$ studied by photoemission spectroscopy: Phase separation and charge localization, Phys. Rev. B. 78 (2008) 235107.

[39] F. Delorme, C.F. Martin, P. Marudhachalam, D. Ovono Ovono, G. Guzman, Effect of Ca substitution by Sr on the thermoelectric properties of $Ca_3Co_4O_9$ ceramics, J. Alloys Compd. 509 (2011) 2311–2315.

[40] D. Kenfaui, D. Chateigner, M. Gomina, J.G. Noudem, Texture, mechanical and thermoelectric properties of $Ca_3Co_4O_9$ ceramics, J. Alloys Compd. 490 (2010) 472–479.

[41] J.G. Noudem, A new process for lamellar texturing of thermoelectric $Ca_3Co_4O_9$ oxides by spark plasma sintering, J. Eur. Ceram. Soc. 29 (2009) 2659–2663.

[42] J.Y. Cho, O.J. Kwon, Y.K. Chung, J.S. Kim, W.S. Kim, K.J. Song, C. Park, Effect of Trivalent Bi Doping on the Seebeck Coefficientand Electrical Resistivity of $Ca_3Co_4O_9$, J. Electron. Mater. 44 (2015) 3621–3626.

[43] S. Porokhin, L. Shvanskaya, V. Khovaylo, A. Vasiliev, Effect of NaF doping on the thermoelectric properties of $Ca_3Co_4O_9$, J. Alloys Compd. 695 (2017) 2844–2849.

[44] D. Kenfaui, G. Bonnefont, D. Chateigner, G. Fantozzi, M. Gomina, J.G. Noudem, $Ca_3Co_4O_9$ ceramics consolidated by SPS process: Optimisation of mechanical and thermoelectric properties, Mater. Res. Bull. 45 (2010) 1240–1249.

[45] T. Yin, D. Liu, Y. Ou, F. Ma, S. Xie, J.-F. Li, J. Li, Nanocrystalline Thermoelectric $Ca_3Co_4O_9$ Ceramics by Sol−Gel Based Electrospinning and Spark Plasma Sintering, J. Phys. Chem. C. 114 (2010) 10061–10065.

[46] T. Sun, H.H. Hng, Q.Y. Yan, J. Ma, Enhanced high temperature thermoelectric properties of Bi-doped c-axis oriented $Ca_3Co_4O_9$ thin films by pulsed laser deposition, J. Appl. Phys. 108 (2010) 83709.

[47] Y. Zhou, I. Matsubara, W. Shin, N. Izu, N. Murayama, Effect of grain size on electric resistivity and thermopower of $(Ca_{2.6}Bi_{0.4})Co_4O_9$ thin films, J. Appl. Phys. 95 (2003) 625–628.

[48] F. Delorme, P. Diaz-Chao, E. Guilmeau, F. Giovannelli, Thermoelectric properties of $Ca_3Co_4O_9$–Co_3O_4 composites, Ceram. Int. 41 (2015) 10038–10043.

[49] Z. Shi, F. Gao, J. Zhu, J. Xu, Y. Zhang, T. Gao, M. Qin, Influence of liquid−phase sintering on microstructure and thermoelectric properties of $Ca_3Co_4O_9$−based ceramics with Bi_2O_3 additive, J. Mater. 5 (2019) 711–720.

[50] C.H. Lim, W.S. Seo, S. Lee, Y.S. Lim, J.Y. Kim, H.H. Park, S.M. Choi, K.H. Lee, K. Park, Anisotropy of the thermoelectric figure of merit (ZT) in textured $Ca_3Co_4O_9$ ceramics prepared by using a spark plasma sintering process, J. Korean Phys. Soc. 66 (2015) 794–799.

[51] D. Kenfaui, B. Lenoir, D. Chateigner, B. Ouladdiaf, M. Gomina, J.G. Noudem, Development of multilayer textured $Ca_3Co_4O_9$ materials for thermoelectric generators: Influence of the anisotropy on the transport properties, J. Eur. Ceram. Soc. 32 (2012) 2405–2414.

[52] D. Kenfaui, D. Chateigner, M. Gomina, J.G. Noudem, BachirOuladdiaf, A. Dauscher, B. Lenoir, Volume Texture and Anisotropic Thermoelectric Properties in $Ca_3Co_4O_9$ Bulk Materials, Mater. Today Proc. 2 (2015) 637–646.

[53] S. Raghavan, M.J. Mayo, H. Wang, R.B. Dinwiddie, W.D. Porter, The effect of grain size, porosity and yttria content on the thermal conductivity of nanocrystalline zirconia, Scr. Mater. 39 (1998) 1119–1125.

[54] M. Gunes, M. Ozenbas, Effect of grain size and porosity on phonon scattering enhancement of $Ca_3Co_4O_9$, J. Alloys Compd. 626 (2015) 360–367.

[55] L. Wu, Q. Meng, C. Jooss, J.-C. Zheng, H. Inada, D. Su, Q. Li, Y. Zhu, Origin of Phonon Glass–Electron Crystal Behavior in Thermoelectric Layered Cobaltate, Adv. Funct. Mater. 23 (2013) 5728–5736.

[56] S.R. Popuri, A.J.M. Scott, R.A. Downie, M.A. Hall, E. Suard, R. Decourt, M. Pollet, J.W.G. Bos, Glass-like thermal conductivity in $SrTiO_3$ thermoelectrics induced by A-site vacancies, RSC Adv. 4 (2014) 33720–33723.

[57] D. Ekren, F. Azough, R. Freer, Enhancing the thermoelectric properties of

$Sr_{1-x}Pr_{2x/3}\square_{x/3}TiO_{3\pm\delta}$ through control of crystal structure and microstructure, Philos. Trans. R. Soc. A Math. Phys. Eng. Sci. 377 (2019) 20190037.

[58] J. Zhang, J. Xu, X. Tan, H. Wang, G.Q. Liu, H. Shao, B. Yu, S. Yue, J. Jiang, Optimized orientation and enhanced thermoelectric performance in $Sn_{0.97}Na_{0.03}Se$ with Te addition, J. Mater. Chem. C. 7 (2019) 2653–2658.

[59] D.O. Demchenko, D.B. Ameen, Lattice thermal conductivity in bulk and nanosheet Na_xCoO_2, Comput. Mater. Sci. 82 (2014) 219–225.

[60] M.E. Song, H. Lee, M.G. Kang, W. Li, D. Maurya, B. Poudel, J. Wang, M.A. Meeker, G.A. Khodaparast, S.T. Huxtable, S. Priya, Nanoscale Texturing and Interfaces in Compositionally Modified $Ca_3Co_4O_9$ with Enhanced Thermoelectric Performance, ACS Omega. 3 (2018) 10798–10810.

[61] J.W. Park, D.H. Kwak, S.H. Yoon, S.C. Choi, Thermoelectric properties of highly oriented $Ca_{2.7}Bi_{0.3}Co_4O_9$ fabricated by rolling process, J. Ceram. Soc. Japan. 117 (2009) 643–646.

[62] S. Butt, W. Xu, W.Q. He, Q. Tan, G.K. Ren, Y. Lin, C.W. Nan, Enhancement of thermoelectric performance in Cd-doped $Ca_3Co_4O_9$ via spin entropy, defect chemistry and phonon scattering, J. Mater. Chem. A. 2 (2014) 19479–19487.

[63] Z. Shi, C. Zhang, T. Su, J. Xu, J. Zhu, H. Chen, T. Gao, M. Qin, P. Zhang, Y. Zhang, H. Yan, F. Gao, Boosting the Thermoelectric Performance of Calcium Cobaltite Composites through Structural Defect Engineering, ACS Appl. Mater. Interfaces. 12 (2020) 21623–21632.

[64] N.B. Feng, Y.W. Liao, S.Y. Li, Y. He, Y. Lu, Y.R. Jin, Anisotropy of thermoelectric composites $0.7Ca_3Co_4O_9/0.3Bi_2Ca_2Co_2O_y$, J. Mater. Sci. Mater. Electron. 30 (2019) 19471–19476.

[65] N. Wu, T.C. Holgate, N. Van Nong, N. Pryds, S. Linderoth, Effects of Synthesis and Spark Plasma Sintering Conditions on the Thermoelectric Properties of $Ca_3Co_4O_{9+\delta}$, J. Electron. Mater. 42 (2013) 2134–2142.

[66] H.Q. Liu, F.P. Wang, F. Liu, Y. Song, Z.H. Jiang, Thermoelectric performance of SPS sintered $[(Ca_{0.95}M_{0.05})_2CoO_3][CoO_2]_{1.61}$, J. Mater. Sci. Mater. Electron. 17 (2006) 525–528.

6. Tuning the Power Factor of Cold Sintered Calcium Cobaltite Ceramics by Optimising Heat-treatment

6.1 Introduction

In Chapters 4 and 5, the calcium cobaltite ceramics were prepared by traditional solid state reaction and spark plasma sintering routes. However, the former technique cannot guarantee production of highly dense samples, whilst the latter one is unsuitable for large-scale production and is heavily restricted by the rigorous experimental conditions (electrical current supply). In addition, both fabrication routes need high sintering temperatures (> 1023 K) for achieving densification, thereby increasing processing costs. By contrast, cold sintering, an emerging sintering technique, provides opportunities to densify ceramic bulks at low temperatures (< 573 K) with low production costs and simple processing.

In general, two phases are basically required for cold sintering: the parent phase (ceramic powders to form green bulks) and the transport phase (liquid to facilitate mass transfer) [1]. The basic process involves the wetting of ceramic powders by mixing with the liquid phase material, followed by the decomposition and dissolution of the solid surface. With the aid of temperature and pressure, the solid particles and the liquid are rearranged to enable densification. Driven by the decrease of the surface energy and surface curvature of particles, atomic clusters or ionic species move towards grain contacts to form a dense solid. Local capillarity forces can also be enhanced through pronounced precipitation via the Gibbs-Marangoni effect, as a result of the transient liquid evaporation in and around the porous network constructed by particles [2]. Therefore, dissolution-based transport, in conjunction with substantial capillarity pressure, are believed to be the dominating densification mechanisms.

To date, inorganic materials densified by cold sintering have been widely employed in the fields of ferroelectrics [3], piezoelectrics [4], microwave dielectrics [5], fuel cell cathodes [6], and refractories [7]. However, only a few attempts have been made to fabricate calcium cobaltite ceramics by cold sintering. Funahashi et al. [8] prepared ZnO-$Ca_3Co_4O_9$ multilayer ceramics by cold sintering but mainly focused on the output voltage of the thermoelectric module, where the power factor of the material was not evaluated. Santos et al. [9] investigated the effects of fabrication routes (solid state reaction and cold sintering) on thermoelectric performance of calcium cobaltite. However, the relative density of the synthesized ceramics only reached < 80 % theoretical; further efforts are still required for achieving higher densification.

In this chapter, highly dense calcium cobaltite ceramics were successfully prepared by cold sintering, using the optimal chemical composition selected in Chapters 4 and 5. Our previous studies have shown that the heat-treatment plays a vital role in controlling microstructural evolution in calcium cobaltite ceramics. Here, the influence of calcination process for powders and annealing conditions for cold sintered bulks on thermoelectric response was studied in detail. By optimizing the heat-treatment, the formation of poorly conducting secondary phases was suppressed, the texture was enhanced and the grain growth was controlled. An 85 % enhancement in power factor of cold sintered calcium cobaltite ceramics was eventually achieved as a result of the modified microstructure.

6.2 Density and Porosity

The cold sintered $Ca_{2.7}Bi_{0.3}Co_{3.92}O_{9+\delta}$ ceramics prepared for this study are listed in Table 6.1. Here, powders calcined at 1203 K for 12 h (once) are denoted as single-fired powders and those calcined at 1203 K for 12 h (twice) are denoted as double-fired powders in the following sections. As-received samples refer to the original cold sintered ceramics without annealing.

Table 6.1 List of compositions, heat-treatment conditions and sample codes for cold sintered samples

Composition	Calcination conditions	Annealing conditions	Sample ID
$Ca_{2.7}Bi_{0.3}Co_{3.92}O_{9+\delta}$	1203 K for 12 h (once)	As received	S1A0
	1203 K for 12 h (once)	1203 K for 12 h	S1A12
	1203 K for 12 h (once)	1203 K for 24 h	S1A24
	1203 K for 12 h (twice)	As received	S2A0
	1203 K for 12 h (twice)	1203 K for 12 h	S2A12
	1203 K for 12 h (twice)	1203 K for 24 h	S2A24

Fig. 6.1 shows the bulk density and porosity of $Ca_{2.7}Bi_{0.3}Co_{3.92}O_{9+\delta}$ ceramics as a function of annealing time. In contrast to the density data for cold sintered calcium cobaltite in an earlier study (about 75 % theoretical) [9], our samples have higher bulk densities within the range 3.96~4.42 g/cm^3 (84.8~94.6 % theoretical), showing at least 10 % enhancement. For S1A0, the bulk density is constant within uncertainty levels, independent of annealing time, whilst the value for S2A0 shows a slight decrease with increasing annealing time. The bulk densities of S2A0, S2A12 and S2A24 (3.96-4.29 g/cm^3) are slightly lower than those of

S1A0, S1A12 and S1A24 (4.25-4.42 g/cm^3). The porosity of all samples is positively correlated with annealing time; the highest value of 13.1 % is obtained for S2A24. This could be ascribed to the phase compositional changes under different heat-treatment conditions and the thickness differences between synthesized samples (S1A0, S1A12 and S1A24: 2.0~3.0 mm; S2A0, S2A12 and S2A24: 4.0~5.0 mm).

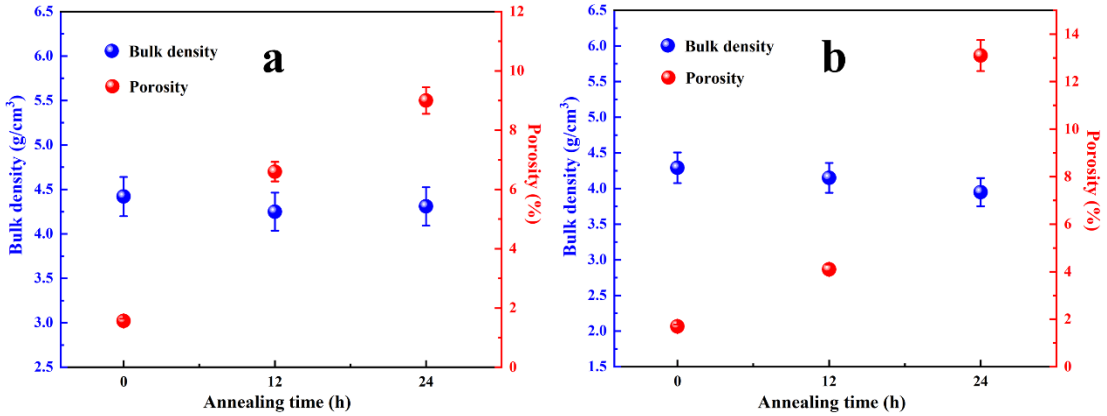

Fig. 6.1 Bulk density and porosity of cold sintered $Ca_{2.7}Bi_{0.3}Co_{3.92}O_{9+\delta}$ ceramics prepared from (a) the single-fired powders and (b) double-fired powders

6.3 XRD Analysis

XRD patterns of $Ca_{2.7}Bi_{0.3}Co_{3.92}O_{9+\delta}$ powders calcined under different conditions (Fig. 6.2) show the main phase in both patterns is indexed as monoclinic $Ca_3Co_{3.744}O_{9.176}$ (JCPDS: # 05-001-0461). However, only the single-fired powders show traces of three minor phases including $Bi_2Ca_3Co_2O_9$ (JCPDS: # 52-0125), $Ca_3Co_2O_6$ (JCPDS: # 51-0311) and Co_3O_4 (JCPDS: # 42-0461). By contrast, X-ray pure calcium cobaltite powders can be fabricated by double calcination at 1203 K for 12 h, indicating that a repeating calcination process is beneficial to eliminating secondary phases.

Fig. 6.3 shows XRD patterns of cold sintered $Ca_{2.7}Bi_{0.3}Co_{3.92}O_{9+\delta}$ ceramics annealed under different conditions. As expected, the main reflections in all patterns are indexed as $Ca_3Co_{3.744}O_{9.176}$ (JCPDS: # 05-001-0461). It is noted that a small amount of secondary phases ($Bi_2Ca_3Co_2O_9$ and Co_3O_4) can still be detected in the original cold sintered $Ca_{2.7}Bi_{0.3}Co_{3.92}O_{9+\delta}$ ceramic prepared from the single-fired powders (S1A0); the absence of $Ca_3Co_2O_6$ should be a natural consequence of phase decomposition during further heat-treatment. After annealing at 1203 K for 12 h or 24 h, the secondary phases in S1A12 and S1A24 are almost eliminated. By marked contrast, there are no impurities for both the original (S2A0) and annealed samples (S2A12 and S2A24) prepared by the double-fired

powders, suggesting that repeating calcination process helps to promote the reaction for forming calcium cobaltite.

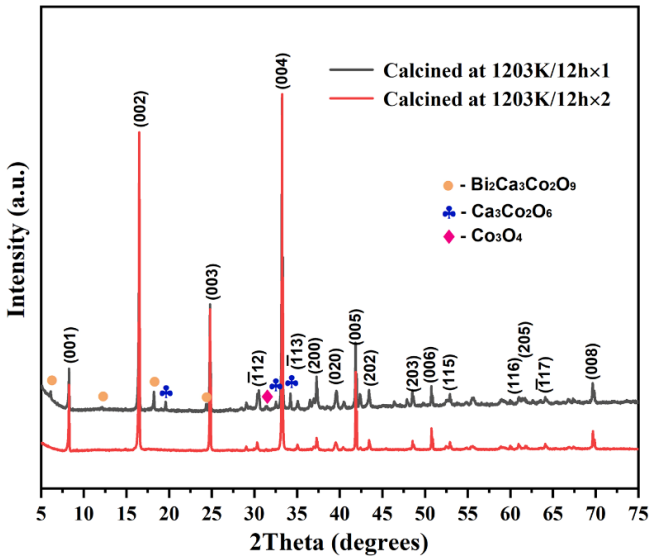

Fig. 6.2 XRD patterns of $Ca_{2.7}Bi_{0.3}Co_{3.92}O_{9+\delta}$ powders calcined at different conditions

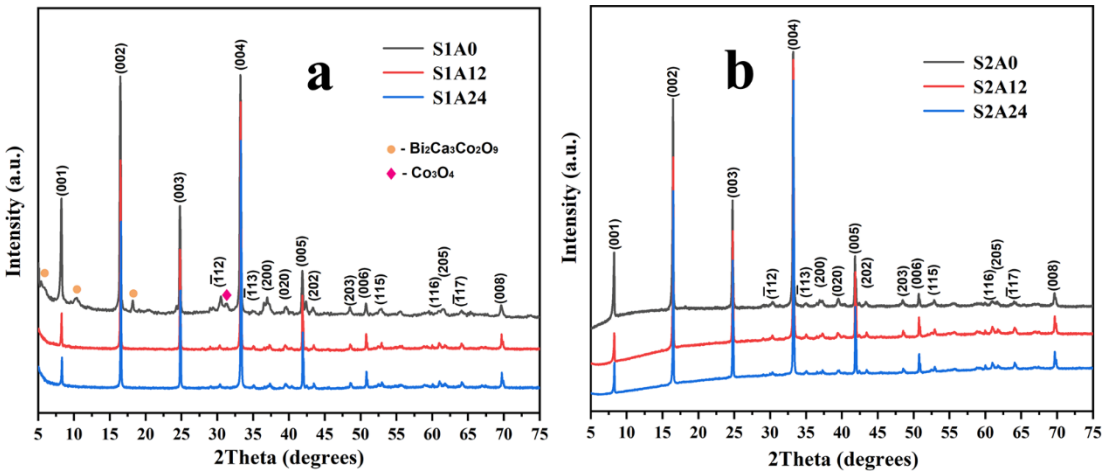

Fig. 6.3 XRD patterns of cold sintered $Ca_{2.7}Bi_{0.3}Co_{3.92}O_{9+\delta}$ ceramics annealed at 1203 K for different times: (a) S1A0: 0h, S1A12: 12 h, S1A24: 24 h, and (b) S2A0: 0 h, S2A12: 12 h, S2A24: 24 h

As the (00l) family of peaks in XRD patterns of annealed cold sintered $Ca_{2.7}Bi_{0.3}Co_{3.92}O_{9+\delta}$ ceramics (Fig. 6.3) shows stronger intensities than other reflection peaks, Lotgering factors were calculated to characterise the grain orientation (Table 6.2; p and p_0 are defined in Equation (3.6)). It is clear that the Lotgering factors for annealed samples vary between 0.79 and 0.89, indicating that strong texture is developed by cold sintering in combination with the annealing process. The texture development can be attributed to the high aspect ratio (*a*-

b/c) planes of calcium cobaltite grains, the axial pressure introduced during sintering and easier grain boundary sliding due to the removal of secondary phases. After subtracting the background of the raw XRD data, the calculated Lotgering factors increase with round of calcination process and sintering time, suggesting that repeating calcination process and extending sintering time help to further reduce the secondary phases that act to pin grains.

Table 6.2 Calculated Lotgering factors of annealed cold sintered $Ca_{2.7}Bi_{0.3}Co_{3.92}O_{9+\delta}$ ceramics

Sample ID	**p**	**p_0**	**Lotgering factor**
S1A0	0.778	0.305	0.68
S1A12	0.812	0.305	0.73
S1A24	0.832	0.305	0.76
S2A0	0.800	0.305	0.71
S2A12	0.858	0.305	0.79
S2A24	0.881	0.305	0.83

Fig. 6.4 shows the Le Bail refinement of the XRD data for annealed cold sintered $Ca_{2.7}Bi_{0.3}Co_{3.92}O_{9+\delta}$ ceramics (Fig. 6.3), using the modulated misfit structure ($[Ca_2CoO_3][CoO_2]_{1.62}$) reported by Grebille et al. [10]. Data for S1A12 and S1A24 show reasonable R_{wp} (9.74 and 9.70) and GoF (2.31 and 2.28) values. Interestingly, S2A12 and S2A24 demonstrate smaller R_{wp} values (2.61 and 3.23) but larger GoF values (5.43 and 6.56); this could result from the distinguishable differences in the background (Fig. 6.3) caused by fluorescent scattering.

The refined lattice parameters of annealed cold sintered $Ca_{2.7}Bi_{0.3}Co_{3.92}O_{9+\delta}$ ceramics are summarised in Table 6.3; they show negligible variation with increasing annealing time. When the annealing time is fixed at 12 h or 24 h, it is noticeable that compared to S1A12 and S1A24, the lattice parameter b_1 and b_2 of S2A12 and S2A24 show a slight increase and a decrease, respectively. It was reported that bismuth is more likely to substitute Ca sites in the crystal lattice of calcium cobaltite, thereby leading to serious distortion in b_1 [11]. Here, the changes in lattice parameter *b* could be related to pronounced bismuth doping effects due to the extended heat-treatment (double calcination).

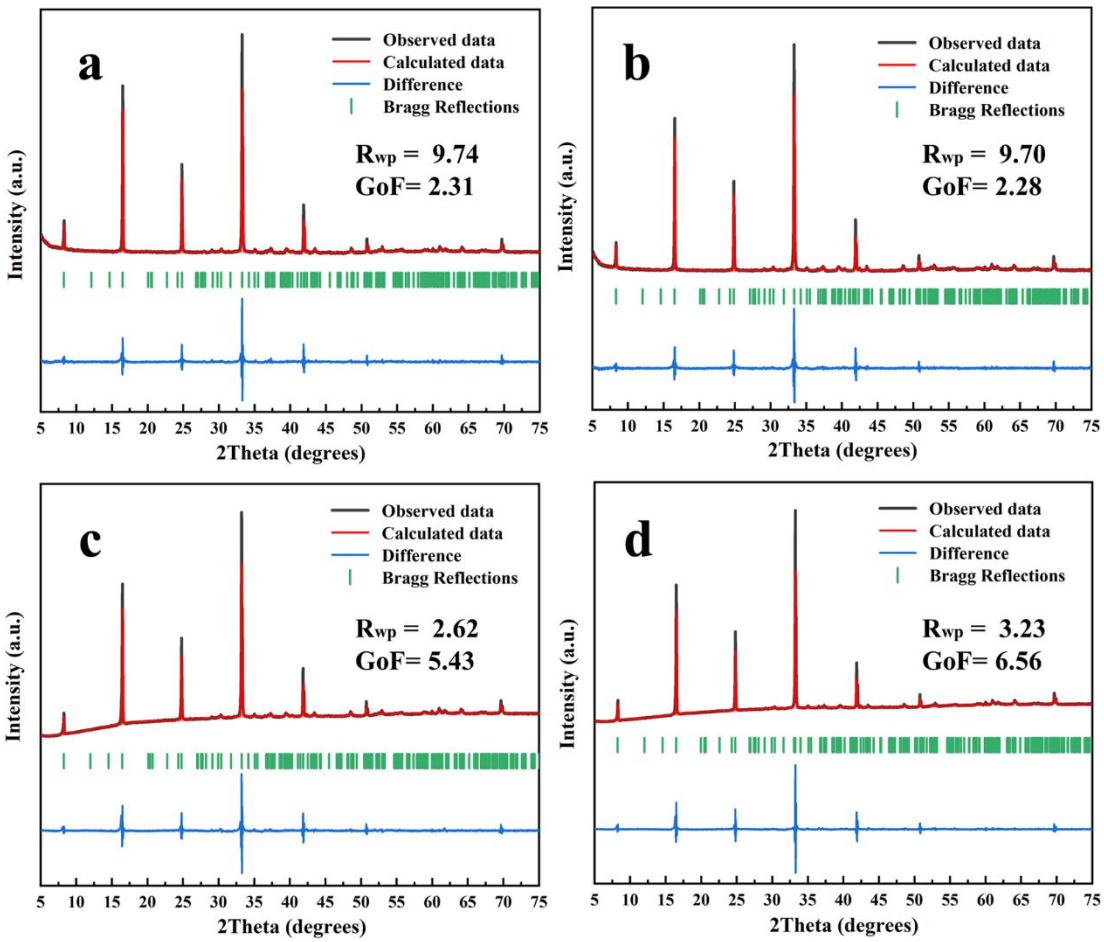

Fig. 6.4 Le Bail refinement data for annealed $Ca_{2.7}Bi_{0.3}Co_{3.92}O_{9+\delta}$ ceramics prepared by cold sintering (a. S1A12, b. S1A24, c. S2A12, d. S2A24)

Table 6.3 Refined lattice parameters for annealed $Ca_{2.7}Bi_{0.3}Co_yO_{9+\delta}$ ceramics prepared by cold sintering

Sample ID	a (Å)	b_1 (Å)	b_2 (Å)	c (Å)	β (°)
S1A12	4.8319(6)	4.5646(2)	2.8269(4)	10.9027(6)	98.319(7)
S1A24	4.8331(5)	4.5647(4)	2.8275(2)	10.9038(6)	98.338(7)
S2A12	4.8341(4)	4.5692(5)	2.8214(3)	10.9043(7)	98.134(7)
S2A24	4.8335(7)	4.5714(4)	2.8218(2)	10.9037(4)	98.062(8)

*b_1 for rock salt layers, and b_2 for CoO_2 layers.

6.4 SEM-EDS Analysis

Fig. 6.5 presents the backscattered electron (BSE) images for both the single-fired and double-fired $Ca_{2.7}Bi_{0.3}Co_{3.92}O_{9+\delta}$ powders. It can be seen that randomly distributed grey particles containing bright secondary phases are present in all samples, indicating the calcination process cannot guarantee complete reaction to form calcium cobaltite. The maximum particle size reaches about 90.0 μm for single-fired powders (Fig. 6.5(a)), showing severe agglomeration compared to that of the double-fired powders (50.0 μm) (Fig. 6.5(c)). Notably, the fractions of bright phases in Fig. 6.5(c) are significantly lower than those in Fig. 6.5(a), suggesting that the bright secondary phases can be efficiently reduced by the double calcination process.

In order to determine the chemical composition of calcined powders, EDS point analyses were performed at sites 1-5 (Fig. 5(b, d)) and the results are displayed in Table 6.4. The bright phases at sites 1 and 4 are confirmed as Bi-rich phases compared to the primary phase (calcium cobaltite), but the latter (site 4) shows cobalt deficiency in contrast to the former (site 1). The main phase at sites 3 and 5 is indexed as $(Ca,Bi)_3Co_4O_9$, indicating that bismuth has been successfully doped into the crystal lattice of calcium cobaltite. The chemical composition of the light grey phase at site 2 approaches the composition of $(Ca,Bi)_3Co_2O_6$, although this phase is absent in double-fired powders. It is therefore inferred that $Ca_3Co_2O_6$ can be eliminated by additional heat-treatment. These EDS results match well with the XRD analysis in Fig. 6.2 and 6.3.

Table 6.4 EDS point analyses at sites 1-5 on the SEM images in Fig. 6.5

Sites	Elements				Calculated Compositions
	Ca (at.%)	Bi (at.%)	Co (at.%)	O (at.%)	
1	16.3	10.2	20.3	53.2	$Ca_{1.6}BiCo_2O_5$
2	19.9	1.0	14.0	65.1	$(Ca,Bi)_3Co_2O_{4.6}$
3	19.7	2.0	27.0	51.3	$(Ca,Bi)_3Co_{3.8}O_7$
4	34.4	16.0	15.9	33.7	Ca_2BiCoO_2
5	16.9	1.9	24.1	57.1	$(Ca,Bi)_3Co_{3.9}O_9$

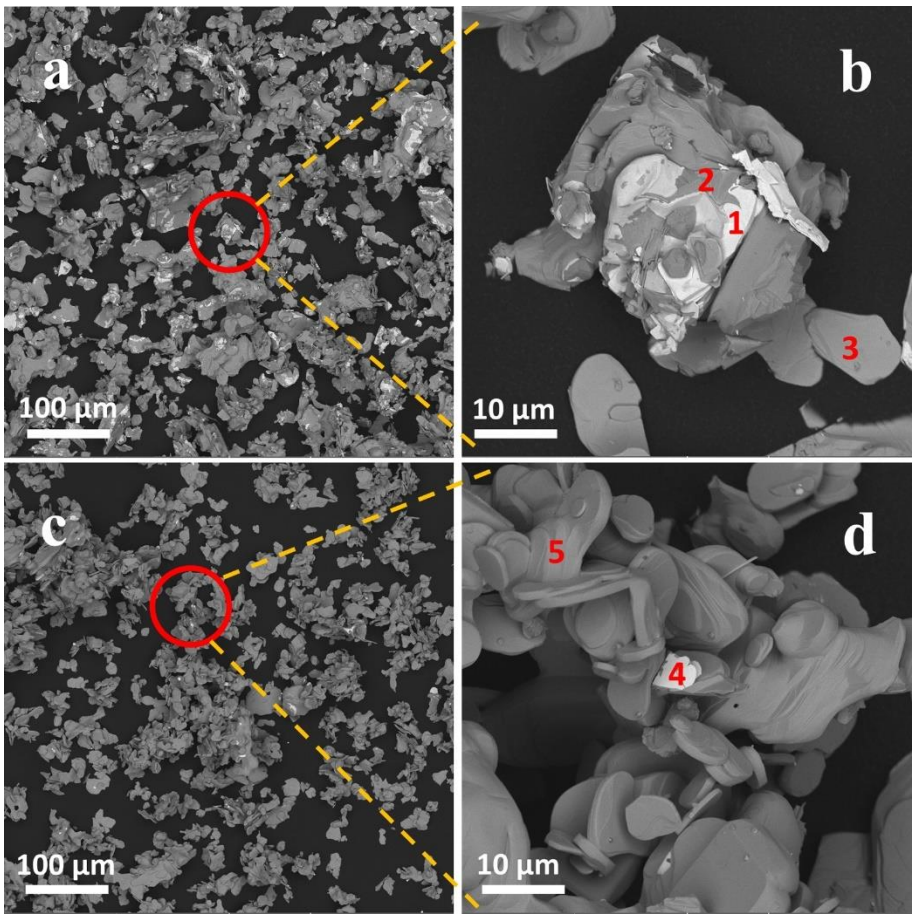

Fig. 6.5 Backscattered electron SEM images for $Ca_{2.7}Bi_{0.3}Co_{3.92}O_{9+\delta}$ powders calcined at 1203 K for 12 h (a, b) and powders calcined twice at 1203 K for 12 h (c, d)

BSE SEM images for polished surfaces of cold sintered $Ca_{2.7}Bi_{0.3}Co_{3.92}O_{9+\delta}$ ceramics prepared from the single-fired powders are displayed in Fig. 6.6. In addition to the plate-like grey phase (main phase: calcium cobaltite), three minor phases are detected, including irregular bright phases (Bi-rich phases), irregular dark phases (Ca-Co-O compound) and granular grey phase (cobalt oxide). It is obvious that the content of the secondary phases falls as the annealing time increases from 0 to 24 h. Notably, the dark phases are almost eliminated when the annealing time exceeds 12 h, whilst certain amounts of pores are observed for the sample annealed at 1203 K for 24 h. The average grain size of both the original (S1A0) and annealed (S1A12 and S1A24) samples are quite similar (12.8-13.6 µm), suggesting that extending the annealing time does not contribute to grain growth of calcium cobaltite.

EDS point analyses for sites 1-10 and mapping data for polished surfaces of cold sintered $Ca_{2.7}Bi_{0.3}Co_{3.92}O_{9+\delta}$ ceramics prepared from the single-fired powders are presented in Table 6.5 and Fig. 6.7. Compositional distributions of Ca, Bi, Co and O are distinguished in

different colours and two minor phases with strong contrast, including Bi-rich phases (sites 1, 5 and 8) and Co-rich phase (sites 3, 6 and 9: cobalt oxide), are confirmed to commonly exist in S1A0, S1A12 and S1A24. With increasing annealing time, the content of the secondary phases decreases. The main phases (sites 4, 7 and 10) are all indexed as bismuth doped $Ca_3Co_4O_9$. The chemical composition of the dark phase at site 2 is $(Ca,Bi)CoO_{2.5}$, matching well with the Ca-Co-O compound ($Ca_2Co_2O_5$). As this phase only shows slight cobalt deficiency compared to the main phase ($Ca_3Co_4O_9$), the contrast of Co for this area is not pronounced.

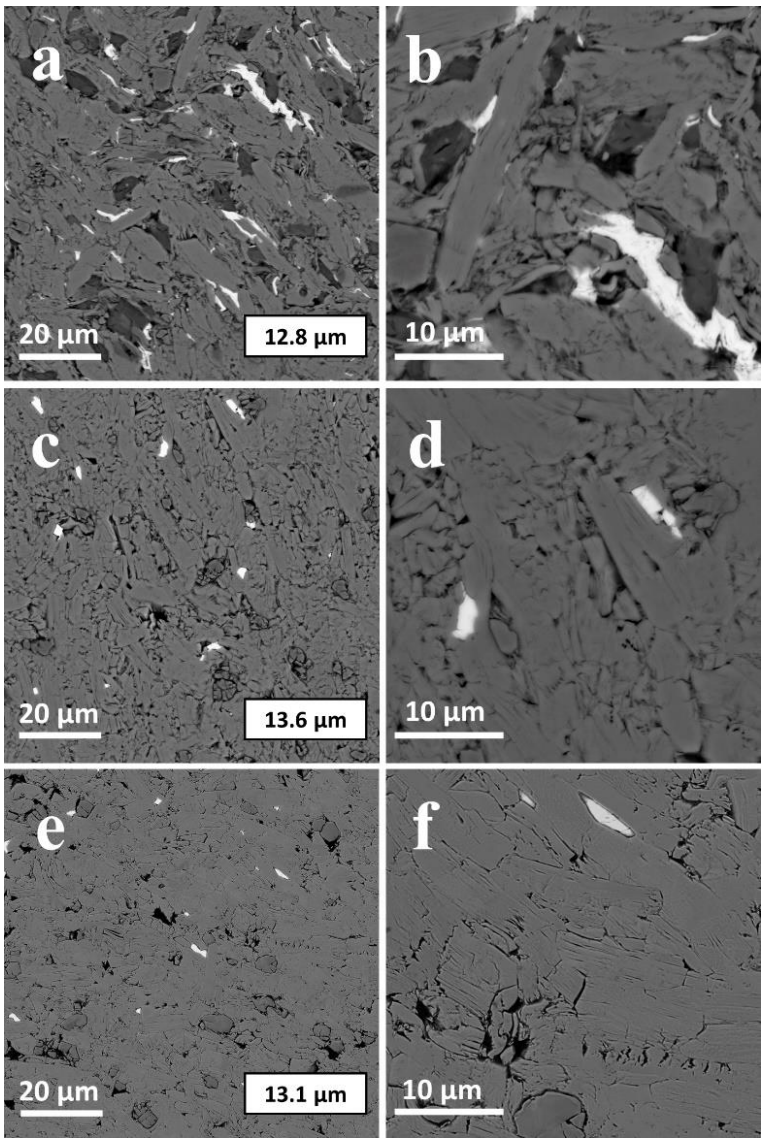

Fig. 6.6 Backscattered electron SEM images for polished surfaces of cold sintered $Ca_{2.7}Bi_{0.3}Co_{3.92}O_{9+\delta}$ ceramics prepared from the single-fired powders (a, b: S1A0; c, d: S1A12; e, f: S1A24; a, c, e: low magnification; b, d, f: high magnification)

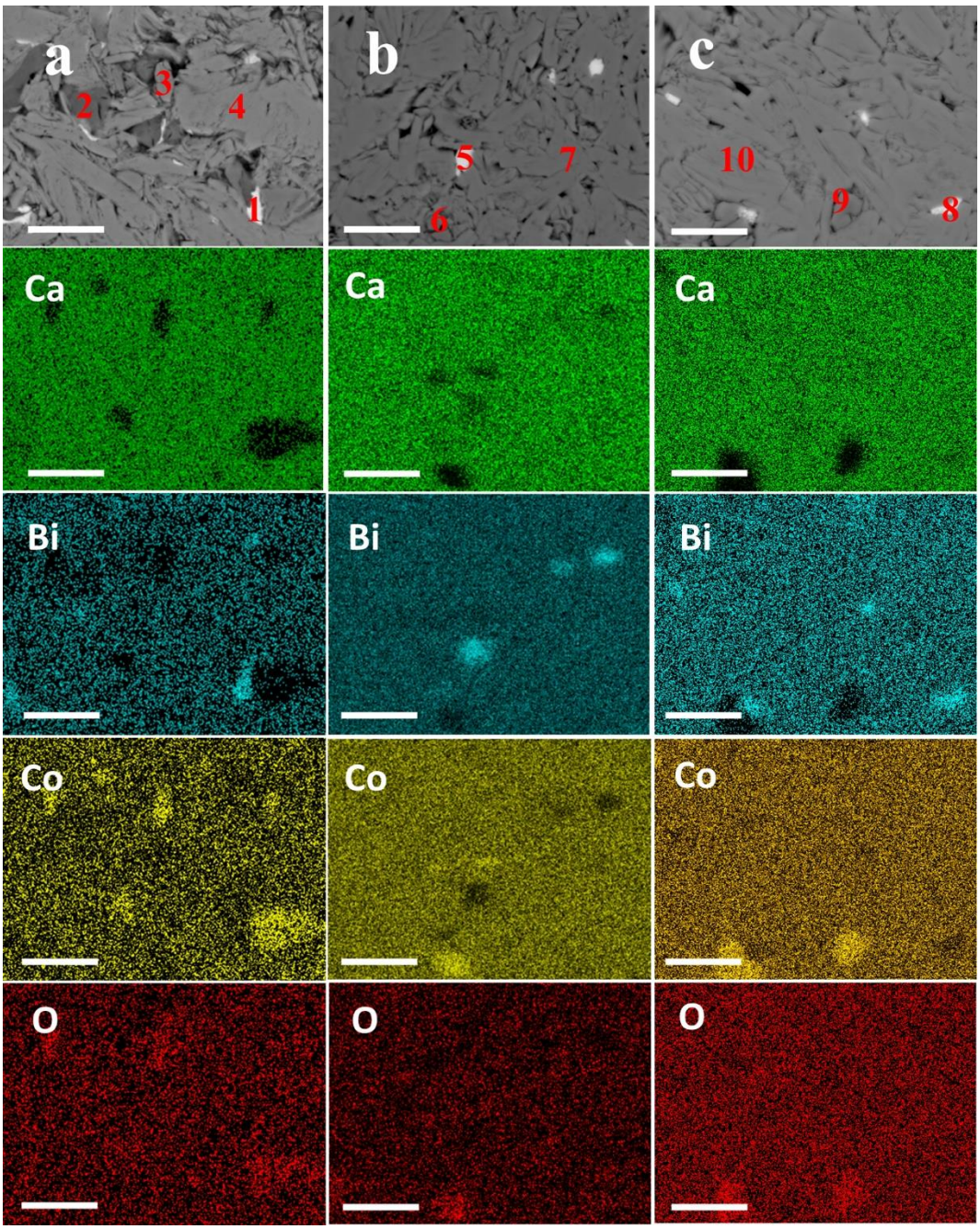

Fig. 6.7 EDS mapping data for polished surfaces of cold sintered $Ca_{2.7}Bi_{0.3}Co_{3.92}O_{9+\delta}$ ceramics prepared from single-fired powders (a. S1A0; b. S1A12; c. S1A24; the scale bar inset is 10 μm)

Table 6.5 EDS point analyses at sites 1-10 on the SEM images in Fig. 6.7

Sites	Elements				Calculated Compositions
	Ca (at.%)	Bi (at.%)	Co (at.%)	O (at.%)	
1	15.6	12.7	15.9	55.8	$Ca_2Bi_{1.6}Co_2O_7$
2	19.7	0.9	21.3	52.8	$(Ca,Bi)CoO_{2.5}$
3	1.1	0	48.9	50.0	(Co,Ca)O
4	18.2	1.8	24.9	55.1	$(Ca,Bi)_3Co_{3.8}O_8$
5	16.8	8.3	13.5	61.4	$CaBiCo_{1.6}O_{7.4}$
6	8.0	0.7	33.9	57.4	$(Co,Ca,Bi)_3O_4$
7	17.9	2.1	24.0	56.0	$(Ca,Bi)_3Co_{4.2}O_{8.5}$
8	18.7	5.0	27.9	48.4	$Ca_{3.8}BiCo_{5.6}O_{9.7}$
9	1.3	0.1	56.6	42.0	$(Co,Ca,Bi)O_{0.7}$
10	18.5	2.1	25.7	53.7	$(Ca,Bi)_3Co_{3.8}O_{7.9}$

Fig. 6.8 shows BSE SEM images for polished surfaces of cold sintered $Ca_{2.7}Bi_{0.3}Co_{3.92}O_{9+\delta}$ ceramics prepared from the double-fired powders. Similar to Fig. 6.7, four phases are detected in the synthesized samples, including the grey main phase (calcium cobaltite), irregular bright phases (Bi-rich phases), irregular dark phases (Ca-Co-O compound) and granular grey phase (cobalt oxide). However, it can be clearly seen that the fractions of the main phase are elevated by the double calcination process and the secondary phases (especially the bright phase) are further reduced compared to the corresponding phase distribution in Fig. 6.8. The phase evolution with increasing annealing time is consistent with that for cold sintered ceramics prepared from the single-fired powders; the main difference lies in the porosity which is significantly increased when the annealing time increases to 24 h. The increased porosity is probably related to the volatilization of Bi-rich secondary phases during the prolonged heat-treatment. The average grain sizes of S2A0 (12.1 μm) and S2A12 (12.7 μm) are quite similar, whereas the value for S2A24 reaches 19.6 μm (about 50 % increase), indicating that extending annealing time helps to increase grain growth of calcium cobaltite prepared from the double-fired powders. This can be attributed to the enhanced mass transfer effects induced by longer heat-treatment time and the more pronounced liquid sintering effects brought by the Bi-rich secondary phases.

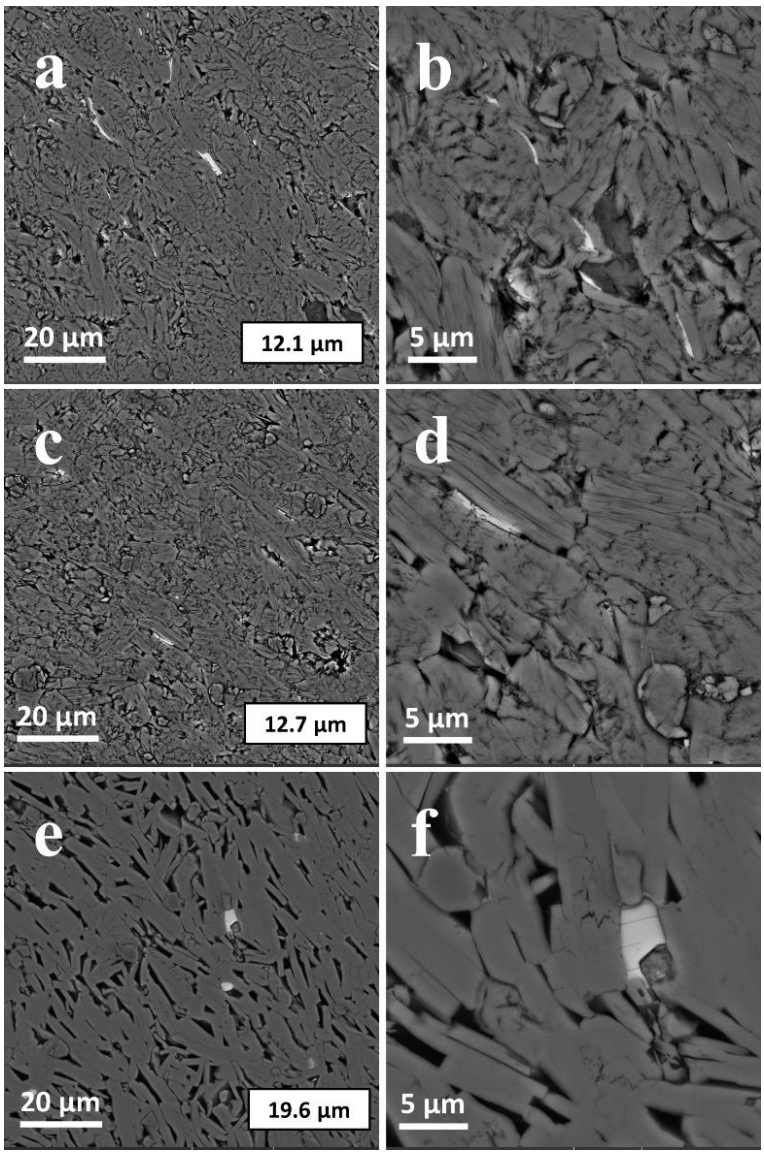

Fig. 6.8 Backscattered electron SEM images for polished surfaces of cold sintered $Ca_{2.7}Bi_{0.3}Co_{3.92}O_{9+\delta}$ ceramics prepared from the double-fired powders (a, b: S2A0; c, d: S2A12; e, f: S2A24; a, c, e: low magnification; b, d, f: high magnification)

EDS point and mapping analyses for polished surfaces of cold sintered $Ca_{2.7}Bi_{0.3}Co_{3.92}O_{9+\delta}$ ceramic prepared from the double-fired powders are presented in Fig. 6.9 and Table 6.6. The presence of high contrast regions for Bi and Co for S2A0, S2A12 and S2A24 confirms the formation of Bi-rich phases (sites 1, 5 and 8) and cobalt oxide (sites 3, 6 and 9). These secondary phases also reduce in volume with increasing annealing time. The main phases (sites 4, 7 and 10) are confirmed as the bismuth doped $Ca_3Co_4O_9$ as expected. Interestingly, the chemical composition of the dark phase (site 2) is $(Ca,Bi)_{0.6}CoO_{2.2}$, which is close to the Ca-Co-O compound (Ca_xCoO_2); this phase demonstrate calcium deficiency compared to site 2 in Fig. 6.7. Nevertheless, this new Ca-Co-O compound can still be eliminated by annealing.

In addition, the increased porosity for the sample annealed at 1203 K for 24 h is clear from the black areas in the elemental map (Fig. 6.9(c)).

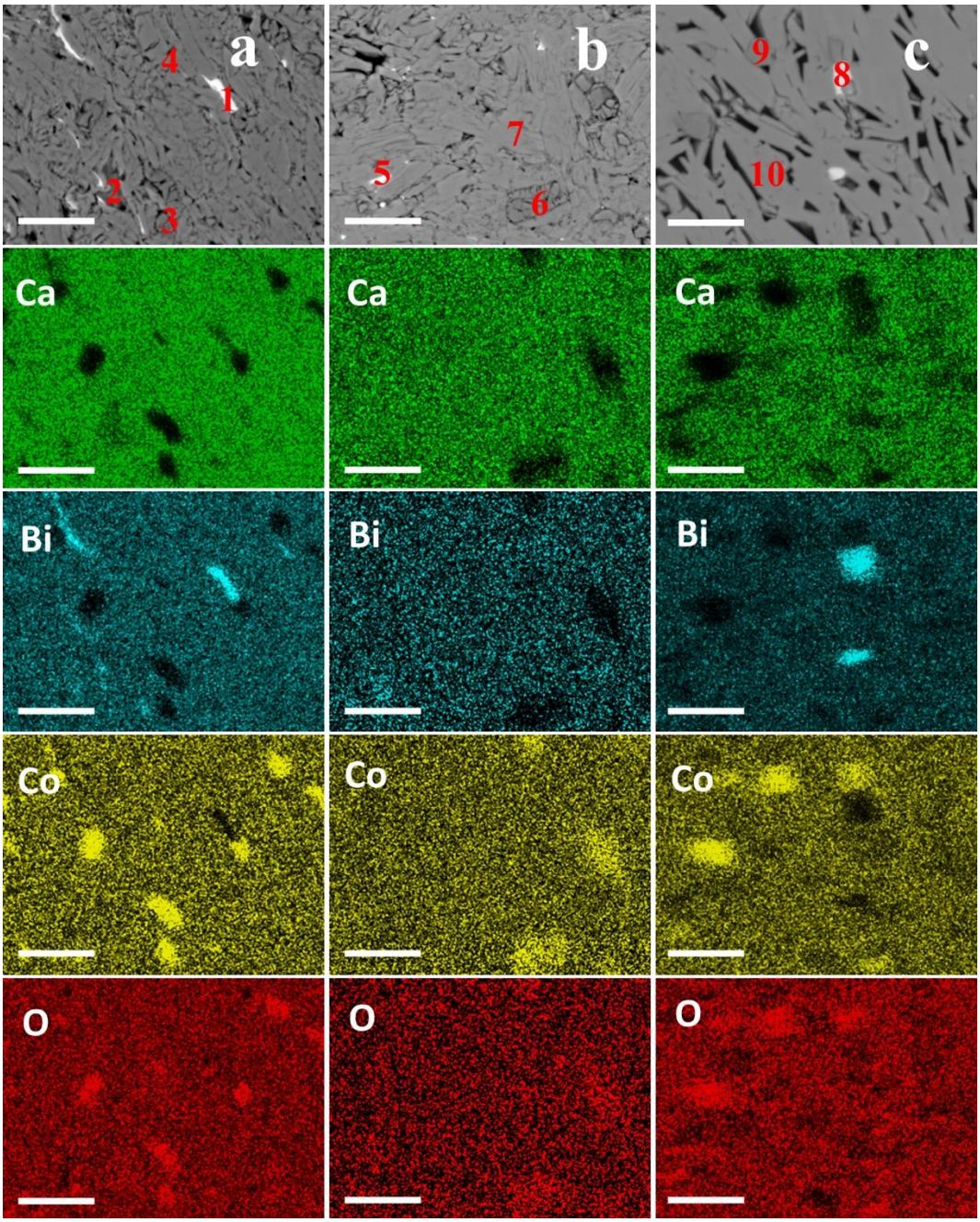

Fig. 6.9 EDS mapping data for polished surfaces of cold sintered $Ca_{2.7}Bi_{0.3}Co_{3.92}O_{9+\delta}$ ceramics prepared from the double-fired powders (a. S2A0; b. S2A12; c. S2A24; the scale bar inset is 10 μm)

Table 6.6 EDS point analyses at sites 1-10 on the SEM images in Fig. 6.9

Sites	Elements				Calculated Compositions
	Ca (at.%)	Bi (at.%)	Co (at.%)	O (at.%)	
1	15.7	10.0	18.6	55.7	$Ca_{1.6}BiCo_{1.9}O_{5.6}$
2	13.7	2.2	26.4	57.7	$(Ca,Bi)_{0.6}CoO_{2.2}$
3	3.2	0.4	35.7	60.7	$(Co,Ca,Bi)O_{1.5}$
4	18.1	2.0	24.3	55.6	$(Ca,Bi)_3Co_{3.6}O_{8.2}$
5	18.0	5.2	19.2	57.6	$CaBi_{0.5}CoO_3$
6	4.4	0.5	42.7	52.4	$(Co,Ca,Bi)O_{1.2}$
7	17.8	2.0	23.9	56.3	$(Ca,Bi)_3Co_{3.6}O_{8.5}$
8	17.6	12.5	9.2	60.7	$Ca_3Bi_2Co_{1.5}O_{9.7}$
9	2.7	0.4	44.4	52.5	$(Co,Ca,Bi)O_{1.1}$
10	17.3	1.9	23.4	57.4	$(Ca,Bi)_3Co_{3.7}O_9$

The volume fractions of different phases in cold sintered $Ca_{2.7}Bi_{0.3}Co_{3.92}O_{9+\delta}$ ceramics annealed under different conditions were determined from BSE SEM images in Fig. 6.6 and Fig. 6.8. The results are summarised in Fig. 6.10. it is evident that the annealing process helps to increase the volume fractions of the main phase (calcium cobaltite: up to about 90 %) and decrease the content of secondary phases including Bi-rich phases (bright phase: down to about 0.3 %) and the cobalt oxide (grey phase: down to about 3 %). Particularly, the Ca-Co-O compounds (dark phase) can be efficiently eliminated when the annealing time is over 12 h. However, porosity shows an increase with increasing annealing time, with the highest fractions of pores (8.3 %) recorded for S2A24; this is consistent with the porosity data determined by the Archimedes' method (Fig. 6.1). In addition, the fractions of the main phase in S2A0 can reach 90 %, about 12 % higher than in S1A0, suggesting that the double calcination process assists decomposition of the secondary phases.

The secondary electron (SE) SEM images for fracture surfaces of X-ray pure cold sintered $Ca_{2.7}Bi_{0.3}Co_{3.92}O_{9+\delta}$ ceramics are displayed in Fig. 6.11. Due to reduction of secondary phases that act to pin grains, these annealed cold sintered samples all show strong texture. It was found that the plate-like grains are generally aligned along *ab* planes, stacking along the *c* axis. However, it seems that texture development is more sensitive to the calcination process rather than the annealing time. The microstructural arrangement is quite similar for a given calcination process. By contrast, the texture (S2A12 and S2A24) can be improved by a double calcination process compared to the single calcination (S1A12 and S1A24). This is also in good agreement with the variation of the Lotgering factors (Table 6.2).

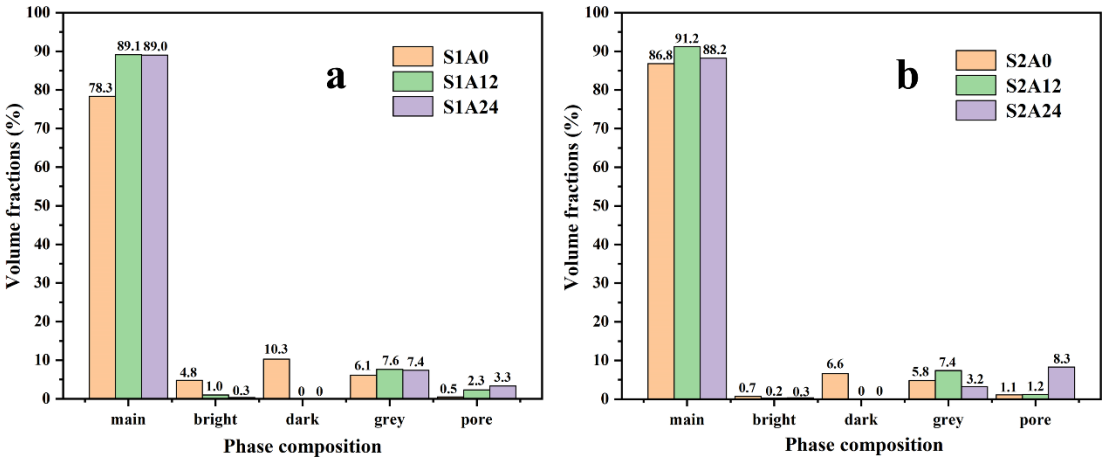

Fig. 6.10 Volume fractions of phases for cold sintered $Ca_{2.7}Bi_{0.3}Co_{3.92}O_{9+\delta}$ ceramics annealed under different conditions (main: calcium cobaltite; bright: Bi-rich phase; dark: Ca-Co-O compound; grey: cobalt oxide)

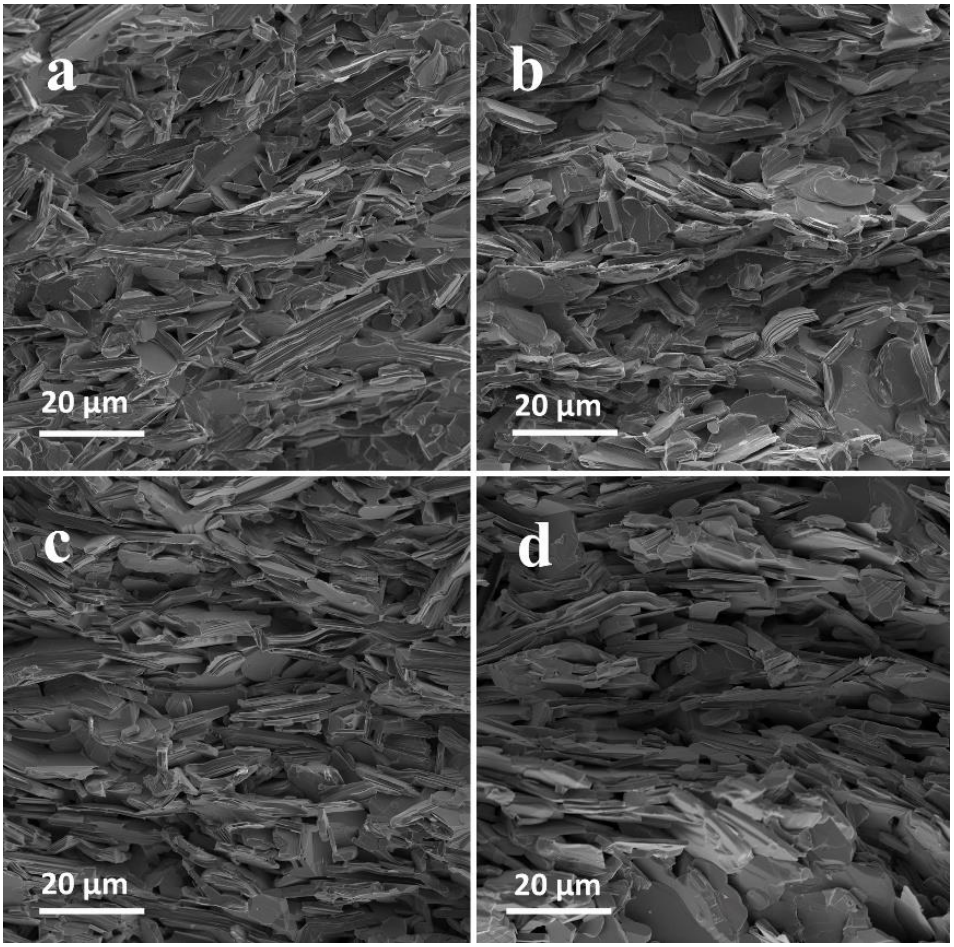

Fig. 6.11 Secondary electron SEM images of fracture surfaces for cold sintered $Ca_{2.7}Bi_{0.3}Co_{3.92}O_{9+\delta}$ ceramics (a. S1A12; b. S1A24; c. S2A12; d. S2A24)

6.5 XPS Analysis

Fig. 6.12 presents high-resolution XPS spectra for Co 2p 3/2 from annealed cold sintered $Ca_{2.7}Bi_{0.3}Co_{3.92}O_{9+\delta}$ ceramics. Three peaks from different cobalt ions are assigned in the Co 2p 3/2 spectra; the peaks at 781.9-782.0 eV (green colour) are assigned to Co^{4+}, the peaks at 780.1-780.2 eV (pink colour) are ascribed to Co^{2+} and the peaks at 779.1-779.2 eV (blue colour) are attributed to Co^{3+}. These results are consistent with the Co XPS data in earlier studies and confirm the presence of three kinds of cobalt ions in the crystal lattice of calcium cobaltite [12–14]. The concentrations of different cobalt ions, calculated from the XPS data in Fig. 6.12, are summarised in Table 6.7. For all the annealed cold sintered samples, the ratio of $[Co^{4+}/(Co^{3+}+Co^{4+})]$ only shows slight variations within 51 % - 55 %, fluctuating at around 52 %, which suggests that the carrier concentration is not significantly modified.

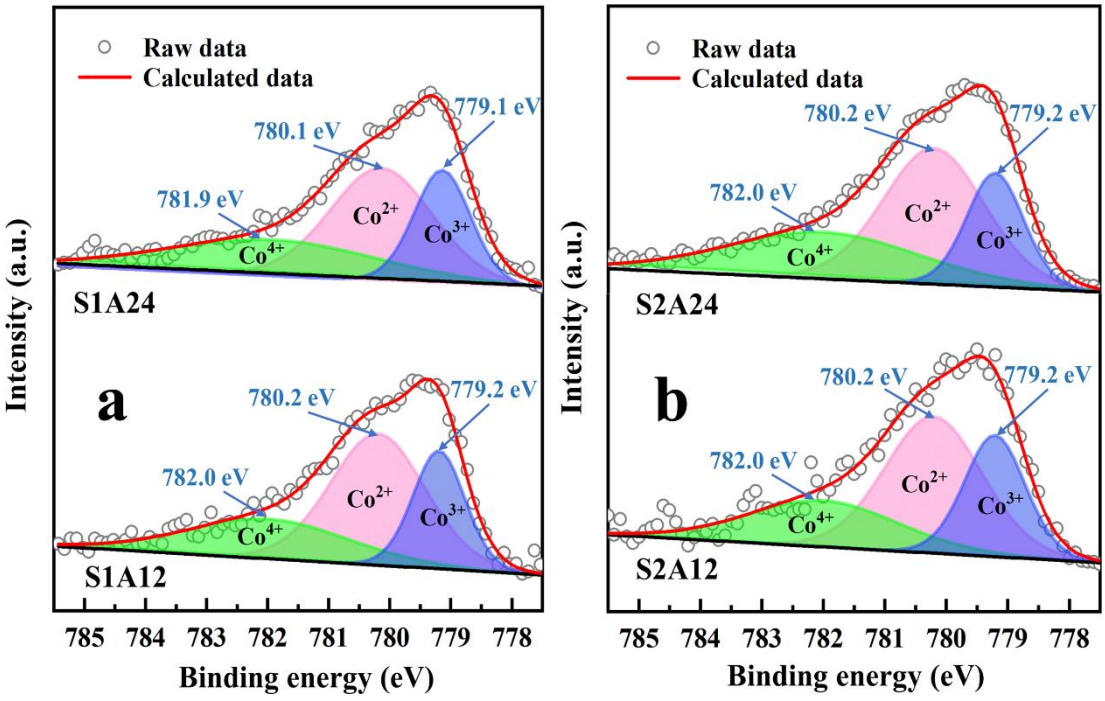

Fig. 6.12 High-resolution XPS spectra of Co 2p 3/2 for annealed cold sintered $Ca_{2.7}Bi_{0.3}Co_{3.92}O_{9+\delta}$ ceramics (a. S1A12 and S1A24; b. S2A12 and S2A24)

Table 6.7 Concentrations of cobalt ions in annealed cold sintered $Ca_{2.7}Bi_{0.3}Co_{3.92}O_{9+\delta}$ ceramics

Sample ID	Co^{3+} (%)	Co^{2+} (%)	Co^{4+} (%)	$Co^{4+}/(Co^{3+}+Co^{4+})$ (%)
S1A12	24.5	49.9	25.6	51.1
S1A24	25.0	44.8	30.2	54.7
S2A12	25.9	46.3	27.8	51.8
S2A24	23.6	49.9	26.5	52.9

6.6 Electrical Transport

Fig. 6.14 shows the electrical transport properties of cold sintered $Ca_{2.7}Bi_{0.3}Co_{3.92}O_{9+\delta}$ ceramics as a function of temperature. The electrical conductivity (σ) for all samples increases with increasing temperature (Fig. 6.14(a)), indicating semiconducting behaviour; the σ varies from 5.2 to 99.9 S/cm at 323 K and 88.6 to 120.1 S/cm at 800 K. The positive Seebeck coefficient (S) in Fig. 6.14(b) demonstrates a hole conduction mechanism, where the value varies from 133.5 to 159.0 μV/K at 323 K and 150.1 to 183.0 μV/K at 800 K. Compared to the cold sintered calcium cobaltite ceramics in earlier studies (σ: 60-70 S/cm at 800 K; S: 120-150 μV/K at 800 K) [8,9], electrical conductivity (σ) in this work (120.1 S/cm at 800 K) represents at least 70 % enhancement and the corresponding S values (150.1 μV/K at 800 K) are similar.

For the samples prepared from the single-fired powders, the lowest σ is recorded in S1A0, whilst σ for S1A12 and S1A24 nearly triple that for S1A0. This can be ascribed to the increased fractions of the primary phase (calcium cobaltite) and the reduction of poorly conducting phases (Fig. 6.10). Only slight changes in S are observed between S1A12 and S1A24, whereas the values are significantly lower than for S1A0. According to the Drude model in Equation (2.4), it is inferred that the carrier concentration (n) is similar for S1A12 and S1A24, much higher than that of S1A0. Similar variations for σ and S are found in the samples prepared from the double-fired powders (Fig. 6.14(a,b)).

Before annealing, sample S1A0 exhibits lower σ than S2A0, mainly due to the lower fraction of the primary phase (Fig. 6.10). The corresponding Seebeck coefficients (S) for S1A0 are larger than those of S2A0, fitting well with the Drude model. After annealing at 1203K for 12h, S2A12 also exhibits enhanced σ compared to S1A12. As there are negligible variations in the ratio of $[Co^{4+}/(Co^{3+}+Co^{4+})]$ for S1A12 and S2A12 (Table 6.7), n should be similar for both. This is also suggested by the similar Seebeck coefficients (S) for S1A12 and S2A12 (Fig. 6.14(b)). Therefore, the increased σ should result from the enhanced carrier mobility

(μ) according to Equation (2.23). It was reported that texture development and larger grain size lead to decreased in-plane grain boundary density, thereby lowering the energy barriers at grain boundaries and hence a larger μ [15,16]. Here, both the Lotgering factors (Table 6.2) and SEM images of fracture surfaces (Fig. 6.11) show that a stronger texture is achieved for S2A12 compared to S1A12, thereby encouraging enhanced mobility. Similarly, S2A24 shows higher σ than S1A24 when the annealing time is extended to 24h.

Fig. 6.14(c) shows that the highest power factor of 0.28 $mWm^{-1}K^{-1}$ was obtained for S2A24 at 800 K; this value shows at least 85 % enhancement compared to the power factors (0.08-0.15 $mWm^{-1}K^{-1}$ at 800 K) for cold sintered calcium cobaltite ceramics in earlier investigations (Fig. 6.14(d)) [8,9].

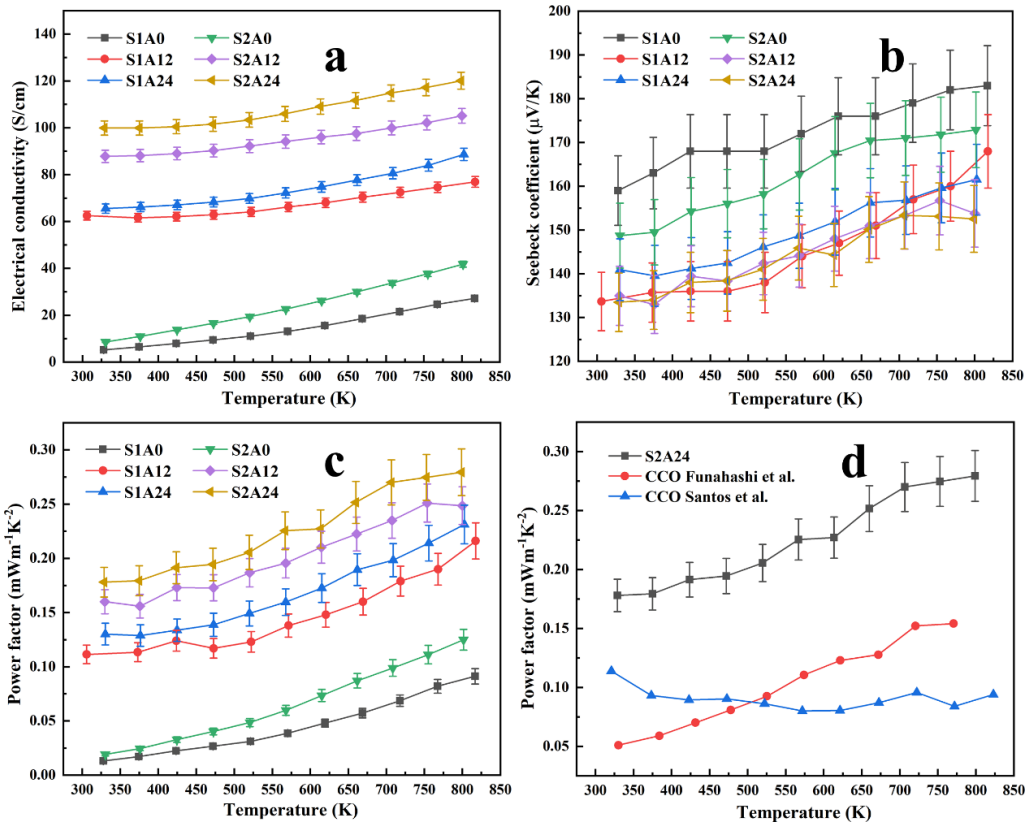

Fig. 6.14 Electrical conductivity (a), Seebeck coefficient (b) and power factor (c) of cold sintered $Ca_{2.7}Bi_{0.3}Co_{3.92}O_{9+\delta}$ ceramics as a function of temperature, and power factors compared with previous work (d) [8,9]

Fig. 6.15 shows electrical conductivity (σ) and Seebeck coefficient (S) at 800 K for cold sintered $Ca_{2.7}Bi_{0.3}Co_{3.92}O_{9+\delta}$ ceramics as a function of annealing time, Lotgering factor and porosity. It is noted that σ for all the samples increases (Fig. 6.15(a)), whilst the corresponding S values decrease with increasing annealing time (Fig. 6.15(b)). In addition, S2 samples show significantly higher σ but slightly lower S than S1 samples. These results

indicate that the power factor can be enhanced by double calcination process and prolonging the annealing time. It is found that the σ is positively correlated with Lotgering factor (Fig. 6.15(c)), whereas the S shows a negative correlation (Fig. 6.15(d)). As stronger texture can lead to reduced in-plane grain boundary density and hence decreased energy barrier at grain boundaries, thereby increasing the carrier mobility and lowering the thermopower (Equation 2.5). Interestingly, the σ and S show an overall increase and decrease with increasing porosity (Fig. 6.15(e, f)). In theory, larger porosity can result in poorer densification and increase energy barriers at grain boundaries, thereby leading to reduced carrier mobility and higher thermopowers. This contradictory result is believed to be ascribed to more pronounced effects of the texture development compared to the porosity.

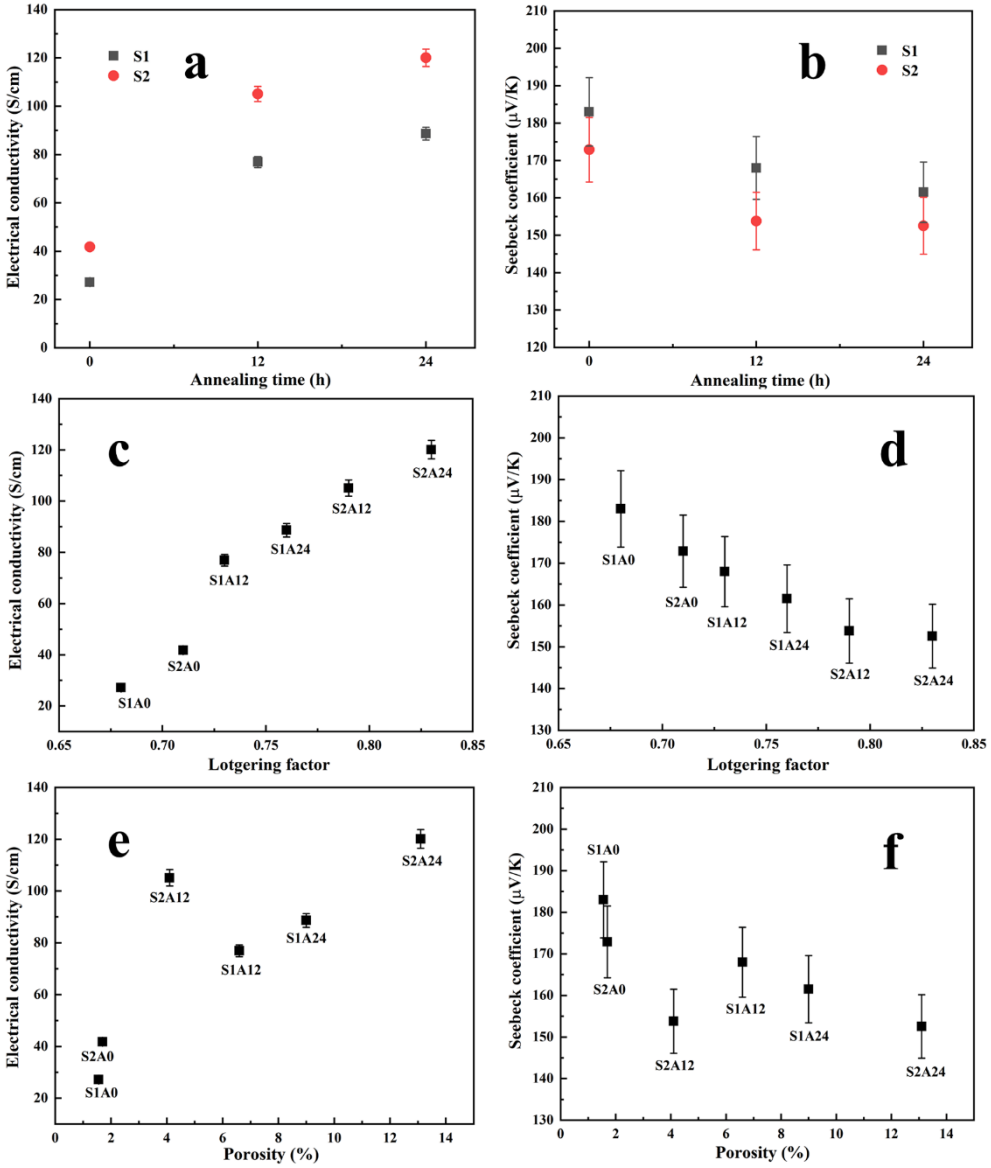

Fig. 6.15 Electrical conductivity and Seebeck coefficient at 800 K for cold sintered $Ca_{2.7}Bi_{0.3}Co_{3.92}O_{9+\delta}$ ceramics as a function of annealing time (a, b), Lotgering factor (c, d) and porosity (e, f)

In order to understand the electrical conduction behaviour, ln(σT) was plotted against reciprocal temperature, and found to fit the small polaron hopping conduction (SPHC) model (Equation (2.25)). As Fig. 6.16(a) shows, a clear linear relationship between ln(σT) and reciprocal of temperatures above 573 K for all samples indicates a hopping conduction mechanism at high temperatures. Overall, activation energies (E_h) (Fig. 6.16(b)) for the samples prepared from the double-fired powders (S2A0, S2A12 and S2A24) are lower than those prepared from the single-fired powders (S1A0, S1A12 and S1A24); this can be attributed to the reduction of secondary phases (that hamper carrier transport) by repeating calcination process (Fig. 6.6, 6.8 and 6.10). Compared to the original samples (S1A0 and S2A0), the significant decrease in E_h (about 80 meV) for annealed samples results from the improved texture (Table 6.2 and Fig. 6.11), which helps to reduce the energy barriers at grain boundaries via reduction of in-plane grain boundaries. Interestingly, E_h for S1A24 (97.8 meV) is slightly higher than that for S1A12 (88.0 meV), while the value for both S2A12 (80.7 meV) and S2A24 (81.9 meV) are quite similar. As S1A24 shows stronger texture than S1A12 (Table 6.2 and Fig. 6.11), E_h is expected to maintain a lower level. This case is also the same for S2A24 and S2A12. However, carrier scattering is also closely related to the pores inside samples. It is noted that the porosity levels of S1A24 and S2A24 reach 9.3 % and 13.1 % (Fig. 6.1) respectively, whereas S1A12 and S2A12 are nearly densified with the porosity level below 6 %; the larger number of pores can act as the carrier scattering centres. Therefore, E_h is slightly higher for S1A24 compared to S1A12. The enhancement in E_h, induced by increased porosity, is not pronounced for S2A24 in contrast to S2A12, and is possibly due to a reduction in the energy barrier caused by larger grain size (S2A24: 19.6 μm; S2A12: 12.7 μm) (Fig. 6.8).

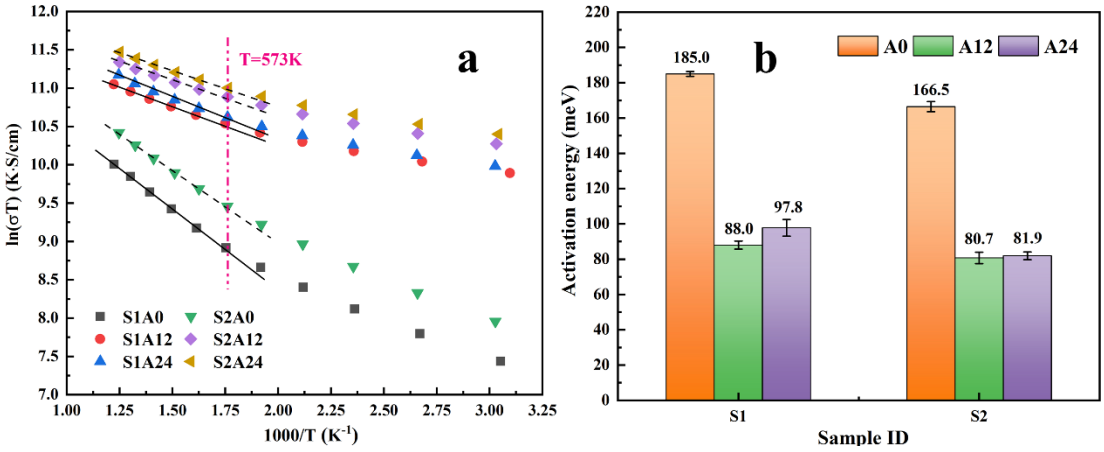

Fig. 6.16 (a) ln(σT) as a function of reciprocal temperature and (b) calculated activation energies for $Ca_{2.7}Bi_{0.3}Co_{3.92}O_{9+\delta}$ ceramics prepared by cold sintering (the lines are fitted by a linear least-square method)

6.7 Summary

In the present work, the effects of calcination processes and annealing time on microstructure and thermoelectric behaviour of cold sintered $Ca_{2.7}Bi_{0.3}Co_{3.92}O_{9+\delta}$ ceramics were investigated in detail.

The double calcination process efficiently suppressed the formation of secondary phases for both resulting powders and unannealed samples, thereby increasing the electrical conductivity through elevated fractions of the primary phase (calcium cobaltite) in the cold sintered $Ca_{2.7}Bi_{0.3}Co_{3.92}O_{9+\delta}$ ceramics. Furthermore, double calcination helped to improve texture development during annealing, thereby increasing carrier mobility via reduction of the in-plane grain boundary density.

By annealing the as-prepared samples at 1203 K, secondary phases were further reduced; the dark Ca-Co-O compounds were absent. By extending the annealing time to 24 h, the electrical conductivity of the sample prepared from the double-fired powders was significantly enhanced, due to (i) increased fractions of the main phase (calcium cobaltite), and (ii) enhanced carrier mobility due to stronger texture and larger grain size. The corresponding Seebeck coefficients were not obviously degraded.

From the combination of factors above, the highest power factor of 0.28 $mWm^{-1}K^{-1}$ at 823 K was obtained for cold sintered $Ca_{2.7}Bi_{0.3}Co_{3.92}O_{9+\delta}$ ceramics prepared from the double-fired powders annealed at 1203 K for 24 h; this represents at least 85 % enhancement compared to results for cold sintered calcium cobaltite ceramics reported in earlier studies. This work demonstrates the huge potential of cold sintering for fabricating thermoelectric ceramics and presents a feasible approach to modulating the power factor of cold sintered samples by controlling microstructural evolution via a simple heat-treatment process.

References

[1] J. Guo, R. Floyd, S. Lowum, J.P. Maria, T. Herisson de Beauvoir, J.H. Seo, C.A. Randall, Cold Sintering: Progress, Challenges, and Future Opportunities, Annu. Rev. Mater. Res. 49 (2019) 275–295.

[2] J. Guo, S.S. Berbano, H. Guo, A.L. Baker, M.T. Lanagan, C.A. Randall, Cold Sintering Process of Composites: Bridging the Processing Temperature Gap of Ceramic and Polymer Materials, Adv. Funct. Mater. 26 (2016) 7115–7121.

[3] H. Guo, A. Baker, J. Guo, C.A. Randall, Protocol for Ultralow-Temperature Ceramic Sintering: An Integration of Nanotechnology and the Cold Sintering Process, ACS Nano. 10 (2016) 10606–10614.

[4] D. Wang, H. Guo, C.S. Morandi, C.A. Randall, S. Trolier-McKinstry, Cold sintering and electrical characterization of lead zirconate titanate piezoelectric ceramics, APL Mater. 6 (2018) 16101.

[5] D. Wang, D. Zhou, S. Zhang, Y. Vardaxoglou, W.G. Whittow, D. Cadman, I.M. Reaney, Cold-Sintered Temperature Stable $Na_{0.5}Bi_{0.5}MoO_4$–Li_2MoO_4 Microwave Composite Ceramics, ACS Sustain. Chem. Eng. 6 (2018) 2438–2444.

[6] J.H. Seo, J. Guo, H. Guo, K. Verlinde, D.S.B. Heidary, R. Rajagopalan, C.A. Randall, Cold sintering of a Li-ion cathode: $LiFePO_4$-composite with high volumetric capacity, Ceram. Int. 43 (2017) 15370–15374.

[7] H. Guo, T.J.M. Bayer, J. Guo, A. Baker, C.A. Randall, Current progress and perspectives of applying cold sintering process to ZrO_2-based ceramics, Scr. Mater. 136 (2017) 141–148.

[8] S. Funahashi, H. Guo, J. Guo, A.L. Baker, K. Wang, K. Shiratsuyu, C.A. Randall, Cold sintering and co-firing of a multilayer device with thermoelectric materials, J. Am. Ceram. Soc. 100 (2017) 3488–3496.

[9] A.M. dos Santos, D. Thomazini, M.V. Gelfuso, Cold sintering and thermoelectric properties of $Ca_3Co_4O_9$ ceramics, Ceram. Int. 46 (2020) 14064–14070.

[10] D. Grebille, S. Lambert, F. Bouree, V. Petricek, Contribution of powder diffraction for structure refinements of aperiodic misfit cobalt oxides, J. Appl. Crystallogr. 37 (2004) 823–831.

[11] J. Yu, K. Chen, F. Azough, D.T. Alvarez-Ruiz, M.J. Reece, R. Freer, Enhancing the Thermoelectric Performance of Calcium Cobaltite Ceramics by Tuning Composition and Processing, ACS Appl. Mater. Interfaces. 12 (2020) 47634–47646.

[12] Y. Huang, B. Zhao, S. Lin, R. Ang, Y. Sun, Enhanced Thermoelectric Performance Induced by Cr Doping at Ca-Sites in $Ca_3Co_4O_9$ System, J. Am. Ceram. Soc. 97 (2014) 3589–3596.

[13] K. Park, D.A. Hakeem, J.S. Cha, Synthesis and structural properties of thermoelectric $Ca_{3-x}Ag_xCo_4O_{9+\delta}$ powders, Dalt. Trans. 45 (2016) 6990–6997.

[14] H. Liu, G.C. Lin, X.D. Ding, J.X. Zhang, Mechanical relaxation in thermoelectric oxide $Ca_{3-x}Sr_xCo_4O_{9+\delta}$ (x = 0, 0.25, 0.5, 1.0) associated with oxygen vacancies, J. Solid State Chem. 200 (2013) 305–309.

[15] Y. Zhou, I. Matsubara, W. Shin, N. Izu, N. Murayama, Effect of grain size on electric resistivity and thermopower of $(Ca_{2.6}Bi_{0.4})Co_4O_9$ thin films, J. Appl. Phys. 95 (2003) 625–628.

[16] T. Sun, H.H. Hng, Q.Y. Yan, J. Ma, Enhanced high temperature thermoelectric properties of Bi-doped c-axis oriented $Ca_3Co_4O_9$ thin films by pulsed laser deposition, J. Appl. Phys. 108 (2010) 83709.

7. Modulation of Thermoelectric Response in Calcium Cobaltite Ceramics Through Co-doping via Different Fabrication Routes

7.1 Introduction

Chapters 3-6 focus on fabrication and characterisation of Bi doped calcium cobaltite ceramics. The single elemental doping strategy is frequently adopted for calcium cobaltite, but there have only been a few studies concentrating on dual-doping effects, leaving plenty of room for exploration. Currently, strontium and barium are popular dopants for single doped calcium cobaltite because they have larger atomic radius and mass than calcium, providing opportunities to optimise thermoelectric properties by either regulating the mismatch degree of sublattices [1] or controlling the phonon scattering effects [2]. Delorme et al. [3] reported a high ZT value of 0.22 at 1000 K for SPS-processed $(Ca_{0.995}Sr_{0.005})_3Co_4O_9$; this was ascribed to the linear decrease in thermal conductivity with increasing Sr content. However, the mechanisms for the enhancement in power factor and the reduction in thermal conductivity were not investigated in detail. Carvillo et al. [4] found that 0.05Ba addition led to enhanced carrier mobility and increased phonon scattering in calcium cobaltite ceramics. Although partial Ba segregation was detected at grain boundaries, this non-stoichiometry affected the elemental homogeneity but did not give rise to any Ba-rich secondary phase.

Our previous investigation (Chapter 4) has already demonstrated that with 10.0 at.% bismuth substitution for calcium the maximum power factor of calcium cobaltite prepared by solid state reaction (SSR) can reach 98.0 $\mu Wm^{-1}K^{-2}$ at 823 K, showing about 20 % enhancement compared to the samples without cobalt deficiency. In this chapter, based on this optimal composition ($Ca_{2.7}Bi_{0.3}Co_{3.92}O_{9+\delta}$), Bi/Sr and Bi/Ba co-doped calcium cobaltites ($Ca_{2.63}Bi_{0.3}M_{0.07}Co_{3.92}O_{9+\delta}$; M = Sr, Ba) were prepared by solid state reaction (SSR) and spark plasma sintering (SPS), respectively. Here, the M value was fixed at 0.07 according to the optimum doping level of Sr and Ba reported in earlier work [5–7]. The roles of different dopants (Bi, Sr and Ba) were identified and the effects of fabrication routes on thermoelectric response in calcium cobaltite were studied. By optimising dopants and fabrication routes, the crystal structure (lattice distortion) and microstructural evolution (porosity, texture and grain size) was efficiently controlled. Consequently, a competitive ZT value of 0.14 was achieved for both the solid state synthesized Bi/Ba co-doped ceramic and annealed SPS-processed Bi/Sr co-doped ceramic at 800 K.

7.2 Density and Porosity

The samples prepared for this study are listed in Table 7.1. Here, SSR processed samples ceramics were sintered in air. SPS-processed samples were sintered under a pressure of 50 MPa in a vacuum of ~ 5 Pascal and then annealed in air.

Table 7.1 List of compositions, fabrication routes, heat-treatment conditions and sample codes for synthesized samples

Compositions	**Routes**	**Sintering conditions**	**Annealing conditions**	**Sample ID**
$Ca_{2.63}Bi_{0.3}Sr_{0.07}Co_{3.92}O_{9+\delta}$	SSR	1203 K for 12 h	-	Sr_SSR
$Ca_{2.63}Bi_{0.3}Ba_{0.07}Co_{3.92}O_{9+\delta}$	SSR	1203 K for 12 h	-	Ba_SSR
$Ca_{2.63}Bi_{0.3}Sr_{0.07}Co_{3.92}O_{9+\delta}$	SPS	1023 K for 5 min	-	Sr_SPS
$Ca_{2.63}Bi_{0.3}Ba_{0.07}Co_{3.92}O_{9+\delta}$	SPS	1023 K for 5 min	-	Ba_SPS
$Ca_{2.63}Bi_{0.3}Sr_{0.07}Co_{3.92}O_{9+\delta}$	SPS	1023 K for 5 min	1203 K for 24 h	Sr_SPSAn
$Ca_{2.63}Bi_{0.3}Ba_{0.07}Co_{3.92}O_{9+\delta}$	SPS	1023 K for 5 min	1203 K for 24 h	Ba_SPSAn

Fig. 7.1 displays the density and porosity data for $Ca_{2.63}Bi_{0.3}M_{0.07}Co_{3.92}O_{9+\delta}$ (M = Sr and Ba) ceramics prepared by different fabrication routes. From Fig. 7.1(a), it is clear that Bi/Ba co-doping helps to improve the bulk density of calcium cobaltite compared to Bi/Sr co-doping. In contrast to the SPS-processed samples, the SSR processed samples show the lowest densities (Sr_SSR: 2.97 g/cm^3; Ba_SSR: 3.07 g/cm^3), which can be ascribed to the poor densification induced by pressure-less sintering. The highest densities of 4.39 g/cm^3 (93.4 % theoretical) and 4.65 g/cm^3 (98.9 % theoretical) were achieved in Bi/Sr and Bi/Ba co-doped samples, respectively. Interestingly, the bulk density shows a slight decrease after annealing (Sr_SPSAn: 4.26 g/cm^3; Ba_SPSAn: 4.37 g/cm^3); this could be related to phase evolution during annealing. The highest porosity of 41.8 % was obtained for Sr_SSR (Fig. 7.1(b)), about 10 % higher than those of Ba_SSR. As expected, the SPS-processed samples show the lowest porosity (Sr_SPS: 3.2 %; Ba_SPS: 0.9 %), consistent with the corresponding bulk density data. It is noted that the porosity of Sr_SPSAn reaches 14.2 %, showing about 10 % increase compared to Sr_SPS; this significant rise indicates that the annealing process leads to decomposition of secondary phases, thereby leaving pores inside the Bi/Sr co-doped samples. Indeed, the porosity of Ba_SPSAn is 6.5 %, about half of the value for Sr_SPSAn, suggesting different microstructural evolution behaviour during heat-treatment for these two types of sample.

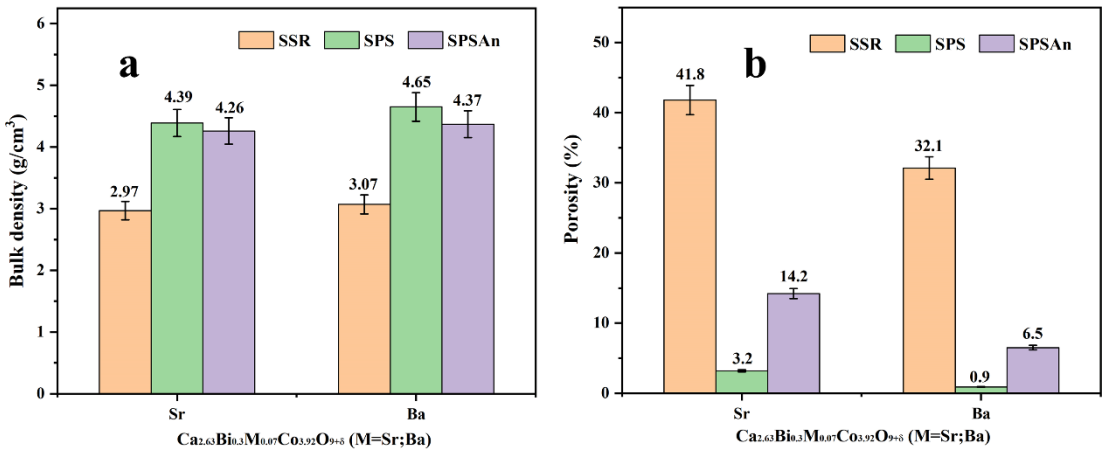

Fig. 7.1 Density and porosity of $Ca_{2.63}Bi_{0.3}M_{0.07}Co_{3.92}O_{9+\delta}$ (M = Sr and Ba) ceramics prepared by different fabrication routes

7.3 XRD Analysis

Fig. 7.2 presents XRD patterns of $Ca_{2.63}Bi_{0.3}M_{0.07}Co_{3.92}O_{9+\delta}$ (M = Sr and Ba) ceramics prepared by different fabrication routes. The main phase in all samples is indexed as monoclinic $Ca_3Co_{3.744}O_{9.176}$ (JCPDS: # 05-001-0461). It is clear that some secondary phases including $Bi_2Ca_3Co_2O_9$ (JCPDS: # 52-0125) and $Ca_3Co_2O_6$ (JCPDS: # 51-0311) are present in the original SPS-processed samples (Sr_SPS and Ba_SPS). After annealing, the impurity phases in Sr_SPSAn are almost eliminated whilst a trace of the newly formed Ba-rich phase ($BaCoO_{3-x}$; JCPDS: # 52-0429) can be observed in Ba_SPSAn, as well as the Bi-rich phases ($Bi_2Ca_3Co_2O_9$). Similarly, the X-ray pure calcium cobaltite can be obtained for Sr_SSR, whereas peaks of the Ba-rich and Bi-rich phases can still be identified in patterns for Ba_SSR. It is therefore concluded that after sufficient heat-treatment Bi/Sr co-doping does not give rise to any significant amount of secondary phase, whilst Bi/Ba doping leads to the formation of Bi-rich and Ba-rich phases. In particular, the reduction of secondary phases by the annealing process is more pronounced for the SPS-processed Bi/Sr co-doped samples.

As there is only a minor amount of secondary phase in both SSR processed and annealed SPS-processed ceramics, the XRD patterns of these samples were selected to determine the Lotgering factors; results are shown in Fig. 7.3. It is apparent that Lotgering factors of ~0.8 for both Sr_SPSAn and Ba_SPSAn are higher than those of Sr_SSR (0.67) and Ba_SSR (0.69). The enhanced preferred grain orientation probably results from the axial pressure applied during the spark plasma sintering, where the plate-like calcium cobaltite grains become well aligned along *ab* planes. However, only slight variation in Lotgering factors is

observed in data for Bi/Sr co-doped and Bi/Ba co-doped samples when the fabrication route is fixed, indicating that the texture development is insensitive to the variety of dopants.

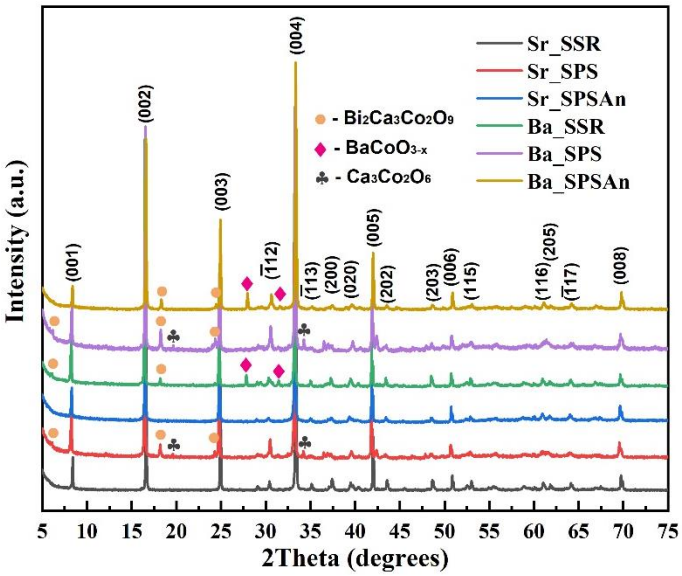

Fig. 7.2 XRD patterns of $Ca_{2.63}Bi_{0.3}M_{0.07}Co_{3.92}O_{9+\delta}$ (M = Sr and Ba) ceramics prepared by different fabrication routes

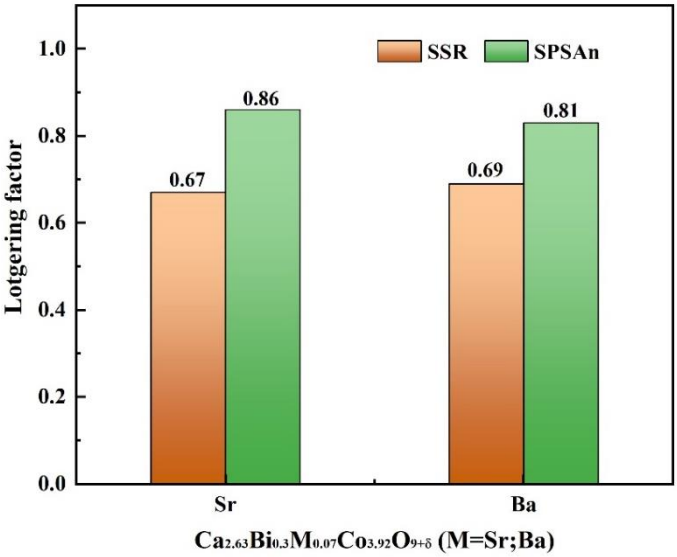

Fig. 7.3 Lotgering factors for $Ca_{2.63}Bi_{0.3}M_{0.07}Co_{3.92}O_{9+\delta}$ (M = Sr and Ba) ceramics prepared by different fabrication routes

Fig. 7.4 shows Le Bail refinement data for $Ca_{2.63}Bi_{0.3}M_{0.07}Co_{3.92}O_{9+\delta}$ (M = Sr and Ba) ceramics prepared by different fabrication routes based on the modulated misfit structure ($[Ca_2CoO_3][CoO_2]_{1.62}$) reported by Grebille et al. [8]. Overall, the R_{wp} and GoF values for all samples are within 10.05-11.52 and 2.28-2.69, respectively. The good match between the

observed and calculated data gives confidence in the reliability of the refined lattice parameters.

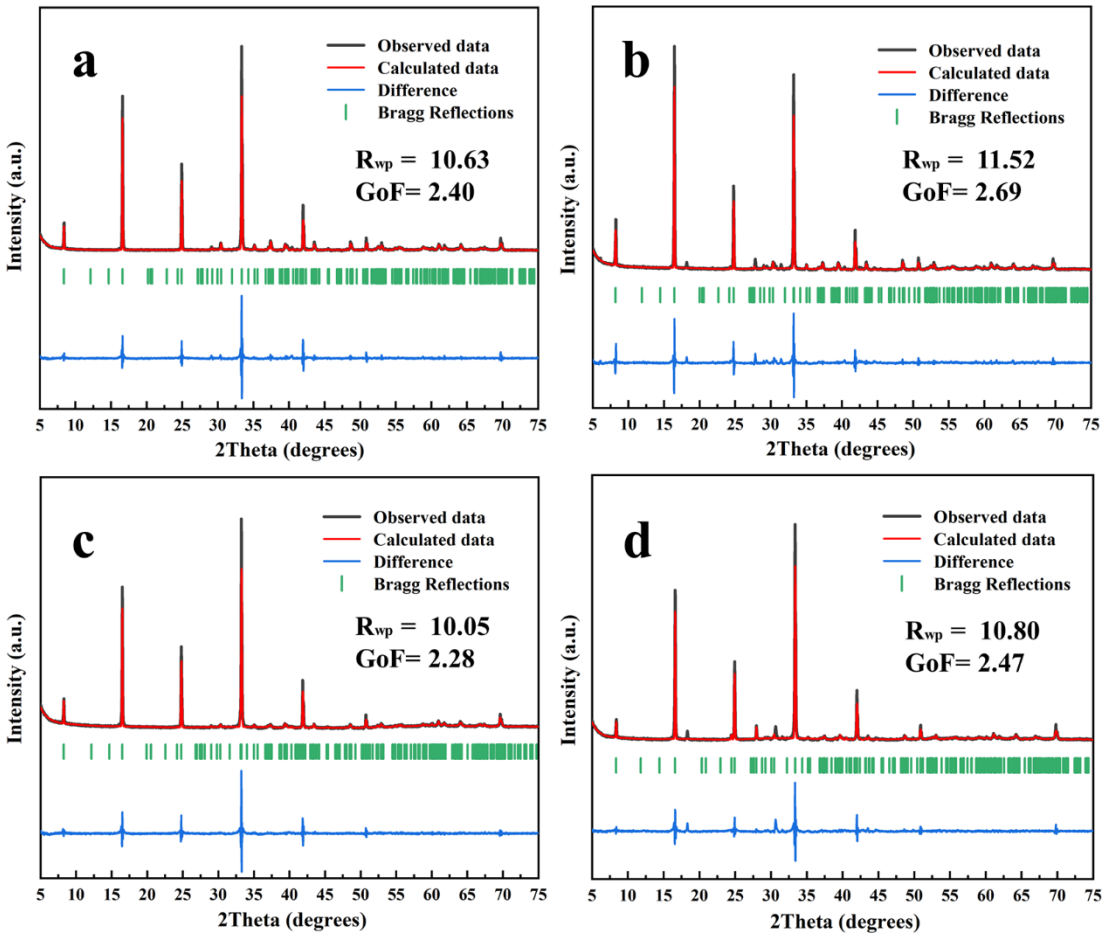

Fig. 7.4 Le Bail refinement data for $Ca_{2.63}Bi_{0.3}M_{0.07}Co_{3.92}O_{9+\delta}$ (M = Sr and Ba) ceramics prepared by different fabrication routes (a. Sr_SSR, b. Ba_SSR, c. Sr_SPSAn, d. Ba_SPSAn)

The refined lattice parameters for $Ca_{2.63}Bi_{0.3}M_{0.07}Co_{3.92}O_{9+\delta}$ (M = Sr and Ba) ceramics prepared by different fabrication routes are summarised in Table 7.2. Compared to the lattice parameters reported for undoped calcium cobaltite (a = 4.83 Å; b_1 = 4.56 Å; b_2 = 2.82 Å; c = 10.83 Å) [8], the lattice parameters for all SSR and SPS-processed samples show higher values, indicating that some dopants enter the crystal lattice. The dopants, including bismuth, strontium and barium, are likely to substitute for Ca sites in the rock salt layers or Co sites in the $[CoO_2]$ layers, but the substitution contribution for each element is quite complicated. Our earlier work (Chapter 5) determined the refined b lattice parameter for single Bi-doped calcium cobaltite ($Ca_{2.7}Bi_{0.3}Co_{3.92}O_{9+\delta}$): b_1 = 4.566 Å and b_2 = 2.830 Å. By contrast, b values for Bi/Ba co-doped samples (SSR: b_1 = 4.553 Å and b_2 = 2.823 Å; SPSAn: b_1 = 4.558 Å and b_2 = 2.828 Å) shows a slight decrease, suggesting that the barium does not enter the crystal

lattice; the slight changes in *b* values could be ascribed to different levels of bismuth solubility. However, the Bi/Sr co-doped samples exhibit much larger b_1 values (SSR: b_1 = 4.570 Å and b_2 = 2.832 Å; SPSAn: b_1 = 4.574 Å and b_2 = 2.822 Å), indicating that strontium probably enters the Ca sites, similar to single bismuth doping. In general, b_1, b_2 and *c* values for Sr_SSR are larger than those for Ba_SSR, despite a smaller *a* value. Although Sr_SPSAn shares similar b_2 and *c* values with Ba_SPSAn, the *a* and b_1 values show an increase. Therefore, it can be concluded that Bi/Sr co-doping leads to an overall lattice expansion compared to Bi/Ba co-doping, regardless of fabrication route.

Table 7.2 Refined lattice parameters for $Ca_{2.63}Bi_{0.3}M_{0.07}Co_{3.92}O_{9+\delta}$ (M = Sr and Ba) ceramics prepared by different fabrication routes

Route	M	a (Å)	b_1 (Å)	b_2 (Å)	c (Å)	β (°)
SSR	Sr	4.8376(4)	4.5700(3)	2.8316(2)	10.9140(6)	98.343(5)
SSR	Ba	4.8474(5)	4.5526(3)	2.8226(2)	10.8812(3)	98.487(6)
SPSAn	Sr	4.8523(1)	4.5736(2)	2.8223(1)	10.8952(6)	98.199(5)
SPSAn	Ba	4.8424(5)	4.5582(4)	2.8277(3)	10.8951(5)	98.468(8)

*b_1 for rock salt layers, and b_2 for CoO_2 layers.

7.4 SEM-EDS Analysis

BSE SEM micrographs of sintered or polished surfaces for $Ca_{2.63}Bi_{0.3}M_{0.07}Co_{3.92}O_{9+\delta}$ (M = Sr and Ba) ceramics prepared by different fabrication routes are shown in Fig. 7.5; the corresponding EDS point analyses (sites 1-17) are summarised in Table 7.3. As expected, both the SSR processed ceramics show poor densification with the presence of pores, in good agreement with the porosity data (Fig. 7.1). It is noted that there is a Ba-rich phase at site 7 (bright phase: Ba/Ca/Bi = 2:0.8:1) in Ba_SSR, whereas the secondary phases are almost eliminated in Sr_SSR. The average grain size of Ba_SSR is about 20.1 μm, slightly larger than that of Sr_SSR (18.6 μm). The phase assemblages for the SPS-processed ceramics are complex. In the original SPS-processed ceramics, there are three minor phases including the Bi-rich phases (bright phase: sites 8 and 11), $Ca_3Co_2O_6$ (dark phase: sites 9 and 12) and cobalt oxides (grey phase: sites 10 and 13), in addition to the calcium cobaltite (main phase: sites 3 and 4); these results are consistent with the phase analyses for the single bismuth doped calcium cobaltite in our previous investigation (Chapter 5). After annealing samples at 1203 K for 24 h, most of the secondary phases are eliminated in Sr_SPSAn, except for the cobalt oxide (grey phase: site 14). By contrast, in Ba_SPSAn, only the dark phase ($Ca_3Co_2O_6$) is eliminated whilst the traces of Bi-rich phases (site 16) and cobalt oxides

(site 17) can still be detected. Notably, a newly formed Ba-rich phase (light grey phase: site 15) is also found, similar to the phase analyses for Ba_SSR. Overall, the average grain sizes of annealed SPS-processed samples are significantly larger than for the original ones, especially for Sr_SPSAn (27.8 μm). In contrast to the highly dense Sr_SPS and Ba_SPS ceramics, the Sr_SPAn and Ba_SPSAn ceramics also show higher levels of porosity, the highest being 14.2 % (Fig. 7.1) in Sr_SPSAn.

The volume fractions of different phases in SPS-processed samples determined from Fig.7.5(c-f) based on phase contrast are shown in Table 7.4. It is clear that by annealing the fraction of the main phase increases whilst the fractions of the bright and dark phases decrease. However, it seems that the grey phase is insensitive to the heat-treatment. Furthermore, large fractions of pores and light grey phases are found in Sr_SPSAn and Ba_SPSAn, respectively. For the original SPS-processed samples, the fraction of the main phase in Sr_SPS is about 10 % higher than in the Ba_SPS sample, while differences between Sr_SPSAn and Ba_SPSAn samples are much smaller (about 3 %).

In order to understand the mechanisms of pore formation, detailed SEM-EDS analyses were performed on the surface of Sr_SPSAn (Fig. 7.6). It is evident that there is still a small amount of residual bright phases in the matrix, highlighted by the red circle in Fig. 7.6(b), although many pores are easily distinguished in the low magnification SEM image (Fig. 7.6(a)). The irregular shape of this bright phase is quite similar to the morphology of the pores. It is therefore inferred that the increased fractions of pores are probably due to the volatilization of this bright phase during heat-treatment. The corresponding EDS point analyses show a complex elemental balance for the secondary phase, where the ratio of Ca/Bi/Sr = 1:0.35:0.05, showing higher levels of Bi and Sr solubility compared to the nominated chemical composition $Ca_{2.63}Bi_{0.3}Sr_{0.07}Co_{3.92}O_{9+\delta}$ (Ca/Bi/Sr = 1:0.11:0.025). This nonstoichiometric composition cannot readily be indexed using the ICDD/JCPDS database; it is probably a mixture of Bi-rich and Sr-rich phases. It was reported that the calcium bismuth cobalt oxide [9] and strontium bismuth cobalt oxide [10] are able to melt to form liquid phases at 1093 K and 1196 K, respectively; both melting points are lower than the annealing temperature in this work (1203 K). Higher annealing temperatures provide opportunities to convert this bright phase into the liquid phase, followed by sufficient volatilization during the heating process, thereby leaving pores inside the matrix.

To understand the roles of the dopants (Bi/Sr and Bi/Ba), EDS point analyses were collected for the main phases (sites 1-6 in Table 7.3) and are shown in Fig. 7.7. It is clear that all

samples contain some Bi, indicating that bismuth is successfully doped into the crystal lattice of calcium cobaltite. In addition, peaks for Sr can also be detected in Bi/Sr co-doped samples, regardless of fabrication route. However, there are no traces of Ba in Bi/Ba co-doped samples, indicating that barium mainly takes part in forming the Ba-rich secondary phases rather than entering the crystal lattice. These results support the phase composition analysis in Fig. 7.5.

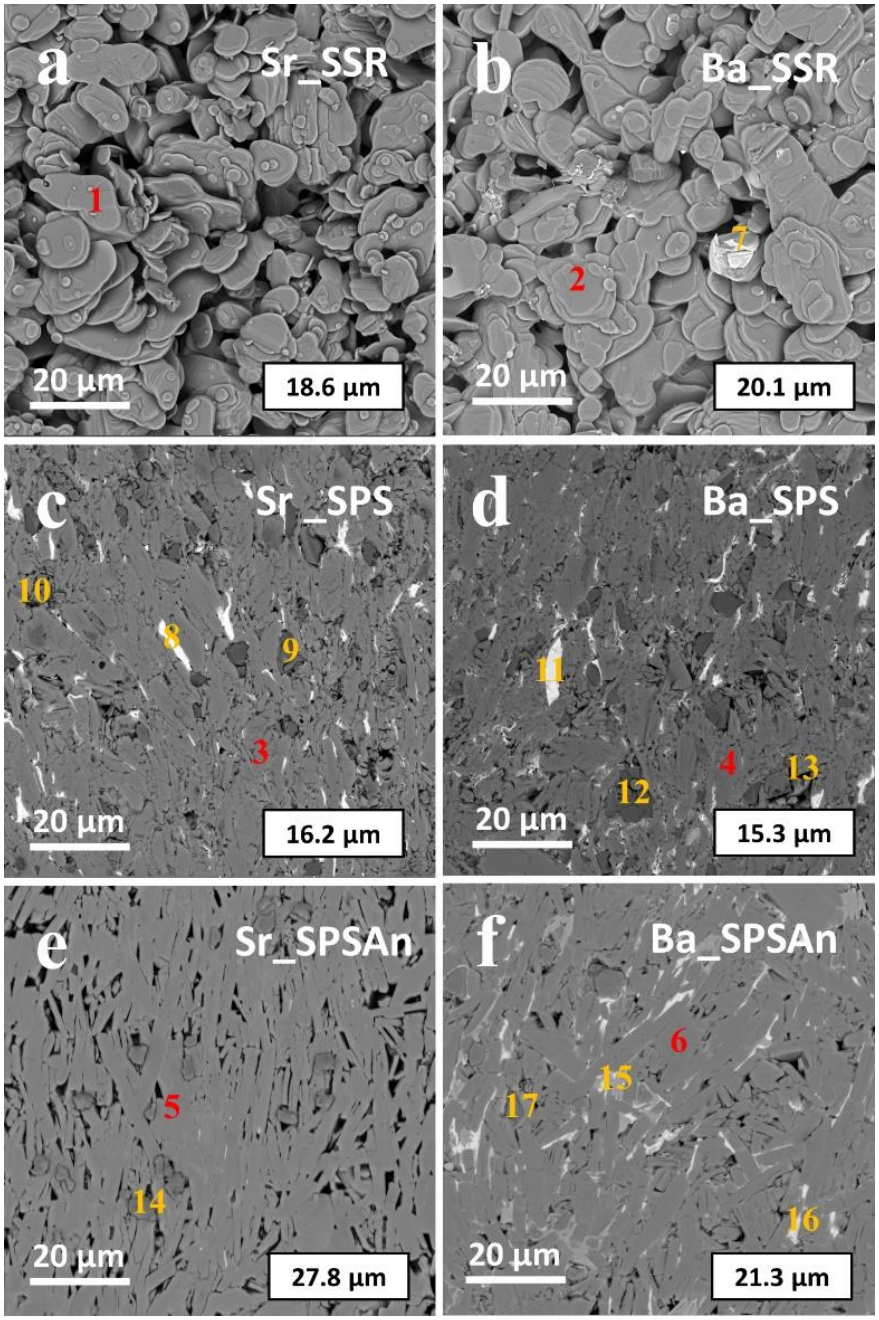

Fig. 7.5 Backscattered electron SEM images of sintered (a, b) and polished (c-f) surfaces for $Ca_{2.63}Bi_{0.3}M_{0.07}Co_{3.92}O_{9+\delta}$ (M = Sr and Ba) ceramics prepared by different fabrication routes

Table 7.3 EDS point analyses at sites 1-17 on the SEM images in Fig. 7.5

Sites	Elements (at.%)						Calculated Compositions
	Ca	Bi	Sr	Ba	Co	O	
1	11.8	1.6	0.4	0	19.2	67.0	$(Ca,Bi,Sr)_3Co_{4.1}O_{14}$
2	14.9	1.6	0	0	23.5	60.0	$(Ca,Bi)_3Co_{4.2}O_{10.9}$
3	13.9	1.5	0.3	0	18.5	65.8	$(Ca,Bi,Sr)_3Co_{3.6}O_{12.7}$
4	17.0	1.7	0	0	23.5	57.8	$(Ca,Bi)_3Co_{3.8}O_{9.3}$
5	16.9	2.1	0.5	0	24.0	56.5	$(Ca,Bi,Sr)_3Co_{3.7}O_{8.7}$
6	18.0	1.8	0	0	26.0	54.2	$(Ca,Bi)_3Co_{3.9}O_{8.2}$
7	5.8	8.1	0	16.3	16.0	53.8	$Ca_{0.4}Bi_{0.5}BaCoO_{3.4}$
8	11.6	9.2	0.8	0	13.3	65.1	$Ca_{1.3}BiSr_{0.1}Co_{1.4}O_7$
9	20.8	0.6	0.4	0	14.5	63.7	$(Ca,Bi,Sr)_3Co_2O_{8.7}$
10	1.0	0	0	0	39.2	59.8	$(Co,Ca)_3O_{4.5}$
11	14.8	8.1	0	0.1	15.8	61.2	$Ca_{1.8}BiBa_{0.01}Co_2O_{7.5}$
12	19.5	1.1	0	0.1	16.6	62.7	$(Ca,Bi,Sr)_3Co_{2.4}O_9$
13	4.9	1.2	0	0.1	38.2	55.6	$CaBi_{0.2}Ba_{0.02}Co_{7.8}O_{11}$
14	9.7	1.3	0.3	0	29.0	59.7	$CaBi_{0.1}Sr_{0.03}Co_{2.9}O_6$
15	1.7	0.6	0	7.4	33.2	57.1	$Ca_{0.2}Bi_{0.1}BaCo_{4.5}O_8$
16	16.5	6.3	0	0.1	21.2	55.9	$Ca_{2.6}BiBa_{0.02}Co_{3.4}O_9$
17	2.1	0.3	0	0	45.2	52.5	$(Co,Ca)_3O_{3.3}$

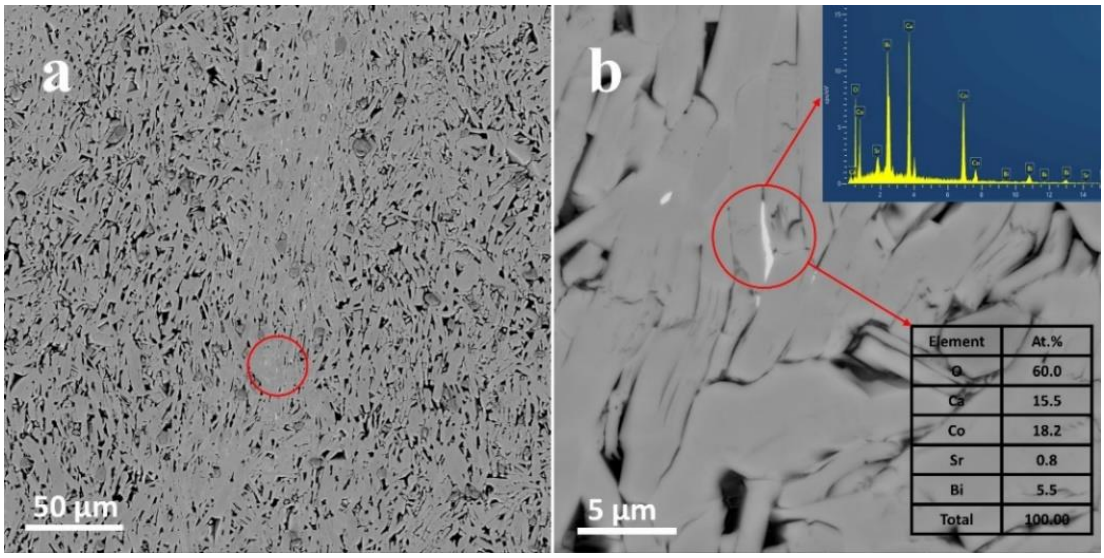

Fig. 7.6 Backscattered electron SEM images of polished surfaces and corresponding EDS data for SPS-processed $Ca_{2.63}Bi_{0.3}Sr_{0.07}Co_{3.92}O_{9+\delta}$ ceramics annealed at 1203 K for 24 h (a. low magnification: ×1k; b. high magnification: ×10k)

Table 7.4 Volume fractions of different phases in $Ca_{2.63}Bi_{0.3}M_{0.07}Co_{3.92}O_{9+\delta}$ (M = Sr and Ba) ceramics prepared by different fabrication routes

Phases	Volume Fractions (%)			
	Sr_SPS	Sr_SPSAn	Ba_SPS	Ba_SPSAn
Main Phase	79.1	86.1	70.8	82.4
Bright Phase	4.0	0.1	4.3	2.1
Grey Phase	3.6	4.1	5.1	2.7
Light Grey Phase	0	0	0	10.6
Dark Phase	12.3	0	18.5	0
Pores	1.0	12.7	1.3	2.2

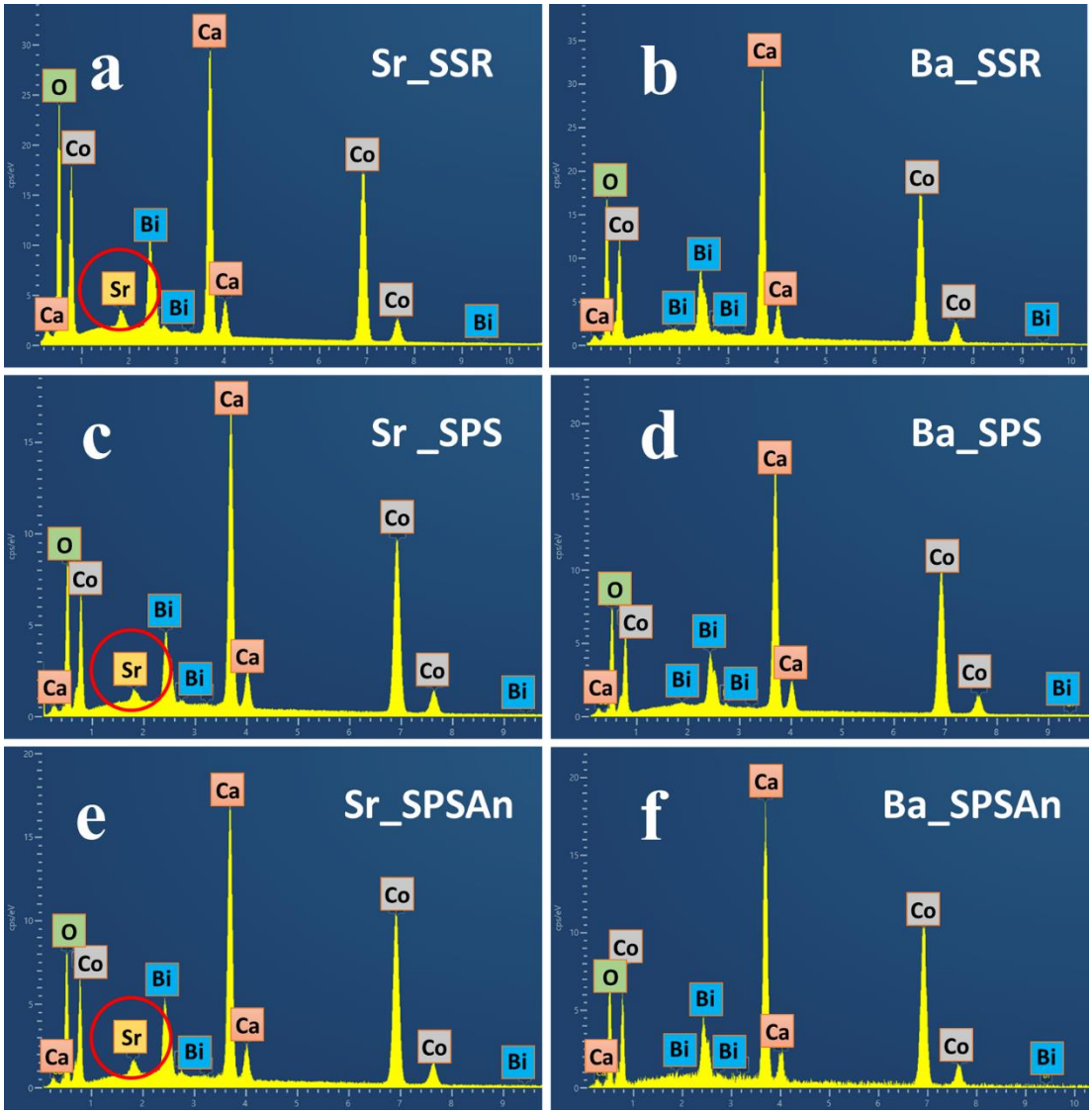

Fig. 7.7 EDS point spectra of the main phase for $Ca_{2.63}Bi_{0.3}M_{0.07}Co_{3.92}O_{9+\delta}$ (M = Sr and Ba) ceramics prepared by different fabrication routes (a-f: sites 1-6 in Fig. 7.5)

Fig. 7.8 shows EDS mapping data of sintered and polished surfaces for $Ca_{2.63}Bi_{0.3}M_{0.07}Co_{3.92}O_{9+\delta}$ (M = Sr and Ba) ceramics prepared by different fabrication routes. The compositional distribution of Co and O, with high contrast, confirms the presence of cobalt oxides in both Bi/Sr and Bi/Ba co-doped samples, indicating that cobalt oxides cannot be totally eliminated through optimised heat-treatment. Furthermore, the coverage of Bi and Ba in the Bi/Ba co-doped samples confirms the formation of Bi-rich and Ba-rich secondary phases, respectively. In addition, the uniform distribution of Sr in the main phase of the Bi/Sr co-doped samples supports the successful doping of Sr into the crystal lattice of the main phase. However, the locally concentrated distribution of Ba in the Bi/Ba co-doped samples indicates Ba-rich phase segregation to grain boundaries during heat-treatment.

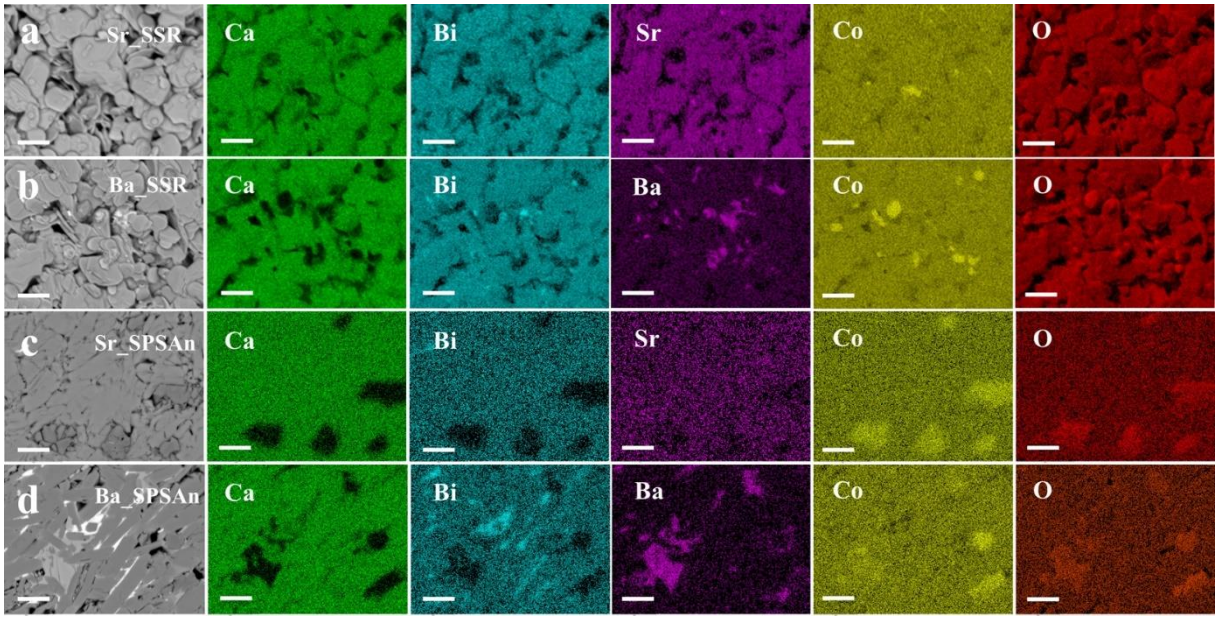

Fig. 7.8 EDS mapping data for sintered and polished surfaces for $Ca_{2.63}Bi_{0.3}M_{0.07}Co_{3.92}O_{9+\delta}$ (M = Sr and Ba) ceramics prepared by different fabrication routes (a, b: sintered surfaces; c, d: polished surfaces; the inserted scale bars represent 10 μm)

Fig. 7.9 presents the fracture surfaces for $Ca_{2.63}Bi_{0.3}M_{0.07}Co_{3.92}O_{9+\delta}$ (M = Sr and Ba) ceramics prepared by different fabrication routes. It is clear that the plate-like calcium cobaltite grains are randomly distributed in the SSR processed samples. By contrast, in the annealed SPS-processed samples, the grains are well aligned along *ab* planes and stacked in the *c* axis, suggesting that a strong texture is developed. Thus, grains in Sr_SPSAn show larger degree of orientation than grains in Ba_SPSAn, consistent with Lotgering factors (Fig. 7.3).

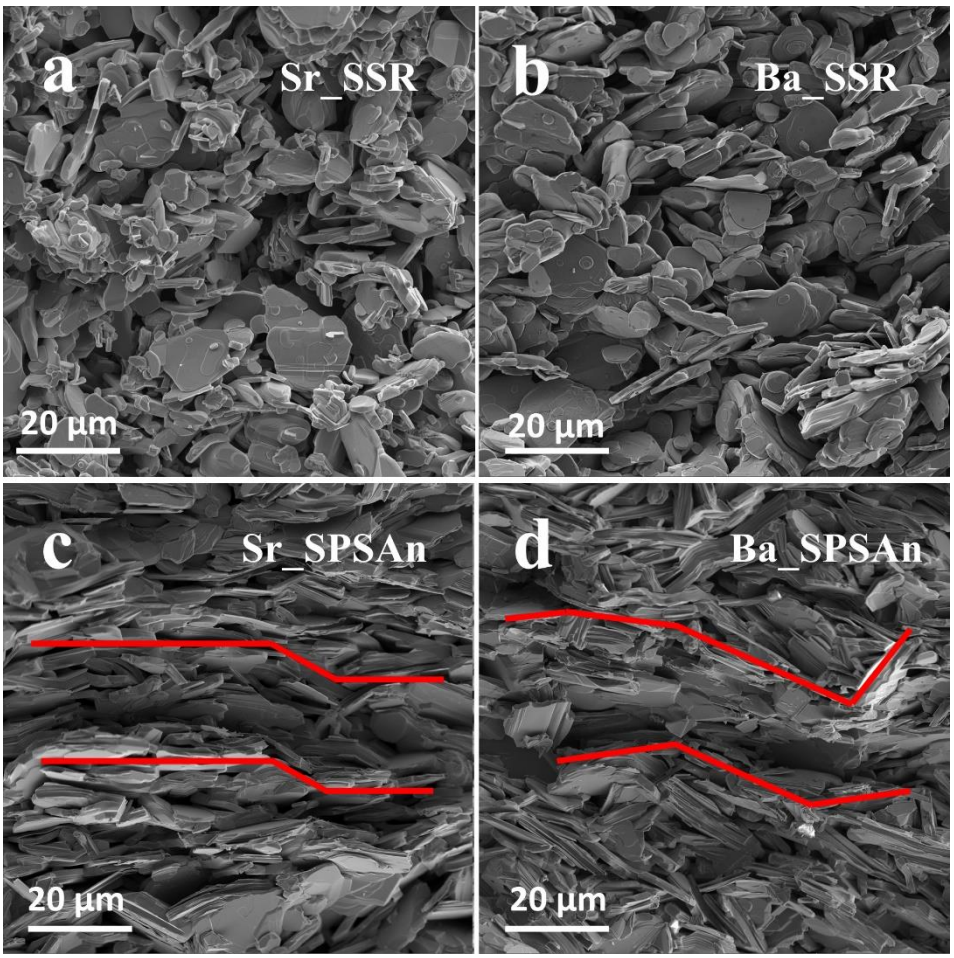

Fig. 7.9 Secondary electron SEM images of fracture surfaces for $Ca_{2.63}Bi_{0.3}M_{0.07}Co_{3.92}O_{9+\delta}$ (M = Sr and Ba) ceramics prepared by different fabrication routes

7.5 TEM Analysis

Fig. 7.10 shows TEM images and corresponding SAED patterns for $Ca_{2.63}Bi_{0.3}Ba_{0.07}Co_{3.92}O_{9+\delta}$ ceramic prepared by solid state reaction. By tilting the region denoted by the orange circle in Fig. 7.10(a) along [-111] zone axis, the diffraction spot in the SAED patterns (Fig. 7.10(b)) can be indexed as (202), (422) and (220) crystal planes, using JCPDS: # 43-1003 in ICDD/JCPDS database; this confirms the formation of Co_3O_4 as the secondary phase in Ba_SSR samples. By directing the electron beam in [001] zone axis of the red circular area in Fig. 7.10(c), the SAED patterns of $Ca_3Co_4O_9$ are obtained; a layered structure composed of both rock salt sublayers (red arrow) and [CoO_2] sublayers (orange arrow) can be identified (Fig. 7.10(d)). The latter misfit structure shows a common lattice parameter *a* but two different lattice parameters *b*, matching well with the [001] SAED patterns in earlier studies [11,12].

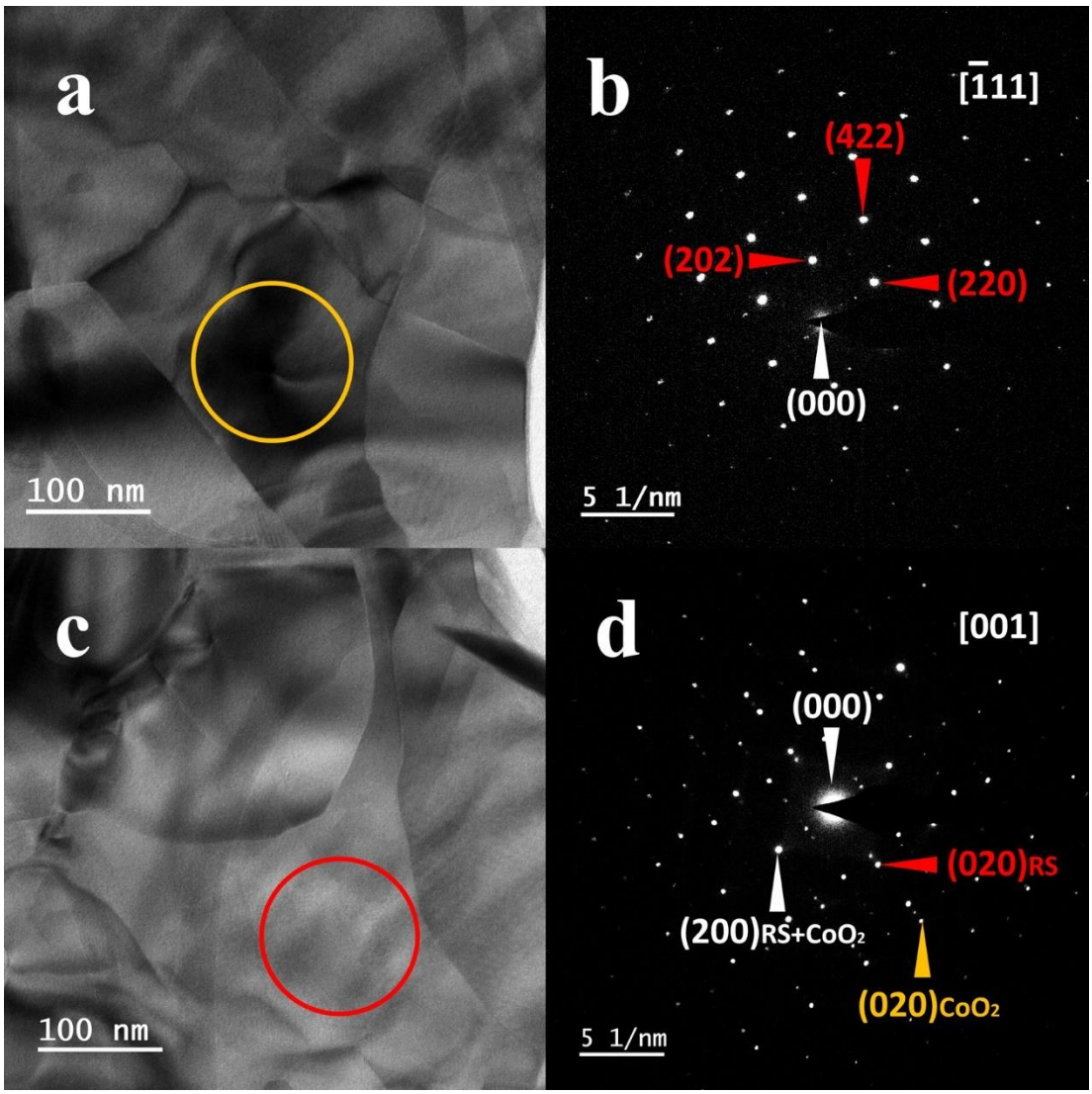

Fig. 7.10 TEM images (a, c) and corresponding SAED patterns (b, d) of $Ca_{2.63}Bi_{0.3}Ba_{0.07}Co_{3.92}O_{9+\delta}$ ceramic prepared by solid state reaction

Fig. 7.11 displays the HRTEM image of the interface between the main phase and secondary phase and their corresponding FFT and IFFT images. Area 1 (Fig. 7.11(a)) is indexed as Co_3O_4, based on the corresponding FFT image (Fig. 7.11(b)) which is the same as the SAED patterns in Fig. 7.10(b). The filtered HRTEM image of Area 1 (Fig. 7.11(d)) shows a d-spacing of 0.28 nm, matching well with (220) crystal plane of Co_3O_4. However, Area 2 exhibits different FFT pattern (Fig. 7.11(c)) compared to that of Co_3O_4, indicating the existence of another phase. Although the FFT data are not of the highest quality, the d-spacing in the corresponding IFFT image (Fig. 7.11(e)) is determined to be 1.07 nm, in good agreement with the (001) crystal plane of calcium cobaltite. Combined with XRD data in Fig. 7.2, it can be concluded that in Ba_SSR the layered calcium cobaltite can be fabricated with minor Co_3O_4 as the secondary phase in addition to the Bi-rich and Ba-rich phases.

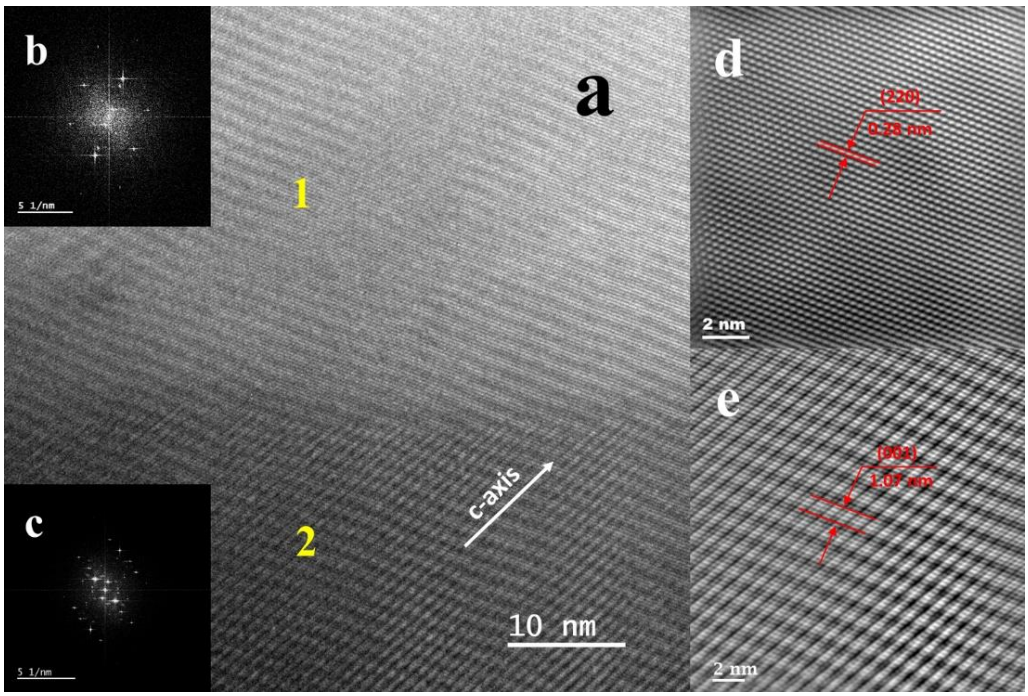

Fig. 7.11 HRTEM data for $Ca_{2.63}Bi_{0.3}Ba_{0.07}Co_{3.92}O_{9+\delta}$ ceramic prepared by solid state reaction (a. HRTEM image; b. FFT image of Area 1; c. FFT image of Area 2; d. IFFT image of Area 1; e. IFFT image of Area 2)

Fig. 7.12(a) shows a TEM image of the secondary phase detected in Sr_SPSAn. The corresponding SAED patterns (Fig. 7.12(b)) can also be indexed as the Co_3O_4, sharing the same crystal structure ([-111] zone axis) with the secondary phase in Fig. 7.10(a). Therefore, the cobalt oxide present in Fig. 7.5(e) can be confirmed to have a Co/O ratio of 3/4. It is also inferred that the presence of Co_3O_4 as the secondary phase is common for both Bi/Ba and Bi/Sr co-doped ceramics.

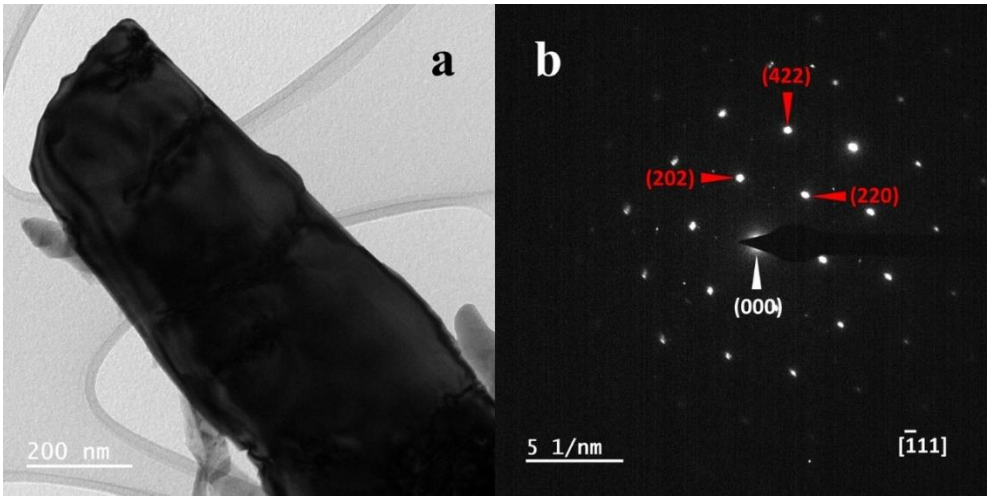

Fig. 7.12 TEM image (a) and corresponding SAED patterns (b) of secondary phases in SPS-processed $Ca_{2.63}Bi_{0.3}Sr_{0.07}Co_{3.92}O_{9+\delta}$ ceramics annealed at 1203 K for 24 h

7.6 XPS Analysis

High-resolution XPS spectra of Co 2p 3/2 for $Ca_{2.63}Bi_{0.3}M_{0.07}Co_{3.92}O_{9+\delta}$ (M = Sr and Ba) ceramics prepared by different fabrication routes are presented in Fig. 7.13. The Co 2p 3/2 signal can be deconvoluted into three peaks: the first peak at 778.8-779.1 eV corresponding to Co^{3+}, the second peak at 779.8-780.1 eV assigned to Co^{2+} and the last peak at 781.6-781.9 eV ascribed to Co^{4+}; these results confirm a mixture of three different cobalt ions in calcium cobaltite and are consistent with published XPS Co 2p 3/2 data in previous investigations [13–15]. The concentrations of different cobalt ions derived from the XPS data in Fig. 7.13 are summarised in Table 7.5. It is apparent that the ratio of [Co^{4+}/(Co^{3+}+Co^{4+})] of both the SSR and SPSAn processed samples slightly varies around 45.0 %, regardless of the dopants employed; the negligible variation indicates that a similar level of carrier concentration is achieved in the synthesized materials.

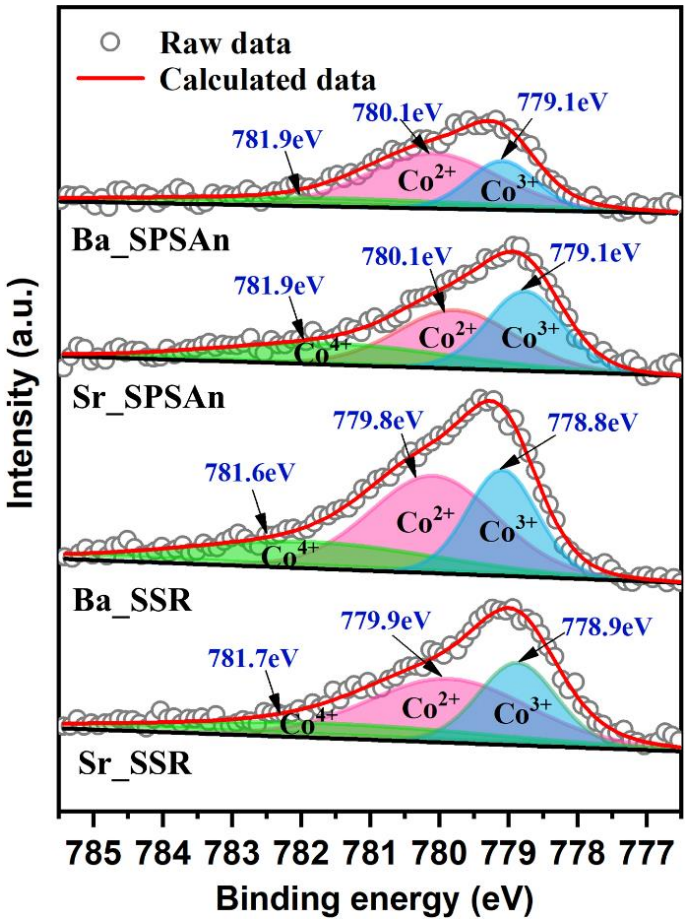

Fig. 7.13 High-resolution XPS spectra of Co 2p 3/2 for $Ca_{2.63}Bi_{0.3}M_{0.07}Co_{3.92}O_{9+\delta}$ (M = Sr and Ba) ceramics prepared by different fabrication routes

Table 7.5 Concentrations of cobalt ions in $Ca_{2.63}Bi_{0.3}M_{0.07}Co_{3.92}O_{9+\delta}$ (M = Sr and Ba) ceramics prepared by different fabrication routes

Route	M	Co^{3+} (%)	Co^{2+} (%)	Co^{4+} (%)	$Co^{4+}/(Co^{3+}+Co^{4+})$ (%)
SSR	Sr	29.5	47.2	23.3	44.1
SSR	Ba	33.5	38.2	28.3	45.8
SPSAn	Sr	29.0	47.3	23.7	45.0
SPSAn	Ba	25.7	53.4	20.9	44.8

7.7 Electrical Transport

Fig. 7.14 shows the electrical transport properties of $Ca_{2.63}Bi_{0.3}M_{0.07}Co_{3.92}O_{9+\delta}$ (M = Sr and Ba) ceramics prepared by different fabrication routes. Notably, for the SPS-processed samples the electrical conductivity (σ) is measured parallel to the *ab* plane of the calcium cobaltite grains; the data show σ for all samples increases with increasing temperature (Fig. 7.14(a)), indicating semiconducting behaviour. Basically, the sintered ceramics exhibit different ranges of σ between 323 K and 823 K: 19.7-44.1 S/cm for the SSR processed samples, 3.1-55.8 S/cm for the original SPS-processed samples and 79.8-135.3 S/cm for the annealed SPS-processed samples. These results are comparable to σ reported for both solid state synthesized (5.0-40.0 S/cm) and SPS-processed (66.0-125.0 S/cm) calcium cobaltite based ceramics in earlier studies [16–19]. The positive Seebeck coefficients (S) of all samples (Fig. 7.14(b)) suggest a hole conduction mechanism for calcium cobaltite. The S values for both the SSR and annealed SPS samples are quite similar, increasing from 134.4 to 160.0 μV/K within the temperature range of 323-823 K, consistent with published thermopower data (130.0-165.0 μV/K) [16,17,20,21]. By contrast, the original SPS-processed samples show larger Seebeck coefficients. The S value for Ba_SPS varies from 180.0 to 204.0 μV/K, significantly higher than S values for the Sr_SPS samples (144.5-174.3 μV/K).

In view of the similar thermopower data obtained for the SSR processed samples and annealed SPS-processed samples, it is inferred that S is dominated by the carrier concentration (n) which maintains a similar level according to the Drude model in Equation (2.4). This matches well with the trend of the ratio of $[Co^{4+}/(Co^{3+}+Co^{4+})]$ in Table 7.5. On the basis of Equation (2.23), lower σ values for the SSR processed samples are ascribed to low carrier mobility (μ) controlled by the enhanced carrier scattering caused by the higher porosity. The slight increase in mobility of Ba_SSR compared to Sr_SSR should result from the lower porosity (Fig. 7.1(b)) and larger grain size (Fig. 7.5(b)), because higher porosity

and smaller grain size can lead to increased energy barriers at the grain boundaries, thereby increasing the carrier scattering and hence a lower μ [22]. As expected, higher σ values are achieved for the dense annealed SPS-processed samples with preferred grain orientation, mainly due to the enhanced μ. It is noticeable that σ for Sr_SPSAn shows an overall 20 % enhancement compared to Ba_SPSAn, which is mainly attributed to larger grain size and the successful Sr doping in the crystal lattice. In spite of higher porosity in Sr_SPSAn (Fig. 7.1(b)), the larger grain size (Sr_SPSAn: 27.8 μm; Ba_SPSAn: 21.3 μm in Fig. 7.5(b)) and improved texture (Fig. 7.9) can reduce the grain boundary density, thereby partially offsetting the increased energy barriers at the grain boundaries induced by the higher porosity. It was reported that the substitution of larger radius atoms in the rock salt sublayers of calcium cobaltite would induce a strain field on the [CoO_2] sublayers, thereby decreasing the electronic density of state (DoS) and hence a smaller effective mass (m*) [23]. The corresponding μ for Sr_SPSAn is therefore enhanced based on Equations (2.23) and (2.24). However, the increase in S for Ba_SPS, in contrast to Sr_SPS, should originate from the differences in n according to the Drude model. Although the original SPS-processed samples contain considerable amounts of secondary phases, the fractions of the main phase (calcium cobaltite) in Ba_SPS are lower than those in Sr_SPS (Table 7.4), thereby leading to lower overall σ [24]. As a result, the highest power factor of 0.34 $mWm^{-1}K^{-1}$ is obtained for Sr_SPSAn at 800 K (Fig. 7.14(c)), showing at least 20 % enhancement compared to previous studies (0.125-0.27 $mWm^{-1}K^{-2}$ at 800 K) [17,20,25].

In order to further understand the electrical transport behaviour, σ is plotted as a function of reciprocal temperature (Fig. 7.15(a)). The linear region of the plot, data above 573 K, matches well with the small polaron hopping conduction (SPHC) model (Equation (2.25)). The calculated activation energies (E_h) are displayed in Fig. 7.15(b). Given a fixed chemical composition, it is not surprising that the original SPS-processed samples show the highest E_h (Sr_SPS: 115.6 meV; Ba_SPS: 199.1 meV), mainly due to the high fractions of poorly conducting secondary phases (Table 7.4). The fall of E_h in annealed SPS-processed samples compared to the solid state synthesized ones (Bi/Sr co-doping: $\Delta E_h \approx 20$ meV; Bi/Ba co-doping: $\Delta E_h \approx 10$ meV) is ascribed to the weakening of carrier scattering caused by the increased bulk density (Fig. 7.1) and stronger texture (Fig. 7.3). Overall, the Bi/Sr co-doped samples show lower E_h than the Bi/Ba co-doped samples. E_h is derived from the slope of the linear plot over 573 K, where carrier hopping starts to be pronounced. The refined lattice parameters (Table 7.2) in conjunction with the EDS data (Fig. 7.7) confirm that the dopants (Bi and Sr) enter the crystal lattice of calcium cobaltite except Ba. For the Bi/Sr co-doped

samples, the induced strain field leads to a smaller m* and a narrower band gap [23], which contributes to lower E_h in the Bi/Sr co-doped samples. However, only a slight difference in E_h is observed between Sr_SSR and Ba_SSR, because the enhanced carrier scattering caused by the higher porosity (41.8 % in Fig. 7.1) in Sr_SSR samples partially compensates for the reduction in E_h described above.

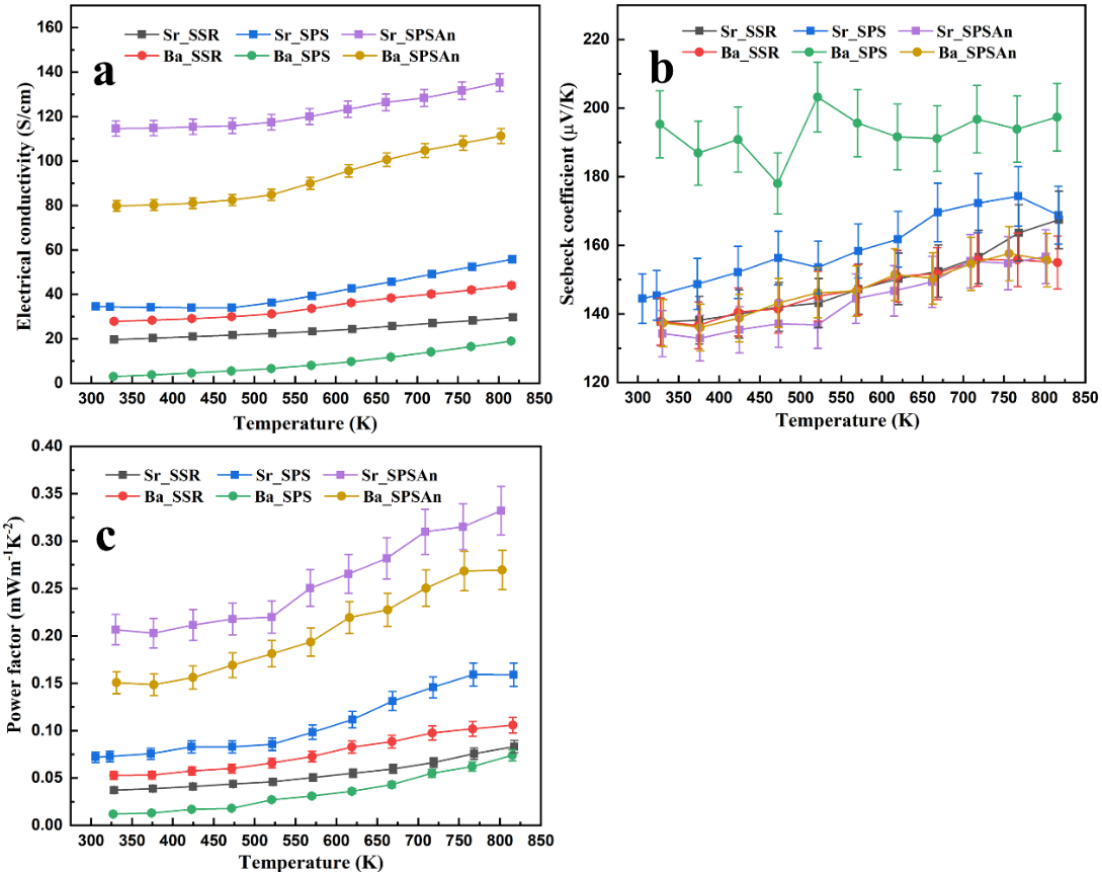

Fig. 7.14 Electrical conductivity (a), Seebeck coefficient (b) and power factor (c) of $Ca_{2.63}Bi_{0.3}M_{0.07}Co_{3.92}O_{9+\delta}$ (M = Sr and Ba) ceramics prepared by different fabrication routes

The variation of both n and μ for $Ca_{2.63}Bi_{0.3}M_{0.07}Co_{3.92}O_{9+\delta}$ (M = Sr and Ba) ceramics prepared by different fabrication routes (estimated by Equations (2.10) and (2.23) at room temperature) are shown in Fig. 7.15(c, d). The calculated n values for all samples are stable at around 5.5×10^{20} cm^{-3}, matching well with the trend of ratio of $[Co^{4+}/(Co^{3+}+Co^{4+})]$ in Table 7.5. As expected, the annealed SPS-processed samples show higher μ than the solid state synthesized samples. The calculated μ of Sr_SSR is slightly lower than that of Ba_SSR, because the carrier scattering at low temperatures are dominated by the density of grain boundaries and the numbers of pores. With a larger grain size (lower grain boundary density) and a lower porosity (Fig. 7.2), Ba_SSR demonstrates weaker carrier scattering. Similarly,

the larger grain size (Fig. 7.5) and improved texture (Fig. 7.9) still play key roles in reducing the energy barrier at grain boundaries in Sr_SPSAn in spite of slightly increased porosity in contrast to Ba_SPSAn (Fig. 7.1), thereby leading to a higher carrier mobility.

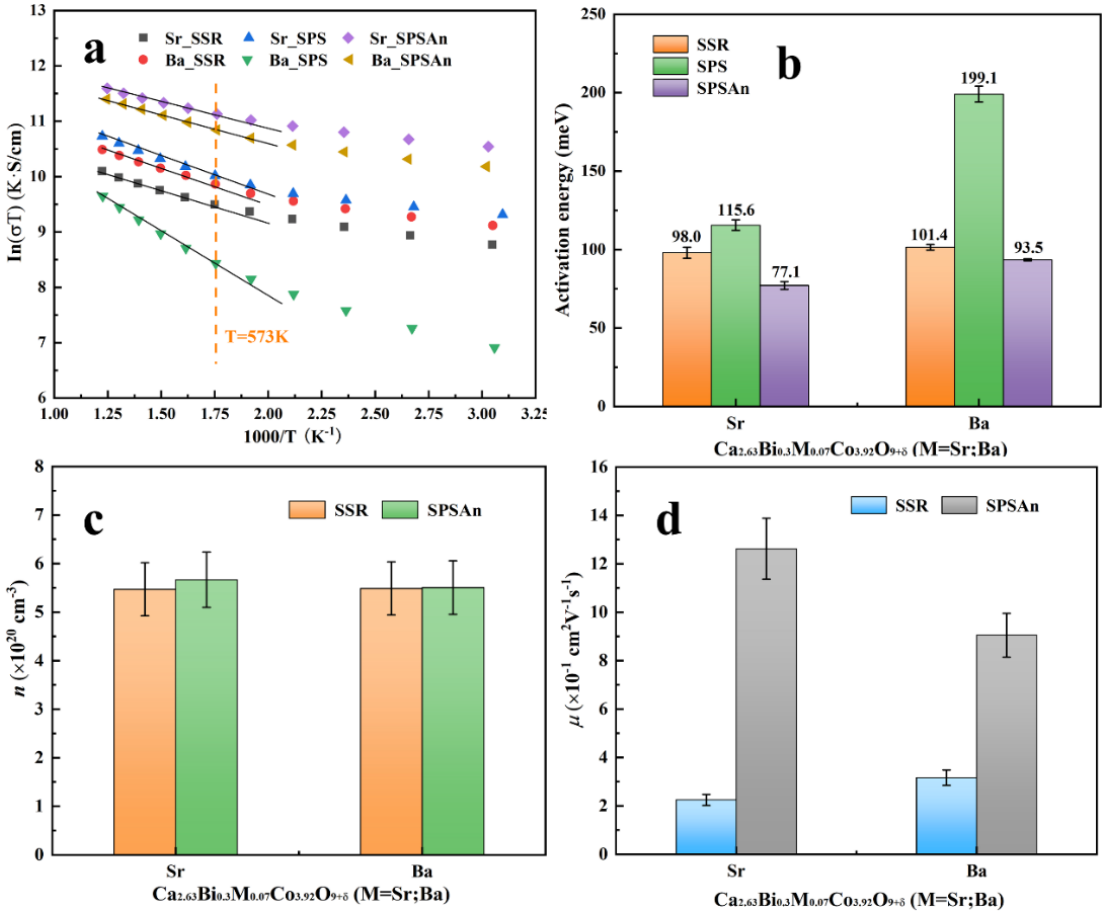

Fig. 7.15 Electrical conductivity as a function of reciprocal temperature (a), calculated activation energies (b), calculated carrier concentration (c) and calculated carrier mobility (d) for $Ca_{2.63}Bi_{0.3}M_{0.07}Co_{3.92}O_{9+\delta}$ (M = Sr and Ba) ceramics prepared by different fabrication routes

Assuming that there are high fractions of primary phase (calcium cobaltite) after adequate heat-treatment, the effects of porosity, texture and average grain size on electrical transport properties of $Ca_{2.63}Bi_{0.3}M_{0.07}Co_{3.92}O_{9+\delta}$ (M = Sr and Ba) ceramics prepared by SSR and SPSAn routes were investigated (Fig. 7.16). It is clearly seen that the electrical conductivity (σ) is positively correlated with Lotgering factor and average grain size (Fig. 7.16(c, e)), whereas the Seebeck coefficient (S) is independent of all the correlative factors (Fig. 7.16(b, d, f). Therefore, it can be inferred that the enhanced σ for Sr_SPSAn sample is mainly attributed to the enhanced carrier mobility originating from the improved texture and increased grain size.

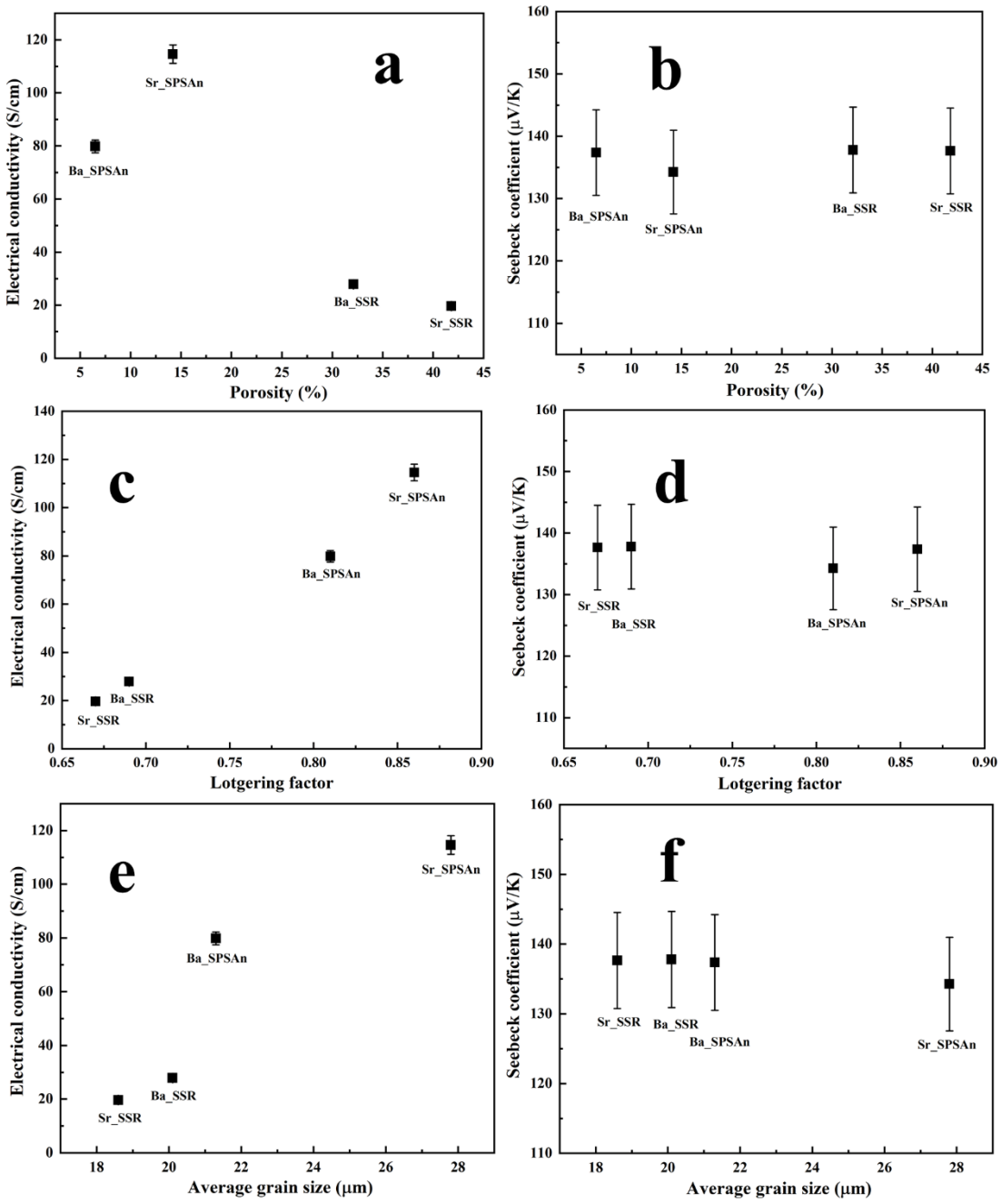

Fig. 7.16 Electrical conductivity and Seebeck coefficient at 323 K for $Ca_{2.63}Bi_{0.3}M_{0.07}Co_{3.92}O_{9+\delta}$ (M = Sr and Ba) ceramics prepared by SSR and SPSAn routes as a function of porosity (a, b), Lotgering factor (c, d) and average grain size (e, f)

7.8 Thermal Transport

The thermal conductivity of $Ca_{2.63}Bi_{0.3}M_{0.07}Co_{3.92}O_{9+\delta}$ (M = Sr and Ba) ceramics prepared by different fabrication routes was measured parallel to the *ab* planes of calcium cobaltite. As Fig. 7.17(a) shows, a low thermal conductivity (κ: 0.83-0.54 $Wm^{-1}K^{-1}$ between 323 K and 823 K) was achieved for solid state synthesized samples. The κ for Ba_SSR samples reaches 0.84 $Wm^{-1}K^{-1}$ at 323 K, slightly higher that the value for Sr_SSR samples (0.69 Wm^{-}

$^{1}K^{-1}$); this result is consistent with the published κ data (0.5-0.9 $Wm^{-1}K^{-1}$ at 323 K) for bismuth doped calcium cobaltite prepared by solid state reaction [18]. By contrast, the κ value for SPS-processed samples is nearly tripled at 823 K. Interestingly, κ values for Ba_SPS, Sr_SPS and Sr_SPSAn are quite similar (2.6-1.8 $Wm^{-1}K^{-1}$ between 323 K and 823 K); the high temperature value is comparable to κ for the 0.3Sr substituted $Ca_3Co_4O_9$ (1.5 $Wm^{-1}K^{-1}$ at 1000 K) [3] and the 0.05Ba added $Ca_3Co_4O_9$ (1.7 $Wm^{-1}K^{-1}$ at 1000 K) [4] ceramics prepared by the SPS route. However, a higher κ (3.0-2.3 $Wm^{-1}K^{-1}$ between 323 K and 823 K) is obtained for Ba_SPSAn. The lattice ($\kappa_{lattice}$) and electronic ($\kappa_{electronic}$) thermal conductivities calculated from the Wiedemnn-Franz formula (Equations (2.28) and (2.29)) are shown in Fig. 7.17(b). It is clear that $\kappa_{electronic}$ shows limited variations with dopants and fabrication routes, increasing slightly from 0.02 $Wm^{-1}K^{-1}$ to 0.3 $Wm^{-1}K^{-1}$. By marked contrast, $\kappa_{lattice}$ plays a dominating role in thermal conduction and shows a downward trend with temperature. The phonon contribution represents ~95 % of the total at 323 K, followed by a slight decline to ~85 % of the total at 823 K for both the solid state synthesized and SPS-processed samples.

The original SPS-processed samples (Fig. 7.2 and Fig. 7.5(c, d)) contain considerable amounts of secondary phases; in particular there are high fractions of the dark phase ($Ca_3Co_2O_6$), between 12 % and 19 % (Table 7.4). In fact, $Ca_3Co_2O_6$ is also a promising thermoelectric phase although it shows lower κ compared to $Ca_3Co_4O_9$ [26,27]. In view of this case, the contributions from different phases to thermal conduction are complex and difficult to be distinguished unambiguously. Nevertheless, the increased κ should mainly result from the higher densification induced by spark plasma sintering (Fig. 7.1).

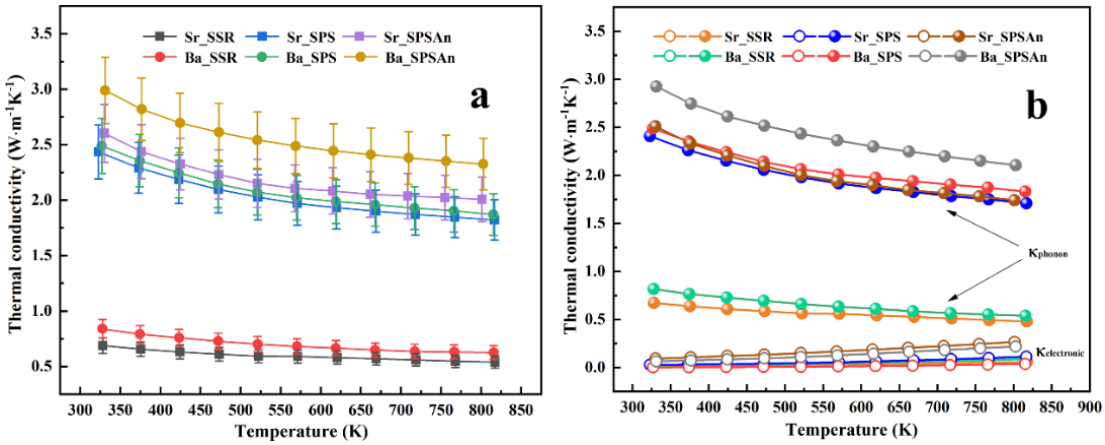

Fig. 7.17 Total thermal conductivity (a) and lattice and electronic thermal conductivity (b) of $Ca_{2.63}Bi_{0.3}M_{0.07}Co_{3.92}O_{9+\delta}$ (M = Sr and Ba) ceramics prepared by different fabrication routes

In order to understand the thermal conduction mechanism in the SSR and SPSAn samples, where the secondary phases are further reduced through optimised heat-treatment, $\kappa_{lattice}$ data are plotted as a function of reciprocal temperature [28], shown in Fig. 7.18(a). The linear dependence is revealed in the regions above 473 K and 573 K for the SSR and SPSAn samples, respectively; this is the characteristic of phonon-phonon interactions during the Umklapp process. The low-temperature thermal conduction behaviour is believed to be controlled by grain boundary scattering and pores [29,30]. The differences between the transformation temperatures (ΔT = 100 K) can be explained by the different degrees of phonon scattering at low temperatures. It was reported that closed pores inside samples could be regarded as secondary phases composed of air [31]. The effects of porosity on κ can be therefore characterised using Equation (2.37) [32]. Consequently, pronounced phonon scattering is induced by the high porosity in SSR samples, thereby leading to a lower transformation temperature. Similar ΔT (towards lower temperatures) arising from increased grain boundary scattering was also found in nano-sized polycrystalline $Ca_3Co_4O_9$ ceramics [33]. The variational trend for the phonon mean free path is evaluated using Equation (2.31). Fig. 7.18(b) shows that the length of mean free path (l_{ph}) at 823 K is shorter than the value at 323 K; the enhanced phonon scattering probably results from the stronger lattice vibration at high temperatures. Overall, the SPSAn samples exhibit larger l_{ph} compared to the SSR samples, mainly due to the reduced porosity. Furthermore, smaller l_{ph} values are obtained for Bi/Sr co-doped samples in contrast to Bi/Ba co-doped ones, especially for SPSAn samples ($\Delta l_{ph} \approx 3$ Å). Although the densification is promoted by spark plasma sintering, Sr_SPSAn still contain porosity ~14.2 %, about two times the value for Ba_SPSAn (6.5 %), as a consequence of the volatilization of secondary phases. Consequently, for Sr_SPSAn samples more opportunities are available to enhance phonon scattering at low temperatures. In addition, the effects of point defect scattering induced by elemental doping should be taken into consideration; the latter can be described by the Debye–Callaway model [34,35], using Equations (2.32-2.35). Here, Bi and Sr have been shown to enter the crystal lattice of calcium cobaltite, whilst Ba participates in forming Ba-rich secondary phases. The difference in thermal transport between these two chemical compositions ($Ca_{2.63}Bi_{0.3}Sr_{0.07}Co_{3.92}O_{9+\delta}$ and $Ca_{2.63}Bi_{0.3}Ba_{0.07}Co_{3.92}O_{9+\delta}$) should mainly originate from the different roles of Sr and Ba dopants in the synthesized materials. The successful Sr doping gives rise to both mass variations and generation of a strain field, resulting in a larger Γ and hence a smaller τ_D. By contrast, Ba (in the form of Ba-rich secondary phases) mainly makes contribution to modifying grain boundaries and interfaces rather than performing as a dopant in the crystal

lattice, although Ba shows larger atomic mass and radius than Sr. Therefore, the Bi/Sr co-doped samples exhibit shorter l_{ph} compared to the Bi/Ba co-doped ones.

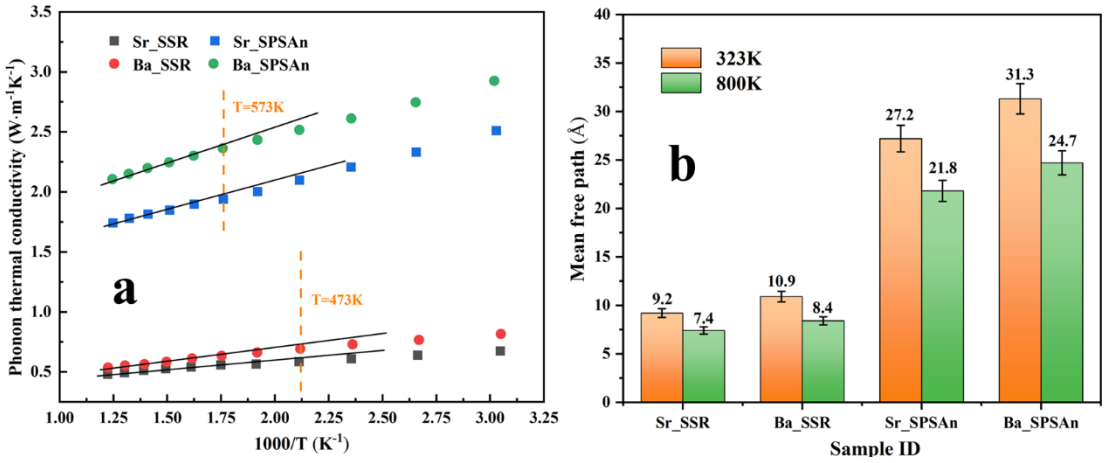

Fig. 7.18 (a) Lattice thermal conductivity as a function of reciprocal temperature and (b) phonon mean free path length of $Ca_{2.63}Bi_{0.3}M_{0.07}Co_{3.92}O_{9+\delta}$ (M = Sr and Ba) ceramics prepared by different fabrication routes

7.9 Thermoelectric Figure of Merit (ZT)

Fig. 7.19 shows the temperature dependence of ZT values of $Ca_{2.63}Bi_{0.3}M_{0.07}Co_{3.92}O_{9+\delta}$ (M = Sr and Ba) ceramics prepared by different fabrication routes. All ZT values increase with increasing temperature. It is not surprising that the ZT values of the original SPS-processed samples are lower than other groups as a result of a low power factor arising from the presence of considerable amounts of poorly conducting phases and a high thermal conductivity induced by the promoted densification. It is also noted that the ZT values of Ba_SSR and Sr_SPSAn are quite similar, where the maximum value of 0.14 is achieved at 800 K, showing the possibility of increasing the thermoelectric performance of calcium cobaltite by either minimising the thermal conductivity or maximising the electrical conductivity. The ZT value of the Sr_SPSAn samples are comparable to published data for SPS-processed calcium cobaltite [24,25,36,37]. Furthermore, the similar ZT obtained for Ba_SSR is very competitive, showing 75 % increase at 800 K compared to undoped solid state synthesized calcium cobaltite [38]. This is also consistent with the data for $0.25B_4C$ added calcium cobaltite ceramics at 800 K; the ZT value of this previously reported optimised composition could reach 0.24 at 1073 K, which is the highest value among the solid state synthesized samples [38].

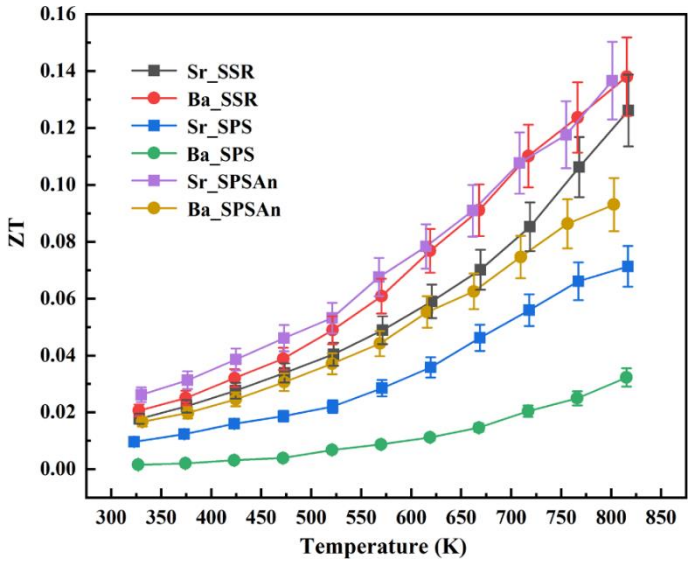

Fig. 7.19 ZT values for $Ca_{2.63}Bi_{0.3}M_{0.07}Co_{3.92}O_{9+\delta}$ (M = Sr and Ba) ceramics prepared by different fabrication routes

7.10 Summary

This chapter provides insight and understanding of the microstructure-property relationships in calcium cobaltite ceramics which are controlled by dopants and fabrication routes. In addition, a facile and economical solid state synthesis route for $Ca_{2.63}Bi_{0.3}Ba_{0.07}Co_{3.92}O_{9+\delta}$ ceramics is demonstrated, achieving high thermoelectric performance, comparable to that of the SPS-processed $Ca_{2.63}Bi_{0.3}Sr_{0.07}Co_{3.92}O_{9+\delta}$ samples.

The roles of Bi/Sr and Bi/Ba dual dopants in $Ca_{2.63}Bi_{0.3}M_{0.07}Co_{3.92}O_{9+\delta}$ (M = Sr and Ba) ceramics have been clarified. At 1203 K, it was demonstrated that Bi successfully entered the crystal lattice of calcium cobaltite. However, Sr was more likely to substitute at Ca sites in the rock salt sublayer, whilst Ba mainly participated in forming Ba-rich secondary phases.

In contrast to the low density samples obtained by solid state reaction, the SPS route in conjunction with an annealing process enables lower porosity, development of texture and reduction of the secondary phases. The electrical conductivity of annealed SPS-processed Bi/Sr co-doped samples was significantly enhanced. The increased carrier mobility is consistent with the reduced effective mass (induced by successful Bi/Sr co-doping) as well as the lower energy barrier at grain boundaries caused by combined effects of improved texture, increased grain size and promoted densification. By contrast, the annealed SPS-processed Bi/Ba co-doped samples showed inferior electrical transport properties mainly due to the reduced lattice distortion and the effects of the poorly conducting Ba-rich phases.

Despite a low electrical conductivity, limited by high porosity in solid state synthesized $Ca_{2.63}Bi_{0.3}M_{0.07}Co_{3.92}O_{9+\delta}$ (M = Sr and Ba) ceramics, these samples showed more pronounced phonon scattering at low temperatures. Although the in-plane thermal conductivity showed an overall increase in the samples prepared by the SPS route, the annealed SPS-processed Bi/Sr co-doped samples showed stronger phonon scattering because of the mass variation and strain field induced by the pronounced lattice expansion and higher porosity arising from the volatilization of bright phases during heat-treatment. As a result, the highest ZT value of 0.14 was achieved in both Ba_SSR and Sr_SPSAn samples at 800 K. Through Bi/Ba co-doping, the ZT value of solid state synthesized calcium cobaltite is enhanced, comparable to the dense SPS-processed Bi/Sr co-doped samples. This value also represents about 75 % enhancement compared to the undoped samples and is very competitive among the solid state synthesized calcium cobaltite ceramics in earlier studies.

References

[1] A. Maignan, D. Pelloquin, S. Hebert, Y. Klein, M. Hervieu, Thermoelectric power in misfit cobaltites ceramics: Optimization by chemical substitutions, Bol. La Soc. Esp. Ceram. y Vidr. 45 (2006) 122–125.

[2] Y. Zhang, J. Zhang, Rapid reactive synthesis and sintering of textured $Ca_3Co_4O_9$ ceramics by spark plasma sintering, J. Mater. Process. Technol. 208 (2008) 70–74.

[3] F. Delorme, C.F. Martin, P. Marudhachalam, D. Ovono Ovono, G. Guzman, Effect of Ca substitution by Sr on the thermoelectric properties of $Ca_3Co_4O_9$ ceramics, J. Alloys Compd. 509 (2011) 2311–2315.

[4] P. Carvillo, Y. Chen, C. Boyle, P.N. Barnes, X. Song, Thermoelectric Performance Enhancement of Calcium Cobaltite through Barium Grain Boundary Segregation, Inorg. Chem. 54 (2015) 9027–9032.

[5] G. Constantinescu, S. Rasekh, M.A. Torres, J.C. Diez, M.A. Madre, A. Sotelo, Effect of Sr substitution for Ca on the $Ca_3Co_4O_9$ thermoelectric properties, J. Alloys Compd. 577 (2013) 511–515.

[6] C. Boyle, L. Liang, Y. Chen, J. Prucz, E. Cakmak, T.R. Watkins, E. Lara-Curzio, X. Song, Competing dopants grain boundary segregation and resultant seebeck coefficient and power factor enhancement of thermoelectric calcium cobaltite ceramics, Ceram. Int. 43 (2017) 11523–11528.

[7] C. Romo-De-La-Cruz, L. Liang, S.A.P. Navia, Y. Chen, J. Prucz, X. Song, Role of oversized dopant potassium on the nanostructure and thermoelectric performance of calcium cobaltite ceramics, Sustain. Energy Fuels. 2 (2018) 876–881.

[8] D. Grebille, S. Lambert, F. Bouree, V. Petricek, Contribution of powder diffraction for structure refinements of aperiodic misfit cobalt oxides, J. Appl. Crystallogr. 37 (2004) 823–831.

[9] C. Di, J.H. Pan, S.T. Dong, Y.Y. Lv, X.J. Yan, J. Zhou, S.H. Yao, H. Lu, V.E. Gusev, Y.F. Chen, M.H. Lu, Ultralow cross-plane lattice thermal conductivity caused by Bi–O/Bi–O interfaces in natural superlattice-like single crystals, CrystEngComm. 21 (2019) 6261–6268.

[10] E. Combe, R. Funahashi, T. Barbier, F. Azough, R. Freer, Decreased thermal conductivity in $Bi_2Sr_2Co_2O_x$ bulk materials prepared by partial melting, J. Mater. Res. 31 (2016) 1296–1305.

[11] W. Seo, S. Lee, Y. Lee, M. Lee, Y. Masuda, K. Koumoto, High-resolution transmission electron microscopy study of $Ca_3Co_4O_9$, Microscopy. 53 (2004) 397–401.

[12] K. Yubuta, X. Huang, Y. Miyazaki, T. Kajitani, High-Resolution Electron Microscopy Study of $[(Ca, Bi)_2CoO_3]_{0.62}CoO_2$, J. Phys. Soc. Japan. 77 (2008) 94603.

[13] K. Park, D.A. Hakeem, J.S. Cha, Synthesis and structural properties of thermoelectric $Ca_{3-x}Ag_xCo_4O_{9+\delta}$ powders, Dalt. Trans. 45 (2016) 6990–6997.

[14] R. Zhang, Y. Lu, L. Wei, Z. Fang, C. Lu, Y. Ni, Z. Xu, S. Tao, P. Li, Synthesis and conductivity properties of $Gd_{0.8}Ca_{0.2}BaCo_2O_{5+\delta}$ double perovskite by sol–gel combustion, J. Mater. Sci. Mater. Electron. 26 (2015) 9941–9948.

[15] H. Liu, G.C. Lin, X.D. Ding, J.X. Zhang, Mechanical relaxation in thermoelectric oxide $Ca_{3-x}Sr_xCo_4O_{9+\delta}$ (x = 0, 0.25, 0.5, 1.0) associated with oxygen vacancies, J. Solid State Chem. 200 (2013) 305–309.

[16] F. Zhang, Q. Lu, T. Li, X. Zhang, J. Zhang, X. Song, Preparation and thermoelectric transport properties of Ba-, La- and Ag-doped Ca3Co4O9 oxide materials, J. Rare Earths. 31 (2013) 778–783.

[17] Z. Shi, F. Gao, J. Zhu, J. Xu, Y. Zhang, T. Gao, M. Qin, Influence of liquid−phase sintering on microstructure and thermoelectric properties of $Ca_3Co_4O_9$−based

ceramics with Bi_2O_3 additive, J. Mater. 5 (2019) 711–720.

[18] I. V Matsukevich, A.I. Klyndyuk, E.A. Tugova, A.N. Kovalenko, A.A. Marova, N.S. Krasutskaya, Thermoelectric properties of $Ca_{3-x}Bi_xCo_4O_{9+\delta}$ ($0.0 \leqslant x \leqslant 1.5$) ceramics, Inorg. Mater. 52 (2016) 593–599.

[19] D. Kenfaui, G. Bonnefont, D. Chateigner, G. Fantozzi, M. Gomina, J.G. Noudem, $Ca_3Co_4O_9$ ceramics consolidated by SPS process: Optimisation of mechanical and thermoelectric properties, Mater. Res. Bull. 45 (2010) 1240–1249.

[20] F. Delorme, P. Diaz-Chao, E. Guilmeau, F. Giovannelli, Thermoelectric properties of $Ca_3Co_4O_9$–Co_3O_4 composites, Ceram. Int. 41 (2015) 10038–10043.

[21] T. Yin, D. Liu, Y. Ou, F. Ma, S. Xie, J.-F. Li, J. Li, Nanocrystalline Thermoelectric $Ca_3Co_4O_9$ Ceramics by Sol−Gel Based Electrospinning and Spark Plasma Sintering, J. Phys. Chem. C. 114 (2010) 10061–10065.

[22] Y. Zhou, I. Matsubara, W. Shin, N. Izu, N. Murayama, Effect of grain size on electric resistivity and thermopower of $(Ca_{2.6}Bi_{0.4})Co_4O_9$ thin films, J. Appl. Phys. 95 (2003) 625–628.

[23] J.D. Baran, M. Molinari, N. Kulwongwit, F. Azough, R. Freer, D. Kepaptsoglou, Q.M. Ramasse, S.C. Parker, Tuning Thermoelectric Properties of Misfit Layered Cobaltites by Chemically Induced Strain, J. Phys. Chem. C. 119 (2015) 21818–21827.

[24] J. Yu, K. Chen, F. Azough, D.T. Alvarez-Ruiz, M.J. Reece, R. Freer, Enhancing the Thermoelectric Performance of Calcium Cobaltite Ceramics by Tuning Composition and Processing, ACS Appl. Mater. Interfaces. 12 (2020) 47634–47646.

[25] D. Moser, L. Karvonen, S. Populoh, M. Trottmann, A. Weidenkaff, Influence of the oxygen content on thermoelectric properties of $Ca_{3-x}Bi_xCo_4O_{9+\delta}$ system, Solid State Sci. 13 (2011) 2160–2164.

[26] M. Mikami, R. Funahashi, The effect of element substitution on high-temperature thermoelectric properties of $Ca_3Co_2O_6$ compounds, J. Solid State Chem. 178 (2005) 1670–1674.

[27] D. Lu, G. Chen, J. Pei, X. Yang, H. Xian, Effect of erbium substitution on thermoelectric properties of complex oxide $Ca_3Co_2O_6$ at high temperatures, J. Rare Earths. 26 (2008) 168–172.

[28] S. Raghavan, M.J. Mayo, H. Wang, R.B. Dinwiddie, W.D. Porter, The effect of grain size, porosity and yttria content on the thermal conductivity of nanocrystalline zirconia, Scr. Mater. 39 (1998) 1119–1125.

[29] E.S. Toberer, A. Zevalkink, G.J. Snyder, Phonon engineering through crystal chemistry, J. Mater. Chem. 21 (2011) 15843–15852.

[30] H. Lee, D. Vashaee, D.Z. Wang, M.S. Dresselhaus, Z.F. Ren, G. Chen, Effects of nanoscale porosity on thermoelectric properties of SiGe, J. Appl. Phys. 107 (2010) 94308.

[31] Y. Liu, Y. Lin, Z. Shi, C.-W. Nan, Z. Shen, Preparation of $Ca_3Co_4O_9$ and Improvement of its Thermoelectric Properties by Spark Plasma Sintering, J. Am. Ceram. Soc. 88 (2005) 1337–1340.

[32] J.L. Mi, T.J. Zhu, X.B. Zhao, J. Ma, Nanostructuring and thermoelectric properties of bulk skutterudite compound $CoSb_3$, J. Appl. Phys. 101 (2007) 54314.

[33] M. Gunes, M. Ozenbas, Effect of grain size and porosity on phonon scattering enhancement of $Ca_3Co_4O_9$, J. Alloys Compd. 626 (2015) 360–367.

[34] G.K. Ren, J.L. Lan, K.J. Ventura, X. Tan, Y.H. Lin, C.W. Nan, Contribution of point defects and nano-grains to thermal transport behaviours of oxide-based thermoelectrics, Npj Comput. Mater. 2 (2016) 16023.

[35] Y. Zheng, M. Zou, W. Zhang, D. Yi, J. Lan, C.W. Nan, Y.H. Lin, Electrical and thermal transport behaviours of high-entropy perovskite thermoelectric oxides, J. Adv. Ceram. 10 (2021) 377–384.

[36] H.Q. Liu, F.P. Wang, F. Liu, Y. Song, Z.H. Jiang, Thermoelectric performance of SPS sintered $[(Ca_{0.95}M_{0.05})_2CoO_3][CoO_2]_{1.61}$, J. Mater. Sci. Mater. Electron. 17 (2006) 525–528.

[37] N. Wu, T.C. Holgate, N. Van Nong, N. Pryds, S. Linderoth, High temperature thermoelectric properties of $Ca_3Co_4O_{9+\delta}$ by auto-combustion synthesis and spark plasma sintering, J. Eur. Ceram. Soc. 34 (2014) 925–931.

[38] H. Amaveda, M. Mora, O.J. Dura, M.A. Torres, M.A. Madre, S. Marinel, A. Sotelo, Drastic enhancement of mechanical properties of $Ca_3Co_4O_9$ by B_4C addition, J. Eur. Ceram. Soc. 41 (2021) 402–408.

8. Conclusions and Recommendations for Future Work

8.1 Conclusions

In this study, the calcium cobaltite bulk and film ceramics were successfully prepared by solid state reaction, spark plasma sintering, cold sintering and screen printing, with assist of optimised heat-treatment process. The power factor and ZT value of the optimal composition in different chapters are summarised in Table 8.1.

Table 8.1 The power factor and ZT value of the optimal composition in different chapters

Composition	**Route**	**Power factor ($\mu Wm^{-1}K^{-2}$)**	**ZT**
$Ca_{2.7}Bi_{0.3}Co_{3.92}O_{9+\delta}$	Solid state reaction	98.0 at 823 K	-
$Ca_{2.7}Bi_{0.3}Co_{3.92}O_{9+\delta}$	Screen printing	55.5 at 673 K	-
$Ca_{2.7}Bi_{0.3}Co_{3.92}O_{9+\delta}$	Spark plasma sintering	340.0 at 823 K	0.16 at 823 K
$Ca_{2.7}Bi_{0.3}Co_{3.92}O_{9+\delta}$	Cold sintering	280.0 at 800 K	-
$Ca_{2.63}Bi_{0.3}Ba_{0.07}Co_{3.92}O_{9+\delta}$	Solid state reaction	105.8 at 800 K	0.14 at 800 K

Notably, the film sample was measured to a maximum temperature of 673 K, mainly due to the upper limit working temperature of the tool used for assembling. The $Ca_{2.7}Bi_{0.3}Co_{3.92}O_{9+\delta}$ thick film exhibits the lowest power factor because of the low densification caused by decomposition of organic binders and constrained sintering effects. The maximum power factor and ZT value of the SPS-processed $Ca_{2.7}Bi_{0.3}Co_{3.92}O_{9+\delta}$ sample reach 340.0 $\mu Wm^{-1}K^{-2}$ and 0.16 at 823 K, respectively. This is due to the enhanced electrical conductivity induced by the texture development and the reduced thermal conductivity caused by heavy elemental doping. Although the power factor of cold sintered $Ca_{2.7}Bi_{0.3}Co_{3.92}O_{9+\delta}$ ceramic only reaches 280.0 $\mu Wm^{-1}K^{-2}$ at 800 K, inferior to the SPS-processed sample, it shows at least 85 % enhancement compared to published data for cold sintered calcium cobaltite. The Bi/Ba co-doping strategy helps to increase the power factor of the solid state synthesized calcium cobaltite by 10 %; this enhancement in electrical conductivity is highly restricted by the large porosity inside these samples.

The specific conclusions for each chapter were listed in following sections.

8.1.1 Modulation of electrical transport in calcium cobaltite ceramics and thick films

In Chapter 4, $Ca_{2.7}Bi_{0.3}Co_yO_{9+\delta}$ (y = 3.92, 3.96 and 4.0) ceramics were first prepared by solid state reaction. Subsequently, the optimal composition ($Ca_{2.7}Bi_{0.3}Co_{3.92}O_{9+\delta}$) was selected to fabricate the thick films by screen printing. The effects of chemical compositions and sintering conditions on thermoelectric performance were investigated for bulk ceramics and thick films, respectively. This work provides different insights into the grain growth mechanisms and enables enhanced power factors through controlling microstructural evolution by simply optimising the heat-treatment for thick film fabrication. The following conclusions can be drawn from the experimental results:

1) By introducing 2.0 at.% cobalt deficiency and 10.0 at.% Bi^{3+}substitution for Ca^{2+} in calcium cobaltite, the largest lattice expansion was revealed and the poorly conducting secondary phases were efficiently reduced. However, the electrical conductivity showed stronger correlation with the porosity; lower porosity led to a weakened carrier scattering and hence a higher carrier mobility.

2) The $Ca_{2.7}Bi_{0.3}Co_{3.96}O_{9+\delta}$ bulk ceramic showed the most complex phase assemblage, including the main phase (calcium cobaltite), $Ca_3Co_2O_6$ and Bi-rich phases, thereby leading to the most pronounced stoichiometric deviation from the theoretical <349> structure. This was responsible for the shrinkage of b_2 lattice parameter and preventing bismuth from entering the crystal lattice of calcium cobaltite.

3) The highest power factor of 98.0 $\mu Wm^{-1}K^{-2}$ was achieved for $Ca_{2.7}Bi_{0.3}Co_{3.92}O_{9+\delta}$ ceramics at 823 K, mainly due to the enhanced electrical conductivity, showing about 20.0 % enhancement compared to solid state synthesized calcium cobaltite ceramics in earlier studies.

4) When $Ca_{2.7}Bi_{0.3}Co_{3.92}O_{9+\delta}$ thick films were sintered at 1203 K for 8 h, the products were single-phase and yielded the maximum power factor of 55.5 $\mu Wm^{-1}K^{-2}$ at 673 K. Compared to the control groups sintered at 1153 K, the enhanced electrical transport properties resulted mainly from the higher carrier concentration and improved carrier mobility that was induced by larger grain size and stronger texture.

5) An order-disorder transition in the structural grain arrangements of the thick film could be found near the interface with the alumina substrate. The grain growth was closely correlated with the constrained sintering caused by the tensile stresses due to the mismatch of the thermal expansion coefficients between calcium cobaltite and alumina.

8.1.2 Enhancing thermoelectric performance of calcium cobaltite ceramics by optimising chemical composition and annealing process

In Chapter 5, highly dense $Ca_{3-x}Bi_xCo_yO_{9+\delta}$ (x = 0.1-0.3; y = 3.92-4.0) ceramics were successfully prepared by liquid-phase assisted spark plasma sintering. The effects of bismuth substitution, cobalt deficiency, and annealing processes on the thermoelectric response of calcium cobaltite were investigated in detail. This work demonstrates a simple route to enhance thermoelectric properties of calcium cobaltite by controlling microstructural evolution through tuning the chemical composition and annealing conditions. Based on the experimental evidence, the following conclusions can be drawn:

1) The electrical conductivity of the original SPS-processed samples was heavily limited by the presence of poorly conducting phases, including $Bi_2Ca_3Co_2O_9$, $Ca_3Co_2O_6$ and Co_3O_4. By annealing at 1203 K for 12 h in air, most of the secondary phases were efficiently reduced and even the trace of $Ca_3Co_2O_6$ was absent, thereby increasing the fractions of the primary phase (calcium cobaltite) and hence higher electrical conductivity.

2) The annealing process also helped to improve the texture by removing secondary phases that act to pin grains. This preferred grain orientation resulted in a decreased in-plane grain boundary density, thereby lowering the energy barriers at grain boundaries and hence enhanced carrier mobility.

3) Oxygen diffusion into the crystal lattice of calcium cobaltite was promoted by annealing in air, which efficiently suppressed the reduction of Co^{4+} caused by Bi^{3+} substitution for Ca^{2+}, thereby maintaining the carrier concentration at a high level.

4) The bismuth dopant took key roles in enhancing carrier mobility. The successful substitution of Bi^{3+} at Ca^{2+} sites in the rock salt layers led to severe lattice distortion. Larger lattice expansion with increasing bismuth substitution was responsible for larger inter-site hopping distances. On the other hand, the liquid phase sintering induced by bismuth oxide enabled grain sliding, grain growth and texture development, thereby increasing carrier mobility. The doping of 'heavy' bismuth ion also gave rise in the large mass variations in the crystal lattice, leading to enhanced phonon scattering and hence lower thermal conductivity.

5) Cobalt deficiencies provided more opportunities to generate crystalline defects such as stacking faults and cobalt vacancies; these defects can act as phonon scattering centres, helping to achieve lower thermal conductivity.

6) After annealing $Ca_{2.7}Bi_{0.3}Co_{3.92}O_{9+\delta}$ ceramics at 1203 K for 12 h, the products showed about 25 % increase in power factor (//ab) and 20 % reduction in thermal conductivity ($\perp$ ab) compared to most earlier studies. The maximum ZT value (//ab) of 0.16 at 823 K is very competitive due to use of the eco-friendly dopants and simple processing route.

8.1.3 Tuning the power factor of cold sintered calcium cobaltite ceramics by optimising heat-treatment

In Chapter 6, the optimal composition ($Ca_{2.7}Bi_{0.3}Co_{3.92}O_{9+\delta}$) in Chapter 5 was selected to prepare cold sintered ceramics. The effects of calcination process and annealing time on microstructure and thermoelectric response were investigated in detail. This work shows the great potential of the cold sintering method for fabricating thermoelectric ceramics and presents a feasible approach to modulating the power factor by controlling microstructural evolution via simple heat-treatment process. On the basis of the findings, the following conclusions can be drawn:

1) The double calcination process helped to reduce the content of secondary phases in both calcined powders and original cold sintered ceramics, thereby increasing the electrical conductivity by elevating the fractions of primary phase (calcium cobaltite).

2) Use of double-fired powders for cold sintered ceramics lead to enhanced preferred grain orientation after annealing, thereby increasing carrier mobility via the decrease of the in-plane grain boundary density.

3) By annealing at 1203 K, the secondary phases could be further reduced; the dark Ca-Co-O compounds were almost eliminated. The electrical conductivity was significantly enhanced by extending the annealing time.

4) The highest electrical conductivity was obtained for the cold sintered ceramic prepared from the double-fired powders with the holding time of 24 h, mainly due to the increased carrier mobility induced by the stronger texture and larger grain size. Notably, the corresponding Seebeck coefficients did not degrade significantly.

5) The maximum power factor of 0.28 $mWm^{-1}K^{-1}$ at 823 K was obtained for cold sintered $Ca_{2.7}Bi_{0.3}Co_{3.92}O_{9+\delta}$ ceramics prepared from the double-fired powders annealed at 1203 K for 24 h, showing at least 85 % enhancement compared to the data for cold sintered calcium cobaltite ceramics in previous investigations.

8.1.4 Modulation of thermoelectric response in calcium cobaltite ceramics through co-doping via different fabrication routes

In Chapter 7, $Ca_{2.63}Bi_{0.3}M_{0.07}Co_{3.92}O_{9+\delta}$ (M = Sr and Ba) ceramics were prepared by solid state reaction and spark plasma sintering, respectively. The as-prepared SPS-processed samples were further annealed at 1203 K for 24 h in air. The effects of dopants and fabrication routes on thermoelectric response were studied. This work provides insight and understanding of microstructure-property relationships in calcium cobaltite ceramics controlled by the dopants and fabrication routes. Furthermore, a facile and economical solid state synthesis route for $Ca_{2.63}Bi_{0.3}Ba_{0.07}Co_{3.92}O_{9+\delta}$ ceramics is demonstrated, achieving a high thermoelectric performance comparable to the SPS-processed $Ca_{2.63}Bi_{0.3}Sr_{0.07}Co_{3.92}O_{9+\delta}$ samples. The following conclusions are made based on the experimental results:

1) The roles of Bi/Sr and Bi/Ba dual dopants in $Ca_{2.63}Bi_{0.3}M_{0.07}Co_{3.92}O_{9+\delta}$ (M = Sr and Ba) ceramics were resolved: bismuth successfully entered the crystal lattice of calcium cobaltite; strontium was more likely to substitute calcium in rock salt sublayers; barium mainly participated in forming Ba-rich secondary phases.

2) In contrast to the low density limited by solid state reaction processing, the SPS route in conjunction with an annealing process was responsible for lowering the porosity, developing the texture and reducing the secondary phases.

3) The electrical conductivity of annealed SPS-processed Bi/Sr co-doped samples showed significant enhancement. The increased carrier mobility resulted from the reduced effective mass induced by successful Bi/Sr co-doping as well as the lower energy barriers at grain boundaries caused by combined effects of improved texture, increased grain size and promoted densification.

4) The annealed SPS-processed Bi/Sr co-doped samples showed stronger phonon scattering because of the mass variations and the strain field induced by the pronounced lattice expansion and higher porosity arising from the volatilization of the bright phases (Ca-Bi-Sr-Co-O compounds) during heat-treatment.

5) Despite the high porosity in solid state synthesized $Ca_{2.63}Bi_{0.3}M_{0.07}Co_{3.92}O_{9+\delta}$ (M = Sr and Ba) ceramics, these samples showed more pronounced phonon scattering at low temperatures. The larger porosity and point defect scattering parameters achieved in Bi/Sr

co-doped samples made major contributions to decreasing the phonon mean free path and reducing thermal conductivity.

6) The maximum ZT value of 0.14 was achieved in both the solid state synthesized Bi/Ba co-doped and annealed SPS-processed Bi/Sr co-doped samples at 800 K. Through Bi/Ba co-doping, the ZT value of solid state synthesized calcium cobaltite was increased, showing about 75 % enhancement compared to the undoped sample; this was also comparable to the performance of the dense SPS-processed Bi/Sr co-doped samples.

8.2 Recommended experiments for Future Work

8.2.1 Rietveld refinement fitting for XRD data

Although the Le Bail fitting is sufficient to refine the lattice parameters of calcium cobaltite by the profile intensity partitioning, the Rietveld method allows calculation of the atom occupancies. The changes in Co and O occupancies have significant influence on the presence of cobalt vacancies and oxygen vacancies, which provides insights into the changes in the carrier concentration. However, there are no available cif files for calcium cobaltite in the ICSD database because of its modulated misfit structure. Therefore, it is suggested that the supercell structure of calcium cobaltite should be established using the developer mode in Topas software. The successful creation of the cif file will help to increase the accuracy of the refined data.

8.2.2 Optimising the loading content and selection of the substrate for film fabrication

It can be clearly seen that the sintered calcium cobaltite thick films show about 30 % reduction in the power factor at 673 K compared to the value for sintered bulk ceramic. This should mainly result from the high porosity in the film and the interface layer formed due to constrained sintering. In order to improve densification, it is recommended that the mass ratio of organic binders between the loading powders should be investigated and optimised and that more layers should be printed onto the substrate to increase the green density. It is also recommended to choose an alternative substrate which has a thermal expansion coefficient much closer to that of calcium cobaltite.

8.2.3 Elemental doping at Co sites in calcium cobaltite

The doping strategies adopted in this study mainly focus on substitution at Ca sites in the rock salt layers of calcium cobaltite. However, elemental doping at Co sites in the [CoO_2] layers can also significantly modify the electronic structure of calcium cobaltite due to changes in the spin state of cobalt ions and hence the electronic density of state. Therefore, it would be helpful to explore the effects of dopants at Co sites on the thermoelectric performance based on the optimal composition achieved here.

8.2.4 Direct measurement of carrier concentration and mobility via the Hall effect

The values of carrier concentration (n) and mobility (μ) in the present work were determined by the modified Heikes formula. The approximate values can only be used to verify the variational trends for n and μ. Direct measurement via the Hall effect will yield more reliable data and lead to deeper understanding of the conduction mechanisms.

8.2.5 Preparing thicker cold sintered calcium cobaltite ceramics

This work shows that strong texture can be induced in calcium cobaltite by cold sintering. The electrical transport properties are well characterised whilst measurement of in-plane thermal conductivity is severely restricted by the thickness of the synthesized samples (at least 6 mm thick samples are required). In order to determine valid ZT values for the cold sintered ceramics, further investigations of the cold sintering processing parameters and systems are required to optimise the route. Thick samples without cracks are essential for reliable thermal conductivity measurements.

8.2.6 Advanced characterisation of synthesized samples

Advanced characterisation techniques such as synchrotron radiation X-ray diffraction and atom level super-STEM are recommended to accurately determine the crystal and microstructure structure of calcium cobaltite. This will provide deeper insight into the local atomic arrangements and texture development, because conventional TEM techniques do not have adequate resolution to provide the level of detail required for full unambiguous descriptions.

8.3 Scientific direction for Future Work

This study mainly focuses on modulating the electrical transport properties of calcium cobaltite by controlling the elemental doping and texture development, but limited investigations were conducted on modifying the thermal conductivity. For future work, it is promising to reduce the thermal conductivity through enhancing the phonon scattering by introducing nano-sized inclusions and reducing grain size.

Nano-sized inclusions such as Ag will be embedded at grain boundaries which will efficiently enhance the phonon scattering without degrading the electrical conductivity (Ag is highly conductive). The synthesized calcium cobaltite based materials in this work were prepared from the calcined powders via the mixed oxide route. Due to the characteristic of solid state reaction (mass-mass transfer mechanism during sintering), the resulting powders are usually at the micron size. However, smaller grain sizes can lead to a higher grain boundary density, thereby increasing phonon scattering and hence lower thermal conductivity. Various processing routes, including sol-gel synthesis, mechanical alloying and hydrothermal synthesis, can provide opportunities to produce nano-sized powders and investigate the effects of grain size on thermoelectric response of calcium cobaltite.

9. Appendix: List of Papers and Presentations

1. **J. Yu**, K. Chen, F. Azough, D.T. Alvarez-Ruiz, M.J. Reece, R. Freer, Enhancing the Thermoelectric Performance of Calcium Cobaltite Ceramics by Tuning Composition and Processing, ACS Appl. Mater. Interfaces. 12 (2020) 47634–47646.

2. **J. Yu**, Y. Chang, E. Jakubczyk, B. Wang, F. Azough, R. Dorey, R. Freer, Modulation of electrical transport in calcium cobaltite ceramics and thick films through microstructure control and doping, J. Eur. Ceram. Soc. 41 (2021) 4859–4869.

3. **J. Yu**, X. Liu, S. Shao, M. Nelo, S.J. Haigh R. Freer, Enhancing the thermoelectric performance of cold sintered calcium cobaltite ceramics by optimsing heat-treatment process. To be submitted.

4. **J. Yu**, K. Chen, F. Azough, M.J. Reece, R. Freer, Improved thermoelectric performance of calcium cobaltite by controlling composition and processing conditions, Oral Presentation, The 17th European Conference on Thermoelectrics, Cyprus (2019).

5. **J. Yu**, K. Chen, F. Azough, M.J. Reece, R. Freer, Tuning Composition and Processing Conditions to Enhance the Thermoelectric Performance of Calcium Cobaltite, Oral Presentation, Virtual Thermoelectric Conference (VCT2020) Organised by International Thermoelectric Society, Online (July, 2020)